FRACTURE CONDUCTIVITY BEHAVIOR IN SHALE FORMATIONS

A Dissertation

by

JESSE MATEO GUERRA

Submitted to the Office of Graduate and Professional Studies of
Texas A&M University
in partial fulfillment of the requirements for the degree of

DOCTOR OF PHILOSOPHY

Chair of Committee,	A. Daniel Hill
Committee Members,	Ding Zhu
	Michael Pope
	Nobuo Morita
Head of Department,	Jeff Spath

August 2019

Major Subject: Petroleum Engineering

ABSTRACT

The objective of this study was to further the understanding of fracture conductivity and its dependence on rock mechanical properties, mineralogy, and fracture surface attributes, as well as its impairment due to flowback, based on a systematic experimental study on several mudstone formations. As part of this objective, a practical workflow was developed to extend the measured conductivity behavior to downhole stress conditions.

The experimental measurements conducted in this study used mudstone samples obtained from outcrop and downhole core segments, from the Eagle Ford, the Marcellus, the Mahantango, the Middle Bakken, and the Three Forks formations. Fracture conductivity experiments were conducted utilizing a Modified API Fracture Conductivity Cell by flowing dry nitrogen and/or saline solutions representative of flowback water. As such, undamaged and water-damaged fracture conductivity was measured. Simulated fracture conditions included unpropped and propped fractures. Natural sand proppant, with a commonly used mesh size, was used with a variety of areal concentrations. Additional experiments consisted of evaluating rock mechanical properties, mineralogy, and fracture surface attributes.

A large degree of heterogeneity in properties was observed for each formation. Experimental measurements showed that fracture conductivity under increasing closure stress generally follows an exponential decline rate, which is manifested as a linear relationship on a semi-log plot that is condition-specific. These functions can be representative of the formation fracture conductivity behavior, and can be extended to additional simulated fracture conditions. Furthermore, these laboratory-based measurements can be related to downhole stress conditions predicated on poroelasticity theory. This estimated in-situ fracture conductivity can be used

during the performance evaluation of a hydraulically fractured horizontal well, or during the design of a new treatment.

This study provides an insight into fracture conductivity and its dependence on formation physical properties. Additionally, this study presents a practical application to the measurement of fracture conductivity in mudstones and its importance in evaluating well performance.

DEDICATION

I would like to dedicate this work and everything it represents, as it is a milestone long sought after from my humble beginnings in a far and away place from here, to my family: Dante Guerra, Juan Carlos Guerra, and Dana Marie Tierney.

My parents enabled me the opportunity to ultimately achieve this. Thank you for your love, support, and sacrifices. My brother, the only companion through a long and difficult journey, whom always helped me in more ways than I can recall, and whom without I undoubtedly would have never made it this far. My achievements through life would have not been attained without you.

The road to earning a Ph.D. has developed me both personally and academically, and albeit at times challenging, it has always been and shall always be rewarding.

ACKNOWLEDGEMENTS

I would like to extend my sincerest gratitude and appreciation to Dr. A Daniel Hill and Dr. Ding Zhu for enabling me the opportunity to be part of their research group. I am humbled and honored to have received from them countless learnings, enduring support, consideration, guidance, motivation, and patience. Looking into the future, I know I will continue to learn from them and continue to develop myself as a petroleum engineer.

I would like to thank Dr. Nobuo Morita for his insight and for always willing to discuss my research. I am grateful to have him in my committee.

I would like to thank Dr. Michael Pope for always supporting my research. I am also grateful to him for allowing me to participate in multiple field trips to gather outcrop samples. I not only gained valuable learnings from the geological and geophysics perspective, but I also enjoyed them.

I would like to acknowledge and show my lasting gratitude to Dante Guerra, my brother, for all his enduring support, inspiration, vision, ideas, and knowledge –all of which he shared in friendship and inevitably contributed to my success, and indisputably made everything possible. I would also like to thank my parents for engraving in me the importance of education and hard work.

I would also like to thank Ryan Winner for his support and friendship in and out of the office and laboratory. I would also like to thank all the members of the fracture conductivity research group: Cody Kainer, Omar Enriquez Tenorio, Ashley Knorr, Bill Foran, Mark McGinley, and Junjing Zhang. I would also like to thank Julian Uribe and Eduardo Luna for their assistance. And last but not least, I would like to thank John Maldonado, Sr. for his help and

availability pertaining to all things related to the laboratory and equipment. I would like to thank Don Conlee for his help, as well.

CONTRIBUTORS AND FUNDING SOURCES

Contributors

This work was supervised by a dissertation committee consisting of Professor A. Daniel Hill, primary advisor, Professor Ding Zhu, co-advisor, and Nobuo Morita of the Harold Vance Department of Petroleum Engineering; and Professor Michael Pope of Department of Geology and Geophysics.

The work described in Section 2.4.2 and Section 2.4.3 was completed by student Ashley Knorr under the supervision of Dr. Ding Zhu of the Harold Vance Department of Petroleum Engineering, in collaboration with student.

The work described in Section 3.2.1.3 and 3.2.2.3 was completed by student, in collaboration with student Omar Enriquez of the Harold Vance Department of Petroleum Engineering.

The work described in Section 2.4.5, Section 3.2.1.1, and Section 3.2.2.1 was completed by student, in collaboration with visiting scholar Julian Uribe and visiting scholar Eduardo Luna of the Industrial University of Santander.

All other work conducted for the dissertation was completed by the student independently.

Funding Sources

Graduate study was supported in part by a graduate research assistantship from Texas A&M University.

This work was made possible in part by funding provided by The Research Partnership to Secure Energy for America, Project Number: 11122-07 (Program Name: 2011 Unconventional Resources; and Project Name: Conductivity of Complex Fracturing in Unconventional Shale Reservoirs).

NOMENCLATURE

z	Measured height value on fracture conductivity test sample fracture surface, L, (in.)
d_{50}	Median proppant diameter, L, (in.)
Δz_{max}	Maximum difference in measured heights across fracture conductivity test sample fracture surface, L, (in.)
h	Reservoir thickness, L, (ft)
x_e	Horizontal well length, L, (ft)
y_e	Distance to outer boundary, L, (ft)
A_{cw}	Total matrix/fracture surface area draining into fracture system, L^2, (ft^2)
L	General fracture spacing, L, (ft)
w_f	Fracture width, L, (in.)
k_f	Fracture permeability, L^2, (md)
k_m	Matrix permeability, L^2, (md)
c_t	Total compressibility, $M^{-1}Lt$, (psi^{-1})
C_f	Fracture conductivity, L^3, (md-ft)
σ_c	Closure stress, $ML^{-1}t^{-2}$, (psi)
C_{f0}	Initial fracture conductivity at zero closure stress, L^3, (md-ft)
λ	Exponential decline rate constant, $M^{-1}Lt^2$, (psi^{-1})
p_i	Initial reservoir pressure, $ML^{-1}t^{-2}$, (psi)
p_{wf}	Wellbore flowing pressure, $ML^{-1}t^{-2}$, (psi)
t	Time, t, (days)

q_{DL}	Dimensionless flow rate for a rectangular geometry in a dual porosity model
q_g	Volumetric gas flow rate, L^3t^{-1}, (Mscf/day)

TABLE OF CONTENTS

Page

LIST OF FIGURES

Page

LIST OF TABLES

Page

1. INTRODUCTION

1.1 Background

With the advent of horizontal drilling and hydraulic fracturing, shale gas and oil reservoirs were brought to the forefront of the oil and gas industry. Hydraulic fracturing techniques, as ever evolving as they are, and irrespective of their specifics and variety, in their essence create a network of fractures in these organic-rich mudstones. This fracture network serves as pathways for the reservoir fluids to reach the wellbore, greatly enhancing and in most cases enabling economically-viable production in these low permeability unconventional reservoirs.

These pressure-induced fractures are created by injecting fluid into the formation at pressures above the fracture pressure, also known as the pad stage, and the ensuing proppant-laden stages deliver the proppant into the fracture, allowing for a post-treatment high permeability zone (in which all stages contributed to fracture growth). In addition to these propped fractures, newly created unpropped fractures in combination with possible re-activated natural fractures, define the stimulated reservoir volume.

The ability of these fractures to conduct these fluids is defined as fracture conductivity, a product of the fracture permeability and the fracture width. This metric serves as a means to evaluate fracture deliverability, and ultimately well productivity. The fracture network conductivity, including the effect of proppant distribution and the relation between propped and unpropped fractures, was shown to be of great impact on well performance by numerous studies, including by Mayerhofer et al. (2006), Cipolla et al. (2009), and Cohen et al. (2017).

Fracture conductivity is determined broadly by the fracture treatment design, the physical properties of the formation, and the effective closure stress on the fracture. Additionally, it can be significantly impaired due to water-rock interactions, amongst other damage mechanisms.

These organic-rich mudstones formations, inclusive of shales, are fine-grained sedimentary rocks with complex mineralogy, and are comprised of a composite of biogenic and terrigenous sources of siliciclastic or carbonate debris –or both, subjected to diagenesis (Gamero-Diaz et al., 2013). These rocks are constituted of clay mineral particles and small fragments of other minerals, including calcite and quartz (Zhang, 2014). These liquids-rich formations often have high carbonate content. The sedimentation and stratigraphy of these organic mudstones contributes to their high degree of anisotropy (Passey et al., 2010; Slatt and Abousleiman, 2011; Gamero-Diaz et al., 2013); which can be at a local or regional scale (Suárez-Rivera et al., 2006, 2011). The degree of heterogeneity of these mudstones is also elevated by the presence of high lamination and density of natural fractures present in the formation, all of which add to the complexity of drilling and completion operations in such plays.

Understanding the creation of fracture conductivity, its influencers, and impairment is of great significance to the betterment of hydraulic fracturing operations across shale plays. And with the ongoing discussion of universality between shale properties, academic and industrial, proven to be inconclusive, additional investigations are needed across every major shale play to arrive at conclusive behaviors specific or common to each one of them. Numerous studies, including by Pedlow and Sharma (2014) and Kias et al. (2015), have supported the argument against universality between shale properties, and discussed the implications on fracture design parameters.

Building on this background, this systematic experimental study was undertaken to further the understanding of fracture conductivity of mudstone formations and its dependence on rock mechanical properties, minerology, and fracture surface attributes, as well as the conductivity impairment due to flowback and other special topics. Additionally, a practical workflow was developed to relate the measured fracture conductivity behavior to downhole stress conditions.

1.2 Literature Review

This section presents the relevant framework material for this study, while also providing a summary of the prior body of work. This includes a brief overview of hydraulic fracturing, expected proppant distribution within the fracture, shale formations, background information on fracture conductivity experimental evaluation, its calculation, influencing factors pertaining to the formation and the fracture surface, bedding plane orientation, a special topic related to proppant pack self-channeling, and the impairment of conductivity due to flowback as one of the primary damage mechanisms. Additionally, the performance of a multistage fractured horizontal well is discussed within the framework of this study.

1.2.1 Hydraulic Fracturing

Hydraulic fracturing is one of the most significant and long-lasting technologies in the oil industry, and is the principal method of enlarging and maintaining well productivity (Smith and Montgomery, 2015).

Ever since the first known hydraulic fracturing job was conducted by Stanolind Oil in 1949, over 2.5 million fracture treatments were conducted and presently approximately 60% of

all drilled wells undergo fracturing (Smith and Montgomery, 2015). Since then, the technologies and equipment, fracturing fluids, additives, proppants, and every aspect of what defines a hydraulic fracture treatment is constantly evolving.

For instance, the hydraulic horsepower per treatment has increased from approximately 10 to well over 1,500 HHP on average (Smith and Montgomery, 2015). Fracturing fluids have migrated from the use of gelled crude to refined crude oils, to the use of water with cross-linkers and gelling agents, among other advances which also include environmental considerations. Contemporarily, several fluid systems are available, including water frac, linear gel, cross-linked gels, oil-based fluids, foam/polyemulsions, and others (Gidley et al., 1989; Economides and Nolte, 2000; Economides and Martin, 2007; Smith and Montgomery, 2015).

A method that has gained popularity in shale formations recently is slickwater treatments, also known as water frac or river frac, which utilizes large volumes of water with a friction reducer, or low concentrations of linear gel (10 PPTG), at high injection rates (60-120 bbl/min) to compensate for the inherent low viscosity, enabling for adequate proppant transport (Palisch et al., 2010). Water fracs have the advantage of low cost, ease of mixing, and reuse (Smith and Montgomery, 2015). Although this method relies on very low proppant concentrations (generally below 3 PPGA), it places several hundred thousand to millions of pounds of proppant per stage (Palisch et al., 2010). Furthermore, such method was attributed to creating complex fracture geometries and increased conductivity through displaced fractures, and by such, to a larger stimulated reservoir volume, which in turn leads to higher production, enabling water fracs to be preferred across several shale plays (Fredd et al., 2001; Mayerhofer et al., 2006; Shelley et al., 2008).

The type and quality of proppants have improved drastically from the original screened river sand to industry standard quality sand, International Organization for Standardization (ISO) 13503-2 (2008) and ISO 13503-5 (2008), to now include proppant agents such as sintered bauxite, lightweight ceramics, and resin-coated sands (Smith and Montgomery, 2015). The use of high-quality sand is widespread, in part due to its relatively low cost and availability, and constitutes roughly 90% of the proppant market on a weight basis (Smith and Montgomery, 2015). Presently, pumped proppant concentrations range from a low concentration at the beginning of the job, to a larger concentration at the end of the job. The in situ hydraulic fracture process evolution is shown in **Figure 1a** for an ideal support fluid, where the 5 PPG stage concentrated to a final concentration of 8 PPG (Smith and Montgomery, 2015). For a slickwater-type job, however, proppant settles out of the fluid near the wellbore, and as such this banking fluid behavior results in a high conductivity area near the wellbore, as shown in **Figure 1b**. Added to the previous, larger size proppants are often pumped in the tail-in stage (Coulter et al., 2004).

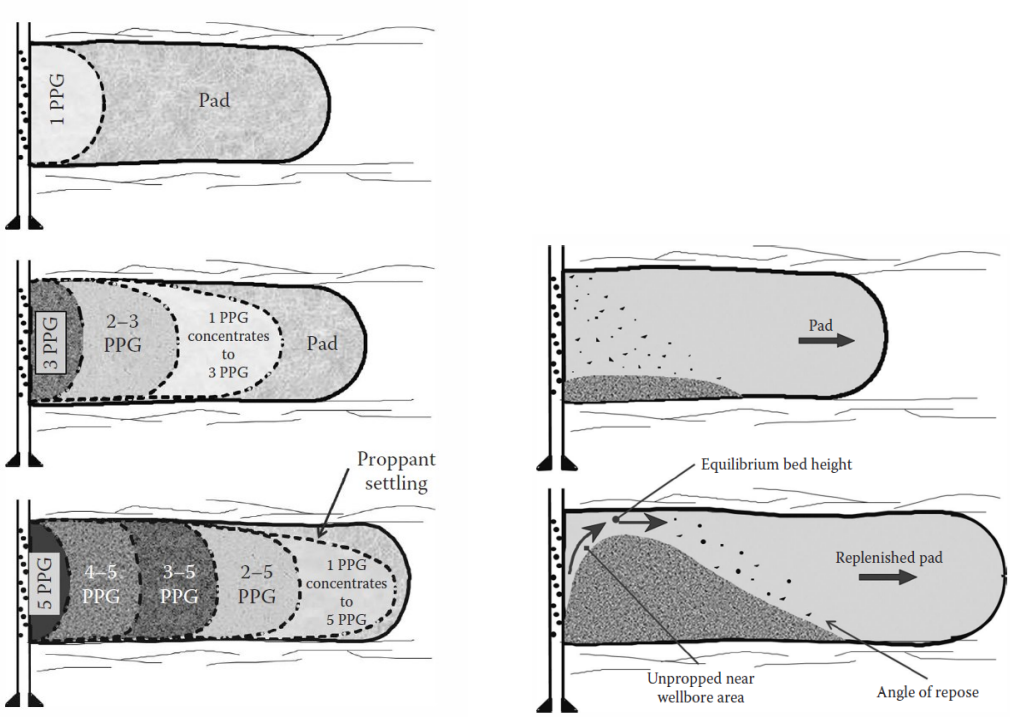

Figure 1 – Perfect Support Fluid Behavior (Smith and Montgomery, 2015).

Current fracture treatments, albeit specific to each shale play and to the operator/service company, have increased drastically in terms of total fluid and total mass of proppant pumped downhole; for instance an example of a contemporary fracture treatment for the Permian Basin entails 50 bbl/ft of fracturing fluid, 3,000 lb_m/ft of proppant, 100 ft stage spacing, and 5 clusters per stage –and even this design is subject to change as new developments are considered.

The concept of proppant pack monolayer and partial monolayer was explored in detail by several studies, including by Darin and Huitt (1959), Brannon et al. (2004), and Palisch et al. (2010). Monolayers and partial monolayers were shown to yield significant conductivity due to the sparse distribution of proppant on the fracture, albeit with strength and non-laminar flow concerns. Laboratory-scale tests conducted by Brannon et al. (2004) showed that an ultra-light

weight proppant forming a partial monolayer could have up to an order of magnitude larger fracture conductivity compared to a similarly sized sand at 1 lb_m/ft^2.

Although the current trend changed somewhat from the monolayer or partial monolayer to now having higher sand concentrations in the fracture (Smith and Montgomery, 2015), low sand concentrations regions are still prevalent. For instance, low concentration slurries, 0.25 to 1.0 PPGA, are typically employed in the early slurry stages in shale gas wells, with the last stages ranging from 2.0 to 3.5 PPGA (Zhang, 2014).

1.2.2 Expected Proppant Distribution within the Fractures

Irrespective of the fracture treatment schedule, it is highly improbable that proppant is evenly distributed across the complex fracture network created in these unconventional formations, due in part to proppant transport limitations inherent to slickwater fracturing (Warpinski et al., 1987, 1991, 2008, 2009; Cipolla et al., 2009).

Under this presumed reality, proppant is transported through fluidization and sedimentation, resulting in fractures that may be unpropped, propped with a wide range of proppant concentrations depending on the location within the fracture, or may be within an arch region where there is no proppant but the fracture faces are not in direct contact due to said region interfacing between a relatively high concentration propped region and an unpropped region (Britt et al., 2006; Cipolla et al., 2009; Warpinski, 2009; Palisch et al., 2010), as shown in **Figure 2a**. **Figure 2b** shows the proppant being transported in the same manner, but due to fracture surface irregularities, the proppant is accumulated at pinch points, pillars, and other surface abnormalities (Palisch et al., 2010). **Figure 2c** shows the fracture having a proppant

monolayer or a partial monolayer, due in part to the proppant grains being forced into narrow openings (Brannon et al., 2004; Palisch et al., 2010).

Further categorization of fracture conditions can include unpropped and propped fractures that can be aligned or displaced –caused by shear slippage (Fredd et al., 2001; Zhang, 2014). Such rock discontinuities in unpropped fractures, can be described by classical models including the one developed by Barton et al. (1985), where fracture width can be related to the resulting contact stress.

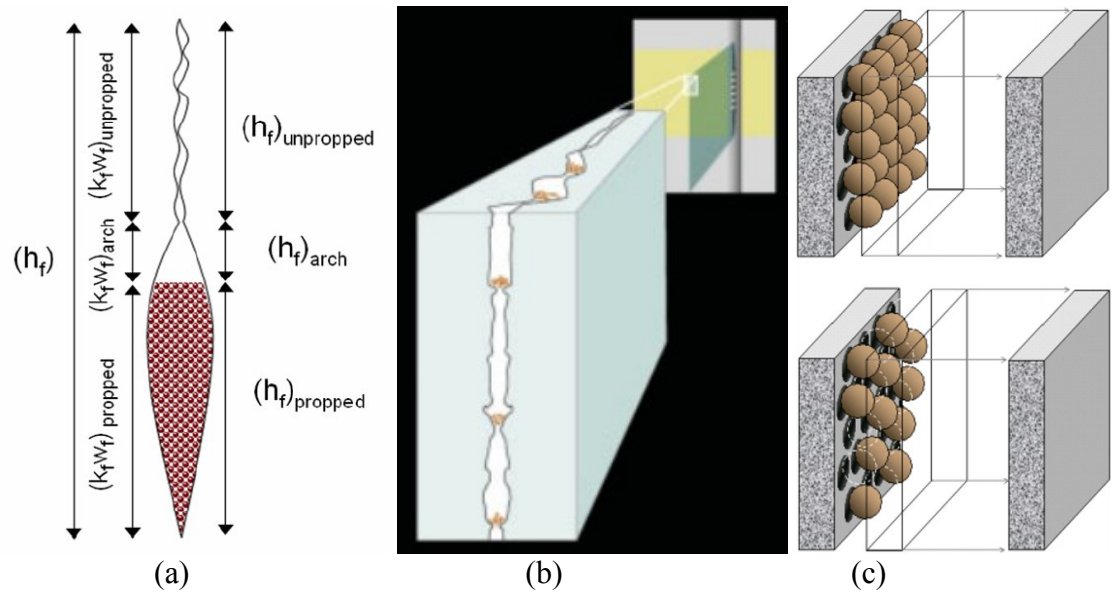

Figure 2 – Vertical Proppant Distribution along the Fracture: (a) Representation of Proppant Bed, Arch, and Unpropped Region Above the Arch (Cipolla et al., 2009); (b) Representation of Proppant Gathering Due to Fracture Face Nodes and Irregularities (Palisch et al., 2010); (c) Representation of a Full Monolayer and a Partial Monolayer (Brannon et al., 2004).

The created complex fracture network, with its considerable fluctuation in concentration and distribution of proppant, and its resulting fracture conductivities, significantly impact the initial and long term production of that particular stimulated reservoir volume (Suárez-Rivera et al., 2013). Understanding the fracture conductivity behavior for these fracture conditions is

paramount to understanding, and ultimately maximizing, the well productivity. Under this premise, one aim of this study was to further the understanding of fracture conductivity behavior considering several fracture conditions (ranging from no proppant to moderate proppant loadings), through a systematic experimental investigation.

1.2.3 Shale Formations

Mudstone reservoirs can be found globally, and according to the U.S. Energy Information Administration (2013), as of 2013 there are 137 technically recoverable shale oil and shale gas resources distributed over 42 countries, including the U.S. However, the development of these mudstone reservoirs has thus far been principally confined to those found in the U.S. and Canada. **Figure 3** illustrates the key tight oil and shale gas regions within the lower 48 states of the U.S. that have driven the majority of the U.S. output growth in recent years (U.S. Energy Information Administration, 2018).

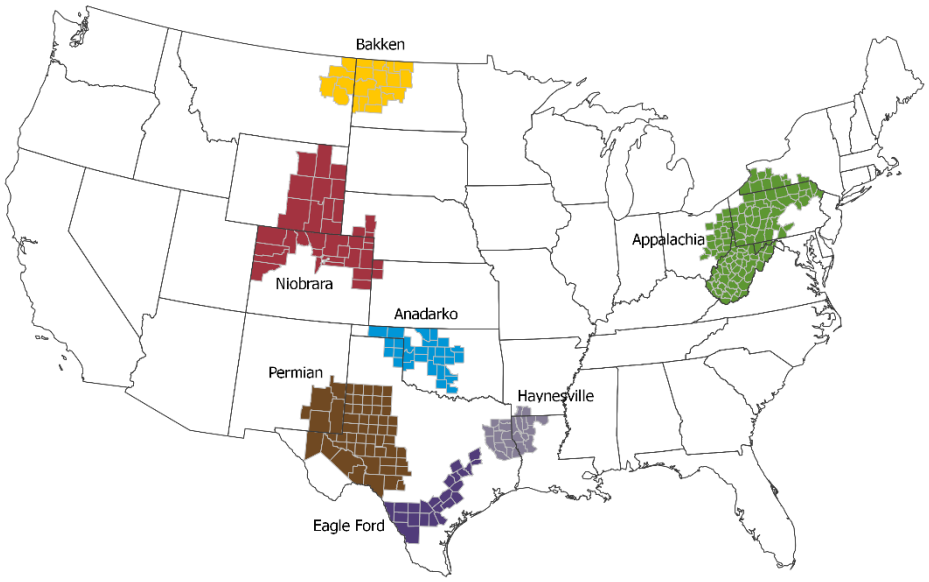

Figure 3 – Key Tight Oil and Shale Gas Regions in the Lower 48 States of the U.S. (U.S. Energy Information Administration, 2018).

This study investigated mudstone formations from the Eagle Ford, the Appalachia, and the Bakken regions as per **Figure 3**, and described in detail in Section 2.2.

1.2.4 Fracture Conductivity: Laboratory-Based Determination

Fracture conductivity can be determined by laboratory-based procedures which rely on a standard ISO or a non-standard (or modified) ISO fracture conductivity test, one attesting to ideal conditions and the other attempting to honor more realistic in-situ conditions, respectively.

Under ideal (non-realistic) conditions, fracture conductivity is estimated based on proppant permeability and loading data. ISO standards dictate repeatable and controllable procedures for conducting laboratory-based fracture conductivity tests, and are typically reliant on the use of a Standard American Petroleum Institute (API) Fracture Conductivity Cell, as shown in **Figure 4**.

A grouping of API/ISO standards prescribe the evaluation and reporting procedures for proppant conductivities (Smith and Montgomery, 2015). These standards include the API RP 19C/ISO 13503-2 (2008), and the API RP 19D/ISO 13503-5 (2008). The API RP 61 (1989) dictates practices for evaluating short-term proppant pack conductivity, whereas the API RP 19D (2008) prescribes practices for long-term conductivity measurements.

Under the these ideal conditions, the typical standard ISO fracture conductivity test involves placing 2 lb_m/ft^2 of proppant between two thin parallel Berea Sandstone platens, and subjecting that proppant pack to a range of loads, during which 2% KCl water is flowed through the fracture. Fracture conductivity results are presented as a function of the stress applied (closure stress).

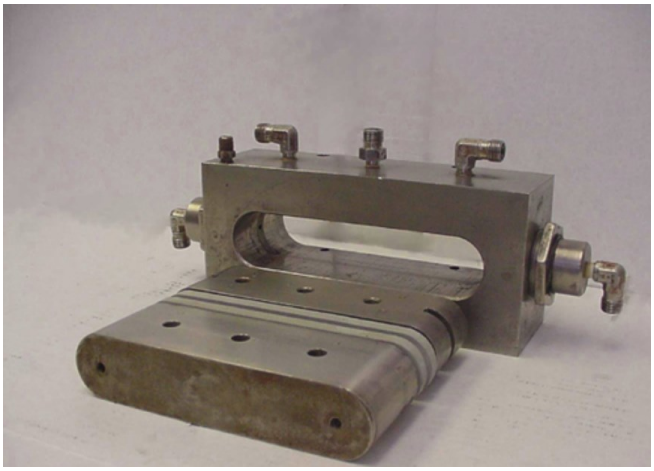

Figure 4 – Standard API Fracture Conductivity Cell for Laboratory-Based Fracture Conductivity Tests (Economides et al., 2013).

These results from idealized testing conditions are often orders of magnitude higher than the realistic fracture conductivity in the downhole fractures, but allow for comparison of proppants (Economides et al., 2013).

Factors that affect the outcome of the test include specifics of the experimental procedures such as duration of the test, the presence of oxygen in the test fluid, and the gathering and placement of the proppant pack (Smith and Montgomery, 2015). Several modifications to the API fracture conductivity procedures were proposed, including by Ereaux (2017) pertaining to proppant placement during experimental testing.

The reproduction of in-situ conditions is an ongoing challenge, historically and contemporarily (Economides et al., 2013; Smith and Montgomery, 2015). There are several factors that greatly reduce the ideal proppant pack permeability, including but not limited to fracture width corrections, proppant embedment, time and temperature effects, cyclic loading, fines migration (due to surface spalling and proppant crushing), fluid damage, non-Darcy flow

effects, and multiphase flow effects (Cooke, 1973; Barree and Conway, 2009; Palisch et al., 2007, 2010; Smith and Montgomery, 2015).

The fracture conductivity estimated under ideal conditions can be corrected to account for the aforementioned in-situ considerations by running more realistic laboratory tests or by predicting fracture conductivity loss with commercial-scale software suites, such as Predict-K (Duenckel et al., 2017; Stim-Lab Proppant Consortium, 2018). In an attempt to better honor the in-situ conditions, under realistic conditions (as best possible), modified ISO fracture conductivity testing procedures and setups were developed, primarily in the academic and research setting. This category of tests include test samples that can be rectangular shaped with rounded edges, or cylindrical-type core plugs (Ramurthy et al., 2011); while also ranging from a smooth saw-cut fracture surface, to a synthetically manufactured or induced rough surface. Cylindrical-type core plugs typically have smaller dimensions than their API-based fracture conductivity cell test sample counterpart.

Some efforts have focused on variants reliant on Hassler-type core holders such as work done by Wu et al. (2017), while others have directed their work centered on the use of a Standard API Fracture Conductivity Cell that was modified to suit their goals and research focus. Numerous works were conducted by utilizing their own specific modifications to the Standard API Fracture Conductivity Cell, including Wen (2007), Pedlow (2013), Awoleke (2013), Zhang (2014), and Shekhawat and Pathak (2016), to name a few. Among the diverse modifications made in several works, the most common was to accommodate for a thicker sample (up to 3 times) to allow for fluid leakoff considerations, expanding the fluids flowed through the fracture to include dry and wet gas, fresh and saline water, and multiphase flow conditions (Zhang, 2014).

For instance, a sampling of prior work includes the following. Darin and Huitt (1959) investigated partial-monolayer considerations and showed that a partial-monolayer could achieve comparable conductivities to that of an approximately 4.0 lb_m/ft^2 proppant pack. Cooke (1973) investigated the effect of brine at elevated temperatures under non-laminar flow at high closure stresses, concluding that the resulting conductivity suffered some hindrance; additionally, the fracture conductivity cell used in that work served as the basis for the presently used Standard API Fracture Conductivity Cell (Zhang, 2014). Cooke (1975) investigated the impact of fracturing fluids and concluded that the residue from the fracturing fluid and proppant characteristics ultimately determined the fracture conductivity. Fredd et al. (2001) investigated the effect of surface asperities and effects of surface displacement, and showed that significant fracture conductivity can be obtained under unpropped fracture conditions. Other considerations such as dynamic proppant placement tests were conducted by Marpaung et al. (2008) and Awoleke et al. (2012), multiphase flow and non-laminar flow was investigated by Barree and Conway (2009), and water sensitivity was investigated by Conway et al. (2011), to name a few.

Amongst the plethora of prior work pertaining to estimating realistic fracture conductivity, the research efforts undertaken by Stim-Lab (Core Laboratories), have showcased a successful workflow that modifies the standard ISO fracture conductivity test results to account for damage mechanisms (derived and measured), resulting in predictive models based on correlations (Zhang, 2014).

Under these considerations, one aim of this study was to attain more realistic fracture conductivity measurements through the use of a modified ISO fracture conductivity test that employs a Modified API Fracture Conductivity Cell, better reflecting in-situ conditions as best as possible.

1.2.5 Fracture Conductivity: Modified API Fracture Conductivity Cell

The Modified API Fracture Conductivity Cell used in this study, which builds upon the Standard API Fracture Conductivity Cell defined by API RP 61 (1989), is a modified ISO fracture conductivity test.

The most notable differences are in sample height due to the induced fracture on the fracture conductivity test sample, as well as the frequent need to utilize sandstone inserts depending on the original size of the acquired mudstone sample. The overall fracture conductivity test sample dimensions are 1.61 in. in width by 6 in. in height by 7.10 in. in length, with rounded ends. The mudrock portion ranges from 2.5 in. up to the entire height, whereas the sandstone inserts serve as a filler to ensure the overall dimensions. These aspects are covered in detail in Section 2.2.4.1.

Major advantages of this testing cell over other versions of Modified API Fracture Conductivity Cells and Hassler-type core holders alike, include the ability to test an actual formation sample with an induced fracture (which results in a rough and tortuous fracture surface –rather than steel or Berea Sandstone platens), a relatively large sample size (allowing for a sufficient distance for flow development), and the ability to flow dry gas or saline water solutions given the ancillary assembled setup –as described in Section 2.4.1.

Use of this particular Modified API Fracture Conductivity Cell has produced reliable results for both non-damaging (dry nitrogen flow) and damaging (water flow) fracture conductivity tests (including Awoleke, 2013; Zhang, 2014; McGinley, 2015; Enriquez, 2016; Guerra et al., 2017).

These modifications still honor the same footprint dimensions set by the API/ISO standards as well as the majority of the procedural reasoning, allowing for measurement

comparison with those results obtained utilizing the Standard API Fracture Conductivity Cell under the standard ISO fracture conductivity test.

1.2.6 Fracture Conductivity: Calculation

Fracture conductivity is calculated by relying on an explicit Darcy-based or non-Darcy-based relationship, as described in detail in Section 2.7. The complexity of said equations rely on several considerations, including accounting for the type of fluid flowed through the fracture. In the experimental setting, the basic premise relies on achieving a steady-state flow rate thought the fracture and measuring a pressure drop between two reference points –which experimentally involves recording the system (or cell) pressure as well, from which a fracture conductivity value can be calculated.

1.2.7 Fracture Conductivity: Inducing Fracture in Test Sample

Several methods of inducing a fracture on a fracture conductivity test sample for use in a Modified API Fracture Conductivity Cell were reported in literature, such as employing masonry rock splitter blades as done by Fredd et al. (2000). More commonly however, test samples are saw-cut and in some cases the surface is roughened, irrespective of whether the test sample is intended for an API-based fracture conductivity cell or a Hassler-type core holder. In this study, an aim was to design and develop a new and improved method for inducing a fracture in the fracture conductivity test samples, by enabling a Mode I fracture to occur, as described in Section 2.2.4.1.

1.2.8 Fracture Conductivity: Influencing Factors – Mechanical Properties

The concept of well productivity depending on contacting good quality reservoir rock with sufficient surface area, and the preservation of fracture conductivity, was discussed by several authors, including Suárez-Rivera et al. (2013) and Johri and Zoback (2013).

Fracture complexity depends in part on the density, mechanical strength, and orientation of weak planes with respect to the in-situ stress (Suárez-Rivera et al., 2013). Further supporting the importance of bulk mechanical properties, Jansen (2014) showed that the Young's modulus had an influence on fracture conductivity decline as closure stress increased. Additionally, as Jansen (2014) concluded, and widely agreed upon by other works, brittle shale intervals with a low Poisson's ratio and a high Young's modulus are ideal for complex fracture network generation. Knorr (2016) also showed that propped fracture conductivity behavior was influenced by proppant properties and rock mechanical properties, manifested in the fracture conductivity decline as closure stress was increased. Furthermore, and adding to the importance of measuring bulk mechanical properties, the three most widely used two-dimensional models to calculate fracture width assuming a constant or average fracture height, according to Economides et al. (2013), are the Perkins and Kern (1961) and Nordgren (1972) PKN (for the case of a Newtonian fluid, in this reference case), the Khristianovic(h) and Zheltov (1955) KGD, and the Geertsma and de Klerk (1969) models; of which the first two require a few known values, which include a value for Young's modulus and Poisson's ratio for the calculation of the plane strain modulus, and the third necessitates the Poisson's ratio amongst its variables.

As discussed in Section 1.2.13, surface hardness is heavily penalized under water-rock interactions. Alramahi and Sundberg (2012) showed that mechanical properties had an inverse relationship with fracture conductivity loss for several shales –a high Young's modulus

corresponded to a low proppant embedment. Similarly, Eagle Ford shale rock mineralogy and mechanical properties were shown to have an effect on fracture conductivity (Jansen, 2014; Enriquez, 2016).

High surface hardness, a surface mechanical property, mitigates embedment between unpropped and propped fractures, contributing to the longevity of fracture conductivity (Suárez-Rivera et al., 2013). Prior work alluding to the importance of surface hardness includes Ramurthy et al. (2011), Enriquez (2016), Kainer (2017), and several others.

Kainer (2017) evaluated a comprehensive database of experimental fracture conductivity values and showed that fracture conductivity decline was correlated to Brinell hardness and Young's modulus, although acknowledging that closure stress and proppant loading had a higher influence on conductivity when compared to rock mechanical properties. With the prior context, another aim of this study was to measure bulk and surface mechanical properties, including Young's modulus and Poisson's ratio, as well as surface mechanical properties such as Brinell hardness, with the intention to contribute to the understanding of their influence on fracture conductivity; by expanding the focus of the investigation to include test samples obtained from formation intervals not previously considered.

1.2.9 Fracture Conductivity: Influencing Factors – Mineralogy

According to Enriquez et al. (2016), there is a direct relationship between fracture conductivity and rock brittleness based on mineralogy, while there is an inverse relationship with the Poisson's ratio; albeit both with relatively low coefficients of determination. Furthermore, Kias et al. (2015) stated that mineralogy played a significant role in mechanical properties as they relate to brittleness, as in the case of hardness when investigating the Floyd, Eagle Ford,

Haynessville, and Barnett shales. Aoudia et al. (2010) suggested that statistical analysis showed a strong influence by clay and quartz content on Poisson's ratio and the Young's modulus, although their investigation was limited to the Woodford shale. As discussed in Section 1.2.13, damage to fracture conductivity showed a correlation to mineralogy for a variety of shales according to Pedlow and Sharma (2014), and many others.

Bulk and surface mineralogy, determined through the use of Standard X-ray Powder Diffraction (XRD) and through X-ray fluorescence (XRF), respectively, was shown to not only be useful but necessary to fully understand the mineral composition of test samples and mudstone units alike, as exemplified by Iriarte (2017), Aguilar (2014), Chatellier et al. (2014), Wu et al. (2017), Guerra et al. (2017), and others.

With the prior context, another aim of this study was to measure bulk and surface mineralogy, with the intention to contribute to the understanding of its influence on fracture conductivity and mechanical properties; by expanding the focus of the investigation to include test samples obtained from formation intervals not previously considered.

1.2.10 Fracture Conductivity: Influencing Factors – Surface Attributes

Measurement of surface mineralogy, as discussed in Section 1.2.9, was included as part of the aims of this study. Other surface attributes, such as surface roughness and area were shown to influence fracture conductivity measurements (McGinley, 2015; Enriquez, 2016; Guerra et al., 2017). These studies showed that a high initial surface roughness correlated to a high initial fracture conductivity. Additionally, surface roughness and mismatched opposing fracture surfaces were attributed to contributing to fracture conductivity in the way of width (Branagan et al., 1996; van Dam and Pater, 1999; Kassis, 2011). Added to the surface

characterization, the acquisition of the fracture surface profile, which includes surface roughness, area, and other considerations, was also undertaken as part of this work for test samples obtained from formation intervals not previously considered.

1.2.11 Fracture Conductivity: Influencing Factors – Bedding Orientation

The effect of bedding plane orientation on fracture conductivity measurements was investigated to some degree by Perez (2015), McGinley (2015), Knorr (2016) and Enriquez (2016) for formations including the Marcellus and the Eagle Ford. These previous studies employed the Modified API Fracture Conductivity Cell utilized in this study, however they unanimously agreed on the need for more experimental work to draw any meaningful conclusions from the influence of bedding plane orientation on fracture conductivity.

However, at a certain scale yet to be determined, bedding plane orientation may play a role in fracture complexity, which amongst other things can result in non-uniform proppant placement. As mentioned earlier, fracture complexity depends in part on the density, mechanical strength, and orientation of weak planes with respect to the in-situ stress (Suárez-Rivera et al., 2013). Considering that most of these mudstone formations are highly heterogeneous and anisotropic, and as such fracturing typically yields complex fracture networks (Daniels et al., 2007), fracture conditions in which flow is on, along, and across the bedding plane probably exist and are inevitable. Under this context, another aim of this study was to investigate the effect of bedding plane orientation on fracture conductivity, with the intent of bringing some clarity to prior fracture conductivity findings whenever applicable.

1.2.12 Fracture Conductivity: Self-Channeling in the Proppant Pack

As a fractured well produces, fracture conductivity usually declines due to proppant crushing and embedment, which reduce both width and permeability of the proppant pack; and fines plugging, which reduces permeability. To create enough permeability and make it last as long as possible, new approaches of packing proppant were studied and also applied in the field. These include pulse injection with fiber material added to the slurry of fracture fluid, often referred to as HiWAY flow-channel fracturing technique (by Schlumberger Limited). Pulse injection of fiber material creates channels in the proppant pack by discontinuously placing the proppant through proprietary techniques, and it was theorized by Gillard et al. (2010) that infinite fracture conductivity could be achieved due to the void spaces generated inside the fracture. Such technique reportedly reduced production decline rates in Eagle Ford shale wells (Thompson and Peña, 2015). Another improved proppant placement method is alternate-slug injection, which alternates the injection fluid viscosity, and where the proppant is transported by the low viscosity fluid (Malhotra et al., 2014).

Major factors in achieving flow channels within the proppant pack are rates of injection during hydraulic fracturing, fluid viscosity, and fracture surface attributes that influence proppant transport and distribution (Raimbay et al., 2015; Gomaa et al., 2016). Inherently the closure stress, the formation properties, and the overall fracture treatment design govern the resulting well productivity. Other recent studies include those by Zhen et al. (2016), who developed expressions for fracture permeability by accounting for the effect of proppant distribution, as well as Hou et al. (2016) who investigated the optimization of channel fracturing via heterogeneous proppant placement, and Nguyen et al. (2014) who investigated the use of low-quality sand as proppant pillars.

Among the battery of fracture conductivity experiments conducted, a channeling effect was observed in the proppant pack for a small subset of these tests, supporting prior results from channeling studies. This study includes a brief investigation of the injection procedure and proppant concentration for this small subset of tests, with the aim to analyze the possible creation of channels in field fracture treatments through the fracture treatment design.

1.2.13 Fracture Conductivity: Water-Induced Impairment

The preservation of fracture conductivity and fracture surface area is a significant economic issue in tight shale plays (Suárez-Rivera et al., 2013; Ghassemi and Suárez-Rivera, 2012). Based on this fact, mitigating damage to fracture conductivity through the understanding of its causes and possible preventative measures is paramount.

Influencing factors on fracture conductivity damage were previously investigated reflecting realistic downhole conditions, including the effect of fracturing fluids by Cooke (1975), measurements under in-situ conditions by Parker and McDaniel (1987), water-fracturing by Fredd et al. (2001), slickwater fracturing by Palisch et al. (2007), sensitivity of fluids in shales by Ramurthy et al. (2011), and the effect of fracturing fluids on rock mechanical properties by Akrad et al. (2011).

Water-induced fracture conductivity loss in shales was previously investigated with respect to proppant embedment and bulk mineralogical composition (i.e., spot analysis via XRD). Zhang et al. (2014) showed the effect of excessive proppant embedment due to fracture surface softening after water exposure, while Zhang et al. (2015) showed that clay content correlated to the fracture conductivity damage by water. The study conducted by Zhang et al. (2015) showed evidence of shale fines migration, while crushed proppant particle migration was

not observed. In the previously mentioned studies, Barnet shale samples were obtained from an outcrop located in San Saba, Texas, while the Eagle Ford shale samples were limited to those gathered from roadcuts northwest of Del Rio, Texas, notably only representing the highest organic content unit across the entire lithostratigrapy of the Eagle Ford shale outcrop.

The formation mineralogy inherently has a role in determining the tendency it has to interact with water. The interactions between water and rock can be chemical, physical, or a combination of both (Ali et al., 2015). These fluid-rock interactions degrade the surface hardness, which contributes to the loss of fracture conductivity and surface area, most pronounced in regions where low proppant concentrations are present (Suárez-Rivera et al., 2013).

From a geochemical perspective, fracture conductivity decline due to water-rock interactions depends broadly on four factors, namely, the chemical makeup of the fracturing fluid; the type, concentration, and distribution of minerals along the fracture surface; the chemical makeup of the formation water (if originally present); and the resulting fluid-rock interactions under downhole conditions during shut-in time and subsequent production. These fracturing fluids when in contact with the formation rock, have the potential to dissolve or transform minerals, and even create precipitates as time progresses, which in turn have an effect on reservoir characteristics including mechanical properties, flow pathways, and produced fluids (Ali et al., 2015). Other works discussing geochemical interactions between proppants and formations include Weaver et al. (2008), and reactive geochemical flow models developed by Crandall et al. (2014). When the well is initially put on production, these aforementioned fluid-rock interactions dictate the resulting chemical composition of the flowback water as well as influencing well performance through the attained fracture conductivity.

Part of this study focused on quantifying the degree of fracture conductivity impairment of the Eagle Ford and the Marcellus formations under laboratory conditions when exposed to saline water with a similar chemical composition as a typical field flowback water, otherwise referred to herein as a water-damaging fracture conductivity test. Additionally, the relationship between the fracture conductivity impairment and the fracture surface elemental characterization (via XRF) for each lithostratigraphic unit of the Eagle Ford formation was investigated. Furthermore, the relationship between clay content and the degree of unrecoverable loss of fracture conductivity due to water damage was also investigated, while considering the effect of fracture surface attributes and mechanical properties.

1.2.14 Fracture Conductivity: Post-Fracturing Performance

Creating hydraulic fractures is an intricate process that is a function of several variables. Critical design parameters to be considered can pertain to the treatment or the formation. Treatment design variables include pump rate (and time), viscosity of the fracturing fluid, and treatment volume. Formation considerations include the gross total fracture height (dependent on in situ stresses), Young's modulus, fluid loss coefficient, and fracture toughness (Smith and Montgomery, 2015).

The effectiveness of the created fracture depends on the fracture conductivity and the fracture area. Since three of these parameters (fracture height, length and width) pertain to fracture geometry, creating the desired fracture geometry is crucial for a successful hydraulic fracture stimulation (Prats, 1961; Smith and Montgomery, 2015).

In other words, the objective is to maximize productivity through fracture conductivity at the minimum cost, which in turn inevitably improves profitability (Smith and Montgomery,

2015). The importance of fracture conductivity on the productivity of a well cannot be overstated. The effect of overall network conductivity on cumulative production can be observed in **Figure 5**, where reservoir simulations by Mayerhofer et al. (2006) showed that higher conductivities resulted in higher production.

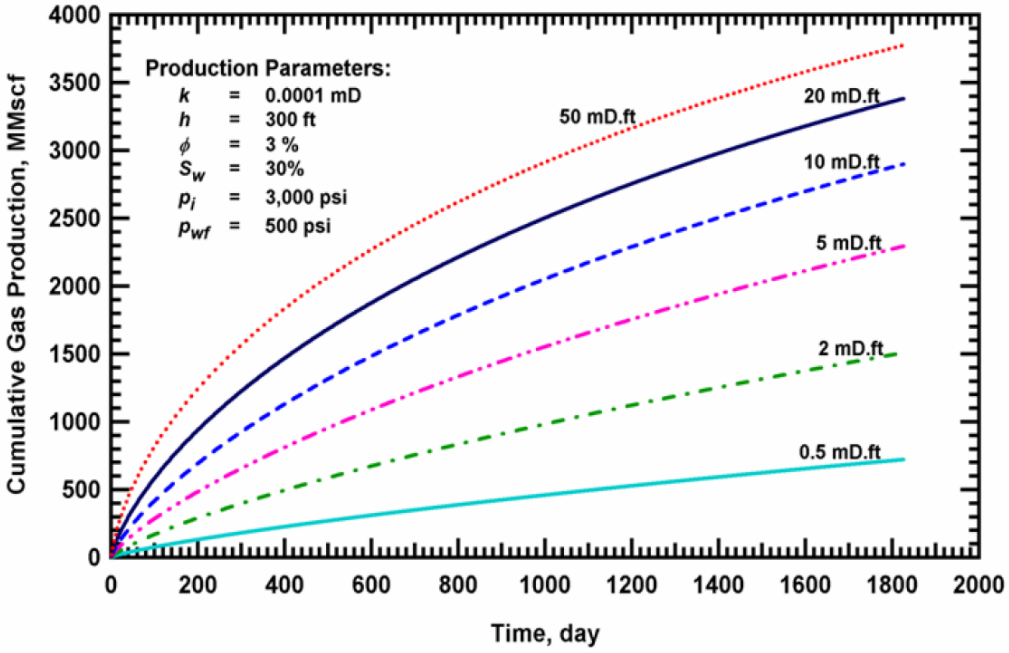

Figure 5 – Cumulative Gas Production as Affected by Overall Network Conductivity (Mayerhofer et al., 2006).

That being said, during the productive life of a multistage fractured horizontal well, different flow periods may be encountered. Depending on the flow period, the effect of fracture conductivity on well production will vary, based on whether or not the fracture conductivity is sufficiently greater than the reservoir's capacity to deliver the fluid to the fracture – a condition referred to as infinite fracture conductivity (Economides et al., 2013).

For these low permeability reservoirs, the flow of a multistage fractured horizontal well during the majority of the productive life can be best modeled as transient linear flow from the matrix into the fracture system, according to work by Bello and Wattenbarger (2010). This transient linear behavior is exhibited by a half-slope on the log-log plot of field production rate as a function of time, as shown in **Figure 6**.

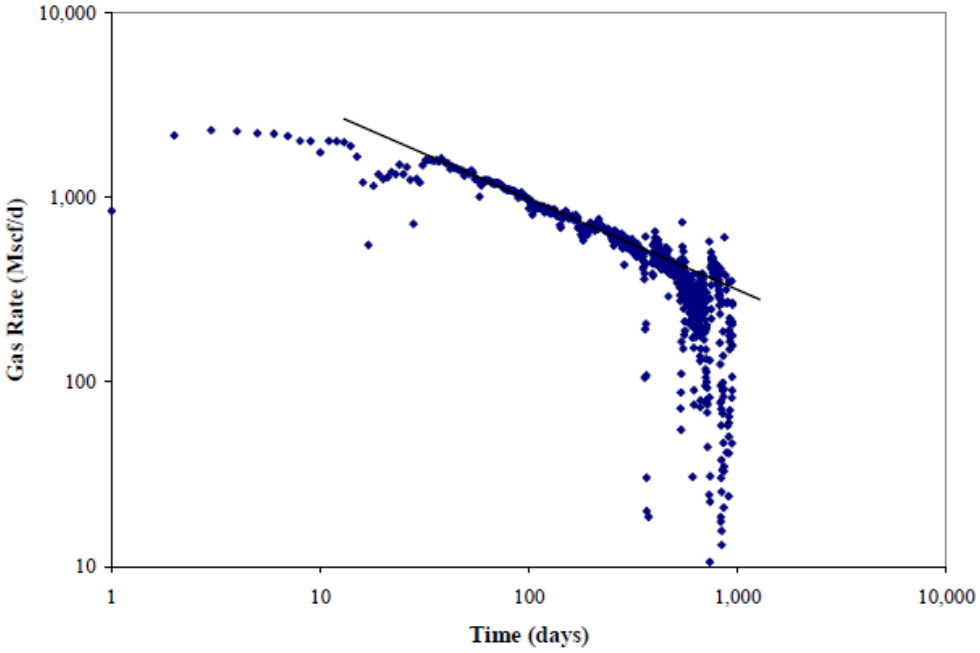

Figure 6 – Field Production Rate as a Function of Time for a Hydraulically Fractured Horizontal Well (Bello and Wattenbarger, 2010).

1.3 Objective

The objective of this study was to further the understanding of fracture conductivity and its dependence on rock mechanical properties, mineralogy, and fracture surface attributes, as well as the conductivity impairment due to flowback; based on a systematic experimental study on several mudstone formations. As part of this objective, a useful workflow was developed to

aid in the fracture treatment design process, by considering the experimentally measured fracture conductivity behavior (which not only accounts for the proppant behavior, but also the formation properties).

As such, this study is broadly categorized with the following aims:

1. Develop and execute a systematic experimental plan that enables a more realistic measurement of fracture conductivity while measuring influencing parameters that include bulk and surface mechanical properties, bulk and surface mineralogy, and surface attributes. The following considerations are also included within this aim:
    a. Develop an improved fracture conductivity test sample fracturing method to induce a fracture that is more representative of in-situ conditions.
    b. Simulate several fracture conditions, both unpropped and propped, while conducting dry nitrogen flow (non-damaging) and saline water flow (damaging) fracture conductivity tests.
    c. As a special topic, investigate the self-channeling effect observed in a small subset of the fracture conductivity experiments; by considering the injection procedure and the proppant concentration.
    d. Evaluate the effect of bedding plane orientation on the fracture conductivity tests.
2. Implement the aforementioned workflow on several mudstone formations, sourced from downhole or outcrop equivalents.

3. Analyze the experimental findings and observed behaviors, discuss trends and correlations, and develop simplified predictive relationships for fracture conductivity whenever adequate and possible.
4. Develop a practical workflow to extend the measured conductivity behavior to downhole stress conditions.
5. Provide useful recommendations for fracture conductivity testing and prediction, applicable universally or play specific.

The previous aims were intended to produce measurements and analysis not previously reported. Based on the specific laboratory equipment utilized in this study, novel insights are provided for several mudstone formations, including formation physical properties and the resulting fracture conductivity behavior under specific simulated fracture conditions. Additionally, a useful approach is presented to relate fracture conductivity measurements to the optimal fracture conductivity, providing insight into the effect different proppant loadings have on productivity, for given a set of well and reservoir parameters. These new findings raise the understanding of fracture conductivity, and ultimately hydraulic fracturing, in mudstone formations.

Given the diversity of tests conducted and the formations considered, this study also contributed to the ongoing database of fracture conductivity measurements representing several locations within the fracture networks in terms of closure stress –which in turn is time dependent during well production.

1.4 Approach

The objective of this study was achieved through an experimental approach and analytical considerations, depending on the specifics of each aim. The following sections discuss the experimental approach and the analytical considerations for this study.

1.4.1 Experimental Approach

A multidimensional battery of laboratory-scale experiments were conducted, with primary and complimentary types of measurements, as shown in **Figure 7**. These experiments were conducted on five unconventional formations: the Eagle Ford, the Marcellus, the Mahantango, the Middle Bakken, and Three Forks. Two categories of mudstone test samples were evaluated depending on availability, test samples obtained from an outcrop rock, and those obtained from downhole core segments provided by industry partners.

The primary set of experiments consisted of fracture conductivity measurements for various types of simulated fracture conditions, with two distinct types. Depending on the fluid being flowed through the fracture, the test was either a non-damaging (baseline) or a damaging fracture conductivity test, depending on whether gas or water was flowed, respectively. The complimentary set of experiments included the measurement of bulk and surface mechanical properties, bulk and surface mineralogy, and fracture surface attributes.

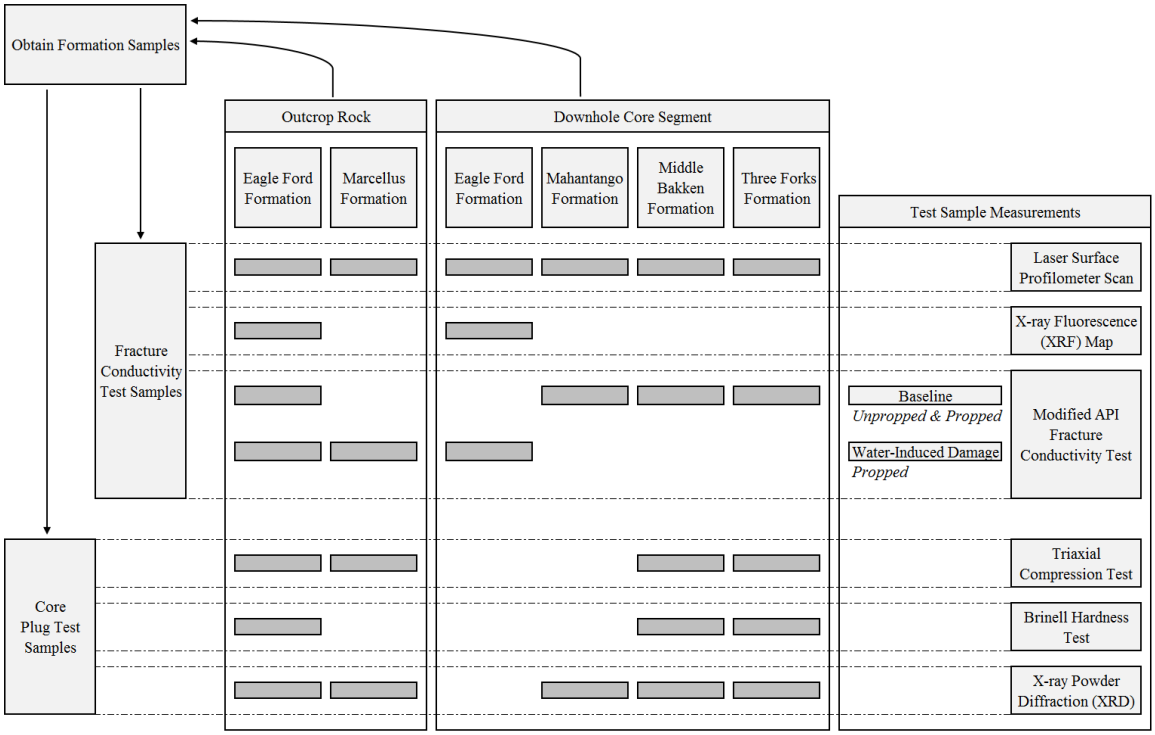

Figure 7 – A Multidimensional Battery of Laboratory-Scale Experiments.

As shown in **Figure 7**, not all formations considered enjoyed the full battery of aforementioned measurements, rather specific influencing factors were investigated depending on the type of fracture conductivity test being performed.

Chapter 2 describes in detail all aspects from the experimental design, as well as contains the measurement results for all the peripheral set of experiments. Section 2.5 contains the general workflow followed. Chapter 3 contains all the measurement results for the fracture conductivity experiments.

1.4.2 Analytical Considerations

A practical workflow was developed to relate the measured fracture conductivity behavior to downhole stress conditions. This estimated in-situ fracture conductivity can be used

during the performance evaluation of a hydraulically fractured horizontal well. This work is presented in Chapter 5.

The workflow consisted of taking the measured fracture conductivity data and representing the behavior via an exponential decline function. These stress dependent functions were then used to predict the expected fracture conductivity behavior downhole, based on the stress on the proppant calculated using poroelasticity theory. Several values were assumed, including well and reservoir parameters, as well as a particular drawdown (over a specified time period). This resulted in predicted fracture conductivity as a function of time.

This new perspective allowed for further insight into what impact the measured fracture conductivity would have on well productivity, in a representative reservoir setting. As such, this workflow can enhance the fracture treatment design process by providing more realistic fracture conductivity estimates.

1.5 Dissertation Outline

The background, literature review, objectives, experimental approach, and the description of the analytical component of work for this study was presented in this Chapter 1.

Chapter 2 presents a description of the test samples, the experimental equipment, testing conditions and materials, and laboratory procedures utilized for the experimental measurements of fracture conductivity as well as influencing properties and attributes. Results for the influencing properties and attributes are presented in this chapter.

Chapter 3 presents the results for all the fracture conductivity experiments that were conducted in this study. Therein, all non-damaging and damaging fracture conductivity test results are presented, for unpropped and propped fracture conditions.

Chapter 4 presents detailed discussions and observations on measured fracture conductivity behavior and its dependence on influencing properties and attributes. Experimentally derived trends, correlations, and general behaviors are included.

Chapter 5 presents the development of the practical workflow that relates the measured fracture conductivity behavior to downhole stress conditions. Multistage fractured horizontal well productivity is discussed.

Chapter 6 presents a summary of conclusions for the study, followed by recommendations for future work.

2. EXPERIMENTAL DESIGN

2.1 Introduction

This chapter presents a description of the test samples, the experimental equipment, testing conditions and materials, and laboratory procedures utilized for the experimental measurements of fracture conductivity as well as influencing properties and attributes.

Fracture conductivity experiments were conducted for various types of simulated fracture conditions across several unconventional formations. Two types of fracture conductivity tests were conducted mainly predicated on the fluid being flowed through the fracture, resulting in a non-damaging and a damaging fracture conductivity test, depending on whether gas or water was flowed, respectively.

The non-damaging fracture conductivity test relied on flowing dry nitrogen through the fracture, limiting any degradation due to fluid-rock interactions and solely focusing on determining stress induced changes. This type of fracture conductivity test is herein referred to as a baseline fracture conductivity test, which in this study encompassed unpropped and propped fracture conditions.

The damaging fracture conductivity test relied on flowing a saline water solution with a similar chemical composition as a typical field flowback water through the fracture, allowing for fluid-rock interactions to be manifested in a variety of mechanisms, which include surface softening and proppant embedment, among other phenomena. This type of fracture conductivity test is herein referred to as a water-damaging fracture conductivity test, which in this study encompassed propped fracture conditions. This specific type of test yielded a quantifiable degree of impairment to fracture conductivity by sequentially flowing dry nitrogen, then the water

solution, and once again dry nitrogen, allowing for the comparison of the measured fracture conductivity before and after flowing the water solution (i.e., the recovered fracture conductivity). This degree of impairment to fracture conductivity is herein referred to as an unrecoverable loss to fracture conductivity.

Influencing factors on fracture conductivity that were investigated included closure stress, bulk and surface rock mechanical properties, rock bulk and surface mineralogy, fracture surface topography, bedding plane orientation, proppant type and concentration, among other factors. Measurement results and relevant information pertaining to influencing properties and attributes are tabulated in this chapter.

The majority of fracture conductivity tests were conducted at room temperature, accounting for Darcy and non-Darcy flow conditions.

All test samples utilized in this study were unpreserved, given the nature and state in which they were acquired. All fracture conductivity tests were considered short-term and static.

2.2 Test Samples

In order to develop a comparative study, five distinct unconventional formations were considered: the Eagle Ford Group, the Marcellus, the Mahantango (both representing the Hamilton Group), the Middle Bakken, and Three Forks (both originating from the Williston Basin). The following subsections describe in detail the type of samples obtained, their mineralogy, and fracture conductivity test sample fracturing, dimensioning, and preparation.

2.2.1 Test Sample Types

In order to investigate fracture conductivity under different simulated fracture conditions, and assess the influence of mechanical properties, mineralogy, and surface attributes, two types of test samples were considered.

The first and primary type of test sample was the fracture conductivity test sample, with overall dimensions of 1.61 in. in width by 6 in. in height by 7.10 in. in length, with rounded ends. The second type of test sample was a core plug test sample with dimensions of 2 in. in length by 1 in. in diameter, primarily used for the determination of mechanical properties. These two types of test samples are shown schematically in **Figure 8**, and covered in detail in Section 2.2.4.1.

Oil and gas bearing formations, under nominal conditions, typically have a downhole stress state such that the overburden represents the maximum principal stress (σ_1), and the other two principal stress lay on a horizontal plane, where the maximum horizontal stress (σ_2) and the minimum horizontal stress (σ_3) are smaller than (σ_1). Conceptually, when a fracture is created under these conditions, its plane is propagating perpendicular to the minimum principal stress, or in other words, the fracture aperture is widening along the direction of minimum principal stress. This fracture plane crosses several bedding planes as it grows in height, and the ensuing production flow within this fracture can have some dependency on them.

In an effort to acknowledge the influence of bedding plane orientation with respect to flow and mechanical properties, fracture conductivity test samples were obtained such that the fracture to be induced in this test samples would result on either the bedding plane (Z orientation), across the bedding plane (X90 orientation), or along the bedding plane (X0 orientation), as shown in **Figure 8**. Similarly, core plug test samples were obtained such that the bedding plane would be either perpendicular or parallel to its length.

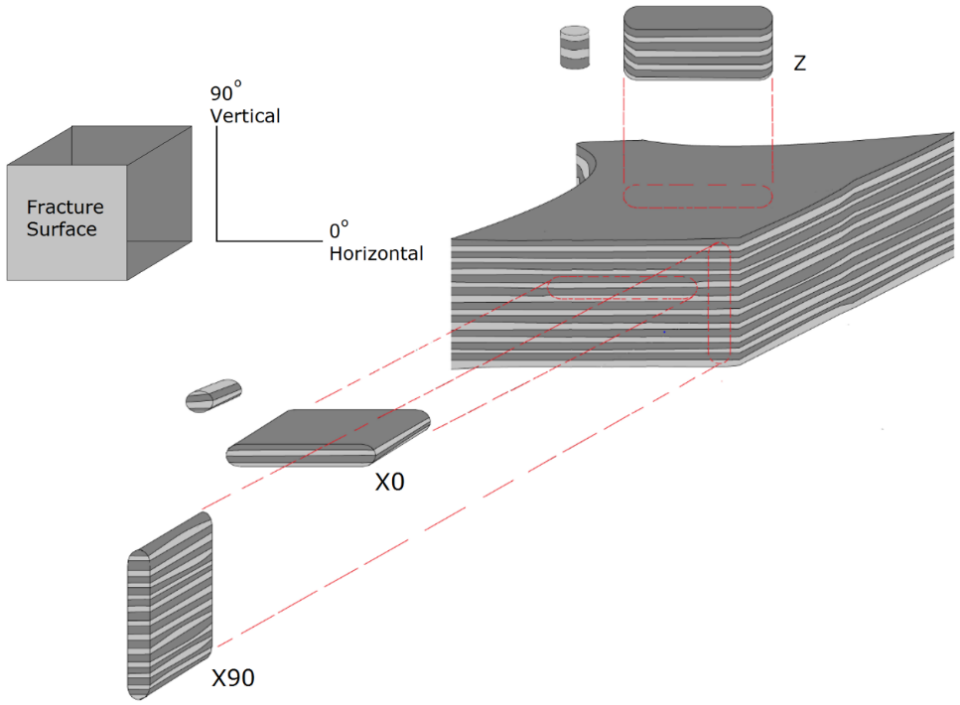

Figure 8 – Schematic of Bedding Plane Orientation with Respect to Fracture Conductivity Test Samples (Core Plug Test Samples also Shown) (Guerra et al., 2018).

It is to be noted that **Figure 8** shows the fracture conductivity test samples prior to inducing a fracture in said test sample. Section 2.2.4.1 details test sample fracturing.

2.2.2 Test Sample Collection

Two categories of mudrock test samples were evaluated depending on availability, test samples obtained from an outcrop rock and test samples obtained from downhole core segments provided by industry partners. The following subsections describe in detail each considered formation.

2.2.2.1 Eagle Ford Formation

The outcrop rock was obtained from Lozier Canyon and Antonio Creek, Terrell County, Texas, a site currently leased by BP (**Figure 9**). This Eagle Ford formation outcrop in West Texas is characterized by a heterogeneity discretized in a vertical facies succession as described by Donovan and Staerker (2010) and Donovan et al. (2012). The nomenclature followed in this study is an adaptation of Gardner et al. (2013), where five different lithostratigraphic units can be considered equivalent to the Eagle Ford formation subsurface in South Texas. Outcrop rocks were gathered for each unit and selected sub-units. The downhole core was provided by Pioneer Natural Resources Company, representing the downhole equivalent of unit B at a depth exceeding 10,000 ft. (TVD).

Typical dimensions for the gathered outcrop rocks were at a minimum of 1 ft. each direction, in order to satisfy test sample fracturing and dimensioning requirements; whereas the downhole core segments were prescribed to a 4 in. diameter with a 1/3 diameter slabbed, with selected intervals preferably having at least 8 in. of intact length (**Figure 10**).

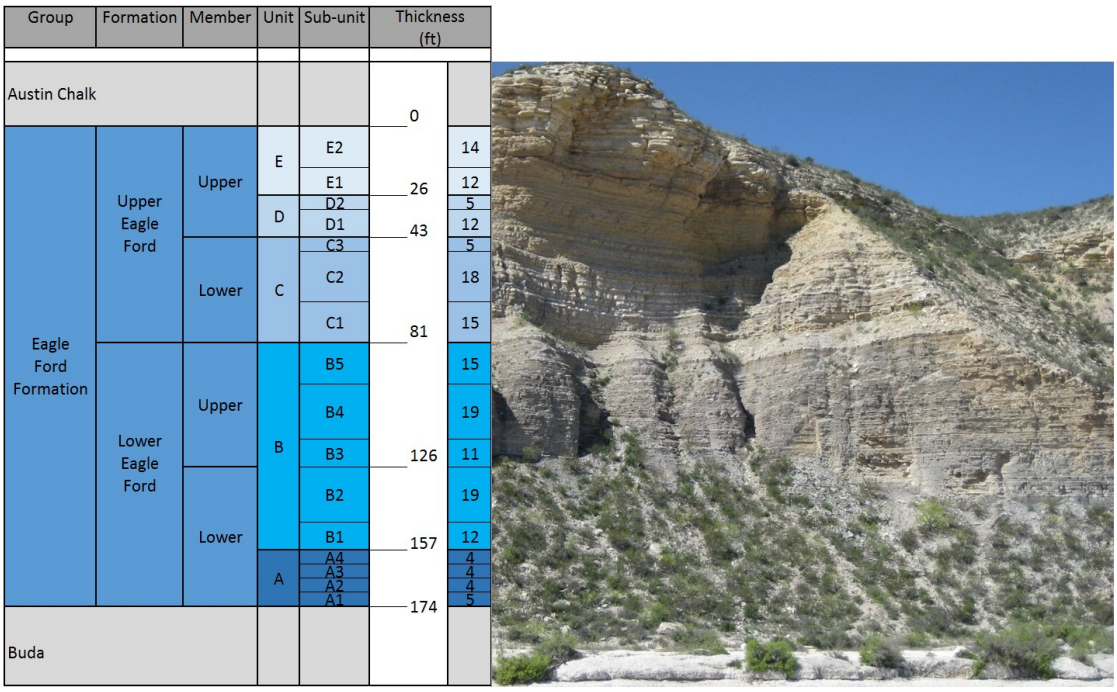

Figure 9 – Lozier Canyon (West Portion) Outcrop Face and the Exposed Eagle Ford Formation Lithostratigraphic Units and Sub-units (Guerra et al., 2018).

Figure 10 – Antonio Creek Outcrop Rock Sample from Unit B (left) and a Downhole Core Segment from the Subsurface Equivalent of Unit B (right) (Guerra et al., 2018).

A total of eight outcrop rocks were gathered, from unit A, C, D, and E, with unit B being discretized to include sub-unit B1, B2, and B3. Given the limited availability and the received state of the downhole core segments, only three segments were selected and deemed suitable for fracture conductivity test sample fracturing and dimensioning, over a depth interval of 10,391 – 10,501 ft. (TVD). The gathered outcrop rocks and the selected downhole core segments with their corresponding depth (or stratigraphic location) and yielded test(s) sample(s) are listed in **Table 1**.

Table 1 – Gathered Eagle Ford Formation Outcrop Rock and Selected Eagle Ford Formation Downhole Core Segment Data Summary.

Outcrop Rock Name / Core No.	Collection Location / App. Core Depth (ft)	Fracture Conductivity		Core Plug	
		Test Sample Name	Test Sample Orientation	Test Samples Obtained	Test Sample Orientation
E	unit E	E	Z	1 1	Z X90
D	unit D	D	Z	1 1	Z X90
C	unit C	C	Z	1 1	Z X90
B	unit B	EF-1	Z		
		EF-2	Z		
		EF-3	Z		
B3	sub-unit B3	B3	Z	1 1	Z X90
B2	sub-unit B2	B2	Z	1 1	Z X90
B1	sub-unit B1	B1	Z	1 1	Z X90
A	unit A	A	Z	1 1	Z X90
1	10,391.00	Core 1	X90		
2	10,432.00	Core 2	X90		
3	10,476.00	Core 3	X90		

2.2.2.2 Marcellus Formation

The outcrop rock was obtained from two locations established to be representative of the Marcellus formation as described by McGinley (2015), one from a quarry in Elimsport, Lycoming County and the other from a site in Allenwood, Union County –both located in Pennsylvania. Allenwood site outcrop rocks were excavated 20 ft. below the surface, while Elimsport quarry samples were ensured to have the least weathering.

Typical dimensions for the gathered outcrop rocks were at a minimum of 1 ft. in each direction, in order to satisfy fracture conductivity test sample fracturing and dimension requirements (**Figure 11**).

Figure 11 – Marcellus Formation Outcrop Rock Sample Obtained from the Elimsport Quarry.

A total of eight outcrop rocks were gathered, four from each location. The gathered outcrop rocks with their corresponding collection location and yielded test sample are listed in **Table 2**.

Table 2 – Gathered Marcellus Formation Outcrop Rock Data Summary.

Outcrop Rock Name	Collection Location	Fracture Conductivity	
		Test Sample Name	Test Sample Orientation
Elimsport 1	Elimsport, PA Quarry	Elimsport 1	Z
Elimsport 2	Elimsport, PA Quarry	Elimsport 2	Z
Elimsport 3	Elimsport, PA Quarry	Elimsport 3	X90
Elimsport 4	Elimsport, PA Quarry	Elimsport 4	X90
Allenwood 1	Allendwood, PA Site	Allenwood 1	Z
Allenwood 2	Allendwood, PA Site	Allenwood 2	Z
Allenwood 3	Allendwood, PA Site	Allenwood 3	X90
Allenwood 4	Allendwood, PA Site	Allenwood 4	X90

2.2.2.3 Mahantango Formation

The downhole core was provided by Range Resources Corporation, originating from Washington County, Pennsylvania, at a depth exceeding 6,500 ft. (TVD).

The cross-sectional dimensions for the downhole core segments were prescribed to a 4 in. diameter with a 1/3 diameter slabbed, with selected intervals preferably having at least 8 in. of intact length in order to satisfy fracture conductivity test sample fracturing and dimensioning requirements (**Figure 12**).

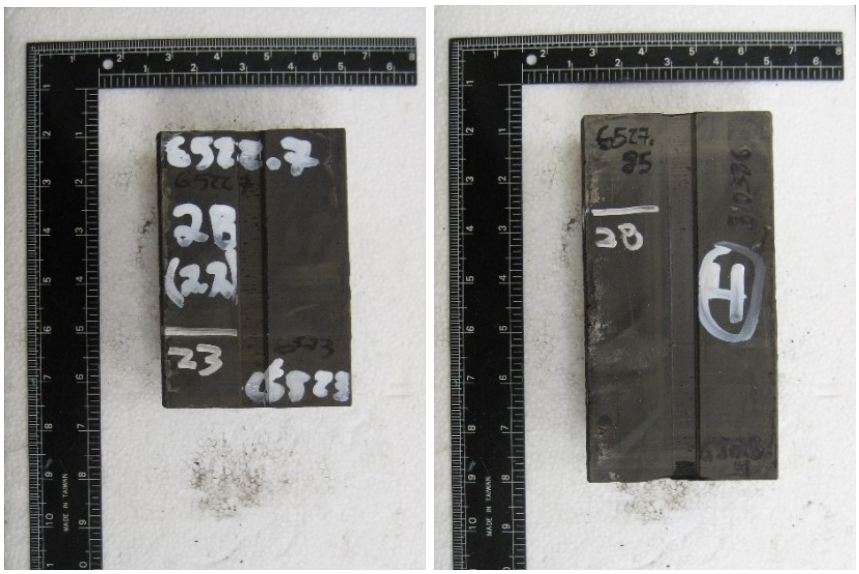

Figure 12 – Typical Mahantango Formation Downhole Core Segment (Writing on Segments From Depth Interval).

Given the received state of the core segments, only two segments were selected and deemed suitable for fracture conductivity test sample fracturing and dimensioning, over a depth interval of 6,517 – 6,547 ft. (TVD). The selected downhole core segments with their corresponding depth and yielded test sample are listed in **Table 3**.

Table 3 – Selected Mahantango Formation Downhole Core Segment Data Summary.

Core No.	Top Depth (ft)	Bottom Depth (ft)	Fracture Conductivity	
			Test Sample Name	Test Sample Orientation
1	6,522.70	6,523.50	Core #2	X90
2	6,523.50	6,528.40	Core #1	X90

2.2.2.4 Middle Bakken Formation and Three Forks Formations

The downhole core was provided by Hess Corporation, originating from McKenzie County, North Dakota, with a depth exceeding 10,600 ft. (TVD).

The cross-sectional dimensions for the downhole core segments were prescribed to a 4 in. diameter with a 1/3 diameter slabbed, with selected intervals preferably having at least 8 in. of intact length in order to satisfy fracture conductivity test sample fracturing and dimensioning requirements (**Figure 13**).

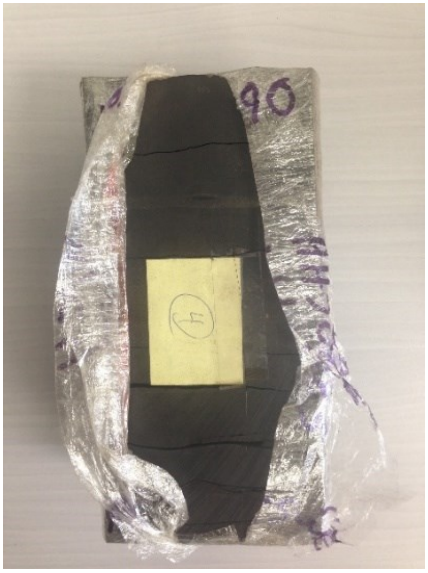

Figure 13 – Downhole Core Segment From the Middle Bakken Formation.

Given the received state of the core segments, only six segments were selected and deemed suitable for fracture conductivity test sample fracturing and dimensioning, over a depth interval of 10,673 – 10,834 ft. (TVD). The selected downhole core segments with their corresponding depth and yielded test(s) sample(s) are listed in **Table 4** for the Middle Bakken formation, and in **Table 5** for the Three Forks formation.

Table 4 – Middle Bakken Formation Downhole Core Segment Data Summary.

Core No.	Top Depth (ft)	Bottom Depth (ft)	Fracture Conductivity		Core Plug	
			Test Sample Name	Test Sample Orientation	Test Samples Obtained	Test Sample Orientation
1	10,673.05	10,674.05	Core No. 2	X90	2 2	Z X90
2	10,706.89	10,707.65	Core No. 5	X90	2	X90
3	10,724.89	10,725.70	Core No. 6	X90	2	X90

Table 5 – Three Forks Formation Downhole Core Segment Data Summary.

Core No.	Top Depth (ft)	Bottom Depth (ft)	Fracture Conductivity		Core Plug	
			Test Sample Name	Test Sample Orientation	Test Samples Obtained	Test Sample Orientation
4	10,787.15	10,787.80	Core No. 8	X90	2	X90
5	10,805.00	10,805.80	Core No. 9	X90	1 2	Z X90
6	10,833.20	10,833.95	Core No. 10	X90		

2.2.3 Test Sample Mineralogy

Test sample bulk mineralogy was determined by performing XRD on core plug test samples that were obtained. After mechanical properties were measured via a triaxial compression test, a powdered sample was obtained from the core plug test sample and evaluated using a Bruker D8 Advanced Eco XRD. The powdered sample was first crushed, then sieved such that the particle size did not exceed 90 micrometers.

The results from the mineralogy testing pertaining to the test sample core plugs, for each considered formation, are listed in the following subsections.

2.2.3.1 Eagle Ford Formation

For this formation, bulk mineralogy was determined throughout the lithostratigraphy of the Eagle Ford formation, unit A through E, on all the core plug test samples obtained from outcrop rock. The averaged results are listed in **Table 6**.

Table 6 – Average Mineral Composition (via XRD) for Each of the Eagle Ford Formation Outcrop Rock Core Plug Test Samples (Adapted from Guerra et al., 2018).

Test Sample Name	Component (%)								Clay (%)
	Calcite	Quartz	Pyrite	Dolomite	Albite	Chlorite	Kaolinite	Illite	
E	90.49	3.95	0.70	2.40			2.56		2.56
D	93.71	2.42	0.56	1.01			2.71		2.71
C	76.75	10.78	0.93	1.47		3.12	2.12	4.85	10.09
B3	55.67	28.98	2.03	3.43			6.45		6.45
B2	56.65	25.55	1.97	2.38			13.46		13.46
B1	82.69	11.41	0.71	0.81			4.40		4.40
A	85.07	7.37		3.41	2.42	0.84	2.62		3.46

Throughout the units, calcite was the most predominant mineral, ranging from 55.67 to 93.71% as shown in **Table 6**. Sub-unit B3 was considered representative of sub-unit B3 through B5, and sub-units of units A, C, and D, and E were considered uniform.

Miceli-Romero (2014) performed Rock Eval pyrolosis on test samples obtained from the same outcrop located in Lozier Canyon and Antonio Creek, and measured the Total Organic Content (TOC). Sub-unit B1 and B2 had the highest average TOC values, that of 5.5%, while unit A had 3.0%, unit B3 had 2.0%, unit C had 1.2%, unit D had 0.70%, and unit E had 0.10%.

Three types of clay were present in the test sample core plugs tested, Kaolinite, Chlorite, and Illite. The highest contents of quartz and kaolinite were in unit B, while unit C had all three clays present. The total clay ranged from 2.56% to 13.46%, as shown in **Table 6**.

2.2.3.2 Marcellus Formation

For this formation, bulk mineralogy was tested by McGinley (2015) and Perez et al. (2016) on several core plug test samples obtained from the same batch of collected outcrop rocks, from both the Elimsport Quarry as well as the Allenwood Site. The averaged results are listed in **Table 7**.

Table 7 – Average Mineral Composition (via XRD) for Each of the Marcellus Formation Outcrop Rock Core Plug Test Samples.

Test Sample Name	Component (%)					Clay (%)
	Calcite	Quartz	Pyrite	Dolomite	Albite	
Elimsport 1–4	4.00	56.00	6.00	1.40	3.50	28.00
Allenwood 1–4	17.00	46.00	7.00	1.40	3.20	25.00

Core plug test samples obtained from the Allenwood collection site had similar mineralogy to the Elimsport Quarry collection site, as previously shown by McGinley (2015). Quartz was the predominant mineral with a value of 46% to 56%, as also shown by Perez (2015). The total clay for the Marcellus formation outcrop core plug test samples ranged from 25 to 28%, as shown in **Table 7**.

2.2.3.3 Mahantango Formation

For this formation, bulk mineralogy was tested on recovered residual fragments from the selected downhole core segments, after fracture conductivity test sample fracturing and dimensioning. The results are listed in **Table 8**.

Table 8 – Mineral Composition (via XRD) for Each of the Mahantango Formation Downhole Core Segment Test Samples.

Test Sample Name	Component (%)						Clay (%)
	Calcite	Quartz	Pyrite	Vermiculite	Kaolinite	Illite	
Core #1	11.70	47.53	3.03	0.13	10.74	26.87	37.61
Core #2		60.90	4.34	0.13	11.74	22.90	34.64

The most predominant mineral in the core plug test samples evaluated was Quartz with a value ranging from approx. 48% to 61%. Both the test samples tested also had a high content of Illite, with an average of approx. 25%. The total clay for the Mahantango formation downhole test samples had an average of 36%. Vermiculite was the least present component, and considered negligible for this data set.

2.2.4.3 Middle Bakken Formation and Three Forks Formations

For these formations, bulk mineralogy was tested on core plug test samples obtained from most of the selected downhole core segments. The results are listed in **Table 9** and **Table 10**, for the Middle Bakken and Three Forks formations, respectively.

Table 9 – Mineral Composition (via XRD) for Each of the Middle Bakken Formation Downhole Core Segment Core Plug Test Samples.

Test Sample Name	Component (%)							Clay (%)
	Calcite	Quartz	Pyrite	Dolomite	Feldspar	Kaolinite	Illite	
Core No. 2	68.59	11.07		2.67		2.89	14.79	17.68
Core No. 5	4.29	34.92	0.88	36.07	3.83	2.37	17.64	20.01
Core No. 6	10.78	50.78	0.66	15.35	6.20	2.13	14.10	16.23

Table 10 – Mineral Composition (via XRD) for Each of the Three Forks Formation Downhole Core Segment Core Plug Test Samples.

Test Sample Name	Component (%)							Clay (%)
	Calcite	Quartz	Pyrite	Dolomite	Feldspar	Kaolinite	Illite	
Core No. 8	0.94	18.42		47.43	10.46	6.10	16.47	22.57
Core No. 9		24.81		66.97	3.41		4.77	4.77

A considerable variation was present among the core plug test samples from the Middle Bakken formation. Core No. 2 had the highest Calcite percentage, approx. 69%, while Core No. 5 had the highest Dolomite percentage, approx. 36%, and Core No. 6 had the highest Quartz percentage, approx. 51%. The total clay for this data set averaged 18%. For the Three Forks formation, the highest component presence across said data set was Dolomite, with an average of 57%. The total clay for this data set averaged 14%.

2.2.4 Fracture Conductivity Test Sample Preparation

Whenever outcrop material was used, test samples were cut from the interior of the blocks of rock, avoiding the weathered exterior, thus ensuring the test samples obtained from

outcrop rock accurately represented the formation in question. Experimentally, unpreserved downhole cores exhibited a greater degree of bedding plane delamination and fragility during handling and subsequent fracture conductivity test sample dimensioning and fracturing than the large blocks of outcrop rock that were used. The following subsections describe in detail fracture conductivity test sample fracturing and dimensioning, proppant type and loading, and fracture conductivity test sample preparation.

2.2.4.1 Test Sample Fracturing and Dimensioning

Fracture conductivity test sample dimensions were prescribed by a Modified API Fracture Conductivity Cell, which builds upon the Standard API Fracture Conductivity Cell defined by API RP 61. The most notable differences are in sample height due to the induced fracture on the fracture conductivity test sample, as well as the frequent need to utilize sandstone inserts depending on the original size of the acquired mudrock sample (**Figure 14a**). Awoleke (2013) and Kamenov (2013) outlined in detail the baseline experimental apparatus and procedural departures from the standard API RP 61 (1989).

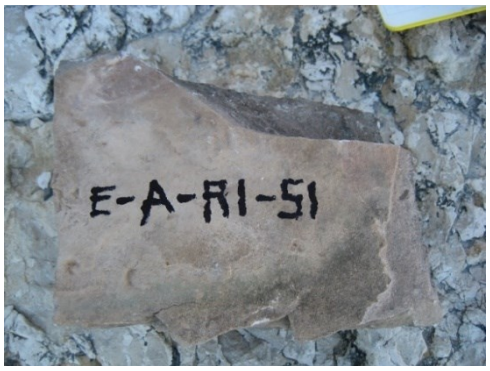

(a)

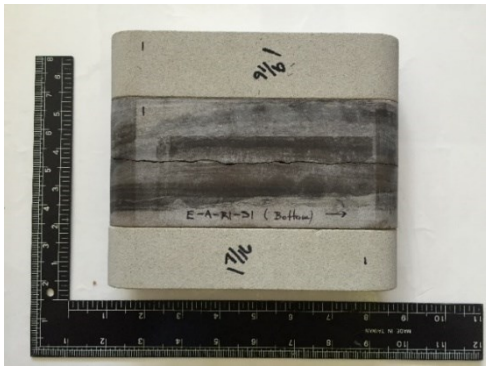

(b)

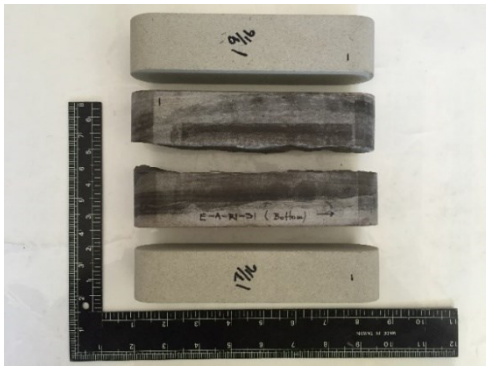

(c)

Figure 14 – Fracture Conductivity Test Sample (Guerra et al., 2018): (a) Outcrop Rock Sample With Writing Reflecting it Came From Unit A of the Eagle Ford Formation (Second Letter); (b) Outcrop Rock Fracture Conductivity Test Sample A After Fracturing and Dimensioning; (c) Fracture Conductivity Test Sample A in an Expanded View.

The overall fracture conductivity test sample dimensions are 1.61 in. in width by 6 in. in height by 7.10 in. in length, with rounded ends (**Figure 14b**). The mudrock portion ranges from

2.5 in. up to the entire height, whereas the sandstone inserts serve as a filler to ensure the overall dimensions (**Figure 14c**).

Several methods of inducing a fracture on a fracture conductivity test sample were reported in the literature, such as employing masonry rock splitter blades as done by Fredd et al. (2000). In this study, a new and improved method was designed to create a Mode I fracture, ensuring that no compressive stress is applied to the fracture surface during the process.

Fracture conductivity test sample preparation consisted of cutting a 2 in. wide by 3 – 4 in. tall by 8 in. long rectangular rock sample from the outcrop rock (**Figure 14a**) or downhole core segment, scoring along the length and all around the rectangular sample to aid in the fracture initiation process, inserting the rectangular sample inside two steel sleeves (**Figure 15a**), placing the assemblage under a load frame (**Figure 15b**), and applying a load until a fracture was induced (**Figure 15c**).

Once the fracture was created, debris were gathered and returned to the fracture face, and the rectangular sample was then put back together by marrying each side of the fracture, at which point, it was saw cut down to fracture conductivity test sample dimension requirements as shown in **Figure 14b**.

(a)

(b)

(c)

Figure 15 – Inducing Fracture on Fracture Conductivity Test Sample (Guerra et al., 2018): (a) Steel Sleeves; (b) Rectangular Sample Inside Steel Sleeves Under Load Frame; (c) Fractured Rectangular Sample (Prior to Saw Cutting to Final Dimensions).

In order to better preserve sample integrity during the process of inducing a fracture, fracture conductivity test samples obtained from outcrop rocks were, in their majority, fractured along the bedding (Z orientation, **Figure 8**). Although horizontal fractures are less prevalent in practice, fracture conductivity samples with Z orientation were shown to be representative while ensuring experimental reproducibility according to Zhang (2014). On the other hand, fracture conductivity samples obtained from downhole core segments were fractured vertically in the X90 orientation (**Figure 8**), given that the downhole core was obtained in the vertical section of the well.

Core plug test samples were obtained from the residual carcass of the outcrop rock or the downhole core segment utilized to obtain the fracture conductivity test samples. This was done by simply drilling out the 2 in. in length by 1 in. in diameter core plug, as shown in **Figure 16** in final state.

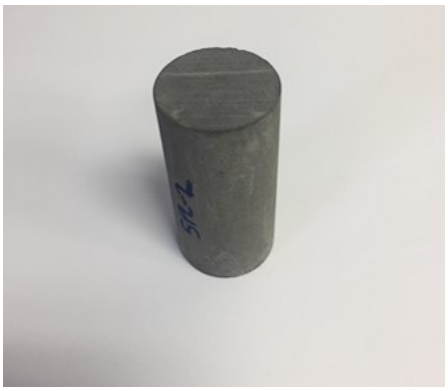

Figure 16 – Core Plug Test Sample from Core No. 5 of the Middle Bakken Formation.

2.2.4.2 Proppant Types and Loading Concentrations

For all propped baseline fracture conductivity tests as well the water-damaging fracture conductivity tests, the proppant type used in the tests was based on a typically employed mesh

size in the field according to each considered formation, allowing for a more realistic simulation of fracture conditions typically expected. A mesh size distribution was selected for each formation in this study, however it is to be noted that a variety of mesh sizes are typically utilized throughout a single fracture treatment job in the field.

The proppant loading varied depending on the type of behavior sought to be investigated, resulting in some fracture conductivity tests having low proppant concentrations, while others had higher values. This inherently placed the measured fracture conductivity values in different zones within the idealized fracture, given the fracture width variation.

In the Eagle Ford formation, a variety of proppant types are used, with some of the more prevalent types being 30/50-mesh, 40/70-mesh, and 100-mesh, according to Enriquez (2016). For propped baseline and water-damaging fracture conductivity tests pertaining to the Eagle Ford formation fracture conductivity test samples, 100-mesh sand was selected given its considerable use in the aforementioned formation, as well as its use during slick-water treatments which are common for gas wells.

A sieve analysis was conducted and the results show that the sand complies with the API standard regarding particle size distribution (**Figure 17** and **Figure 18**). The sand had a bulk density of 101.445 lb_m/ft^3 (1.625 g/cm^3), with average diameter (d_{50}) of 0.0070 in. (177.887 μm).

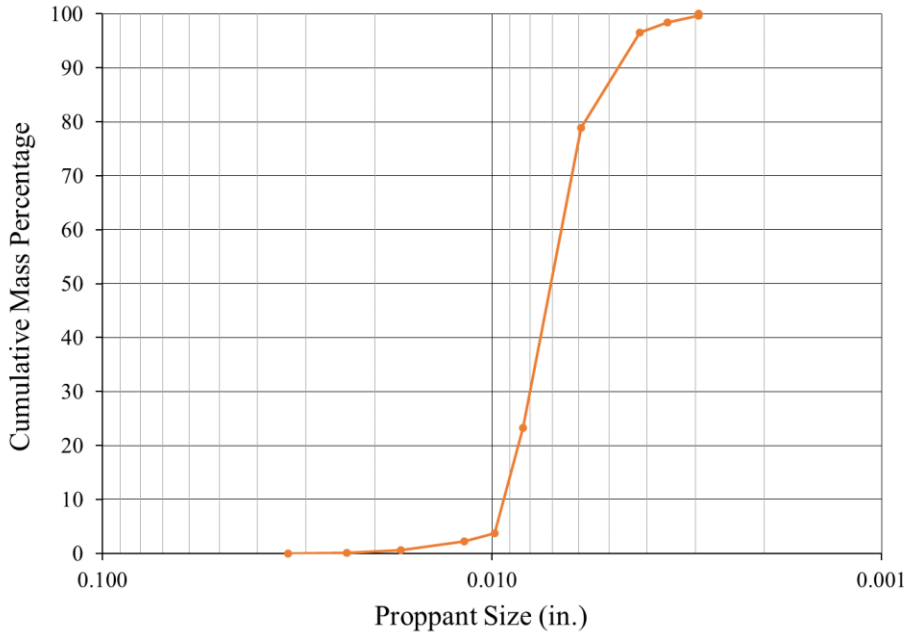

Figure 17 – Sieve Analysis for 100-Mesh Sand: Cumulative Mass Percentage According to Proppant Size (Guerra et al., 2018).

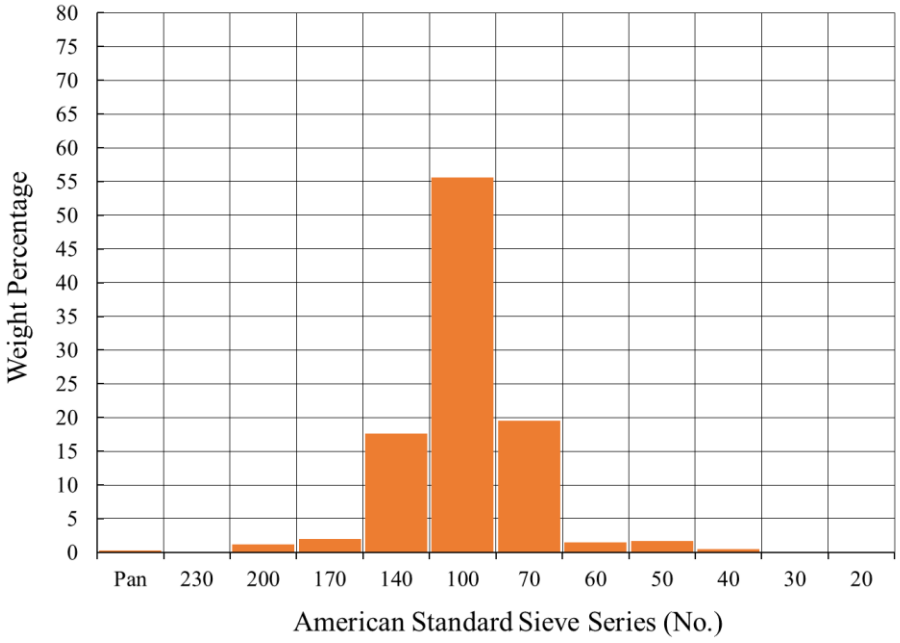

Figure 18 – Sieve Analysis for 100-Mesh Sand: Weight Percentage According to Sieve Series Number (Guerra et al., 2018).

In the Marcellus formation as well as the Mahantango formation, a variety of proppant types are used, with the more prevalent types being 40/70-mesh, 40/80-mesh, and 100-mesh, according to Beard (2011). For propped baseline and water-damaging fracture conductivity tests pertaining to the Marcellus and Mahantango formation fracture conductivity test samples, 40/70-mesh was selected given its considerable use in the aforementioned formations, especially in gas wells.

A sieve analysis was conducted and the results show that the sand complies with the API standard regarding particle size distribution (**Figure 19** and **Figure 20**). The sand had a bulk density of 109.998 lb_m/ft^3 (1.762 g/cm^3), with average diameter of 0.0118 in. (300.574 µm).

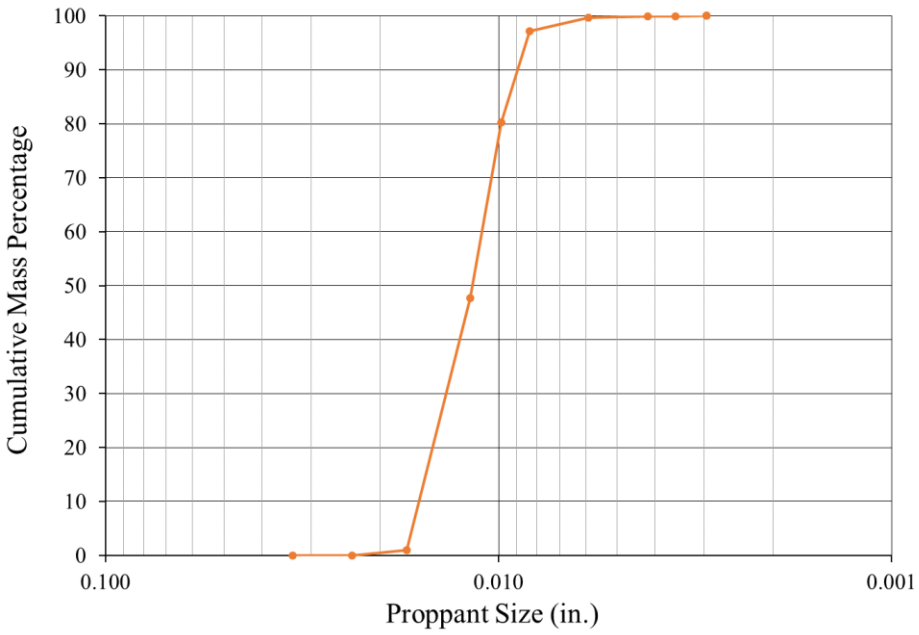

Figure 19 – Sieve Analysis for 40/70-Mesh Sand: Cumulative Mass Percentage According to Proppant Size.

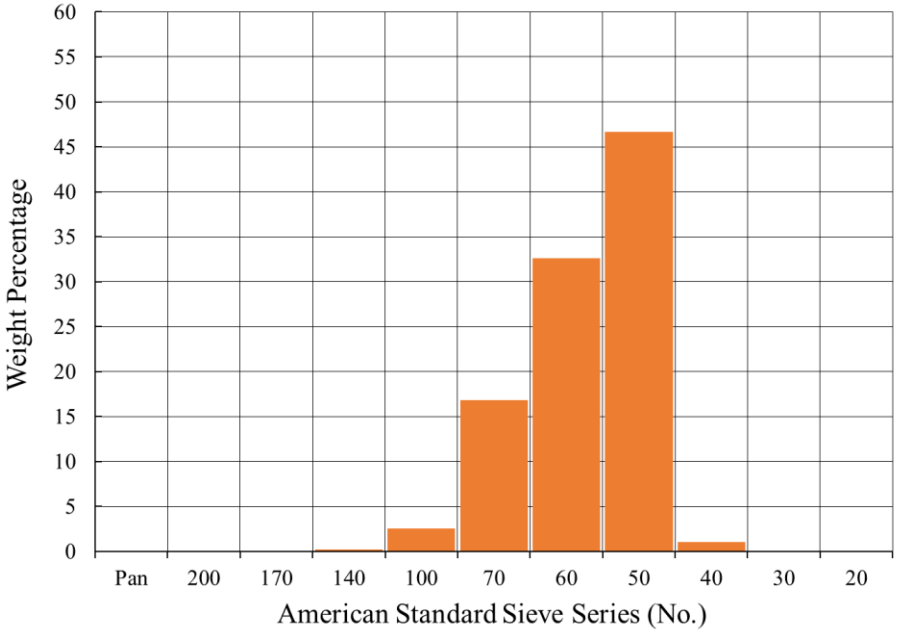

Figure 20 – Sieve Analysis for 40/70-Mesh Sand: Weight Percentage According to Sieve Series Number.

A variety of proppant types are used in the Middle Bakken and the Three Forks formations, with one of the utilized types being 30/50-mesh sand. 30/50-mesh sand was selected for the propped baseline fracture conductivity tests from the aforementioned formations, in part due to interest from industry partners.

A sieve analysis was conducted and the results show that the sand complies with the API standard regarding particle size distribution (**Figure 21** and **Figure 22**). The sand had a bulk density of 109.748 lb_m/ft^3 (1.758 g/cm^3), with average diameter of 0.0160 in. (406.908 µm).

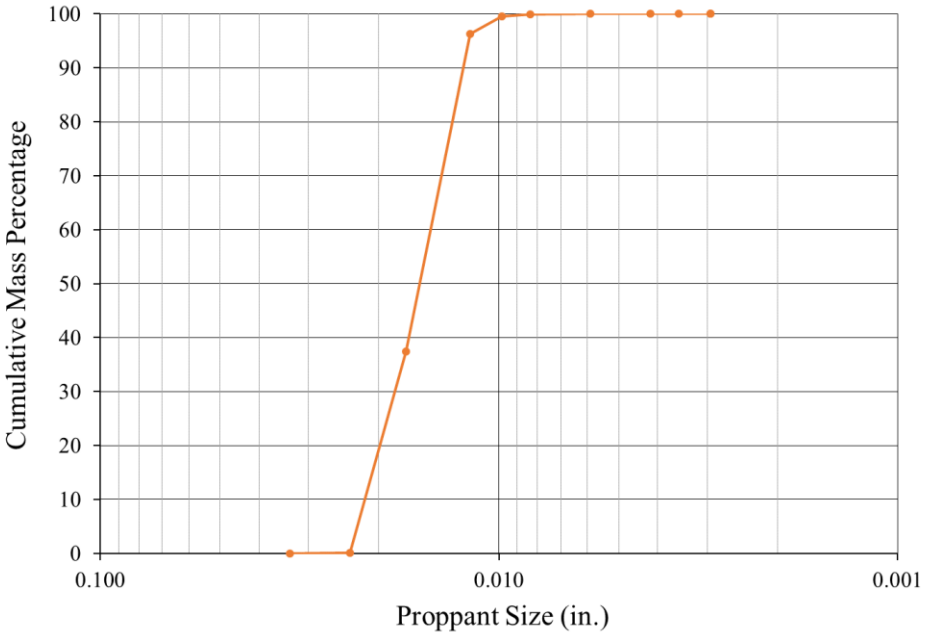

Figure 21 – Sieve Analysis for 30/50-Mesh Sand: Cumulative Mass Percentage According to Proppant Size.

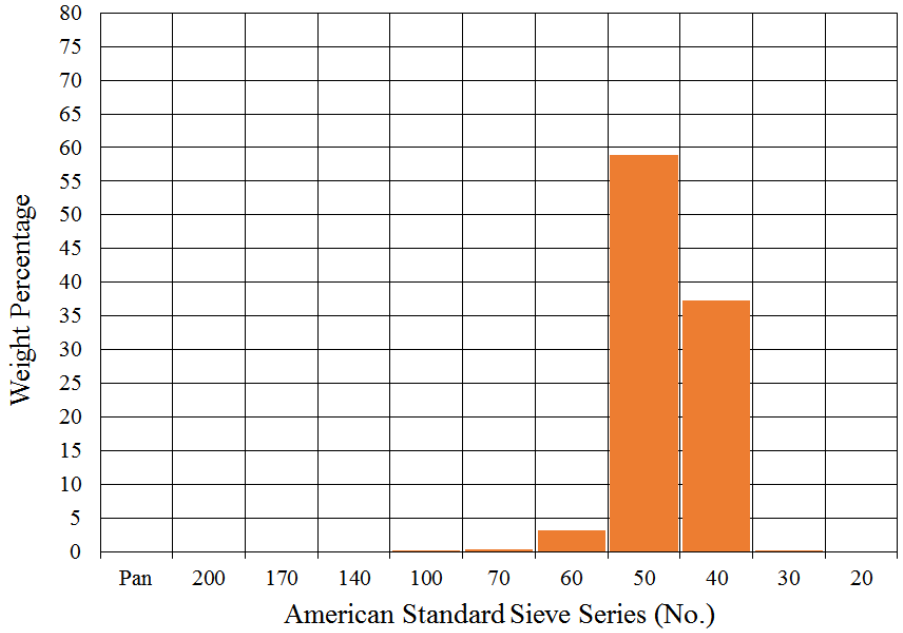

Figure 22 – Sieve Analysis for 30/50-Mesh Sand: Weight Percentage According to Sieve Series Number.

2.2.4.3 Test Sample Proppant Placement & Preparation

In this study, and as mentioned previously, a variety of proppant concentrations were investigated depending on the formation being considered as well as the specific behavior sought to be analyzed.

For the Eagle Ford formation, the majority of the fracture conductivity test samples had a prescribed 0.1 lb_m/ft^2 proppant areal concentration of 100-mesh sand, and utilized for water-damaging fracture conductivity tests. Enriquez (2016) reported this concentration as representative to field values based on fracture width assumptions. Fracture conductivity test samples EF-1, EF-2, and EF-3, were devoted to investigating the effect of proppant concentrations ranging from 0.1 to 0.3 lb_m/ft^2 for propped baseline fracture conductivity tests – after an unpropped test was conducted.

For the Marcellus formation, all the fracture conductivity test samples had a prescribed 0.1 lb_m/ft^2 proppant areal concentration of 40/70-mesh sand, and utilized in water-damaging fracture conductivity tests. This allowed for comparison to other tests.

For the Mahantango formation, all the propped fracture conductivity test samples were were devoted to investigating the effect of proppant concentrations ranging from 0.05 to 0.1 lb_m/ft^2 of 40/70-mesh sand for propped baseline fracture conductivity tests –after an unpropped test was conducted.

For the Middle Bakken and Three Forks formations, all the propped fracture conductivity test samples had a prescribed 0.5 lb_m/ft^2 proppant areal concentration of 30/50-mesh sand, and utilized for propped baseline conductivity tests –after an unpropped test was conducted.

With the selected proppant mesh size and the prescribed proppant concentration, the sand was then manually placed evenly across the bottom fracture surface of the fracture conductivity

test sample –this took place after the unpropped fracture conductivity test, if conducted. At this stage (pre-testing of fracture conductivity test under propped conditions), the proppant was stored at room temperature, which was measured at 70 ^{o}F. **Figure 23** shows proppant placement on the bottom-side fracture surface of test sample A of the Eagle Ford formation. This process remained unchanged for fracture conductivity test samples from other formations and across varying proppant concentrations.

Figure 23 – Proppant Placement (Guerra et al., 2018): Eagle Ford Formation Fracture Conductivity Test Sample A With 0.1 lb_m/ft^2 100-Mesh Sand Distributed Over the Bottom-Side Fracture Surface (left); Test Sample A With Both Fracture Surfaces Coming Together, Being Propped Apart by the 0.1 lb_m/ft^2 100-Mesh Sand (right).

The propped fracture conductivity test sample was then coated with a silicone rubber and cured in an oven at 150 ^{o}F for 4 hours. The previous was accomplished by inserting the propped test sample into a modular clamshell-type mold which was 0.003 in. wider than the Modified API Fracture Conductivity Cell, and 0.15 in. larger than the bare test sample in all dimensions – meaning that the coating was 0.075 in. thick. This interference fit ensured leakage was mitigated at high pressures during the fracture conductivity test. The silicone rubber compound was the two-component Momentive RTV 627. A Momentive SS 4155 rubber adhesive primer was also

utilized. A generalized itemized procedure for sample preparation can be found in McGinley (2015).

Once the coating was cured, the coated fracture conductivity test sample was removed from the modular mold and prepared for insertion into the Modified API Fracture Conductivity Cell (described in further detail in Section 2.4.1.1). Small windows were cut through the silicon rubber and removed to ensure connectivity between the test sample fracture and the pressure sensors as well as the flow inlet and outlet (**Figure 24**). Additionally, sealant tape was placed along and around the sample to prevent leakage and channeling around the sample.

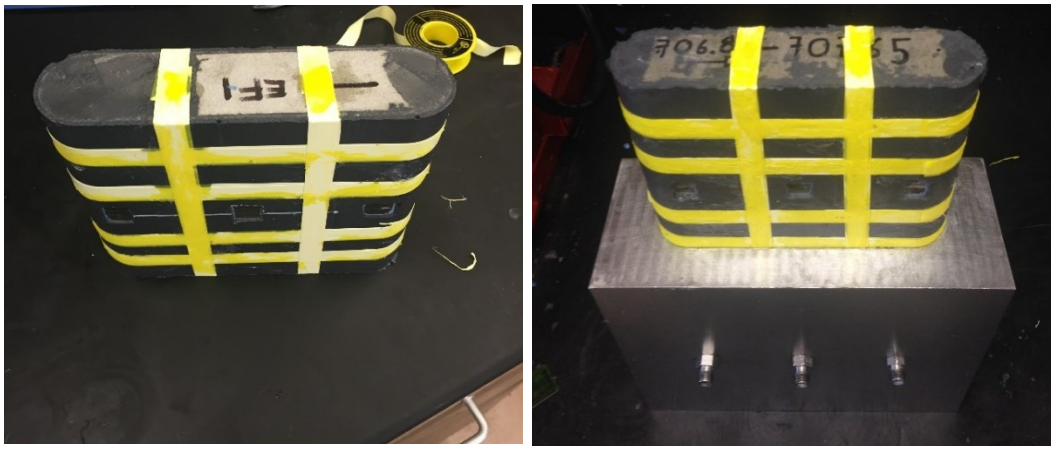

Figure 24 – Test Sample Preparation (Guerra et al., 2018): Eagle Ford Formation Fracture Conductivity Test Sample EF-1 After Silicon Rubber Coating and Curing, with Small Windows Removed for Fracture-Sensor Connectivity and Sealant Tape to Prevent Channeling (left); Prepared Middle Bakken Formation Fracture Conductivity Test Sample Core No. 5 Being Inserted into the Modified API Fracture Conductivity Cell (right).

2.3 Materials Used for Measurements

Fracture conductivity tests relied on flowing dry nitrogen in the case of baseline fracture conductivity tests, or saline water solution in sequence with dry nitrogen as in the case of water-

damaging fracture conductivity tests. The following subsections describe the details of the fluids used in the fracture conductivity tests.

2.3.1 Dry Nitrogen Gas

Industrial grade dry nitrogen was utilized for all baseline fracture conductivity tests, as well as as during the gas flow sequences within the water-damaging fracture conductivity tests. The source aluminum cylinder, as shown in **Figure 29**, was pressurized to 2,000 psi at time of purchase, and flow was controlled by a sensitive spring valve. Whenever the pressure would decrease below 800 psi, it would be replaced to ensure longevity during the following fracture conductivity test.

2.3.2 Reconstituted Flowback Water

Water-damaging fracture conductivity tests were conducted on fracture conductivity test samples from both the Eagle Ford formation as well as the Marcellus formation. In each case, the chemical composition of a typical flowback water sample was determined, which then served as the basis for the reconstitution of the saline water solution used in the fracture conductivity tests.

Saline water with a chemical composition similar to the typical Eagle Ford formation field flowback water was utilized. A typical flowback water sample in the Eagle Ford play has a total dissolved solids (TDS) concentration of 33,015 mg/L according to Slutz et al. (2012). The reconstituted flowback water used in the water-damaging fracture conductivity tests was formulated to have a TDS concentration of 31,406 mg/L with a similar corresponding chemical composition as the typical flowback water (**Table 11**).

Table 11 – Eagle Ford Formation Chemical Composition of the Reconstituted Flowback Water Sample (Adapted from Guerra et al., 2018).

Ion Name	Molecular Formula	Reconstituted Flowback Water Sample (mg/L)	Field Flowback Water Sample (mg/L)
Calcium	Ca^{2+}	1,312	1,270
Sodium	Na^{+}	10,923	10,900
Potassium	K^{+}	2	192
Magnesium	Mg^{2+}	1	111
Strontium	Sr^{2+}		203
Barium	Ba^{2+}		10
Iron	Fe		112
Chloride	Cl^{-}	19,162	19,318
Nitrate	NO_3^{-}	1	
Sulfate	SO_4^{-2}	4	163
Bicarbonate	HCO_3^{-}		736
	TDS	31,405	33,015

Similarly, a typical flowback water sample in the Marcellus play has a total dissolved solids (TDS) concentration of 72,714 mg/L according to Slutz et al. (2012), defining it as brine technically –but referred to as saline in this study. The reconstituted flowback water used in the water-damaging fracture conductivity tests was formulated to have a TDS concentration of 70,750 mg/L with a similar corresponding chemical composition as the typical field flowback water (**Table 12**). Similar results were reported by Hayes (2011).

Table 12 – Marcellus Formation Chemical Composition of the Reconstituted Flowback Water Sample (Adapted from Guerra et al., 2017b).

Ion Name	Molecular Formula	Reconstituted Flowback Water Sample (mg/L)	Field Flowback Water Sample (mg/L)
Calcium	Ca^{2+}	2,979	2,921
Sodium	Na^{+}	24,586	24,445
Potassium	K^{+}	2	190
Magnesium	Mg^{2+}	1	263
Strontium	Sr^{2+}		347
Barium	Ba^{2+}		679
Iron	Fe		26
Chloride	Cl^{-}	43,185	43,578
Nitrate	NO_3^{-}	1	
Sulfate	SO_4^{-2}	4	4
Bicarbonate	HCO_3^{-}		261
	TDS	70,758	72,714

Primary compounds used to reconstitute the saline water solution included Calcium Chloride ($CaCl_2$) and Sodium Chloride (NaCl).

2.4 Experimental Equipment

An experimental apparatus was assembled to enable the measurement of fracture conductivity by flowing dry nitrogen and/or water solutions. This fracture conductivity measurement apparatus made use of several pre-existing components, including the Modified API Fracture Conductivity Cell and the loading system, as previously introduced by earlier studies such as by Awoleke (2013), Kamenov (2013), Zhang (2014), and others. Several

additions and/or modifications were made to the testing system as a whole, and discussed in detail in the following subsections.

Influencing factors on fracture conductivity were experimentally measured through a series of different testing systems. The effect of closure stress was investigated by testing fracture conductivity at several load stages. Bulk mineralogy was determined by conducting XRD, while surface mineralogy was determined via XRF. Rock bulk properties were measured by conducting a triaxial compression test, while rock surface mechanical properties were determined by conducting a Brinell hardness test. Fracture surface topography was ascertained by using a laser profilometer. The following subsections detail each standalone testing system, its function, operation, and measurement results.

2.4.1 Fracture Conductivity Measurement Apparatus

The testing system utilized for baseline fracture conductivity tests was comprised of seven primary components: the Modified API Fracture Conductivity Cell, a GCTS hydraulic load frame, a gas reservoir/injection unit embodied by the pressurized dry nitrogen aluminum cylinder, cell pressure transducer and differential pressure transducer, gas flowmeter, back pressure regulator, and a GCTS control box linked to a PC which contains a data acquisition unit embodied by two platforms –one recording the load applied by the load frame and the pressures registered by the pressure transducers, and the other one recording the gas flow rate registered by the gas flow meter. The schematic of the baseline fracture conductivity measurement apparatus is shown in **Figure 25**, with each major component and its function discussed in the following subsections.

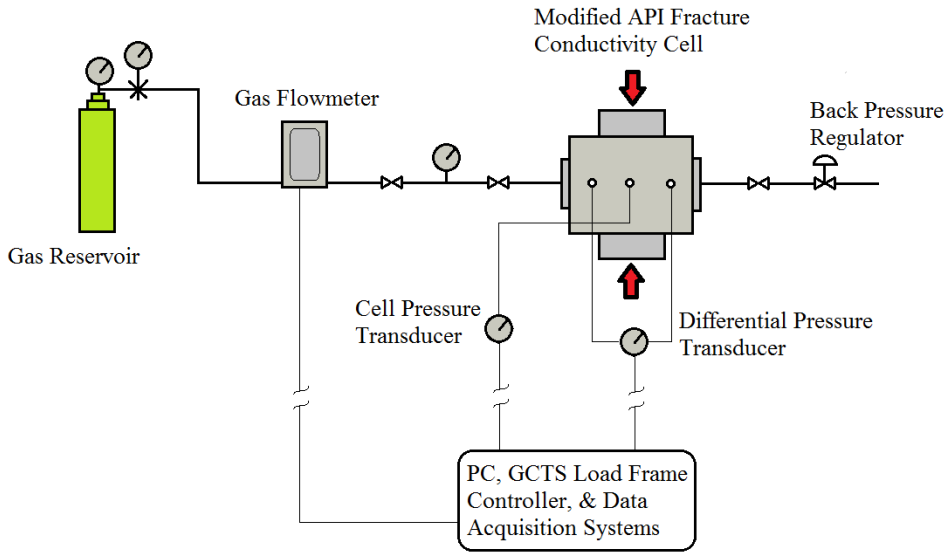

Figure 25 – Major Component Schematic of the Experimental Apparatus Setup for Measuring Baseline Fracture Conductivity.

The testing system utilized for water-damaging fracture conductivity tests employed all previously listed components, in addition to a water reservoir and a syringe pump. The schematic of the water-damaging fracture conductivity measurement apparatus is shown in **Figure 26**, with its differentiating major components and their function discussed in the following subsections.

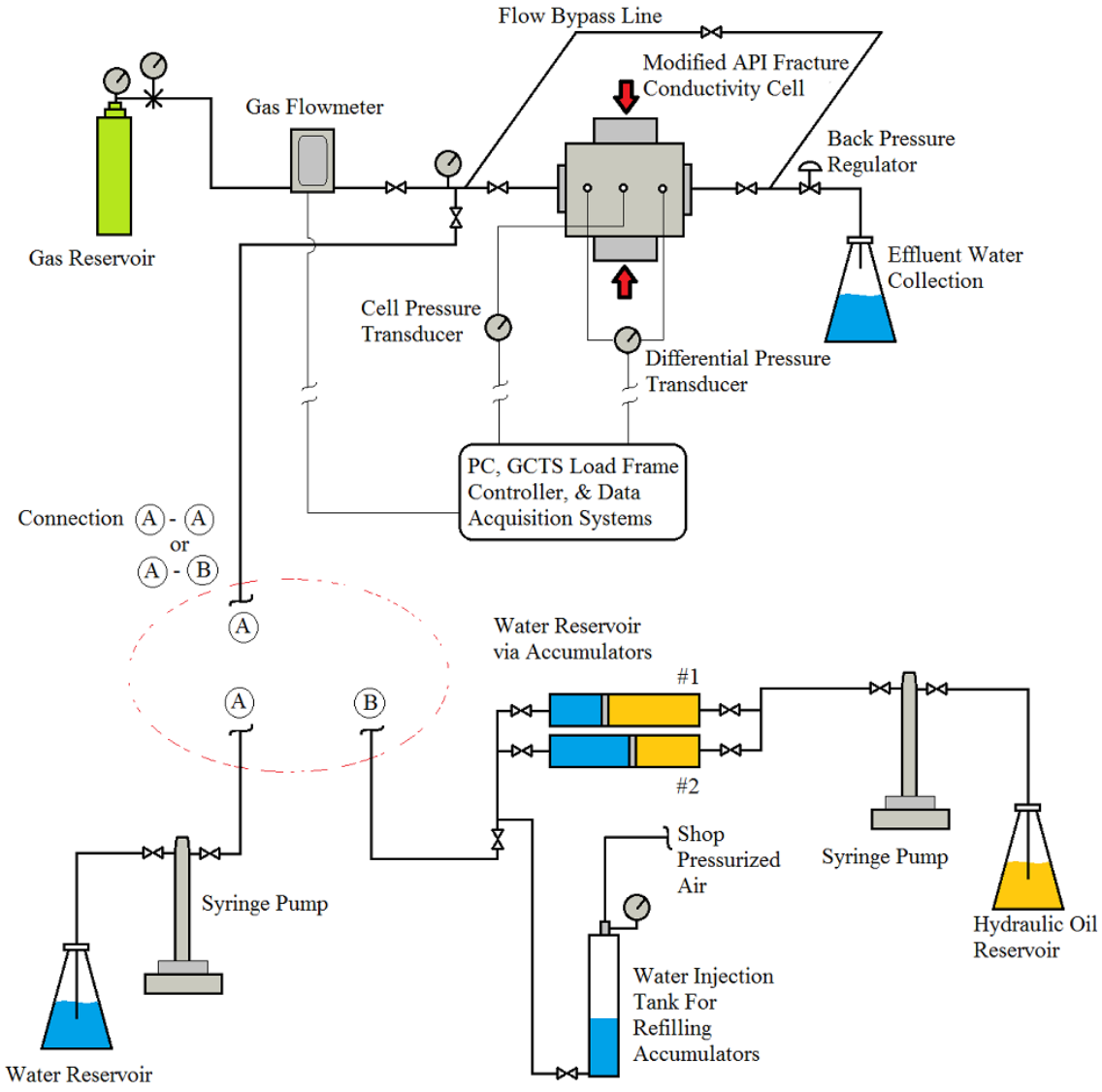

Figure 26 – Major Component Schematic of the Experimental Apparatus Setup for Measuring Water-Damaging Fracture Conductivity (Two Alternate Water Sources).

Figure 27 illustrates the actual fracture conductivity measurement apparatus, with the following subsections housing more detailed imagery of each particular component.

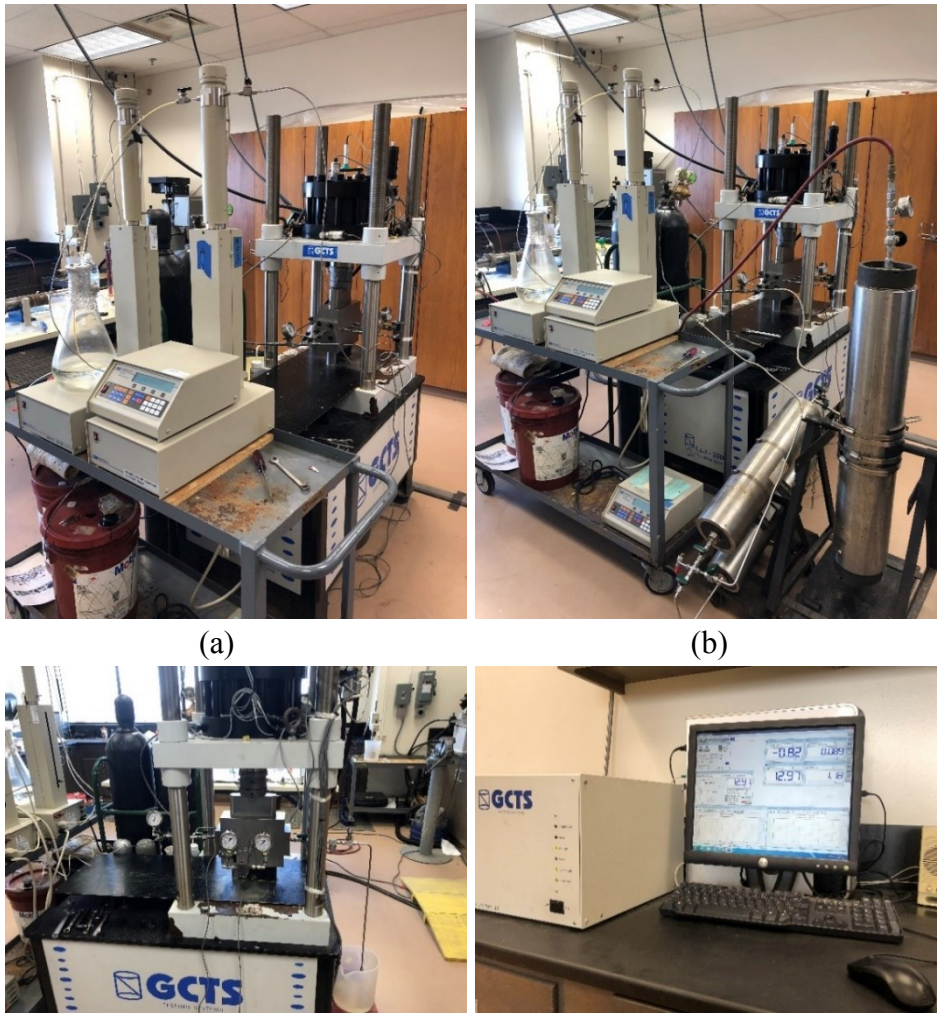

(a) (b)

(c) (d)

Figure 27 – Fracture Conductivity Measurement Apparatus: (a) Assembled Modified API Fracture Conductivity Cell Inside the Load Frame (background), With Syringe Pump(s)/Water Reservoir (foreground); (b) Similar to (a), While Also Showing the Presence of the Accumulators/Air Pressure Vessel (foreground), With Dry Nitrogen Cylinder(s) (background); (c) A Close-up of The Modified API Fracture Conductivity Cell Showing the Top and Bottom Inserts, its End Caps that Connect to the Inlet/Outlet Flow Lines, and the Cell Pressure and Differential Pressure Transducers; (d) A View of the Load Frame Controller and Data Acquisition Layout Displayed in the PC Screen.

Water flow can be directly from the water reservoir and pump, or from one of the accumulators being driven by the pump, as shown in **Figure 26** as connection A-A and A-B, respectively. In the latter, the pump is exposed only to AW-32 hydraulic oil and as such, requires no flushing of acetone between tests for cleaning.

2.4.1.1 Modified API Fracture Conductivity Cell

The Modified API Fracture Conductivity Cell is fabricated from stainless steel, and consists of one main housing with several openings, allowing for the insertion of a top and bottom load piston as well as an inlet and outlet flow insert end cap; additionally, the cell body contains three side ports allowing for connectivity between the cell cavity and the pressure transducers, as shown in **Figure 28**. The only departure from API conductivity cell specifications are the dimensions.

The cell body outer dimensions are 10 in. in length, 4 in. in width, and 8 in. in height. The cell cavity dimensions are 7.2470 in. in length, 1.7570 in. in width, and 8 in. in height –with these dimensions accounting for circular ends of radius 0.8785 in. This inner cell cavity accommodates a fully prepared fracture conductivity test sample as per Section 2.2.4.3, with final test sample dimensions being 7.25 in. in length, 1.76 in. in width, and 6 in. in height (variable to some extent depending on the specific proppant concentration). As mentioned earlier, these final dimensions result in a 0.003 in. gain over all the inner dimensions of the cell cavity.

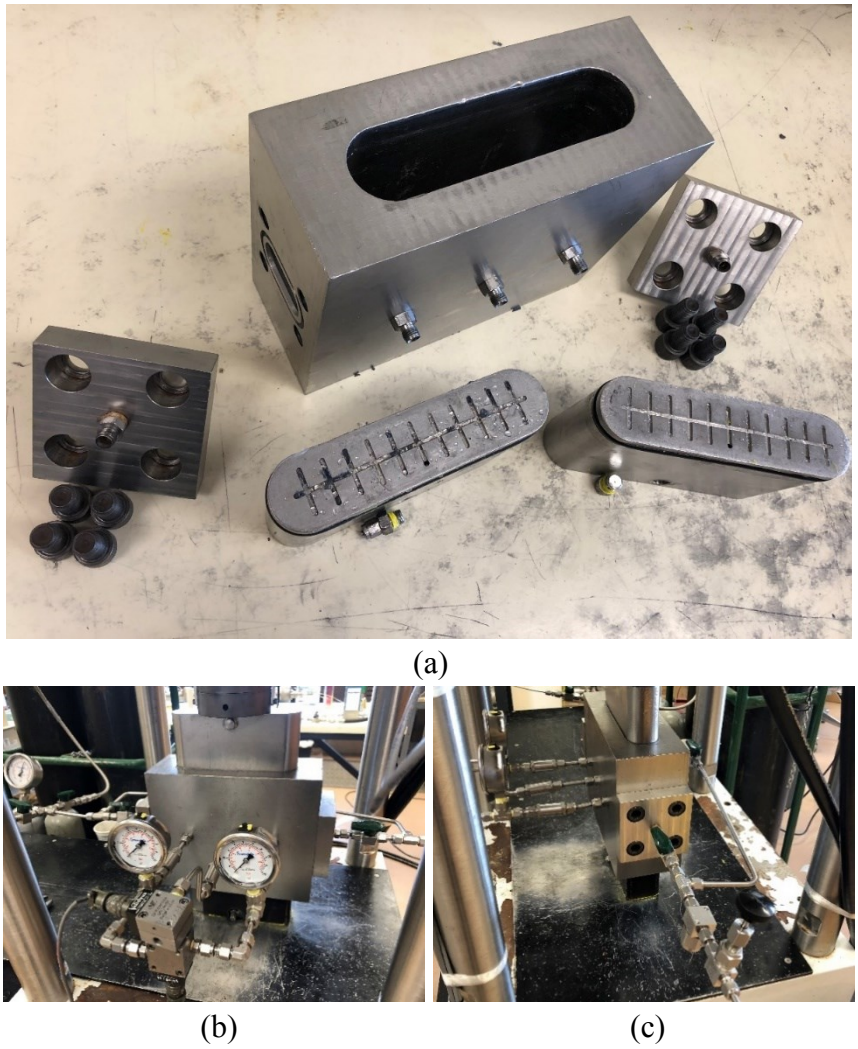

(a) (b) (c)

Figure 28 – Modified API Fracture Conductivity Cell: (a) Cell Body, Top and Bottom Load Pistons (Screws Utilized to Close Leak-off Port), and Upstream and Downstream Flow Insert End Caps (Screws Used During Assemblage); (b) The Cell Fully Assembled and Connected to Pressure Transducers and Upstream and Downstream Flow Lines (Leak-off Ports Closed); and (c) Downstream Flow Line and Back Pressure Regulator.

The top and bottom load piston inserts, as shown in **Figure 28**, hold the fracture conductivity test sample in place, and transfer the load from the load frame to the test sample. Each piston is 7.147 in. in length, 1.657 in. in width, and 3 in. in height. They each have an inner tubular conduit connecting the base of the piston to the outer port, allowing for the installation of leak-off lines –this port was closed during all the fracture conductivity tests in this study, given

that leak-off was not observed or expected. To ensure a correct seal, each piston had a Viton polypack seal o-ring at the inserting end; the same was true for the inlet and outlet flow inserts.

In a typical fracture conductivity test, the sample is first inserted in to the Modified API Fracture Conductivity Cell, then the top and bottom load pistons are inserted, followed by the assembling of the upstream and downstream flow insert end caps on to the cell. The ensuing experimental procedure is covered in detail in Section 2.6.

2.4.1.2 Load Frame

The hydraulic load frame is a GCTS FRM4-1000-50S loading system, as shown in **Figure 27a,b,c**, which has a load capacity of 208,000 lb_f and a loading rate of 1,215 lb_f/min. The load frame and hydraulic pump are controlled by a control box and a linked computer, with a data acquisition system that records data pertaining to load (or stress), piston position (to an accuracy of 4 x 10^{-4} in.), as well as the wired pressure transducers for cell pressure and differential pressure. Other parameters can be recorded as well, and the program suite allows for customization, such as reflecting the load applied as stress by considering the user-input of fracture conductivity test sample cross-section, that of 10.87 in^2. Given the test specimen cross-section, the closure stress that can be applied well exceeds 10,000 psi –a value that far exceeds any fracture conductivity tests conducted in this study.

This load system was described in previous studies, including Kamenov (2013) and Zhang (2014).

2.4.1.3 Gas Reservoir

As mentioned in Section 2.3.1, dry nitrogen was utilized for all baseline fracture conductivity tests, as well as during the gas flow sequences within the water-damaging fracture conductivity tests. The source aluminum cylinder is shown in **Figure 29**. The regulator was used to control the flow into the Modified API Fracture Conductivity Cell, by adjusting accordingly depending on the registered flow rate observed with the flowmeter.

Figure 29 – Industrial Grade Dry Nitrogen Housed in Aluminum Cylinder(s) (left), and Operated via a Regulator with Upstream and Downstream Pressure Gauges (right). Flowmeter Shown in Background.

2.4.1.4 Water Reservoir

The water-damaging fracture conductivity tests were conducted utilizing the apparatus shown in **Figure 26**, where two alternate water sources were available.

The first alternative consisted of the water solution being flowed from a reservoir directly into the syringe pump, and then discharged into the Modified API Fracture Conductivity Cell, as shown in connection A-A in **Figure 26** and **Figure 30a**.

If it is not desirable to have the water solution come in contact with the syringe pump components, an alternate arrangement can be used. This arrangement, shown in **Figure 26** as connection A-B, allowed for the syringe pump components to only come in contact with hydraulic oil, which in turn transferred the prescribed flow rate onto a stainless steel displacement accumulator (shown in **Figure 27b** and **Figure 30b**) that had an inner sliding piston interfacing between the hydraulic oil and the water solution. Under this arrangement, the accumulators were first filled with the water solution by employing a water tank that was pressurized using shop air (at 100 psi pressure). Once the injection tank was pressurized by the air, the ball valves were opened and closed accordingly to allow for the displacement of the sliding piston back to its original position in which the accumulator was filled with the water solution and was ready to be displaced on the opposite side by the hydraulic oil being pumped by the syringe pump.

Both water source arrangements were utilized in the fracture conductivity tests, with no discernable difference in experimental outcomes. Advantages of the accumulator arrangement include less pump maintenance, and the option to have different water solutions in each accumulator. Even though the capacity of the accumulators is 4L, the limiting factor in terms of flow duration (under a specific flow rate) was determined by the capacity of the syringe pump, which is covered in detail in the following section.

(a) (b)

Figure 30 – (a) Water Reservoir Upstream of Syringe Pump; (b) Two-Set Independent Accumulators Acting as an Interface Between the Water Solution and the Hydraulic Oil Used by the Syringe Pump.

2.4.1.5 Syringe Pumps

As shown in **Figure 26** and **Figure 27**, two syringe pumps were available within the fracture conductivity apparatus. The first syringe pump was a Teledyne ISCO Model 100DX with a volume capacity of 100 mL (pressure rated to 10,000 psig). The second syringe pump was a Teledyne ISCO Model 500HP (Custom) with a volume capacity of 500 mL (pressure rated to 5,000 psig). Both syringe pumps were controlled by a single Teledyne ISCO D-Series Pump Controller, as shown in **Figure 31**.

All water-damaging fracture conductivity tests relied on the use of one syringe pump during testing, which was predominantly the pump with the largest volume capacity, thus ensuring the least amount of refills necessary during water flow until steady state was reached.

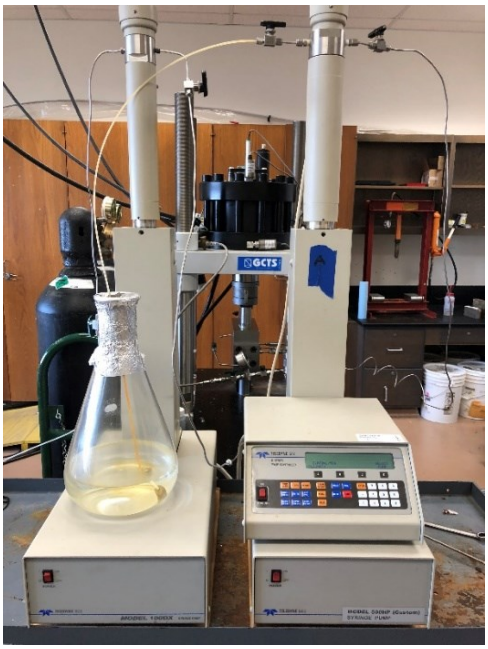

Figure 31 – Syringe Pumps and Pump Controller Utilized During Water-Damaging Fracture Conductivity Tests.

2.4.1.6 Pressure Transducers

The cell pressure and differential pressure was registered by two different Validyne pressure transducers with exchangeable internal sensor diaphragms, as shown in **Figure 32**. Each pressure transducer was wired for live feed into the GCTS control box. The cell pressure transducer housing was Model DP15 50N1S4A with internal sensor diaphragm 3-50 (stress range of $\pm$125 psi), whereas the differential pressure housing was Model DP15-32 with internal sensor diaphragm 3-32F (stress range of $\pm$3.5 psi). The pressure transducers had an accuracy of $\pm$2.5% of full scale pressure.

Sensor calibration was performed before every fracture conductivity test, as per procedure outlined by Awoleke (2013).

Figure 32 – Validyne Pressure Transducers: Cell Pressure Unit with Tubing to Connect to Conductivity Cell and Wiring Unit (left) and Differential Pressure Unit with Upstream and Downstream Tubbing to Connect to Conductivity Cell (right). Upstream and Downstream Tubing Had Pressure Gauges Installed for Redundancy.

2.4.1.7 Flow Meters

The outlet of the gas reservoir supplying the dry nitrogen was connected to an Aalborg XFM17 Digital Mass Flow Meter of either a 1,000 mL/min capacity or a 10,000 mL/min capacity, as shown in **Figure 33**. Both these mass flowmeters were specifically designed, fabricated, and calibrated at the manufacturer for nitrogen gas flow. Both these flowmeters had a mass flow measurement accuracy of $\pm$1% of full scale flow rate. Gas pressures during fracture conductivity tests were below the flowmeter working gas pressure limit.

Figure 33 – Aalborg XFM17 Digital Mass Flow Meter: 1,000 mL/min Capacity (left) and 10,000 mL/min Capacity (right).

In order to reduce the error in flow rate measurement, for unpropped and relatively low proppant concentration fracture conductivity tests, the flowmeter of 1 L/min capacity was employed, while for higher proppant concentration tests, the flowmeter of 10 L/min capacity was utilized. This accounted for the fact that both flowmeters had a measurement accuracy of $\pm 1\%$ of full scale flow rate, meaning that for a registered flow rate of 0.7 L/min, the 1 L/min capacity flowmeter would have ± 10 mL/min measurement error; while the 10 L/min capacity flowmeter would have a ± 100 mL/min measurement error –introducing an unnecessary source of measurement error.

2.4.1.8 Back Pressure Regulator

The needle valve shown in **Figure 34** served as a back pressure regulator. The Modified API Fracture Conductivity Cell was pressurized to a set pressure by flowing dry nitrogen into the

closed system, at which point, flow was regulated by controlling the outflow by operating the needle valve to achieve a desired flow rate for the prescribed cell pressure. Experimental procedures are covered in detail in Section 2.6.

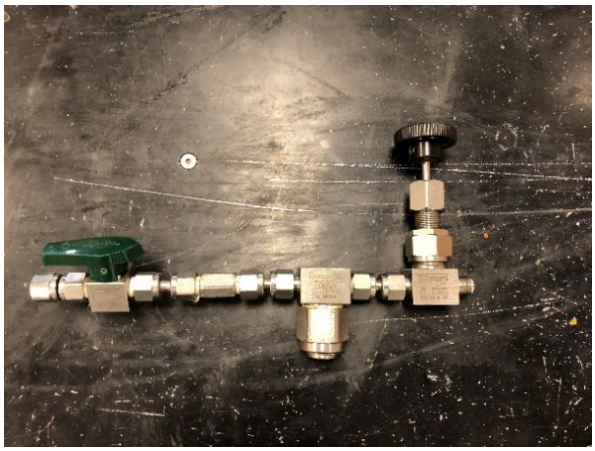

Figure 34 – Needle Valve Serving as a Back Pressure Regulator. Also Shown is a Ball Valve that is Connected at the Downstream Flow Insert End Cap of the Modified API Fracture Conductivity Cell, as well as a Swagelok Filter.

2.4.2 Triaxial Compression Test System

Bulk mechanical property characterization was conducted by utilizing a GCTS RTX-1500 Triaxial Rock Testing System. This system is designed to test rock properties, principally Young's modulus and Poisson's ratio, under a prescribed confining pressure; with a maximum test sample dimension of 4 in. in length by 2 in. in diameter. The system can apply a maximum axial load of 337,200 lb_f and a maximum confining pressure of 20,000 psi. Supplemental to the load frame and the high pressure cell, the data acquisition system allows for the recording of axial and circumferential deformations through the use of Linear Variable Differential Transducers (LVDTs), with a sensitivity of 0.001 mm. It is to be noted that this testing system abides by the International Society of Rock Mechanics (ISRM) standards for triaxial

compression tests on rocks. A standard created by the American Society for Testing and Materials International (ASTM International), ASTM D7012-14, was followed for the measurement of compressive strength and elastic modulus of rock samples. Sample preparation and the operation of this testing system followed procedures outlined by Jansen (2014) and Knorr (2016). Details of applied load cases and respective rates, were as per Knorr (2016). All tests were conducted at 290 psi confining stress.

Triaxial compression tests were conducted on core plug test samples from the Eagle Ford, the Marcellus, the Middle Bakken, and the Three Forks formations. **Table 13** provides a summary of the bulk mechanical properties for the Eagle Ford formation, which are reported in detail by Knorr (2016).

Table 13 – Average Bulk Mechanical Properties for the Eagle Ford Formation Outcrop Rock Core Plug Test Samples.

Test Sample Name	Bulk Mechanical Properties			
	Poisson's ratio (Z Orientation)	Poisson's ratio (X90 Orientation)	Young's modulus (Z Orientation) (psi)	Young's modulus (X90 Orientation) (psi)
E	0.168	0.209	4,760,000	5,600,000
D	0.116	0.184	3,800,000	4,820,000
C	0.127	0.178	2,840,000	3,780,000
B3		0.119		2,850,000
B2	0.138	0.174	3,510,000	3,800,000
B1	0.142	0.172	3,530,000	4,230,000
A	0.109	0.144	3,790,000	3,980,000

Table 13 values for each Eagle Ford formation unit or sub-unit are averaged based on the core plug test samples obtained for this study and additional test samples investigated by Knorr

(2016), both from the same batch of collected outcrop rocks. Considering all tested units and sub-units, the standard deviation between Poisson's ratio measurement results ranged from 3% (B1) up to 52% (B2) for the Z orientation (based on a sampling size of 3 test samples for each of the aforementioned subunits), and for the X90 orientation, it ranged from 2% (B3) up to 33% (B2) based on a sampling size of 2 test samples for each of the aforementioned subunits; reflecting a large degree of heterogeneity between test samples.

Table 14 provides a summary of the bulk mechanical properties for the Marcellus formation, which are reported in detail by McGinley (2015). Perez et al. (2016) and McGinley (2015) tested core plug test samples obtained from the same batch of collected outcrop rocks as in this study.

Table 14 – Average Bulk Mechanical Properties for the Marcellus Formation Outcrop Rock Core Plug Test Samples.

Test Sample Name	Bulk Mechanical Properties			
	Poisson's ratio (Z Orientation)	Poisson's ratio (X90 Orientation)	Young's modulus (Z Orientation) (psi)	Young's modulus (X90 Orientation) (psi)
Elimsport 1–4	0.256	0.283	1,100,000	2,320,000
Allenwood 1–4	0.202	0.161	3,990,000	4,410,000

Poisson's ratio measurement results obtained by Perez et al. (2016) on Marcellus formation core plug test samples, had a standard deviation of 5% (Elimsport) and 15% (Allenwood) for the Z orientation (based on a sampling size of 3 test samples for the Elimsport location, and 5 for the Allenwood location), and for the X90 orientation, a 3% (Elimsport) and 13% (Allenwood) based on a sampling size of 5 test samples for each of the aforementioned

locations; reflecting a smaller degree of heterogeneity between test samples when compared to the Eagle Ford formation.

Table 15 and **Table 16** provide a summary of the bulk mechanical properties for the Middle Bakken and Three Forks formations, respectively.

Table 15 – Bulk Mechanical Properties for the Middle Bakken Formation Downhole Core Segment Core Plug Test Samples.

Test Sample Name	Bulk Mechanical Properties			
	Poisson's ratio (Z Orientation)	Poisson's ratio (X90 Orientation)	Young's modulus (Z Orientation) (psi)	Young's modulus (X90 Orientation) (psi)
Core No. 2	0.259	0.185	5,040,000	5,100,000
Core No. 5		0.154		4,320,000
Core No. 6		0.096		3,120,000

Table 16 – Bulk Mechanical Properties for the Three Forks Formation Downhole Core Segment Core Plug Test Samples.

Test Sample Name	Bulk Mechanical Properties			
	Poisson's ratio (Z Orientation)	Poisson's ratio (X90 Orientation)	Young's modulus (Z Orientation) (psi)	Young's modulus (X90 Orientation) (psi)
Core No. 8		0.126		4,030,000
Core No. 9	0.149	0.046	1,160,000	1,550,000

2.4.3 Brinell Hardness Test System

Surface mechanical property characterization was conducted by utilizing a GCTS PLT-100 apparatus. This apparatus is designed to test surface hardness and measure indentation values that can be used to compute the Brinell Hardness Number (BHN –although commonly referred to as HBW since the material indenter is tungsten carbide). A standard created by

ASTM International, ASTM E10-14, was followed to test Brinell hardness of the rock samples – although originally created for metal-based materials.

The apparatus consists of a manually operated load piston that displaces a 0.125 in. tungsten ball indenter (there are different standard sizes) which in turn applies force to the test sample surface, resulting in a crater-like surface indentation. Some procedural changes were made in order to abide by the ASTM E10-14 standard (Knorr 2016).

Sample preparation and the operation of this testing apparatus followed procedures outlined by Knorr (2016). The cross-sectional surface of the core plug test samples was utilized.

The Brinell Hardness Number was determined for core plug test samples from the Eagle Ford formation, the Middle Bakken, and the Three Forks formations. **Table 17** provides a summary of surface mechanical properties for the Eagle Ford formation, which are reported in detail by Knorr (2016).

Table 17 – Average Surface Mechanical Properties for the Eagle Ford Formation Outcrop Rock Core Plug Test Samples.

Test Sample Name	Surface Mechanical Properties	
	Brinell Hardness Number (Z Orientation) (psi)	Brinell Hardness Number (X90 Orientation) (psi)
E	81,500	129,219
D	131,225	130,371
C	97,160	116,446
B3		128,124
B2	144,111	177,066
B1	129,290	144,808
A	150,255	130,727

Table 18 and **Table 19** provide a summary of surface mechanical properties for the Middle Bakken and Three Forks formations, respectively.

Table 18 – Average Surface Mechanical Properties for the Middle Bakken Formation Downhole Core Segment Core Plug Test Samples.

Test Sample Name	Surface Mechanical Properties	
	Brinell Hardness Number (Z Orientation) (psi)	Brinell Hardness Number (X90 Orientation) (psi)
Core No. 2	59,070	144,154
Core No. 5		131,125
Core No. 6		123,999

Table 19 – Average Surface Mechanical Properties for the Three Forks Formation Downhole Core Segment Core Plug Test Samples.

Test Sample Name	Surface Mechanical Properties	
	Brinell Hardness Number (Z Orientation) (psi)	Brinell Hardness Number (X90 Orientation) (psi)
Core No. 8		97,999
Core No. 9		145,789

2.4.4 X-ray Powder Diffraction (XRD)

As described in detail in Section 2.2.3, XRD was used for the core plug test samples by utilizing a Bruker D8 Advanced Eco XRD system.

2.4.5 X-ray Fluorescence (XRF)

One side of the fracture surface for each fracture conductivity test sample was scanned by XRF microscopy by utilizing a Horiba XGT-7000 X-Ray Analytical Microscope to obtain

element distribution data and ultimately infer fracture surface mineralogy for the Eagle Ford formation. In order to produce maps representing the element distribution along the fracture surface, a resolution of 100 μm was prescribed. Given the dimensions of the sample, four scan sections were typically required. The prescribed group of elements considered during the scanning process was set to include Al, As, Ba, Ca, Cr, Fe, K, Mg, Mn, Rb, S, Si, Sr, Ti, Zn, and Zr.

Background noise maps for the elements of interest were calculated and subtracted from the corresponding element maps using a Java-based image processing software, ImageJ, resulting in gray-scale images for the elements. These images were then stitched together to produce a final image representing the entire fracture surface. **Figure 35** shows the distribution of Ca, Fe, Si, S, and K on the fracture surface for fracture conductivity test sample B1. These elements were the most abundant on the fracture surface.

Variations in observed intensity were a result of varying presence of a particular element on the fracture surface. However, the intensity was also affected by the differences in the distance from the X-ray source to the fracture surface, which inherently was a function of the varying topography along the fracture surface. K distribution along the fracture surface illustrates a slight interference from the aforementioned phenomena (**Figure 35**). These variations were considered an artifact of the procedure itself, and were mitigated during the stitching process by ensuring each scan section element map had the same background intensity.

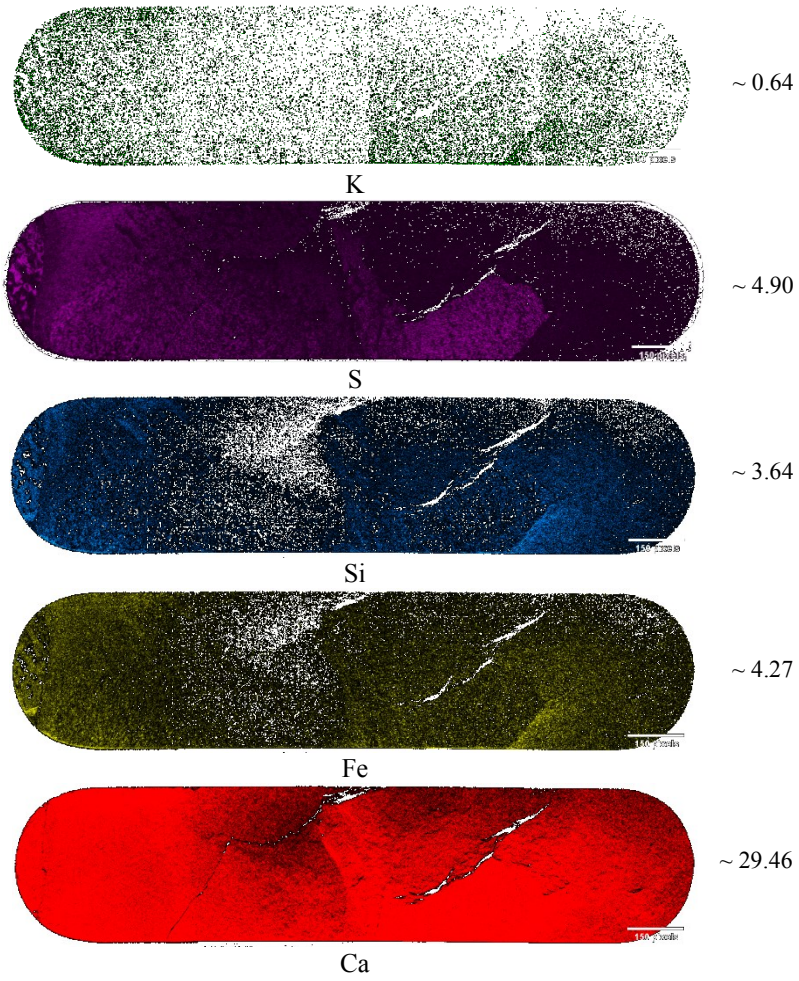

Figure 35 – Eagle Ford Formation Fracture Conductivity Test Sample B1 Ca, Fe, Si, S, and K Distribution along the Fracture Surface (0.1 mm Pixel Width) (Guerra et al., 2018). Values on Right are the Estimated Intensity for Each Particular Element over the Fracture Surface.

Stitched element maps over the full fracture surface were also overlaid on each other producing composite images that served as proxies to mineral presence, as illustrated in **Figure 36**, where Ca, Fe, and Si were overlaid to visualize how the fracture originated in a clay bed and progressed onto a limestone bed for fracture conductivity test sample A (left to right).

(a)

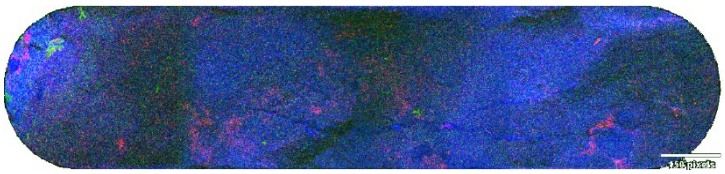

(b)

Figure 36 – Mineral Presence on Fracture Surface (Guerra et al., 2018): (a) Actual Picture of Fracture Surface for Fracture Conductivity Test Sample A; (b) Ca, Fe, and Si Overlaid on Each Other. Ca was Colored Blue, Fe Red, and Si Green.

From a quantitative perspective, the stitched element maps were used to estimate the average intensity over the entire fracture surface for each particular element (**Table 20**). Based on the gathered data and the known mineralogy found in the formation via XRD, the analysis was focused solely on Ca, Fe, Si, and K. The aforementioned elements were selected given their documented reliability as proxies to certain minerals, including clay. Test samples obtained from downhole core carry the nomenclature Core 1, Core 2 and Core 3. As mentioned before, they are all from unit B.

Table 20 – Average Intensity over the Fracture Surface for Each Eagle Ford Formation Fracture Conductivity Test Sample (Adapted from Guerra et al., 2018).

Test Sample Name	Intensity (~)			
	Ca	Fe	Si	K
E	53.491	0.634	0.423	0.289
D	55.670	0.513	0.397	0.301
C	45.372	1.848	3.122	1.422
B3	36.203	5.570	5.971	0.703
B2	30.089	5.278	4.934	0.867
B1	29.460	4.270	3.640	0.640
A	52.079	0.578	0.473	0.368
Core 1	28.601	2.674	2.530	0.573
Core 2	27.534	2.874	2.145	0.509
Core 3	29.235	2.519	2.492	0.498

Based on the gathered data and the abundance of Ca across all samples, a K/Ca element ratio was chosen as a proxy to the presence of clay over the fracture surface. Variability in element distribution along the fracture surface was evident across lithostratigraphic units, with a heavy presence of Ca across all test samples, and a clustered presence of Fe, Si, and K for the zones with the highest TOC.

2.4.6 Laser Profilometer System

The fracture surface of each test sample was scanned using a laser profilometer system which produced measured height, z, values for a specified mesh grid (x, y), as shown in **Figure 37** and **Figure 38**. The laser profilometer apparatus is described in detail by McGinley (2015). In this study, a new data processing code based on MATLAB was developed.

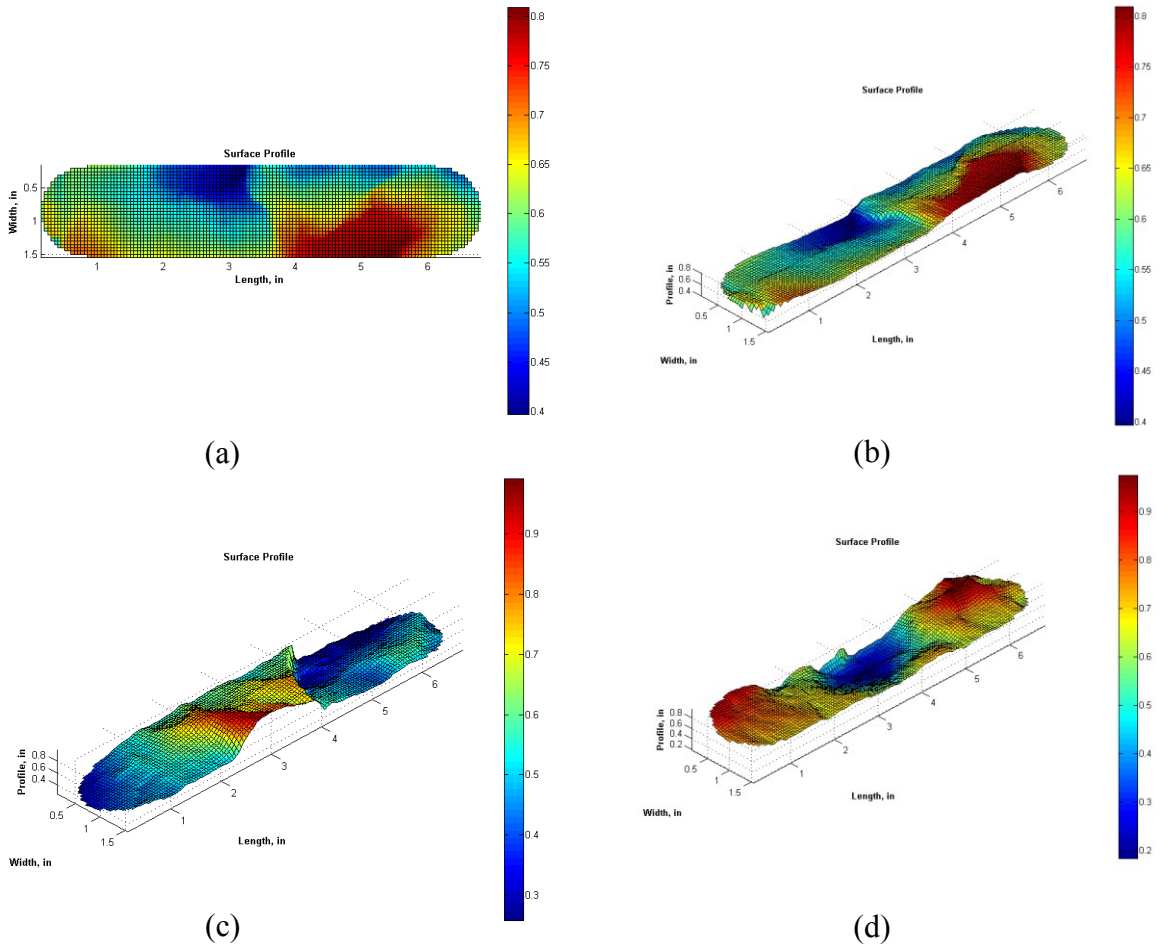

Figure 37 – Surface Topography for the Bottom Side of the Eagle Ford Formation Fracture Conductivity Test Samples (Guerra et al., 2018): (a) Top View of B1 (b) B1; (c) D; (d) E.

z values for a rectangular grid spacing of 0.025 in. were obtained and then processed to generate an interpolated surface based on the measured heights. This surface served as the basis for computations including surface area and surface roughness.

A flat test sample has a computed surface area of 10.87 in.^{2}, with a corresponding x, y mesh grid covering the entire flat surface. In this particular study, the x, y mesh grid covered a smaller portion of the flat surface with only 8.81 in.^{2} surface area, reflecting an inward offset of 0.1 in. all around the sample. This was done to increase the reliability of the readings and avoid

false height readings attributed to the materials used in the sample preparation that run along the edge of the bare test sample. Given that the surface area was used for relative comparison, considering 81% of the original x, y mesh grid sufficed. The surface roughness was computed via the root mean square method, R_{RMS}, as shown in **Eq. 1**.

$$R_{RMS} = \sqrt{\frac{1}{n}\sum_{i=1}^{n} z_i^2} \quad \text{.....} \quad (1)$$

$$z_i = |z - \bar{z}|$$

A significant variation of surface area across the test samples was observed, which resulted in some samples having a longer and/or greater tortuous flow path, such as Eagle Ford formation fracture conductivity test sample E (**Figure 37d**), the Mahantango formation test sample Core #1 (**Figure 38b**), and the Three Forks formation test sample Core No. 9 (**Figure 38d**).

A summary of estimated fracture surface area, maximum surface height difference, Δz_{max}, between the lowest and highest point on the fracture surface, and fracture surface roughness for fracture conductivity test samples from the Eagle Ford formation is provided in **Table 21**, whereas for the Marcellus formation is provided in **Table 22**, the Mahantango formation in **Table 23**, the Middle Bakken formation in **Table 24**, and the Three Forks formation in **Table 25**.

Table 21 – Eagle Ford Formation Fracture Conductivity Test Sample Estimated Fracture Surface Area, Maximum Height Difference along the Fracture, and Fracture Surface Roughness Values (Adapted from Guerra et al., 2018).

Test Sample Name	Surface Area ($in.^2$)	Δz_{max} (in.)	R_{RMS} (in.)
E	9.730	0.790	0.270
D	9.820	0.730	0.230
C	9.050	0.290	0.110
EF-1	8.890	0.140	0.200
EF-2	9.010	0.230	0.200
EF-3	8.970	0.190	0.195
B3	8.900	0.120	0.150
B2	8.930	0.240	0.250
B1	9.150	0.410	0.210
A	9.030	0.400	0.180
Core 1	10.760	0.940	0.310
Core 2	10.430	0.840	0.290
Core 3	10.510	0.890	0.305

The fracture conductivity test samples from downhole core segments, given their relatively small original dimensions, represented several challenges during fracture creation, resulting in fractures that were typically at an angle with respect to the length of the sample, as well as with a clear jaggedness across the length. These fracture surfaces typically had a higher surface area due to their orientation with respect to the test sample, as shown in **Table 21**, **Table 23**, **Table 24** and **Table 25**.

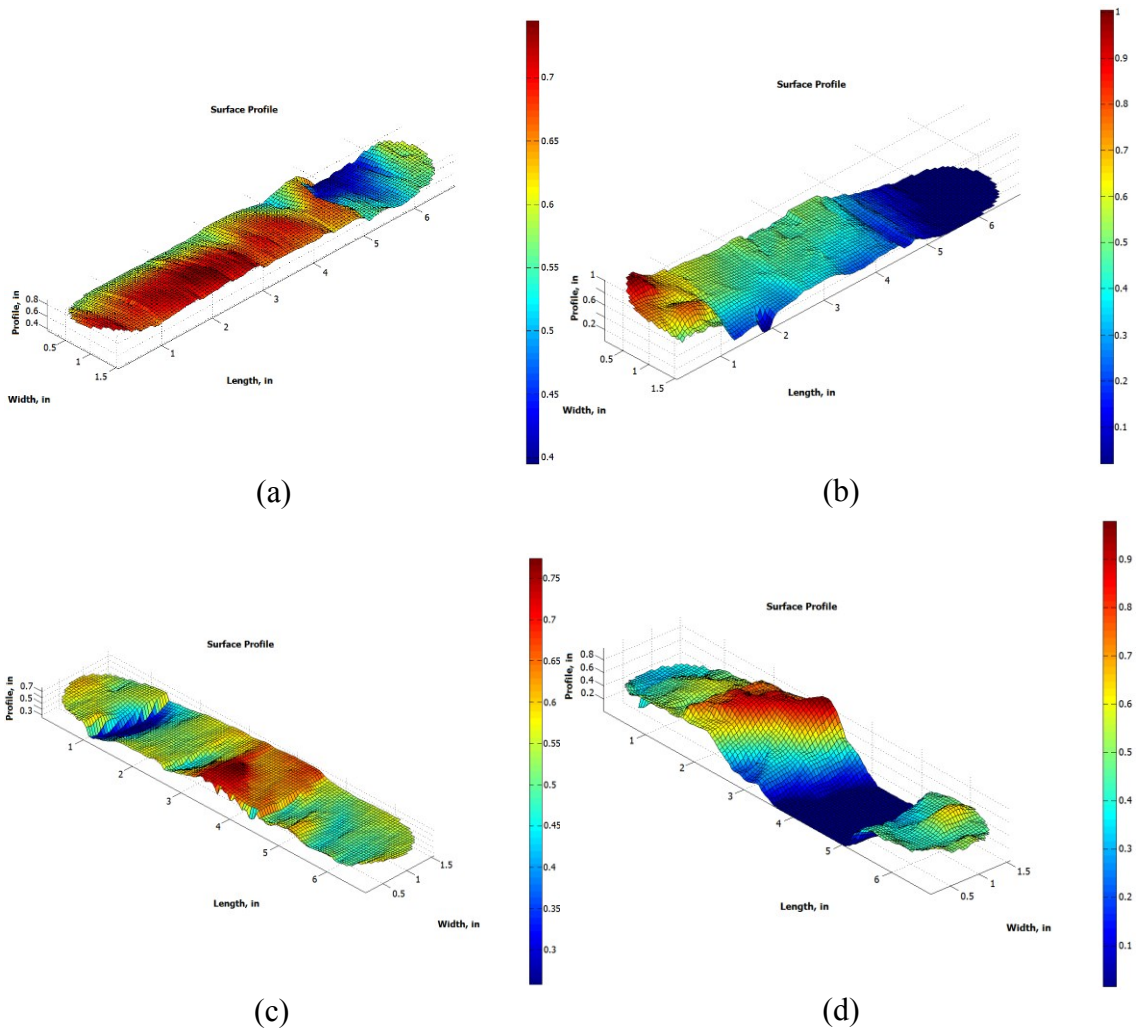

Figure 38 – Surface Topography for the Bottom Side of the Fracture Conductivity Test Samples: (a) Marcellus Formation Test Sample Allenwood 1; (b) Mahantango Formation Test Sample Core #1; (c) Middle Bakken Formation Test Sample Core No. 2; (d) Three Forks Formation Test Sample Core No. 9.

Table 22 – Marcellus Formation Fracture Conductivity Test Sample Estimated Fracture Surface Area, Maximum Height Difference along the Fracture, and Fracture Surface Roughness Values.

Test Sample Name	Surface Area (in.^{2})	Δz_{max} (in.)	R_{RMS} (in.)
Elimsport 1	9.050	0.370	0.130
Elimsport 2	8.950	0.420	0.280
Elimsport 3	9.150	0.670	0.190
Elimsport 4	9.330	0.600	0.220
Allenwood 1	9.380	0.460	0.250
Allenwood 2	9.230	0.430	0.210
Allenwood 3	9.400	0.650	0.250
Allenwood 4	9.180	0.590	0.220

Table 23 – Mahantango Formation Fracture Conductivity Test Sample Estimated Fracture Surface Area, Maximum Height Difference along the Fracture, and Fracture Surface Roughness Values.

Test Sample Name	Surface Area (in.^{2})	Δz_{max} (in.)	R_{RMS} (in.)
Core #1	10.170	0.970	0.280
Core #2	9.370	0.510	0.250

Table 24 – Middle Bakken Formation Fracture Conductivity Test Sample Estimated Fracture Surface Area, Maximum Height Difference along the Fracture, and Fracture Surface Roughness Values.

Test Sample Name	Surface Area (in.^{2})	Δz_{max} (in.)	R_{RMS} (in.)
Core No. 2	9.530	0.520	0.190
Core No. 5	9.360	0.480	0.190
Core No. 6	9.270	0.630	0.230

Table 25 – Three Forks Formation Fracture Conductivity Test Sample Estimated Fracture Surface Area, Maximum Height Difference along the Fracture, and Fracture Surface Roughness Values.

Test Sample Name	Surface Area ($in.^2$)	Δz_{max} (in.)	R_{RMS} (in.)
Core No. 8	10.170	0.900	0.260
Core No. 9	10.350	0.960	0.290
Core No. 10	10.440	0.850	0.230

2.5 General Workflow

A generalized experimental workflow was designed for this study, accounting for all the equipment described in Section 2.4, the type of test sample and the desired measurements. The major action items followed in this study were as follows:

1. Formation samples were obtained and test samples were created, as per Section 2.2, consisting of
    a. Fracture conductivity test samples, and
    b. Core plug test samples.
2. For a core plug test sample, the following was conducted sequentially:
    a. A triaxial compression test as per Section 2.4.2,
    b. A Brinell hardness test as per Section 2.4.3,
    c. XRD as per Section 2.4.4.
3. For a fracture conductivity test sample, the following was conducted sequentially:
    a. A fracture was induced as per Section 2.2.4.1,
    b. Surface topography determination via laser profilometer as per Section 2.4.6,

c. Prior to water-damaging fracture conductivity tests:
    i. XRF as per Section 2.4.5 (only on Eagle Ford formation),
    ii. Saline water reconstitution as per Section 2.3.2,
d. A fracture conductivity test with equipment per Section 2.4.1, and its procedures outlined in upcoming Section 2.6.

2.6 Fracture Conductivity Experimental Procedure

Fracture conductivity test samples were prepared as per Section 2.2.4, and the baseline fracture conductivity tests, as well as the water-damaging fracture conductivity tests, were conducted using the corresponding experimental apparatus setup described in Section 2.4.1.

Previous studies utilizing the Modified API Fracture Conductivity Cell have described earlier generation detailed experimental procedures for measuring fracture conductivity, with differences predicated on the focus of their study –which in some resulted in different type of fracture conductivity tests, both in sample type and fluids flowed through the fracture. Previous work that utilized the Modified API Fracture Conductivity Cell include Kamenov (2013), Zhang (2014), Enriquez (2016), and several others.

The following subsections describe the experimental procedures followed in this study for the measurement of fracture conductivity.

2.6.1 Baseline Fracture Conductivity Test Procedure

Once the fracture conductivity test sample was inserted into the Modified API Fracture Conductivity Cell as per Section 2.4.1.1 and assembled, it was placed inside the load frame, and then the baseline fracture conductivity was measured by flowing dry nitrogen through the

fracture at several closure stresses, going from a low to high value. The following sequential procedure of principal actions was executed to determine the baseline fracture conductivity:

1. The PC was turned on, followed by the GCTS control box.
2. A mass flow meter was selected and affixed to the experimental apparatus, then it was turned on. The basis of the mass flow meter selection is discussed in Section 2.4.1.7.
3. The GCTS CATS Standard application suite was opened, a pre-designed screen layout was launched, and then the hydraulic pump was turned on.
4. Pressure transducers were calibrated, as per Section 2.4.1.6.
5. Through the application suite, the load frame piston was lowered on to the top piston insert of the Modified API Fracture Conductivity Cell without exerting force.
6. A pre-designed load case was initialized, with a loading ramp of 112 psi/min until the load target was reached. The first load case target was preset to 500 psi acting on the fracture conductivity test sample.
7. Once the first load case target was reached, it was held for a fixed amount of time (up to 45 min) to standardize the time under load. This was done for each load case during the test to account for rock creep.
8. The flow lines and pressure transducer ports were then connected. The ball valves were operated to ensure flow into the cell, and the leak-off ports in the top and bottom piston inserts were closed.
9. The back pressure regulator was closed and dry nitrogen was gradually flowed from the pressurized gas reservoir passing through the mass flowmeter and into

the Modified API Fracture Conductivity Cell until a set cell pressure was reached (30 to 50 psi range). The pressure in the system was achieved by operating the regulator affixed to the source aluminum cylinder. The set closed-loop system pressure was then ensured to be stabilized by allowing time to transpire until steady state was reached. At this point, system integrity was checked and leakage was ensured to not be present.

10. Under this load case, four separate measurements of cell pressure and differential pressure were recorded according to four distinct flow rates. The basis of this methodology is discussed in Section 2.7.1. Each flow rate was achieved by operating the needle valve serving as the back pressure regulator, and time was allowed to transpire until steady state was reached. Flow rates were such that the resulting differential pressure did not exceed 5 to 10% of the prescribed cell pressure, in part circumventing gas compressibility issues, and by such, a constant volumetric flow rate was assumed. For instance, for a cell pressure value of approximately 30 psi during flow, the differential pressure was ensured not to exceed 2 psi.

    With the set of four measurements, gas-based fracture conductivity was calculated as per Section 2.7.1.

11. Once the measurements were gathered for the particular load case, the gas reservoir was closed and the entire system gradually lost pressure until the flow rate was zero along the fracture conductivity test sample. The back pressure was then opened completely.

12. The following pre-designed load case was initialized. The same loading rate as in Step 6 was prescribed for all load cases. Typically, the loading regime consisted of achieving a closure stress of 500 psi, followed by 1,000 psi, 2,000 psi, and so on with increments of 1,000 psi until a final load stage was reached, depending on the formation being evaluated –normally between 6,000 psi and 8,000 psi for the fracture conductivity test samples tested in this study.
13. Once the following load case of 1,000 psi was reached, Steps 7, 9, 10, and 11 were conducted to determine the fracture conductivity at that particular load case.
14. Steps 12, 7, 9, 10, 11 were repeated for 2,000 psi, 3,000 psi, 4,000 psi, and so on.
15. Once measurements in the final load stage were recorded, and Step 11 was completed, all the flow lines and pressure transducer ports were disconnected, and the inlet and outlet inserts of the Modified API Fracture Conductivity Cell were unbolted. The load was then gradually removed from the cell until the load frame piston was no longer in contact with the top piston insert of the cell.
16. The hydraulic pump was turned off, and the GCTS CATS Standard application suite was then exited. After that, the GCTS control box was switched off, followed by shutting down the PC.
17. The Modified API Fracture Conductivity Cell was then removed from the load frame. The cell was further disassembled by removing the piston inserts, and the fracture conductivity test sample was then extracted.

In some specific cases, the fracture conductivity measurements were conducted at different load stages, where low closure stress fracture conductivity behavior was of interest, 100 and 300 psi, followed by 500 psi, 1,000 psi, 2,000 psi, 3,000 psi, and 4,000 psi.

2.6.2 Water-Damaging Fracture Conductivity Test Procedure

For water-damaging fracture conductivity tests, the conductivity test sample was inserted into the Modified API Fracture Conductivity Cell as per Section 2.4.1.1 and assembled, and then placed inside the load frame, and then the water-damaging fracture conductivity test was conducted.

This test was conducted by first flowing dry nitrogen through the fracture to ascertain the undamaged initial fracture conductivity at closure stresses of 1,000 psi, 2,000 psi, 3,000 psi, and 4,000 psi. Once the 4,000 psi closure stress was reached, it was held for the remained of the test. Then a saline solution was continuously injected into the fracture until steady state behavior was observed. Lastly, dry nitrogen was once again flowed continuously to quantify the recovered fracture conductivity. The degree of fracture conductivity impairment was determined by comparing the initial dry nitrogen flow-based fracture conductivity measurement with the final dry nitrogen flow-based fracture conductivity measurement to estimate the unrecoverable loss to fracture conductivity. The following sequential procedure of principal actions was executed to determine the unrecoverable loss to fracture conductivity:

1. Baseline fracture conductivity measurements were conducted as per Section 2.6.1, starting from a closure stress of 1,000 psi.
2. Once the baseline fracture conductivity was calculated for the final closure stress of 4,000 psi, the water-damaging fracture conductivity test was conducted. A

water source was selected and the connection was made –either A-A or A-B depending on the setup desired, as per Section 2.4.1.

3. For the water reservoir via connection A-A,
    a. The syringe pump controller and the pump were turned on. The water reservoir was filled with the water solution as per Section 2.3.2 and the syringe pump was filled to capacity. The ball valves were operated to ensure flow towards the cell via connection A-A. Flow was then prescribed at the syringe pump controller and all the flow lines were primed by using the flow bypass line avoiding flow into the Modified API Fracture Conductivity Cell at that point. Once the flow lines were primed, the ball valves were operated such that flow was directed into the cell. Common flow rate values ranged from 0.1 – 0.5 mL/min.
    b. Under the prescribed flow from the syringe pump, a continuous measurement of differential pressure was recorded. Flow was held constant until steady state conditions were reached, which typically involved hours to reach. If the capacity of the syringe pump was spent in reaching steady state, the syringe pump was then refilled with the water solution while holding the system constant.
    c. Once steady state was determined, the Modified API Fracture Conductivity Cell was closed off. Water flow from the syringe pump was stopped and the ball valves were operated such that the gas reservoir was accessed.

With the aforementioned measurements, water-based fracture conductivity was calculated as per Section 2.7.2.

4. For the water reservoir via connection A-B,
    a. The syringe pump controller and the pump were turned on. The displacement accumulators were filled as described in Section 2.4.1.4. The ball valves were operated to ensure flow towards the cell via connection A-B. Following procedures remained the same as in Step 3a-c, albeit under the connection A-B, where the syringe pump is directly displacing hydraulic oil.
5. The back pressure regulator is then closed and dry nitrogen was gradually flowed from the pressurized gas reservoir into the flow lines and bypass line until the pressure gauge at the gas reservoir registered the same cell pressure during gas flow prior to water exposure (Section 2.6.1).
6. Water in the flow lines was displaced by dry nitrogen flow via the bypass line by operating the needle valve that served as the back pressure regulator, and achieving the prescribed gas flow rate, where in this study a common value ranged from 100 – 500 mL/min.
7. Once water was displaced from the flow lines, and with the prescribed flow rate of Step 6, the ball valves were operated such that dry nitrogen flow was directed into the Modified API Fracture Conductivity Cell.
8. Gas flow was continued until steady state conditions were reached (until gas flow rate, cell pressure, and differential pressure became stable). Pressure at the gas

reservoir, cell pressure, differential pressure, and flow rate were continuously recorded.

With the aforementioned measurements, the fracture conductivity was calculated and plotted as a continuous curve.

9. Steps 15 through 17 of Section 2.6.1 were enacted.

2.7 Steady-State Fracture Conductivity Determination

Non-damaging (baseline) fracture conductivity (the gas flow-based fracture conductivity) and water-damaging fracture conductivity (the sequential gas-water-gas flow-based fracture conductivity), were calculated by utilizing fracture conductivity equations developed specifically for the experimental setup described in Section 2.4.1.

Section 2.7.1 describes two forms of the fracture conductivity equation for gas flow, accounting for Darcy and non-Darcy flow regimes inside the fracture. Section 2.7.2 describes the fracture conductivity equation for water flow, which was kept in the Darcy flow regime.

In all fracture conductivity experiments, stable flow conditions were established. Conway et al. (2011) showed that achieving stable flow during fracture conductivity experiments was paramount in obtaining interpretable behaviors.

2.7.1 Gas Flow

Baseline fracture conductivity was calculated based on the Darcy equation (**Eq. 2**) and the Forchheimer equation (**Eq. 3**) for gas flow. After a series of derivations (Tek et al., 1962; Marpaung et al., 2008; Awoleke, 2013), which included applying the real gas law and the conservation of mass principle, an explicit Darcy-based relationship (**Eq. 4**) and explicit non-

Darcy-based relationship (**Eq. 5**) for gas flow was obtained. These explicit equations were rearranged as a straight line equation of the form $y = mx + c$, and utilized in a statistically sound graphical representation based on four separate measurements of volumetric flow rate, cell pressure, and the resulting differential pressure. Subsection 2.7.1.1 details the determination of Darcy flow fracture conductivity, whereas Subsection 2.7.1.2 details the determination of non-Darcy flow fracture conductivity.

$$-\frac{dp}{dL} = \frac{\mu v}{k_f} \quad \text{.....(2)}$$

$$-\frac{dp}{dL} = \frac{\mu v}{k_f} + \beta \rho v^2 \quad \text{.....(3)}$$

In **Eq. 2** and **Eq. 3**, $^{dp}/_{dL}$ is the pressure gradient, μ is the viscosity of the fluid, v is the velocity of the fluid through the porous media, and k_f is the permeability of the porous media – in this case, the fracture permeability. In **Eq. 3**, the added term over **Eq. 2**, is a quadratic correction term to Darcy's law, to make it effective over the range of velocities (Tek et al. 1962), for which inertial effects are important. **Eq. 2** implies that at low velocities, the inertial forces may be neglected, since the viscous forces govern the behavior in the porous media. **Eq. 2** is valid for low flow rates, when flow rate and pressure gradient are linearly dependent.

2.7.1.1 Darcy Flow

Eq. 4 was used when flow inside the fracture was within the Darcy flow regime, following the logic outlined in Section 2.7.1.3. This equation was derived based on the Darcy equation (Tek et al., 1962).

$$\frac{Mp_{cell}\Delta p}{ZRTL} = \frac{\mu\rho q}{h_f}\frac{1}{k_f w_f} \quad \text{.....(4)}$$

In **Eq. 4**, M is the molecular weight (kg/mol), p_{cell} is the cell pressure (Pa), Δp is the differential pressure (Pa), Z is the gas compressibility factor, R is the universal gas constant (J/mol·K), T is the temperature (K), L is the length of fracture over the entire range of pressure drop (m), μ is the viscosity of gas (Pa·s), ρ is the density of gas (kg/m^3), q is the volumetric flow rate of gas (m^3/s), h_f is the height of the fracture (width of the sample) (m), k_f is the fracture permeability (m^2), and w_f is the fracture width (m^2).

By graphing **Eq. 4** rearranged as a straight line equation, the fracture conductivity can be obtained by taking the inverse of the slope of the best fit line, as shown in **Figure 39** for an arbitrary fracture conductivity test sample.

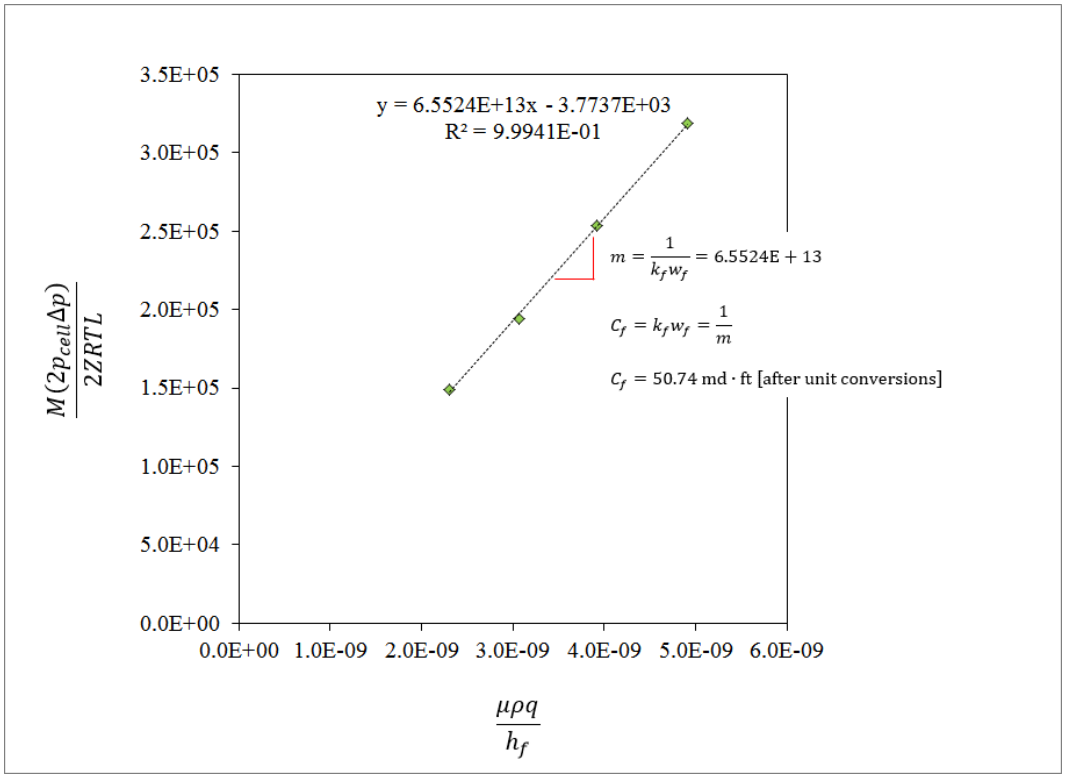

Figure 39 – Graphical Representation of Eq. 4 Rearranged as a Straight Line Equation to Calculate Fracture Conductivity For Darcy Flow in the Fracture.

Experimental data shown in **Figure 39** pertains to the Mahantango formation fracture conductivity test sample Core #1 at 6,000 psi closure stress and 0.05 lb_m/ft^2 proppant loading. Darcy flow was assumed below a flow rate of 0.8 L/min, and validated by ensuring the relationship between flow rate and the differential pressure was linear, as discussed in Section 2.7.1.3.

2.7.1.2 Non-Darcy Flow

Eq. 5 was used when flow inside the fracture was beyond the Darcy flow regime, following the logic outlined in Section 2.7.1.3. This equation was derived based on the Forchheimer equation (Tek et al., 1962).

$$\frac{Mp_{cell}\Delta ph_f}{ZRTL\mu\rho q} = \frac{\beta}{w_f^2}\frac{\rho q}{h_f\mu} + \frac{1}{k_f w_f} \quad \text{.....(5)}$$

In **Eq. 5**, β is the inertial factor ($1/m^2$), and the rest of the variables retain the definitions given for **Eq. 4**. By graphing **Eq. 5** rearranged as a straight line equation, the fracture conductivity can be obtained by taking the inverse of the vertical axis intercept of the best fit line, as shown in **Figure 40** for an arbitrary fracture conductivity test sample. Experimental data shown in **Figure 40** pertains to the Mahantango formation fracture conductivity test sample Core #1 at 1,000 psi closure stress and 0.05 lb_m/ft^2 proppant loading.

Non-Darcy flow was assumed above a flow rate of 0.8 L/min, and validated by observing when the relationship between flow rate and differential pressure became nonlinear, as discussed in Section 2.7.1.3

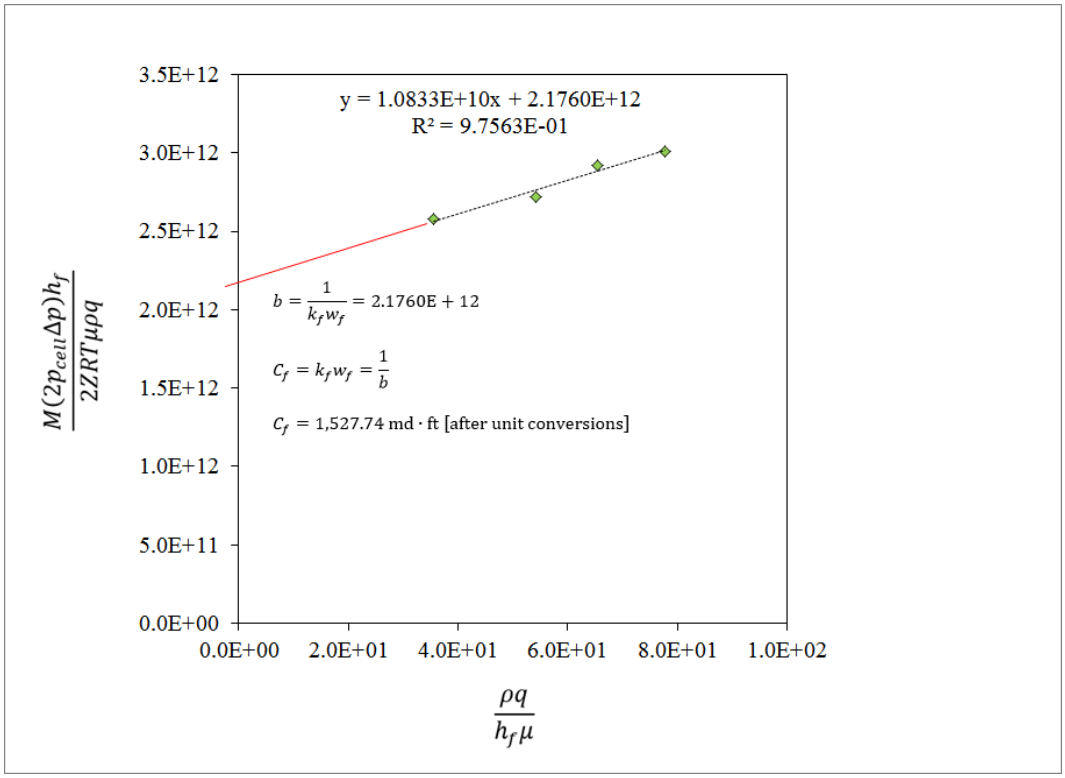

Figure 40 – Graphical Representation of Eq. 5 Rearranged as a Straight Line Equation to Calculate Fracture Conductivity For Non-Darcy Flow in the Fracture.

2.7.1.3 Practical Use of Darcy Flow and Non-Darcy Flow Equations

During the fracture conductivity tests, the gas flow rate and the differential pressure were continuously live-streamed, allowing for the determination of the particular flow rate at which the relationship between them became nonlinear (the flow rate at which the differential pressure increased at a higher rate). This value typically had a range of 0.8 – 1.0 L/min, with a minor degree of variation between test samples. This range was similar to previous fracture conductivity tests conducted by Awoleke (2013) and Zhang (2014).

Awoleke (2013) discussed in detail the applicability and justification of the use of the Darcy equation or the Forchheimer equation for calculating fracture conductivity from pressure-rate data; based on an extensive discussion of proposed relationships between the interstitial velocity, the interstitial Reynolds number, and the proppant pack porosity made by Huang and

Ayoub (2008). Awoleke (2013) recommended plotting the Darcy-based equation (**Figure 39**) to achieve a higher quality fit for low velocity experimental data, while plotting the Forchheimer-based equation (**Figure 40**) for higher velocity data. **Figure 41** shows the impact of flow rate range while recording the four separate measurements of q, p_{cell}, and Δp, on the Darcy-based and Forchheimmer-based equations.

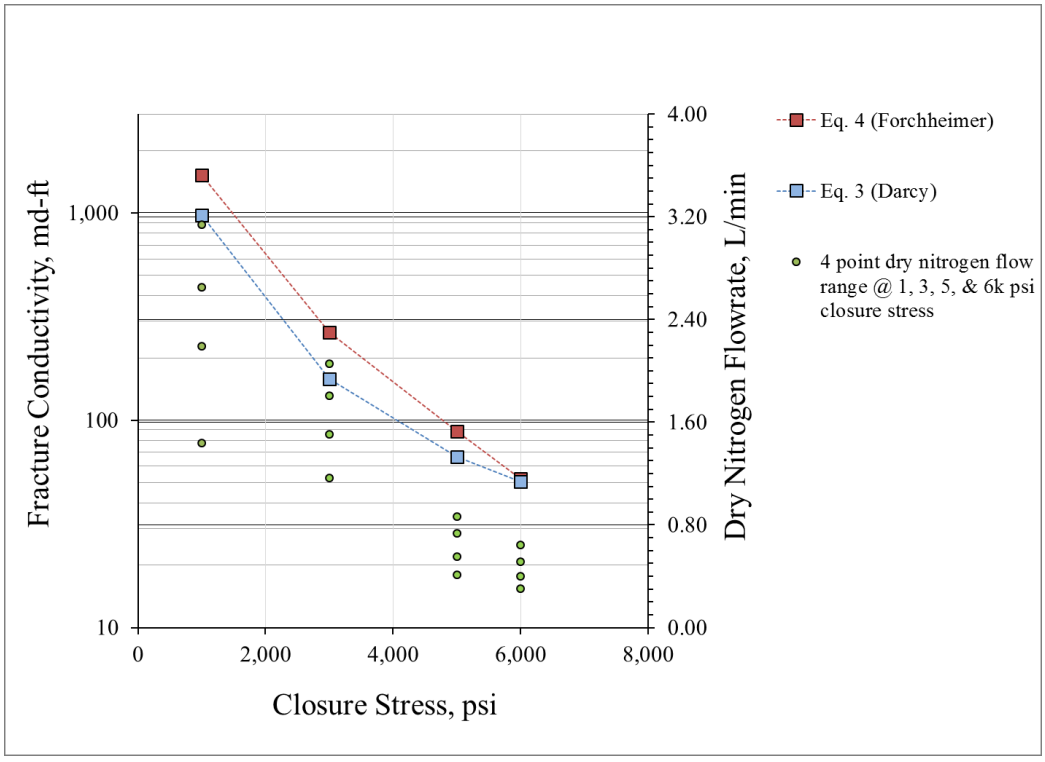

Figure 41 – Fracture Conductivity Calculated by the Darcy-based Equation (Eq. 4) and the Forchheimer-based Equation (Eq. 5) for the Same Experimental Data.

Experimental data shown in **Figure 41** pertains to the Mahantango formation fracture conductivity test sample Core #1 at 0.05 lb_m/ft^2 proppant loading. Observing **Figure 41**, it is noted that at 1,000 psi closure stress, the dry nitrogen flow ranged from approximately 1.5 to 3.1 L/min (green-colored points), and by using the same experimental data in **Eq. 4** and **Eq. 5**, there was a significant difference in calculated fracture conductivity, 1,528 md-ft using the

Forchheimer-based equation, compared to 978 md-ft using the Darcy-based equation. This in contrast to a negligible difference in calculated fracture conductivity of 52 md-ft using the Forchheimer-based equation, compared to 51 md-ft using the Darcy-based equation, at a closure stress of 6,000 psi with a dry nitrogen flow range of approximately 0.30 to 0.64 L/min. This was suggestive of a flow rate boundary that can be defined for the use of **Eq. 4** and **Eq. 5**. This seems to agree with previous fracture conductivity studies, albeit with different fracture conditions in some instances. Awoleke (2013) concluded that for flow rates higher than 0.9 L/min, the Forchheimer equation (**Eq. 5**) should be used, which is consistent with conclusions from Zhang (2015) that indicated that for flow rates below 0.8 L/min, the Darcy equation (**Eq. 4**) should be used.

Based on making the comparisons between **Eq. 4** and **Eq. 5** for each fracture conductivity test, as shown in **Figure 41** for one test sample, the validity of the use of the Darcy-based equation (**Eq. 4**) for flow rates below 0.8 L/min was determined; and for higher flow rates the Forchheimer-based equation (**Eq. 5)** was better suited to fit the experimental data. This was done in support of the live-stream flow rate and differential pressure data, which also showed the flow rate at which nonlinearity occurred.

2.7.1.4 Flow Rate Range

The dry nitrogen flow rate range utilized when conducting the four-point measurements of q, p_{cell}, and Δp for each closure stress, depended not only on the awareness of the flow regime to determine what relationships to be used in the calculation of fracture conductivity, but also on delivering the required flow rate necessary to create a pressure response large enough to be detected by the pressure transducers –described in Section 2.4.1.6. As per Section 2.7.1.3, the

flow rate boundary of 0.8 L/min was determined, in which below said value, the Darcy-based equation should be used.

2.7.2 Water Flow

Water-damaging fracture conductivity was calculated based on the Darcy equation (**Eq. 2**) for water flow. An explicit Darcy-based relationship (**Eq. 6**) for water flow was obtained, given that water flow rate was prescribed such that the flow regime was Darcy flow. Data was recorded continuously such that fracture conductivity by water was calculated constantly thought the water flow interval. Subsection 2.7.2.1 details the determination of Darcy flow fracture conductivity.

2.7.2.1 Darcy Flow

Eq. 6 was used when flow inside the fracture was within the Darcy flow regime, with a Reynolds number, N_{Re}, between 10^{-5} and 2.3, as described in Section 2.7.2.2. This equation was derived based on Darcy's law.

$$C_f = k_f w_f = \frac{q\mu L}{h_f \Delta p} \quad \text{.....(6)}$$

In **Eq. 6**, q is the volumetric flow rate of gas (m^3/s), μ is the viscosity of water (Pa·s), L is the length of fracture over the entire range of pressure drop (m), h_f is the height of the fracture (width of the sample) (m), and Δp is the differential pressure (Pa).

2.7.2.2 Reynold's Number

In order to ensure the water flow was within the laminar flow regime, the Reynolds number for a porous media was calculated as per **Eq. 7**, as outlined by Zhang (2015), where the hydraulic diameter, D_H, is defined by **Eq. 8**.

$$N_{Re} = \frac{\rho v D_H}{\mu(1-\emptyset)} \quad (7)$$

$$D_H = \frac{2h_f w_f}{(h_f + w_f)} \quad (8)$$

Figure 42 shows the calculated Reynolds number for varying flow rates, in which fluid properties reflect those of the water-damaging fracture conductivity tests, and fracture widths corresponded to those estimated in Section 4.5, for both types of proppant utilized in the aforementioned tests under the same proppant loading (0.1 lb_m/ft^2).

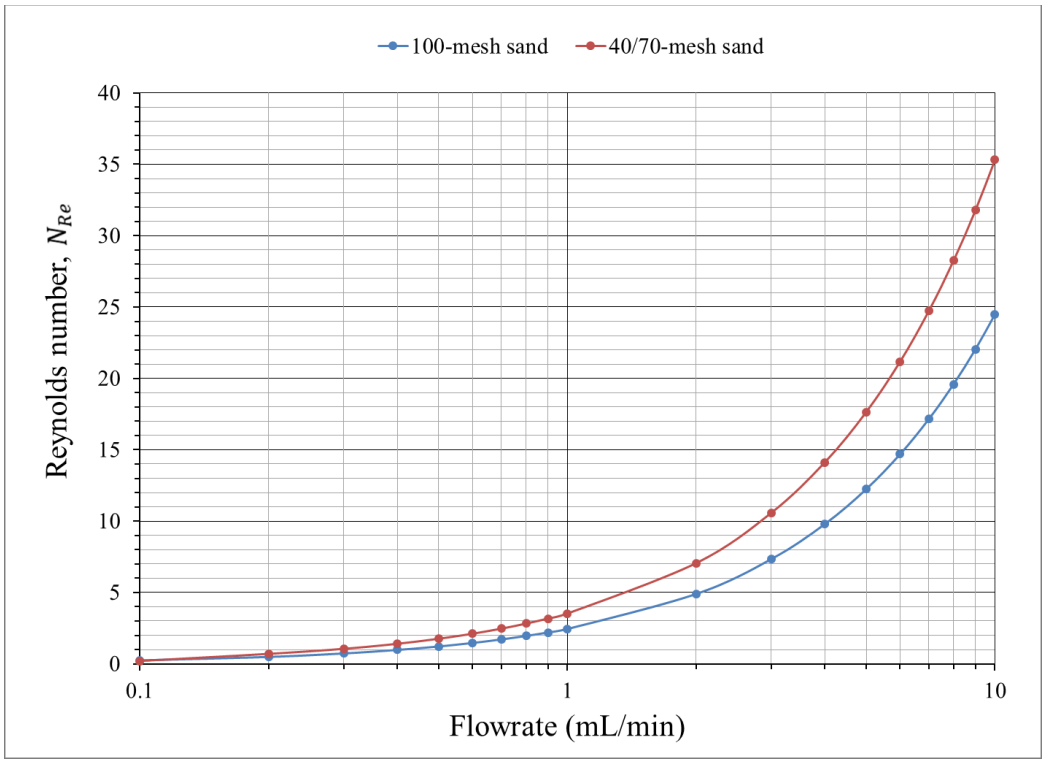

Figure 42 – Reynolds Number for Saline Water Flow Rates.

According to Reinicke (2011), Darcy flow occurs when the N_{Re} is between 10^{-5} and 2.3, with pre-laminar flow occurring below an N_{Re} of 10^{-5} and post-Darcy flow occurring beyond 5; at which point Forchheimer flow occurs up to approximately an N_{Re} of 80, and subsequent turbulent flow at N_{Re} values above 120. Based on **Figure 42**, and given that the aforementioned tests were conducted at a saline water flowate of 0.2 mL/min, the flow regime was clearly laminar –validating the use of the Darcy-based relationship (**Eq. 6**).

3. FRACTURE CONDUCTIVITY TEST RESULTS

3.1 Introduction

This chapter presents all the fracture conductivity experimental results obtained in this study.

As described in Chapter 2, five unconventional formations were investigated, with test samples originating from a combination of outcrop rock and downhole core segments. Fracture conductivity experimental results are presented according to the behavior category being studied, in two main sets of data.

The first data set presents baseline fracture conductivity (undamaged fracture conductivity) experiments (Section 3.2) for both unpropped fracture and propped fracture conditions. The second data set presents propped water-damaging fracture conductivity experimental results (Section 3.3).

Discussions on ancillary measurements pertaining to influencing properties and attributes and their effect on fracture conductivity are presented in Chapter 4. This includes the effect of closure stress, bulk and surface rock mechanical properties, rock bulk and surface mineralogy, fracture surface topography, bedding plane orientation, proppant type and concentration, among other factors.

3.2 Baseline Fracture Conductivity Measurements

Undamaged fracture conductivity was measured for fracture conductivity test samples representing the Eagle Ford, the Mahantango, the Middle Bakken, and Three Forks formations. In this study, baseline fracture conductivity measurements are presented as a function of closure stress. The following subsections contain the experimental results for all baseline fracture conductivity tests for unpropped and propped fracture conditions, Section 3.2.1 and Section 3.2.2, respectively.

3.2.1 Unpropped Fracture Conductivity Measurements

This section contains all the unpropped baseline fracture conductivity results.

3.2.1.1 Eagle Ford Formation

Eagle Ford formation fracture conductivity test samples EF-1, EF-2, and EF-3 were evaluated under unpropped fracture conditions, as shown in **Figure 43**. Fracture conductivity was measured starting from 100 psi in order to capture the behavior at relatively low closure stresses, in contrast to the typical initial closure stress of 500 psi.

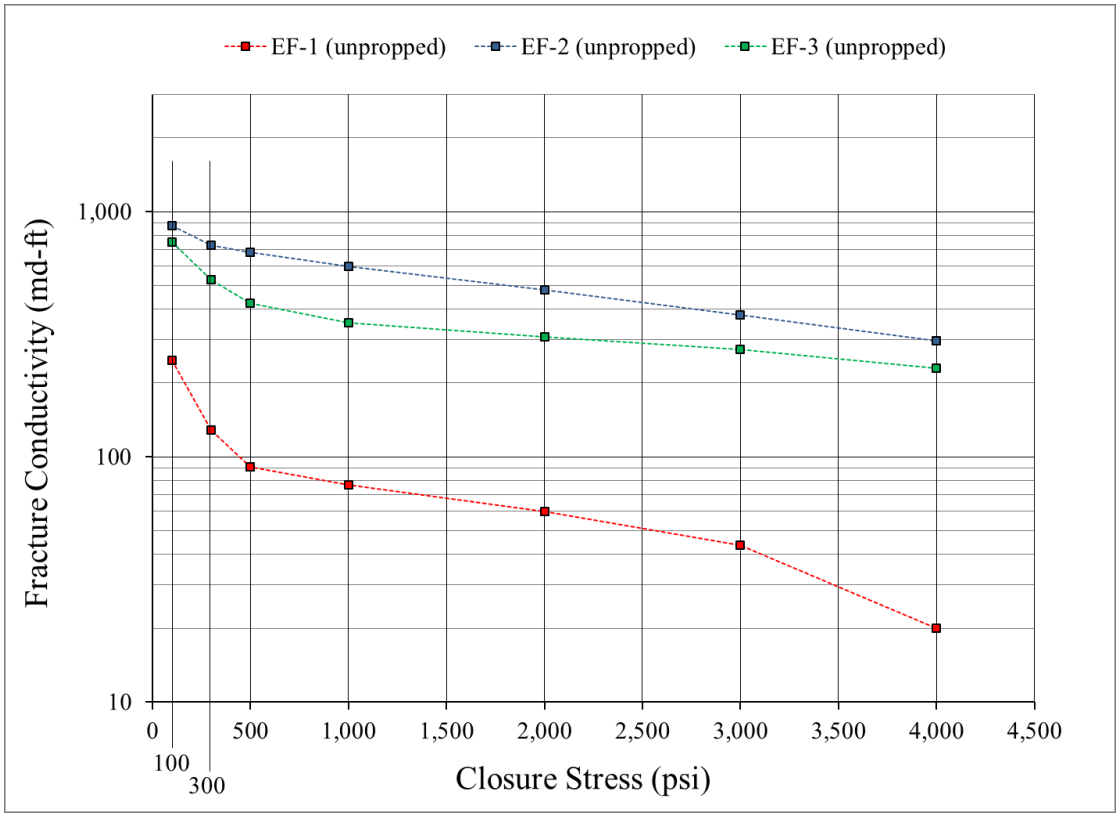

Figure 43 – Eagle Ford Formation Unpropped Fracture Conductivity.

3.2.1.2 Mahantango Formation

Mahantango formation fracture conductivity test samples Core #1 and Core #2 were evaluated under unpropped fracture conditions, as shown in **Figure 44**. Fracture conductivity was measured at initial closure stresses below 500 psi to capture the behavior at relatively low closure stresses.

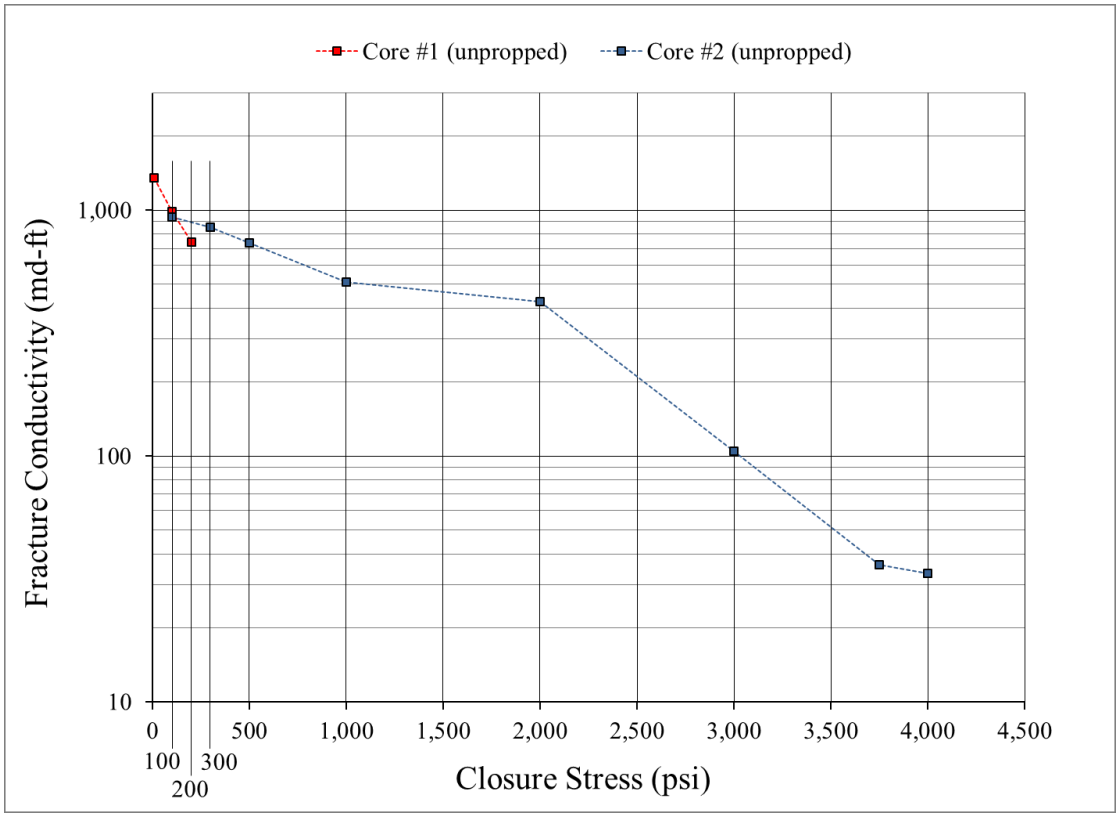

Figure 44 – Mahantango Formation Unpropped Fracture Conductivity.

3.2.1.3 Middle Bakken and Three Forks Formations

The Middle Bakken formation fracture conductivity test samples Core No. 2, 5, and 6, and the Three Forks formation test samples Core No. 8, 9, and 10, were evaluated under unpropped fracture conditions, as shown in **Figure 45** and **Figure 46**, respectively. Fracture conductivity was measured at initial closure stresses below 500 psi to capture the behavior at relatively low closure stresses.

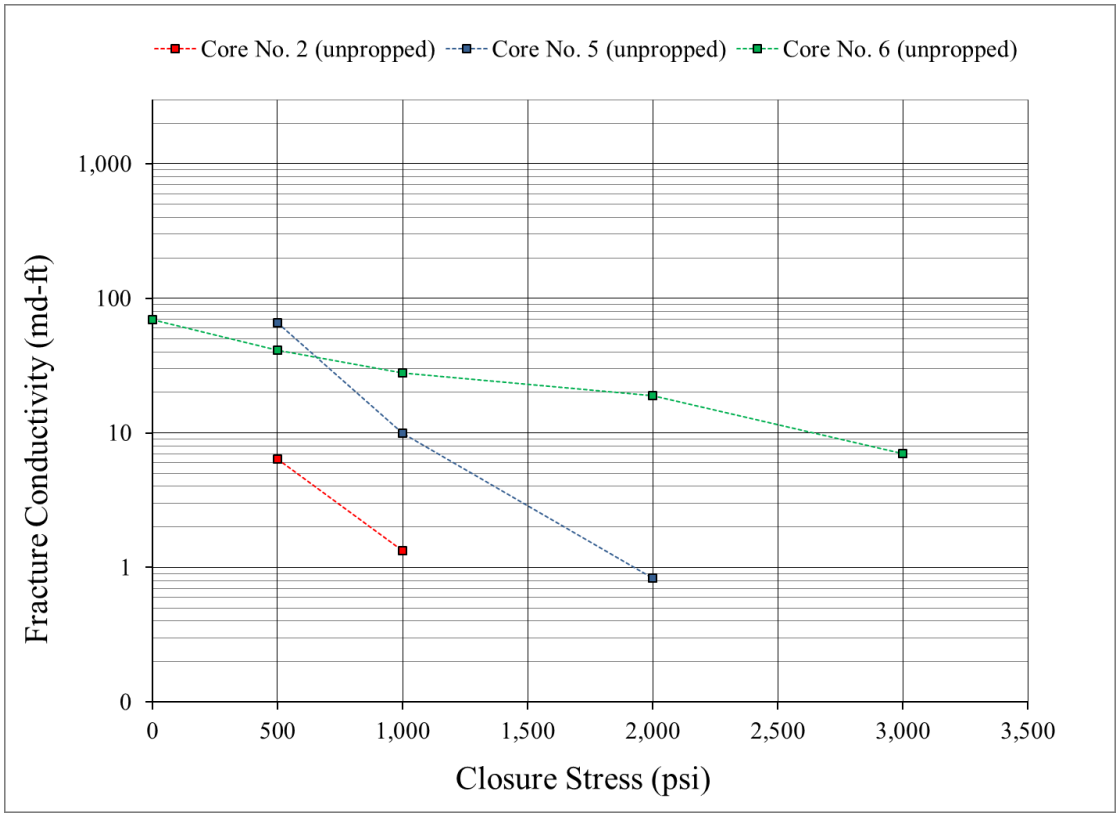

Figure 45 – Middle Bakken Formation Unpropped Fracture Conductivity.

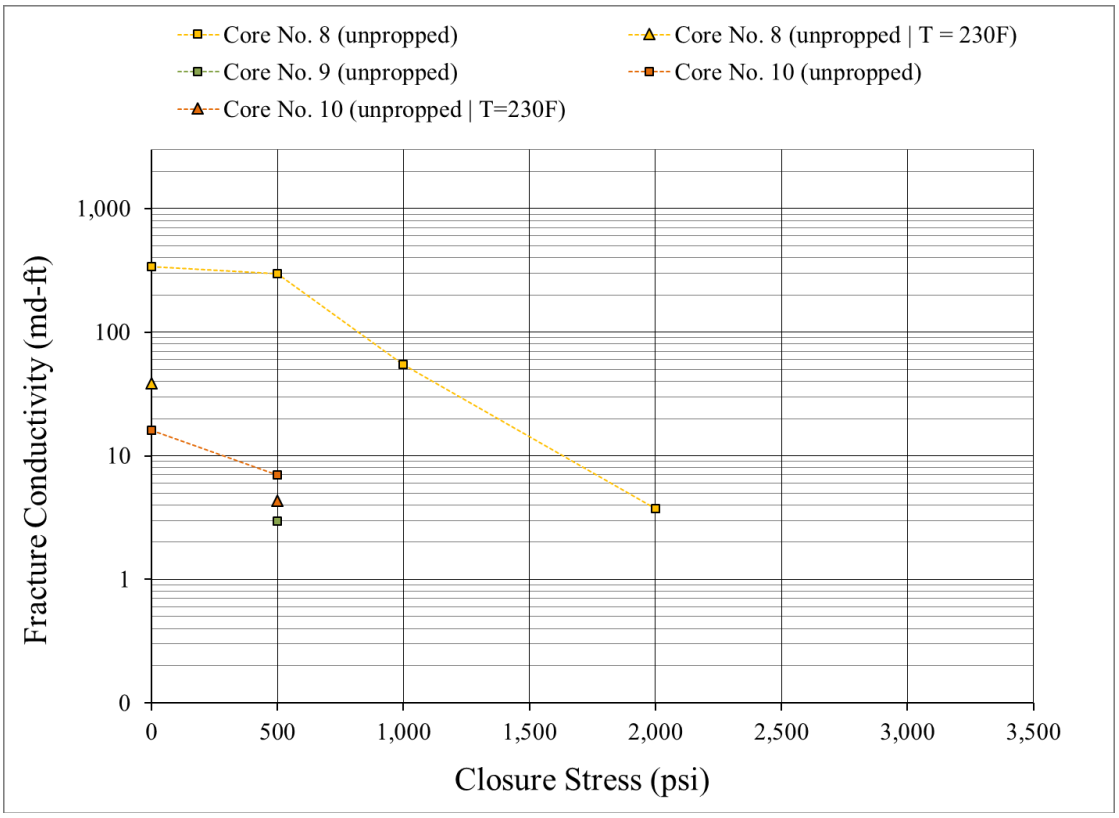

Figure 46 – Three Forks Formation Unpropped Fracture Conductivity.

Most of these test samples were tested up to the closure stress at which flow inside the fracture was not registered and recorded by the testing apparatus described in Section 2.4; this despite the fact that flow most certainly was taking place, just at a low enough magnitude that it was not detected by the flowmeter and pressure transducers.

For the Three Forks formation data set, Core No. 8 and Core No. 10 were tested at room temperature like the rest of the test samples, as well as at a simulated downhole temperature of 230 ^{o}F (**Figure 46**). These test samples showed a decrease in conductivity at 0 and 500 psi under the influence of temperature, as expected.

3.2.2 Propped Fracture Conductivity Measurements

After baseline fracture conductivity under unpropped fracture conditions was evaluated, the fracture conductivity test samples were then subjected to fracture conductivity measurements under propped fracture conditions.

The following subsections contain the propped baseline fracture conductivity measurements performed on test samples from the Eagle Ford, the Mahantango, the Middle Bakken, and the Three Forks formations.

The number of fracture conductivity tests performed on a single fracture conductivity test sample depended on the preservation of the test sample, such in the case of Eagle Ford formation test sample EF-3, where only one additional test beyond the unpropped fracture condition was possible. Sample integrity degradation usually involved rock sample failure exhibited through transverse fracturing and/or rock crumbling (as discussed in Section 4.10).

3.2.2.1 Eagle Ford Formation

Eagle Ford formation fracture conductivity test samples EF-1, EF-2, and EF-3 were evaluated under propped fracture conditions, as shown in **Figure 47**. Fracture conductivity was measured up to a closure stress that ranged between 5,000 psi and 6,000 psi, after which the sample integrity began to degrade.

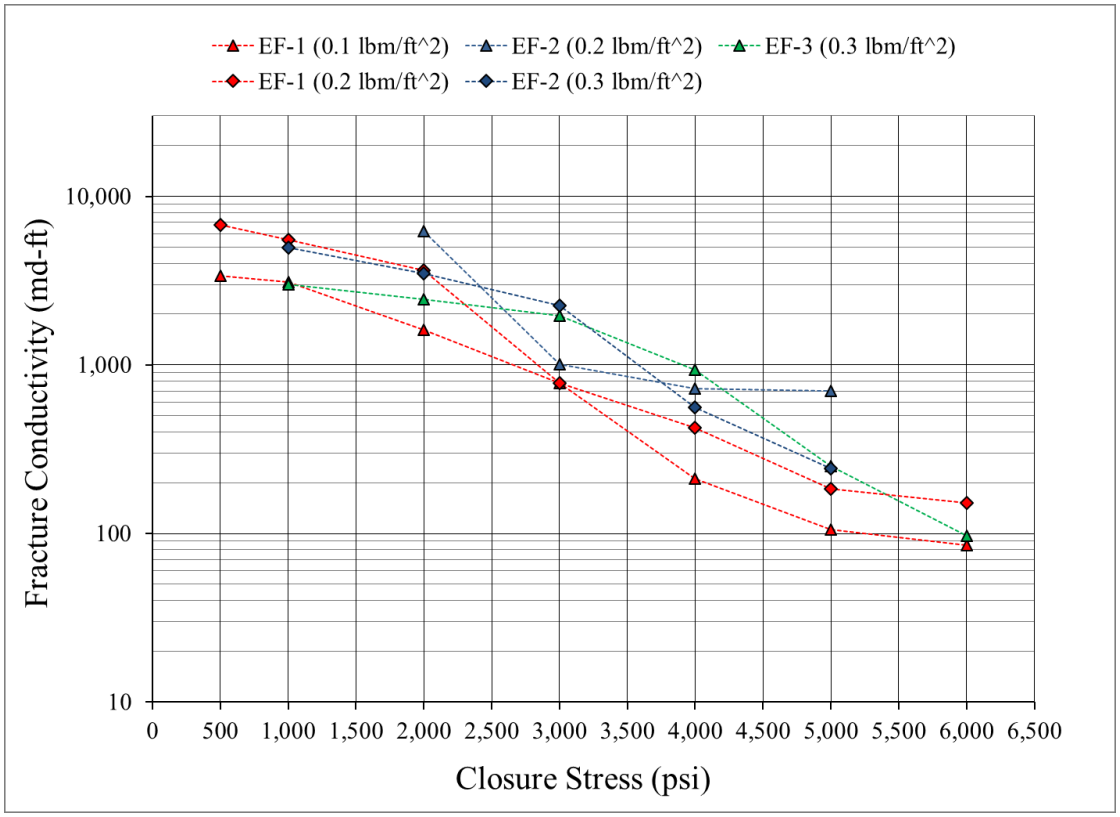

Figure 47 – Eagle Ford Formation Propped Fracture Conductivity.

3.2.2.2 Mahantango Formation

Mahantango formation fracture conductivity test samples Core #1 and Core #2 were evaluated under propped fracture conditions, as shown in **Figure 48**. Fracture conductivity was measured up to a closure stress of 6,000 psi, after which the sample integrity began to degrade.

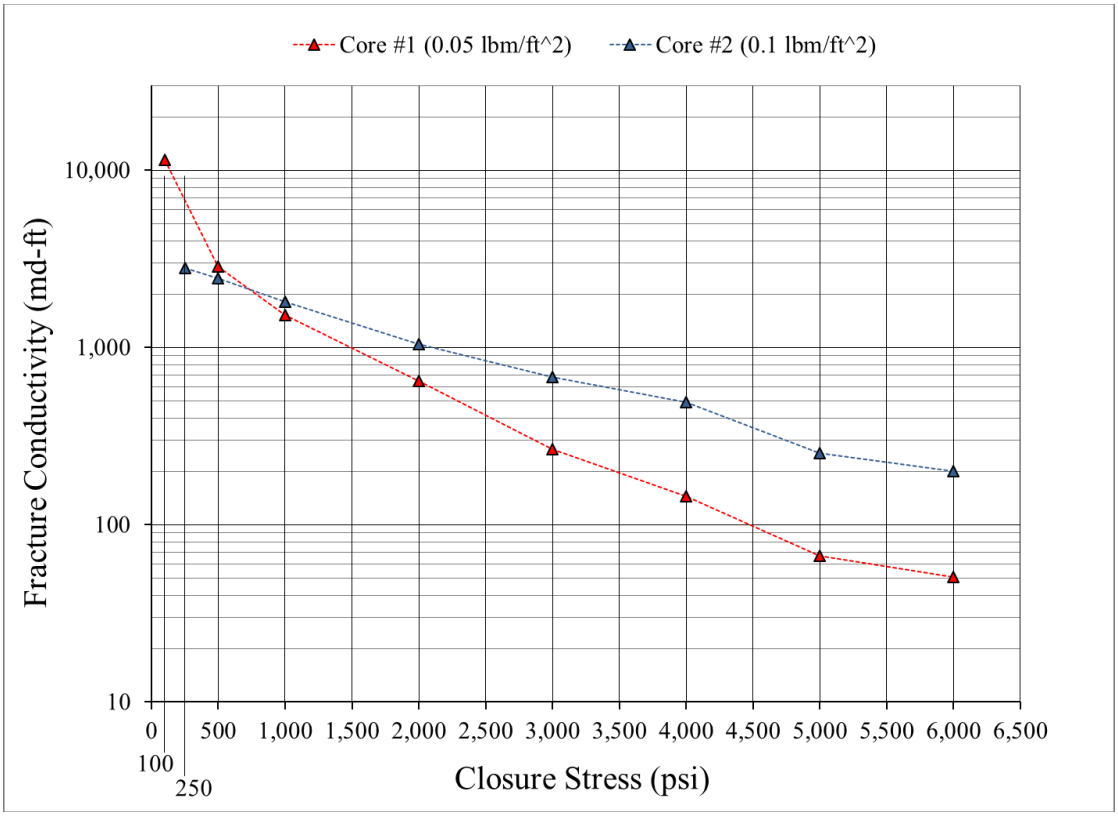

Figure 48 – Mahantango Formation Propped Fracture Conductivity.

3.2.2.3 Middle Bakken and Three Forks Formations

The Middle Bakken formation fracture conductivity test samples Core No. 2, 5, and 6, and the Three Forks formation test samples Core No. 8 and 9, were evaluated under propped fracture conditions, as shown in **Figure 49** and **Figure 50**, respectively. Fracture conductivity was measured up to a closure stress of 8,000 psi, after which the sample integrity began to degrade.

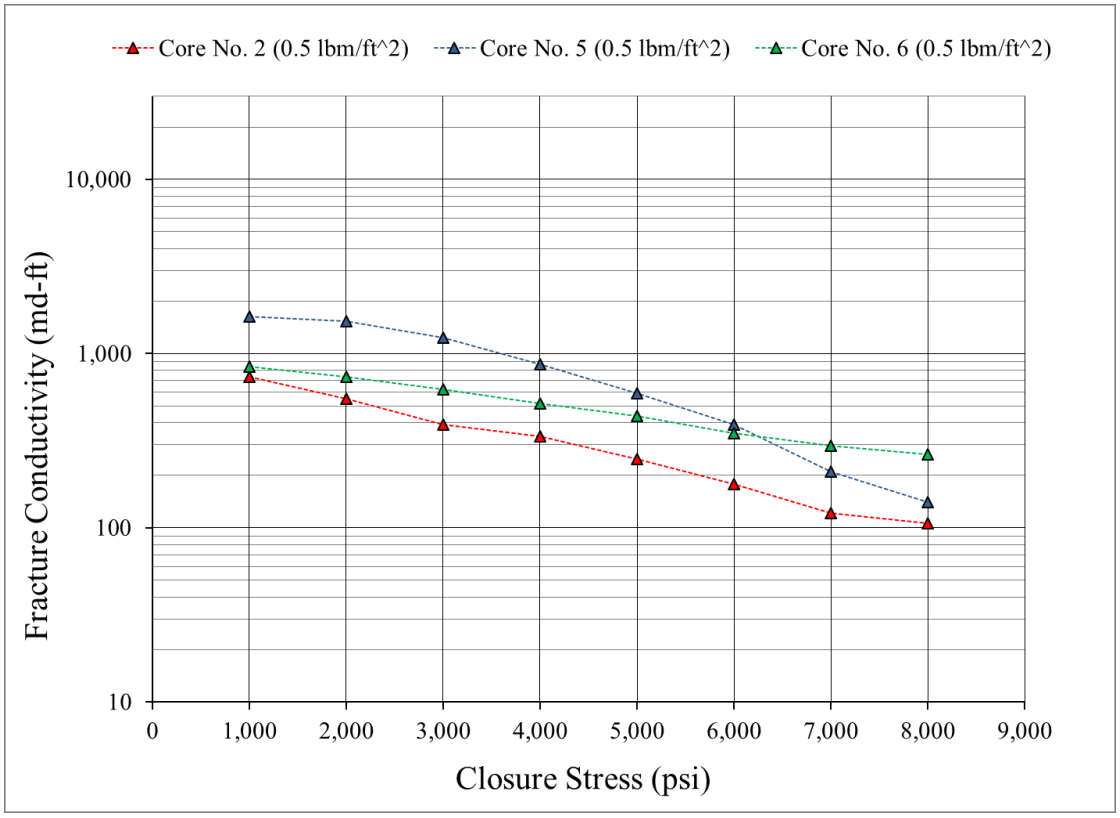

Figure 49 – Middle Bakken Formation Propped Fracture Conductivity.

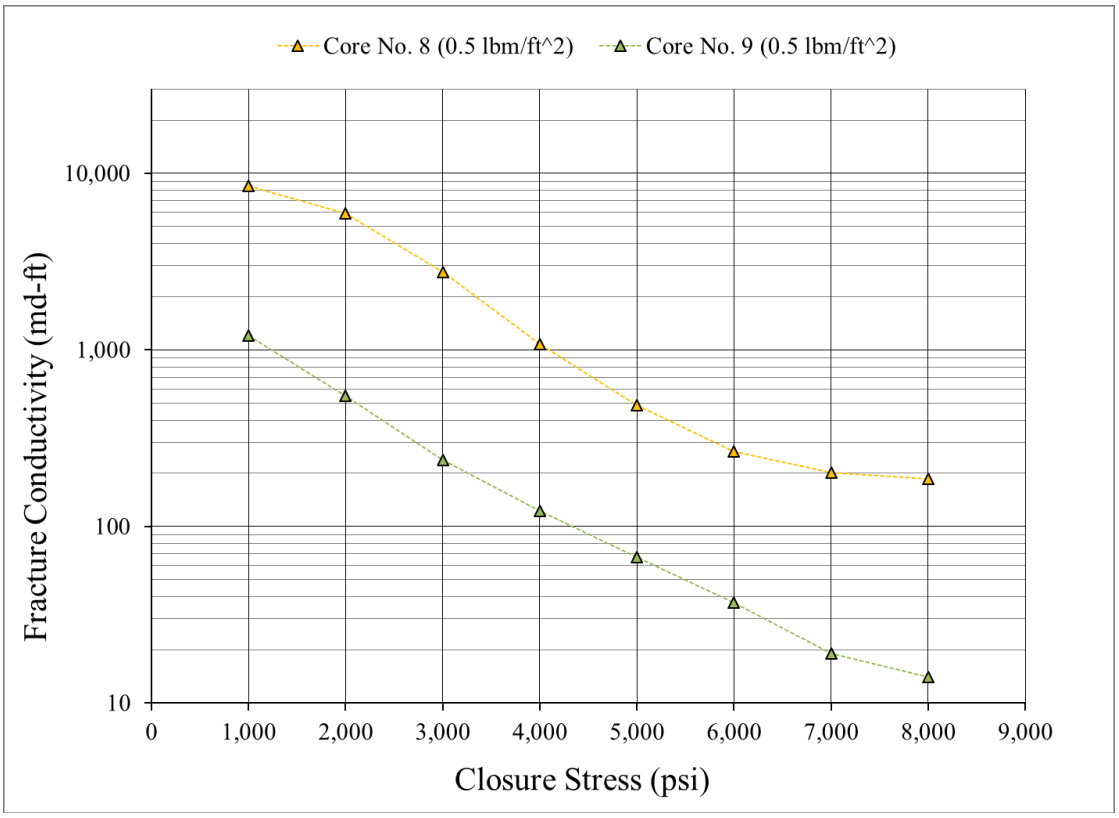

Figure 50 – Three Forks Formation Propped Fracture Conductivity.

3.3 Water-Damaging Fracture Conductivity Measurements

The degree of fracture conductivity impairment when exposed to saline water with a similar chemical composition as a typical field flowback water was determined for both the Eagle Ford formation and the Marcellus formation.

In this study, water-damaging fracture conductivity measurements results are represented by a three-region curve that contrasts fracture conductivity through time against fracture closure stress. The first region consists of four individual readings of fracture conductivity obtained by dry nitrogen flow at closure stresses of 1,000 psi, 2,000 psi, 3,000 psi, and 4,000 psi. Once the closure stress of 4,000 psi was reached, it was held constant for the remainder of the test sequence. The second region consists of a continuous fracture conductivity reading during saline water flow until steady state was achieved. The third region also consists of a continuous fracture

conductivity monitoring by again flowing dry nitrogen until steady state was achieved. The reconstituted flowback water was flowed at a constant rate of 0.2 mL/min until steady state was reached, at which point dry nitrogen was flowed at a rate of 100 mL/min.

The following subsections contain the experimental results for all water-damaging fracture conductivity tests under propped fracture conditions, for the Eagle Ford formation and the Marcellus formation, in Section 3.3.1 and Section 3.3.2, respectively.

3.2.1 Eagle Ford Formation

Figure 51 and **Figure 52** illustrate the typical fracture conductivity behavior for a gas-water-gas test, for Eagle Ford formation test samples B1 and B2, respectively.

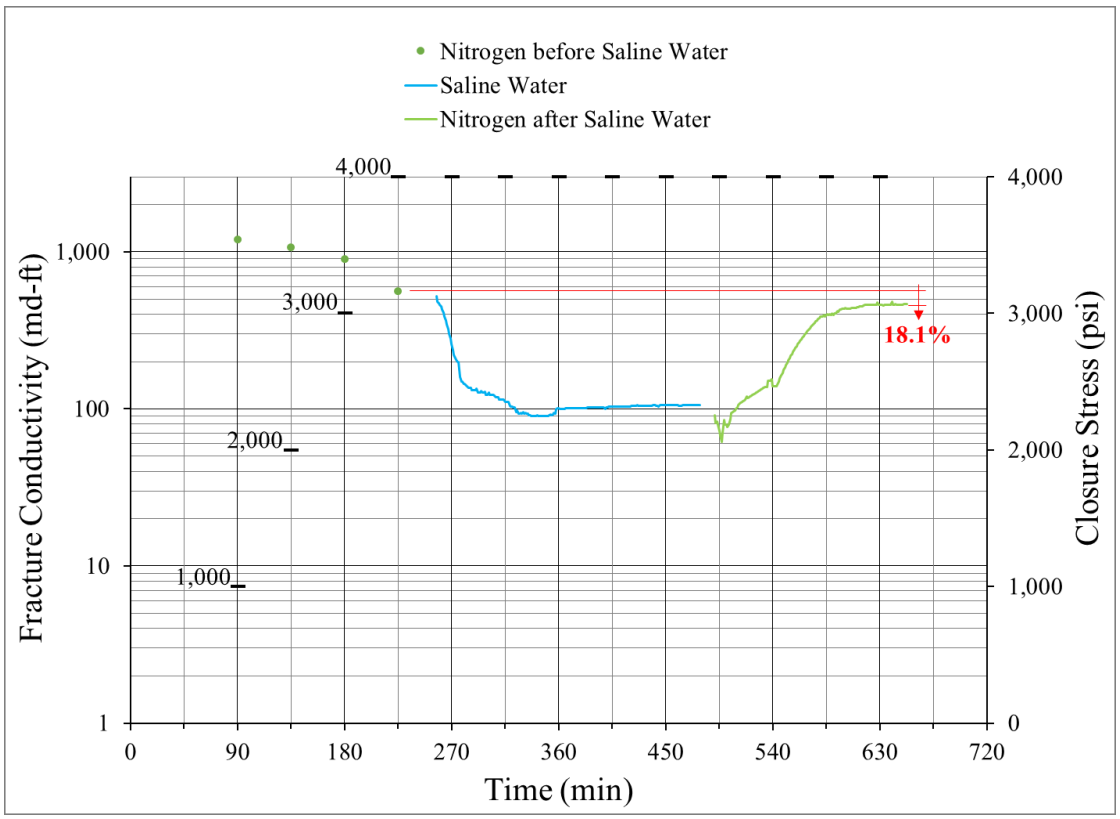

Figure 51 – Eagle Ford Formation Water-Damaging Fracture Conductivity Test (Sample B1) (Adapted from Guerra et al., 2018).

Under a closure stress of 4,000 psi, **Figure 51** shows how fracture conductivity test sample B1 had an initial undamaged fracture conductivity of 565 md-ft, which was reduced to 463 md-ft after saline water was flowed through the fracture. This represented a recovered fracture conductivity of 81.9%, or in other words, an unrecovered fracture conductivity loss of 18.1%. Similarly, **Figure 52** shows how fracture conductivity test sample B2 had an initial undamaged fracture conductivity of 696 md-ft, which was reduced to 537 md-ft after saline water was flowed through the fracture, representing an unrecovered fracture conductivity loss of 22.8%.

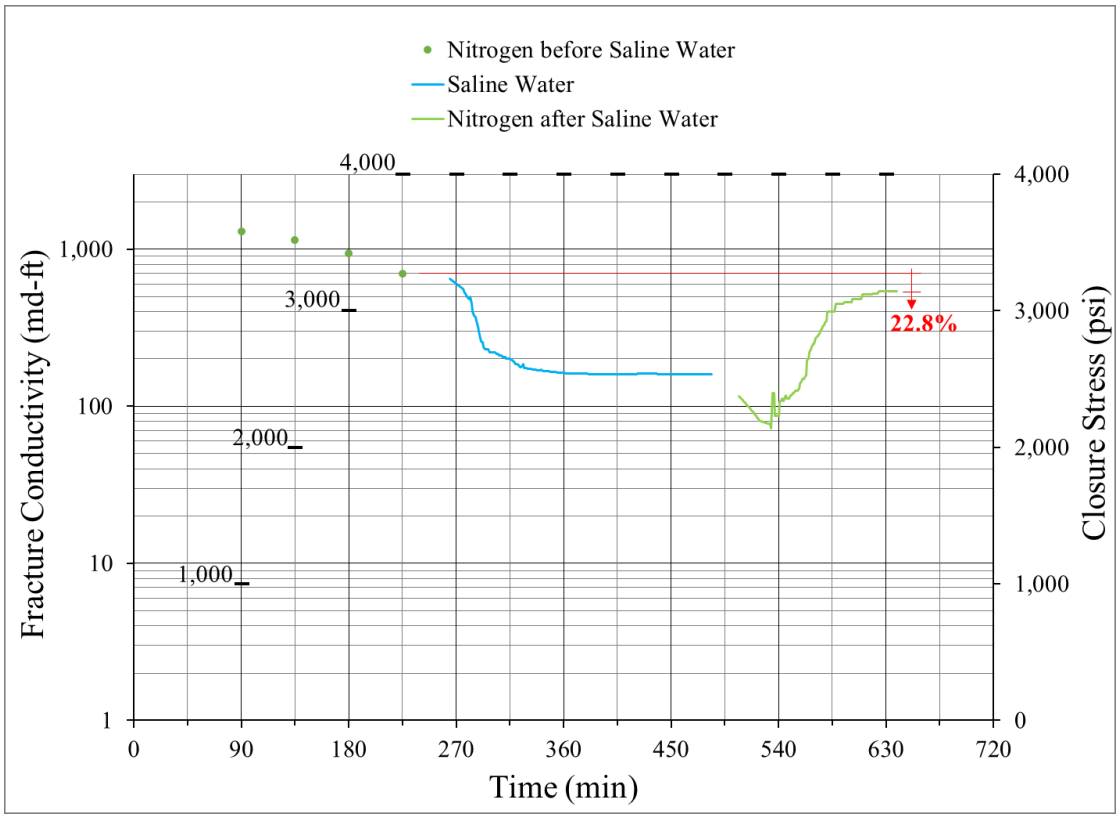

Figure 52 – Eagle Ford Formation Water-Damaging Fracture Conductivity Test (Sample B2) (Adapted from Guerra et al., 2018).

Table 26 summarizes the fracture conductivity measurements at 1,000 psi and 4,000 psi for all Eagle Ford formation fracture conductivity test samples under all flow conditions, as well as the computed unrecoverable percent loss of fracture conductivity.

Table 26 – Summary of Eagle Ford Formation Fracture Conductivity Measurements at 1,000 and 4,000 psi Flowing Dry Nitrogen and Saline Water (Adapted from Guerra et al., 2018).

Test Sample Name	C_f dry nitrogen flow (before saline water) @ 1,000 psi (md-ft)	C_f dry nitrogen flow (before saline water) @ 4,000 psi (md-ft)	C_f saline water flow @ 4,000 psi (md-ft)	C_f dry nitrogen flow (after saline water) @ 4,000 psi (md-ft)	Unrecoverable Loss of C_f @ 4,000 psi (%)
E	1,120	308	59	295	4.2
D	1,290	280	73	268	4.3
C	1,009	589	118	443	24.8
B3	1,024	651	153	544	16.4
B2	1,301	696	160	537	22.8
B1	1,201	565	105	463	18.1
A	1,038	441	159	416	5.6
Core 1	968	210	84	179	14.6
Core 2	988	198	69	170	14.1
Core 3	940	232	101	199	14.1

The largest loss of conductivity took place in Eagle Ford formation sub-units B1, B2, and B3, as well as unit C. Downhole core test samples had very little variation in loss of fracture conductivity across the set.

3.2.2 Marcellus Formation

The Marcellus formation test samples contained a high quartz content, as well as a considerable calcite content. The Marcellus formation has a high level of lamination, directly

impacting the collection of large intact samples. Nevertheless, the test samples in this study constituted the best attainable quality of outcrop rock.

Figure 53 illustrates the fracture conductivity behavior for a gas-water-gas test for the Marcellus formation test sample Allenwood 1.

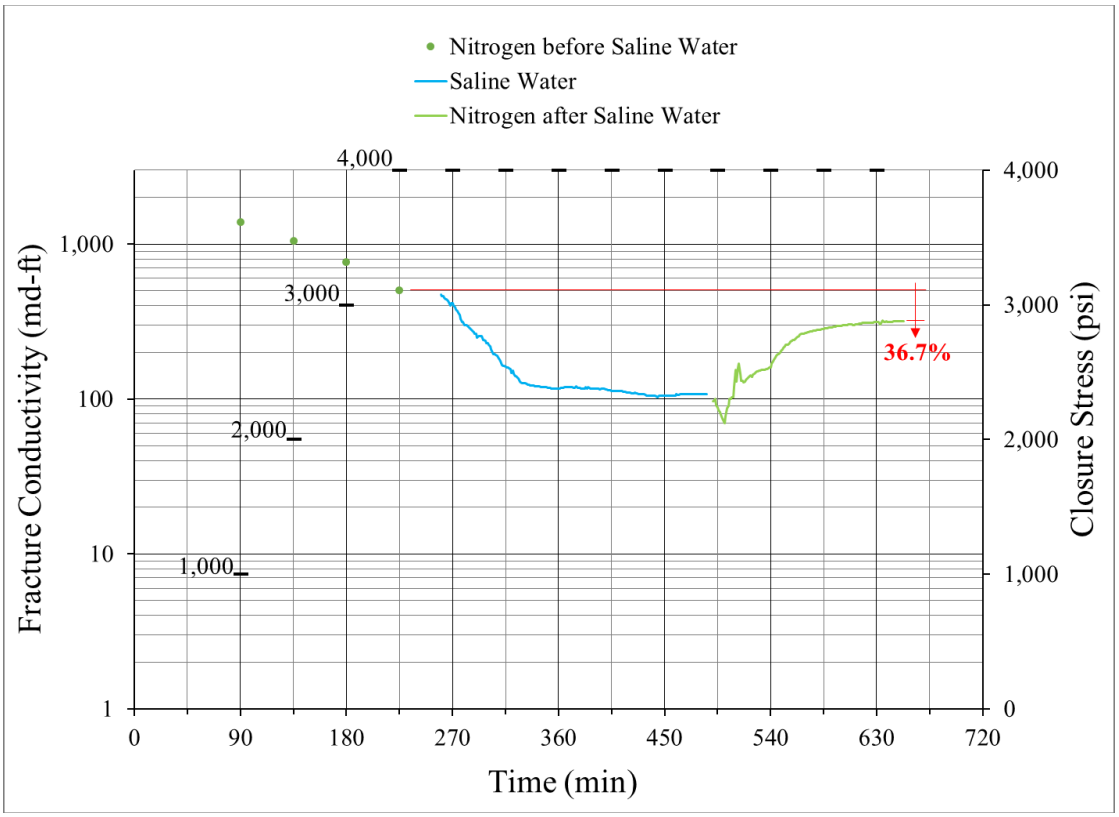

Figure 53 – Marcellus Formation Water-Damaging Fracture Conductivity Test (Sample Allenwood 1) (Adapted from Guerra et al., 2017b).

Under a closure stress of 4,000 psi, **Figure 53** shows how fracture conductivity test sample Allenwood 1 had an initial undamaged fracture conductivity of 502 md-ft, which was reduced to 318 md-ft after saline water was flowed through the fracture, representing an unrecoverable fracture conductivity loss of 36.7%.

Table 27 summarizes the fracture conductivity measurements at 1,000 psi and 4,000 psi for all Marcellus formation fracture conductivity test samples under all flow conditions, as well as the computed unrecoverable percent loss of fracture conductivity.

Table 27 – Summary of Marcellus Formation Fracture Conductivity Measurements at 1,000 and 4,000 psi Flowing Dry Nitrogen and Saline Water (Adapted from Guerra et al., 2017b).

Test Sample Name	C_f dry nitrogen flow (before saline water) @ 1,000 psi (md-ft)	C_f dry nitrogen flow (before saline water) @ 4,000 psi (md-ft)	C_f saline water flow @ 4,000 psi (md-ft)	C_f dry nitrogen flow (after saline water) @ 4,000 psi (md-ft)	Unrecoverable Loss of C_f @ 4,000 psi (%)
Elimsport 1	1,090	489	35	289	40.9
Elimsport 2	1,417	465	39	257	44.7
Elimsport 3	1,125	387	74	202	47.8
Elimsport 4	1,198	405	58	216	46.7
Allenwood 1	1,386	502	107	318	36.7
Allenwood 2	1,287	498	99	303	39.2
Allenwood 3	1,232	411	47	236	42.6
Allenwood 4	1,223	425	56	248	41.6

The largest loss of conductivity took place in test samples Elimsport 2 through 4, as well as Allenwood 3.

4. UNDERSTANDING FRACTURE CONDUCTIVITY IN SHALE FRACTURES

4.1 Introduction

This chapter presents in depth discussions and observations from the experimental measurements outlined in Chapter 2 and Chapter 3. This includes the fracture conductivity behavior and dependencies. This includes the effect of bulk and surface mechanical properties, bulk and surface mineralogy, fracture surface topography, and proppant type and concentration.

This chapter contains several sections pertaining to baseline fracture conductivity behavior. Additional sections pertain to water-damaging fracture conductivity behavior and the self-channeling behavior that was observed in a small subset of test samples. Both the baseline and water-damaging fracture conductivity sections in this chapter consider the effect of all the support experiments outlined and presented in Chapter 2.

An exponential trend line can be fitted to each conductivity measurement, resulting in a representative function that best captures the fracture conductivity behavior. As such, the measurements can be translated into empirically-derived predictive functions that have two main parameters, an initial fracture conductivity and an exponential decline constant. These parameters can serve for comparison against influencing factors, such as mechanical properties.

4.2 Exponential Decline Function Representing Conductivity Behavior

When fracture conductivity is presented as a function of varying stress, a linear relationship on a semi-log plot is produced (Jansen, 2014). As such, an exponential decline rate closely represents the fracture conductivity behavior, as shown with the exponential trend line

fitted to averaged unpropped fracture conductivity values for the Eagle Ford, Mahantango, Middle Bakken, and Three Forks formations (**Figure 54)**.

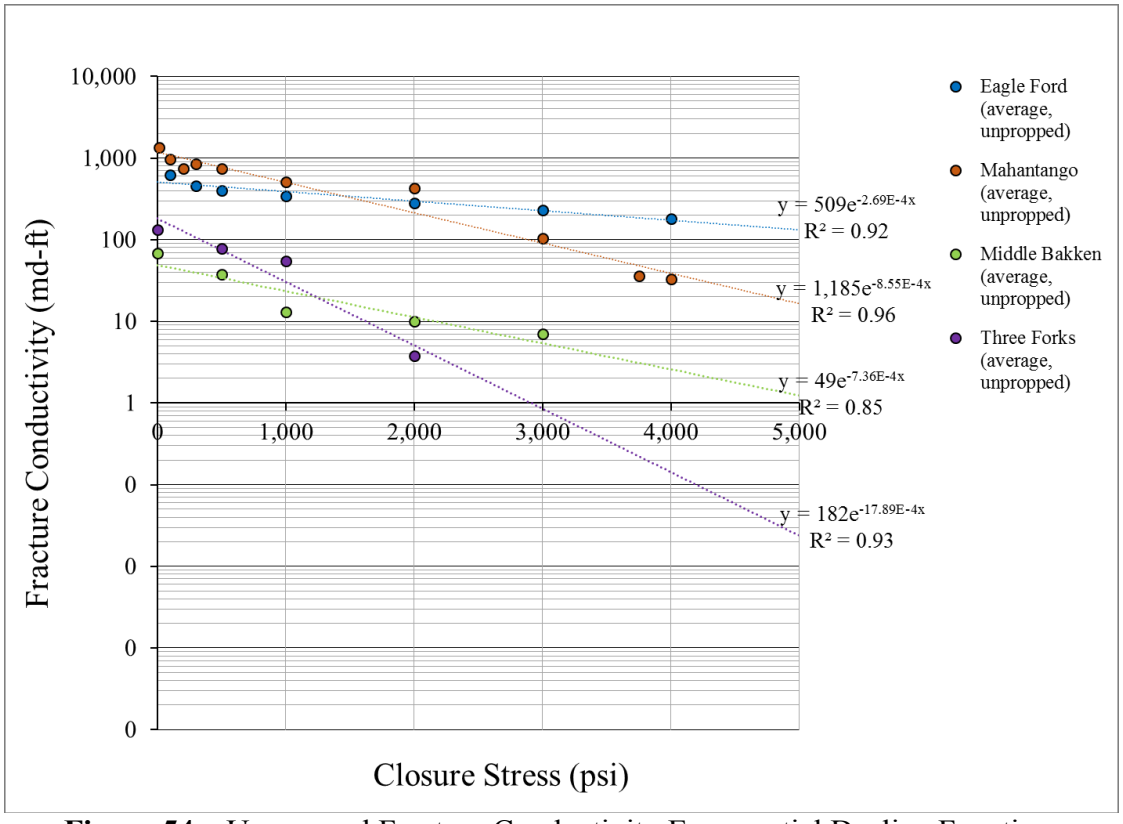

Figure 54 – Unpropped Fracture Conductivity Exponential Decline Function.

As illustrated in **Figure 54**, the exponential decline function can be represented in the form shown in **Eq. 9**, where C_f is the predicted fracture conductivity (md-ft) across the closure stress range, C_{f0} is the initial fracture conductivity at zero closure stress, λ is the exponential decline rate constant (psi^{-1}), and σ_c is the closure stress (psi).

$$C_f \cong C_{f0} e^{-\lambda \sigma_c} \qquad \text{..... (9)}$$

It is worth mentioning that fracture conductivity measurements, and their observed behaviors and trends, rely heavily on statistical significance, wherein a large data set inevitably leads to stronger findings, especially under the premise of averaging test sample conductivities per formation. Additionally, correlations in the form of **Eq. 9** are heavily dependent on the range of the curve fit. For example, as can be seen in **Figure 54**, the average conductivity values used to fit the exponential decline function for the Mahantango formation had an average conductivity value at 200 psi closure stress that was lower than the following closure stress point, and due to the fact, there was only one data point contributing to the average at that closure stress.

As illustrated in **Figure 54**, the initial conductivities and decline rates for each included formation differ, acknowledging that each formation has unique properties that influence the resulting fracture conductivity.

4.2.1 Impact of Proppant Concentration

Adding proppant to a fracture, as universally known, increases conductivity by at least an order of magnitude, as illustrated with the unpropped and propped averaged data for the Middle Bakken test samples, shown in **Figure 55**. 30/50-mesh sand at 0.5 lb_m/ft^2 proppant loading was used for the propped data.

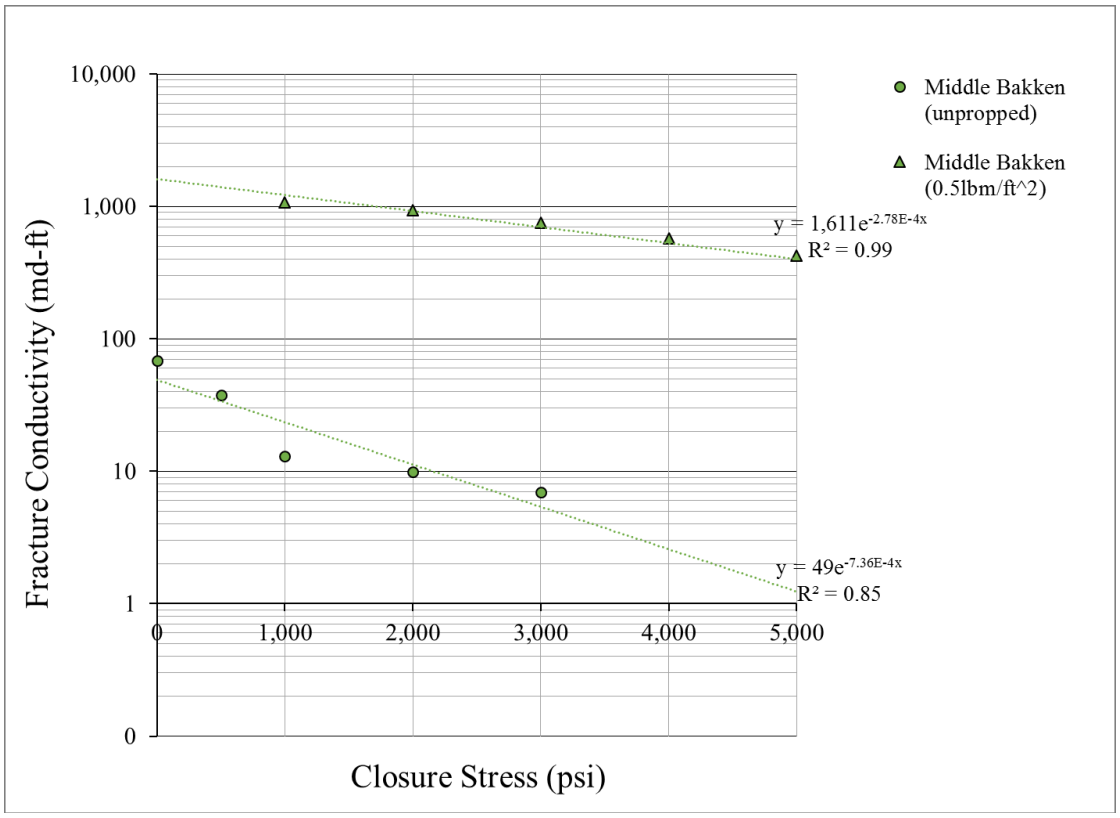

Figure 55 – Middle Bakken Formation Average Unpropped and Propped Fracture Conductivity and Representative Exponential Decline Functions.

As observed in **Figure 55**, the fracture conductivity exponential decline rate changed due to the influence of the proppant pack, modifying the conductivity behavior from being dominated in part by surface attributes for unpropped conditions to now relying more on mechanical properties and proppant concentration. In the absence of proppant, surface topography and rock mechanical properties determine the conductivity behavior under closure stress. Based on **Figure 55**, the fracture conductivity decline rate constant (λ) for the Middle Bakken formation was -2.78E-4 psi^{-1} for propped conditions using 30/50-mesh sand, compared to -7.36E-4 psi^{-1} for unpropped conditions.

Figure 56 shows the increased conductivity obtained by adding very low proppant concentrations to an original unpropped fracture for the Mahantango formation test samples. 40/70-mesh sand at 0.05 and 0.1 lb_m/ft^2 was used for the propped data.

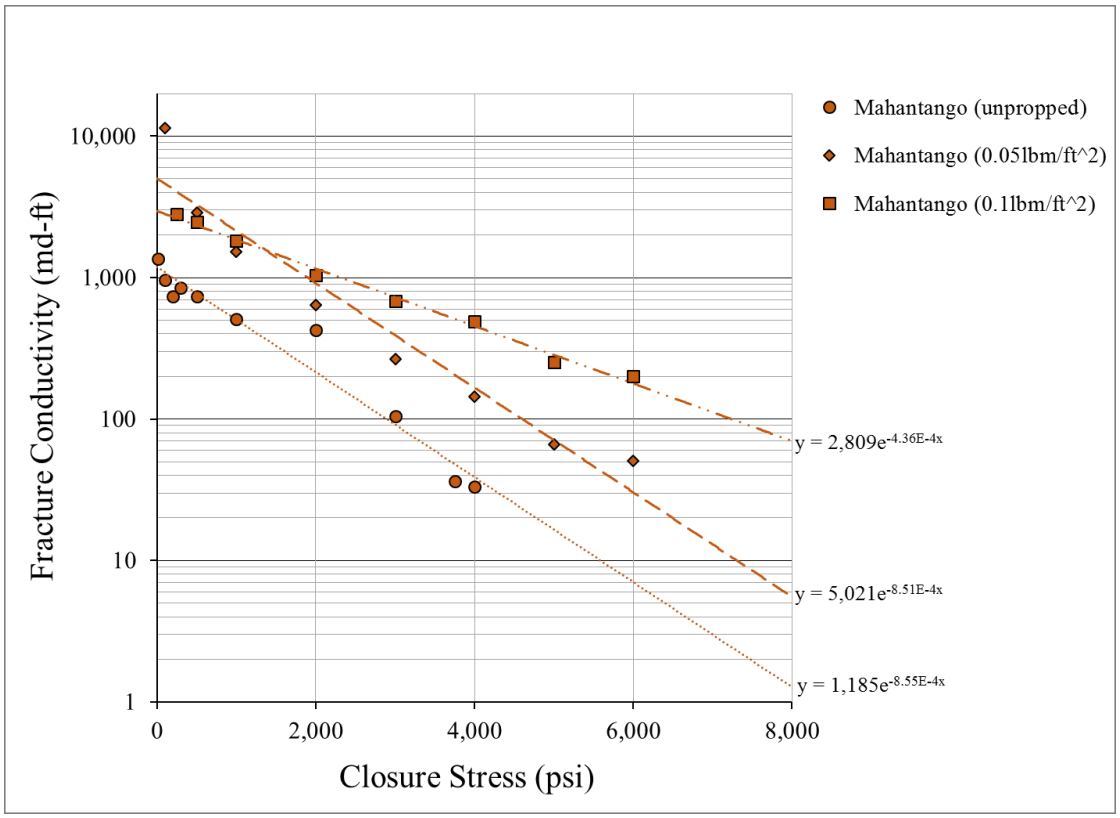

Figure 56 – Mahantango Formation Average Unpropped and Propped Fracture Conductivity and Representative Exponential Decline Functions.

As can be seen in **Figure 56**, a low proppant concentration can greatly increase the fracture conductivity of the fracture, wherein a proppant monolayer behavior is occurring since the theoretical proppant pack width is below 1 proppant layer (described and calculated in Section 4.5).

Figure 57 shows the effect of increasing proppant concentration starting from unpropped conditions up to 0.3 lb_m/ft^2 of 100-mesh sand for the Eagle Ford formation test samples.

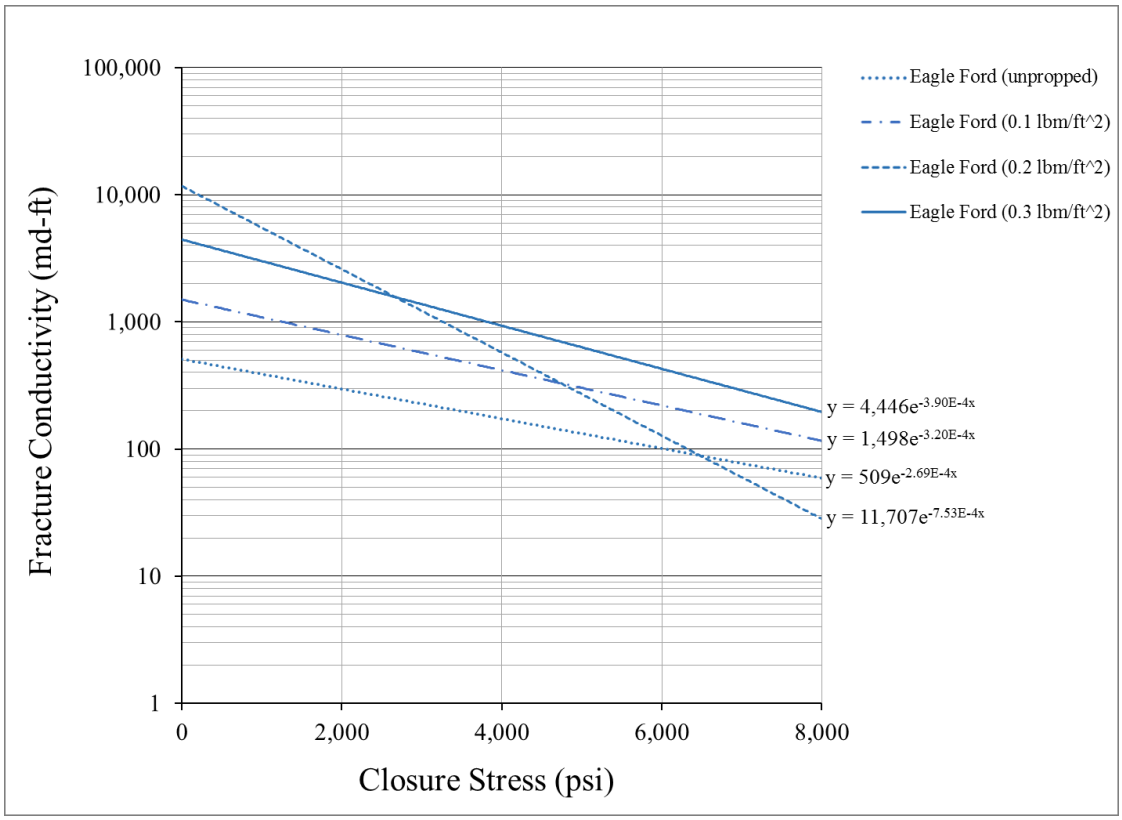

Figure 57 – Eagle Ford Formation Average Unpropped and Propped Fracture Conductivity and Representative Exponential Decline Functions.

In general, increasing the proppant concentration results in increased conductivity across the closure stress range. In some cases, as in the case of the 0.2 lb_m/ft^2 loading in **Figure 57**, less conductivity was achieved at 8,000 psi when compared to the unpropped conductivity, but this is believed to be an artifact of only obtaining data up until 4,000 psi for most of the test samples contributing to the averaging, since the majority of the 0.1 lb_m/ft^2 tests were utilized for water-damaging tests after reaching 4,000 psi.

The Marcellus formation also showed the same general dependency on proppant concentration and closure stress, however this study did not include unpropped testing for that formation. However, some similarity in fracture conductivity behavior at the same proppant

loading was observed between the Marcellus and the Mahantango formations, as shown in **Figure 58**. In this case, both formations used 40/70-mesh sand at 0.1 $lb_m/ft2$ proppant loading.

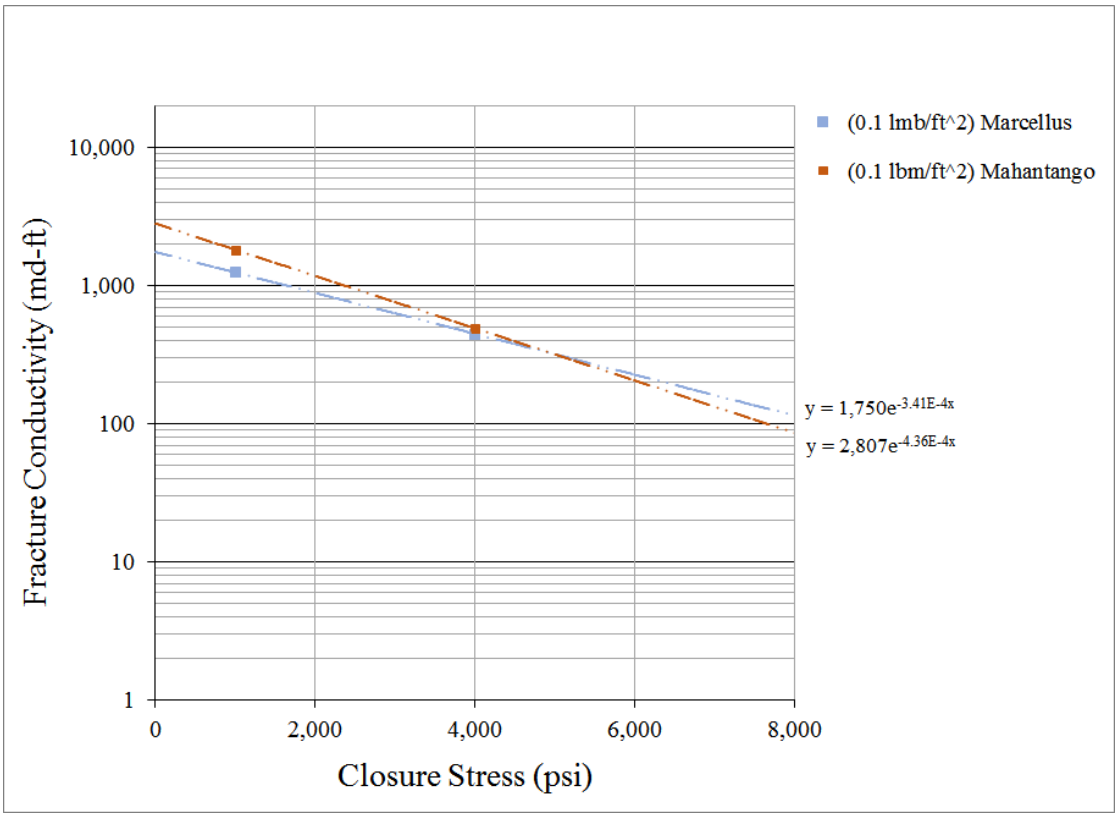

Figure 58 – Marcellus and Mahantango Formations Average Unpropped and Propped Fracture Conductivity and Representative Exponential Decline Functions.

4.2.2 Effect of Proppant Size

By comparing the Eagle Ford formation test samples at 0.1 lb_m/ft^2 proppant loading of 100-mesh sand to the Middle Bakken formation test samples at 0.5 lb_m/ft^2 of 30/50-mesh sand, as shown in **Figure 59**, it was observed that the Eagle Ford formation test samples, albeit with a lower concentration, had a relatively similar conductivity throughout the range.

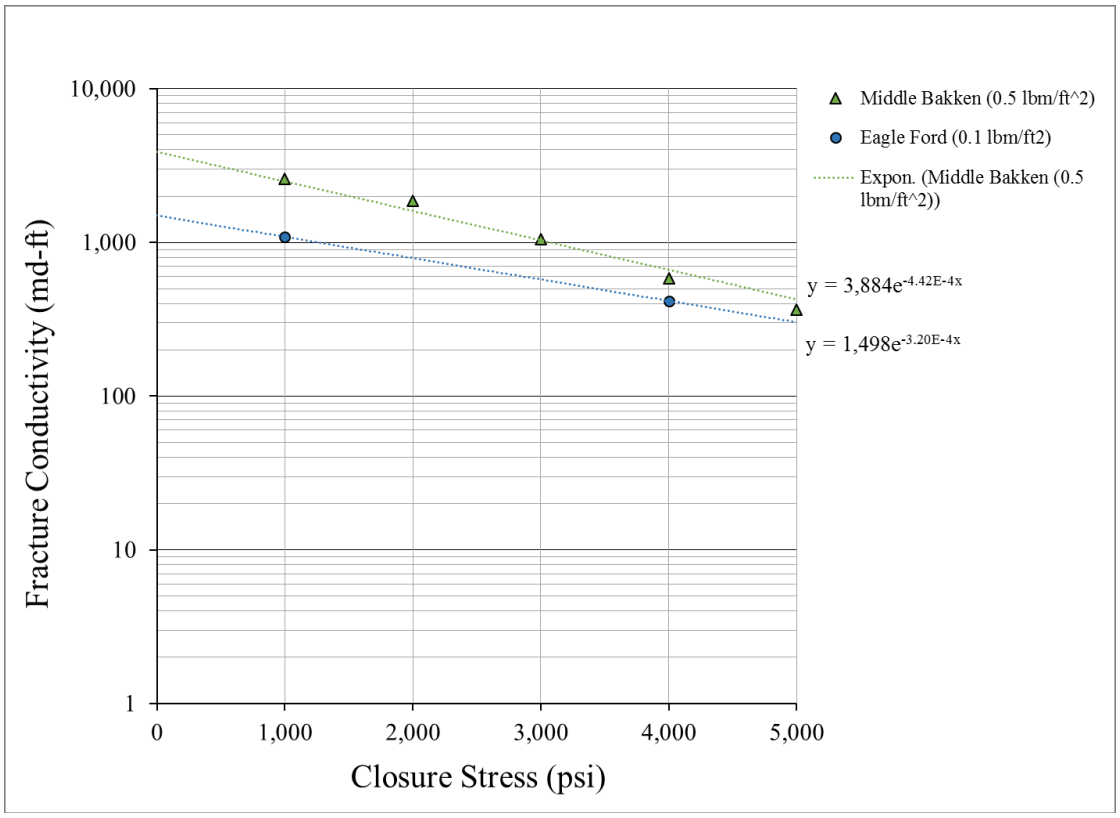

Figure 59 – Eagle Ford and Middle Bakken Formations Average Unpropped and Propped Fracture Conductivity and Representative Exponential Decline Functions.

Another interesting observation is the effect of proppant size, as shown in **Figure 60**, where fracture conductivity for two different mesh sizes is compared (30/50-mesh and 100-mesh sand) under the same testing conditions at low proppant concentration (0.1 lb_m/ft^2). **Figure 60** shows that the effect of proppant size is relatively insignificant, and the difference in conductivity decreased as closure stress increased. At 6000 psi, the two tests yielded very close conductivity values.

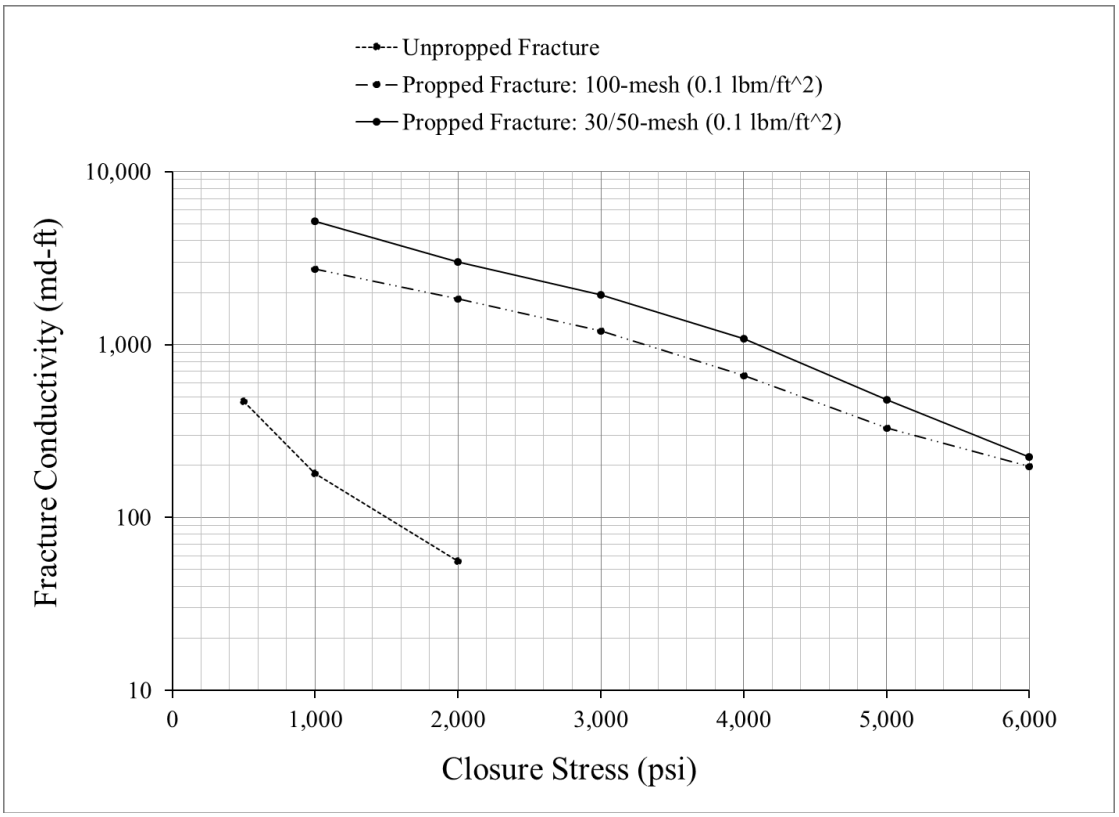

Figure 60 – Fracture Conductivity Comparison for Different Proppant Mesh Sizes (Adapted from Enriquez et al., 2016).

4.3 Test Sample Brittleness and Ductility

In order to support the reasoning for most of the fracture conductivity measurements having a relative high fracture conductivity, the brittleness and ductility of the formations were investigated.

By relying on measured mechanical properties, the test samples can be identified as being relatively ductile or brittle, by employing an empirically derived relationship between Poisson's ratio and Young's modulus as proposed by Grieser and Bray (2007), which is predicated on a term called Brittleness Average, *BA*, as shown in **Eq. 10**. The underlying theory is that brittle rocks tend to exhibit a low Poisson's ratio and a moderately high Young's modulus, while ductile rocks tend to exhibit a high Poisson's ratio and a moderately low Young's modulus

(Grieser and Bray, 2007; Sone and Zoback, 2013). By normalizing the Poisson's ratio and the Young's modulus per their respective ranges, the scaled elastic parameters $v_{brittlenes}$ and $E_{brittlenes}$, as per **Eq. 10** and **Eq. 11**, respectively, are used to define the brittleness average, BA, (**Eq. 12**):

$$E_{brittlenes} = \frac{E - E_{min}}{E_{max} - E_{min}} \quad \ldots\ldots\ldots\

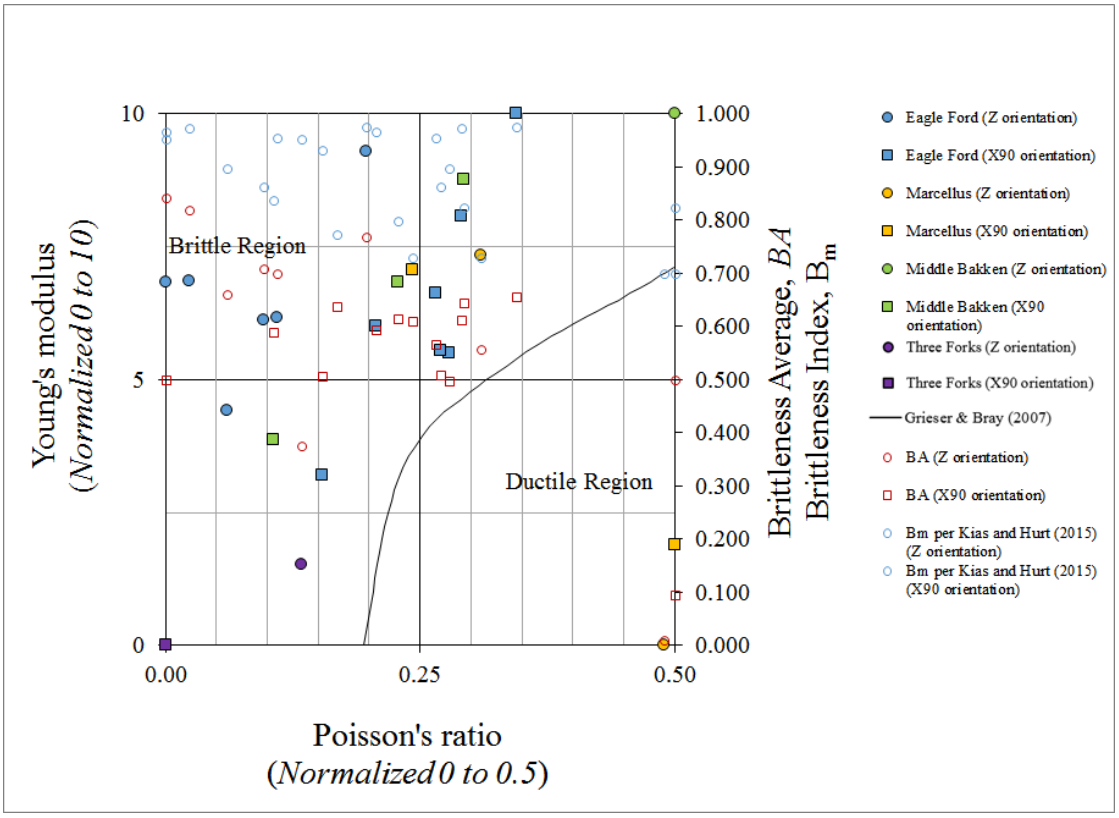

Figure 61 – Normalized Cross-Plot of Young's modulus, Poisson's ratio, and Brittleness Average.

As can be observed in **Figure 61**, the majority of the tested core plug test samples fall on the brittle region of the normalized and ranged cross-plot. Even though this cross-plot can be improved by increasing the sampling size, the sampling size in this study sufficed to indicate that for the most part, all the formations test samples evaluated for both outcrop rock and downhole core segments, tended to be brittle. And according to Grieser and Bray (2007), this high Brittleness Average serves as a potential indicator as to the high propensity of the formation to contain natural fractures, as well as a high probability of fracture network creation during hydraulic fracturing operations –in contrast to conventional formations that typically lay on the ductile region.

Similarly, **Figure 61** shows the Brittleness Index, B_m, defined by Kias et al. (2015):

$$B_m = \frac{V_{KSP} + V_{QTZ} + V_{CAL} + V_{DOL} + V_{PLA}}{V_{KSP} + V_{QTZ} + V_{CAL} + V_{DOL} + V_{PLA} + V_{SID} + V_{CLAY}} \quad \ldots\ldots\ldots\ldots\ldots\ldots\ldots\ldots\ldots\ldots (13)$$

In the aforementioned equations, V is the weight fraction of the mineral, KSP stands for k-feldspar, QTZ stands for quartz, CAL stands for calcite, DOL stands for dolomite, PLA stands for plagioclase, and SID stands for siderite.

As observed in **Figure 61**, the Brittleness Index, in general, also suggests that the majority of the test samples were all brittle. This suggests that both a mechanical properties-based brittleness index (BA) and a mineralogy-based brittleness index (B_m) tended to agree, broadly, with the test sample classification as being relatively brittle or ductile. This is also indicative that all gathered test samples came from a brittle zone within the formations considered.

4.4 Test Sample Mineralogy and the Relationship to Mechanical Properties

By considering the measured bulk mechanical properties and the mineralogy of the test samples via XRD, several relationships were investigated. This included comparing the Young's modulus with the quartz content by weight percent, also with the clay content, and the carbonate content; Brinell Hardness Number was also compared with the aforementioned mineral weight percentages. From these relationships, given the large scatter in the data, no discernable trends could be ascertained. Despite that fact, a slightly positive correlation with the carbonate content was observed, as shown in **Figure 62**, for the Eagle Ford, Marcellus, Middle Bakken, and Three Forks formations.

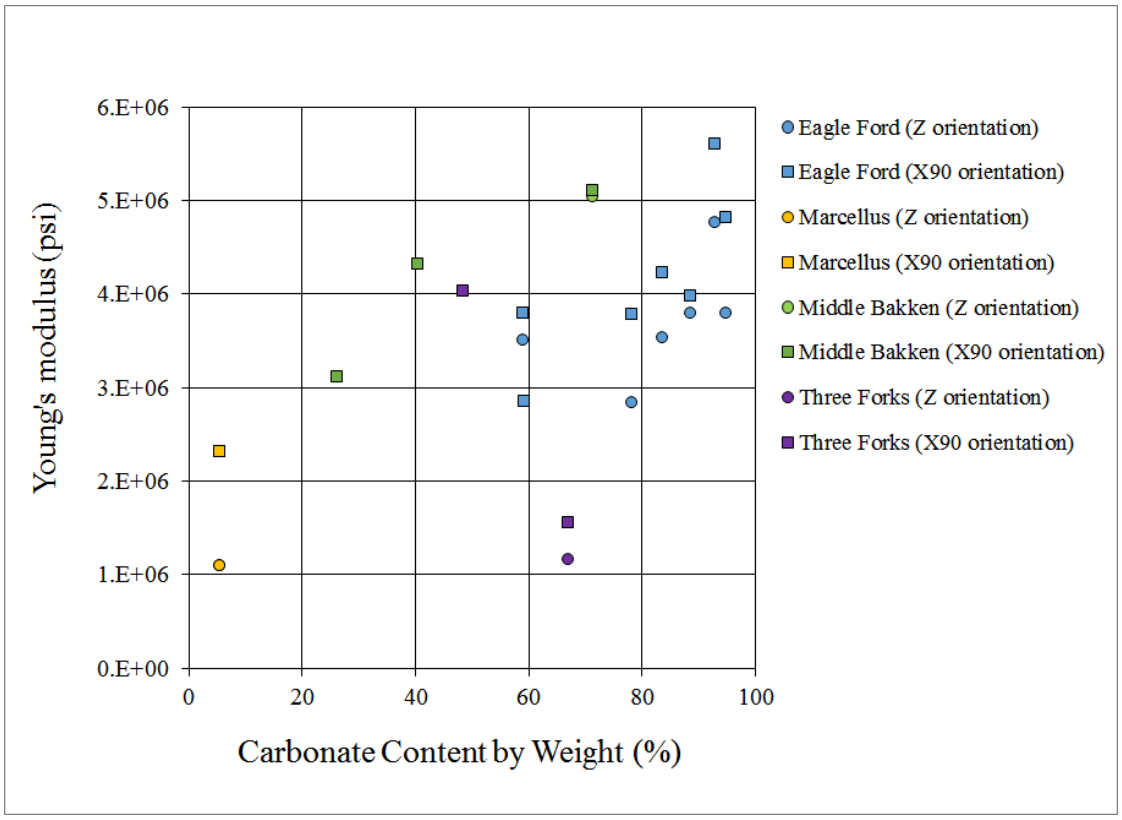

Figure 62 – Relationship of Young's Modulus and Carbonate Content.

In **Figure 62**, no discernable difference between the Z and X90 orientations were noticed. In general, however, the overall soft trend suggests that a gain in rock stiffness is expected as carbonate content increases, given that carbonate serves as a cementing agent in shale formations (Kias et al., 2015).

Similarly, the Brinell Hardness Number was compared against carbonate content, which also exhibited a slightly positive correlation, as shown in **Figure 63**.

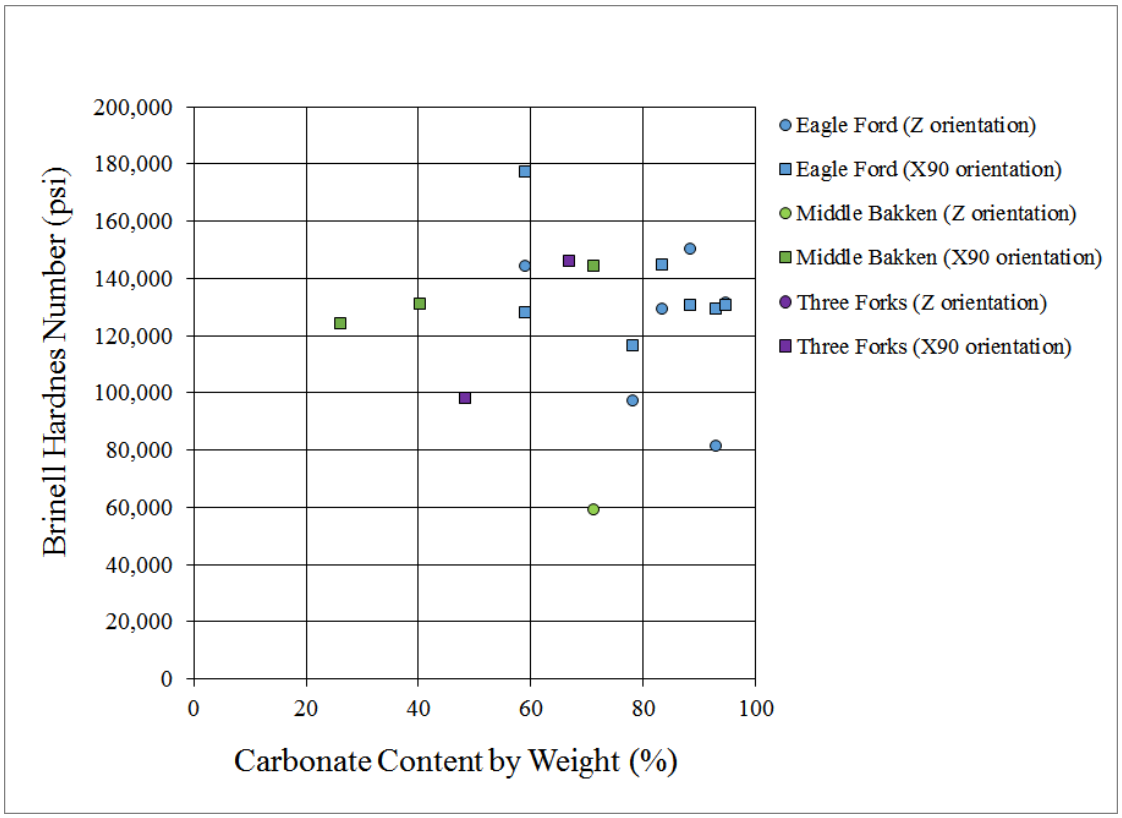

Figure 63 – Relationship of Brinell Hardness Number and Carbonate Content.

Correlations between mineral content and bulk mechanical properties, as between surface mechanical properties, may differ due to the size of the data set as well as the scale in which the measurements were conducted. This may result in correlations between mineral content and Young's modulus being weaker, in comparison to hardness. **Figure 64** shows the relationship between Brinell Hardness Number and the Young's modulus for each formation that produced the relevant data.

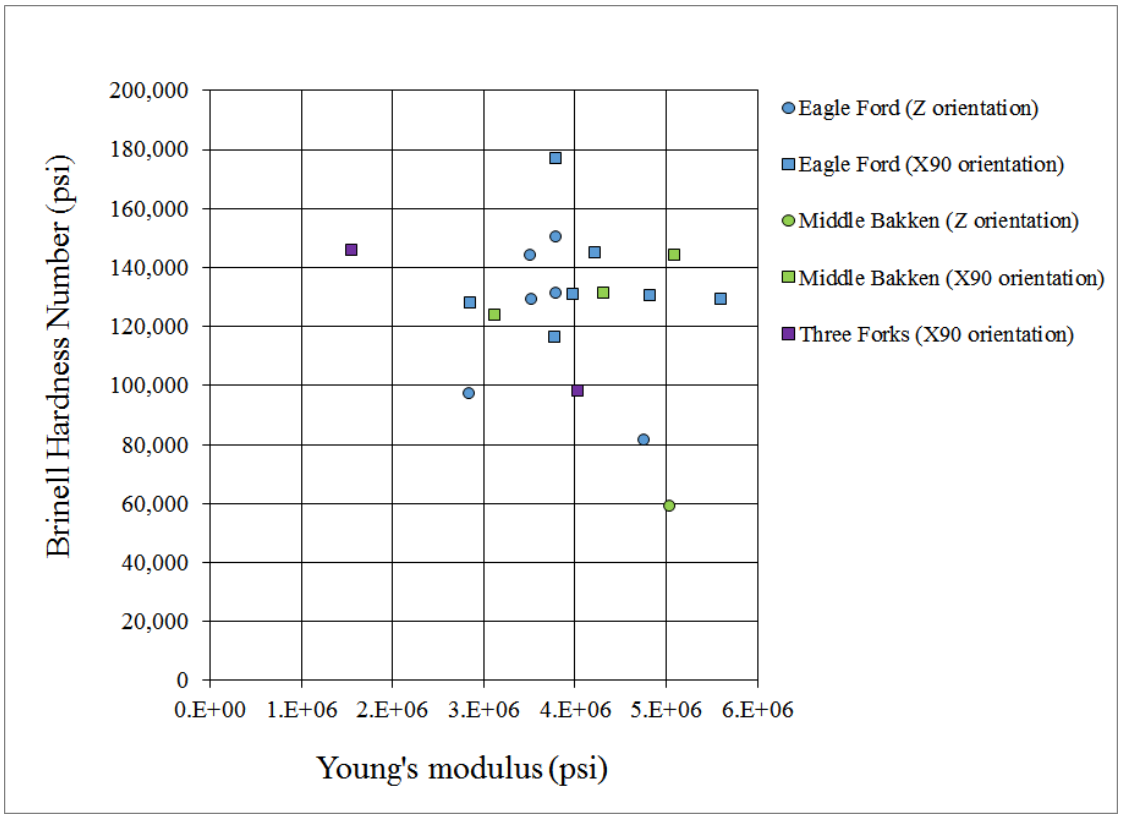

Figure 64 – Relationship of Brinell Hardness Number and Young's Modulus.

There is an appreciable anisotropy of the mechanical properties, and differences in trends from the mechanical properties between the formations, albeit no general correlation was observed in **Figure 64**. It is to be noted that both data sets also differ on the fact that the Eagle Ford formation test samples originated from outcrop rock, while the Middle Bakken formation and Three Forks formation test samples originated from downhole core segments.

4.5 Theoretical Proppant Pack Width and Number of Proppant Layers

The theoretical propped fracture width, w_f, can be computed with **Eq. 14** based on the areal proppant concentration, C_{lb_m/ft^2}, and relying on bulk density values reported in Section 2.2.4.2.

$$w_{f(in.)} = \frac{C_{lb_m/ft^2}}{\rho_{bulk(lb_m/ft^3)}}\left(12\left(\frac{in.}{ft}\right)\right) \quad \text{.....(14)}$$

Figure 65 shows the dependence of propped fracture width on areal proppant concentration for the three proppant types considered in this study.

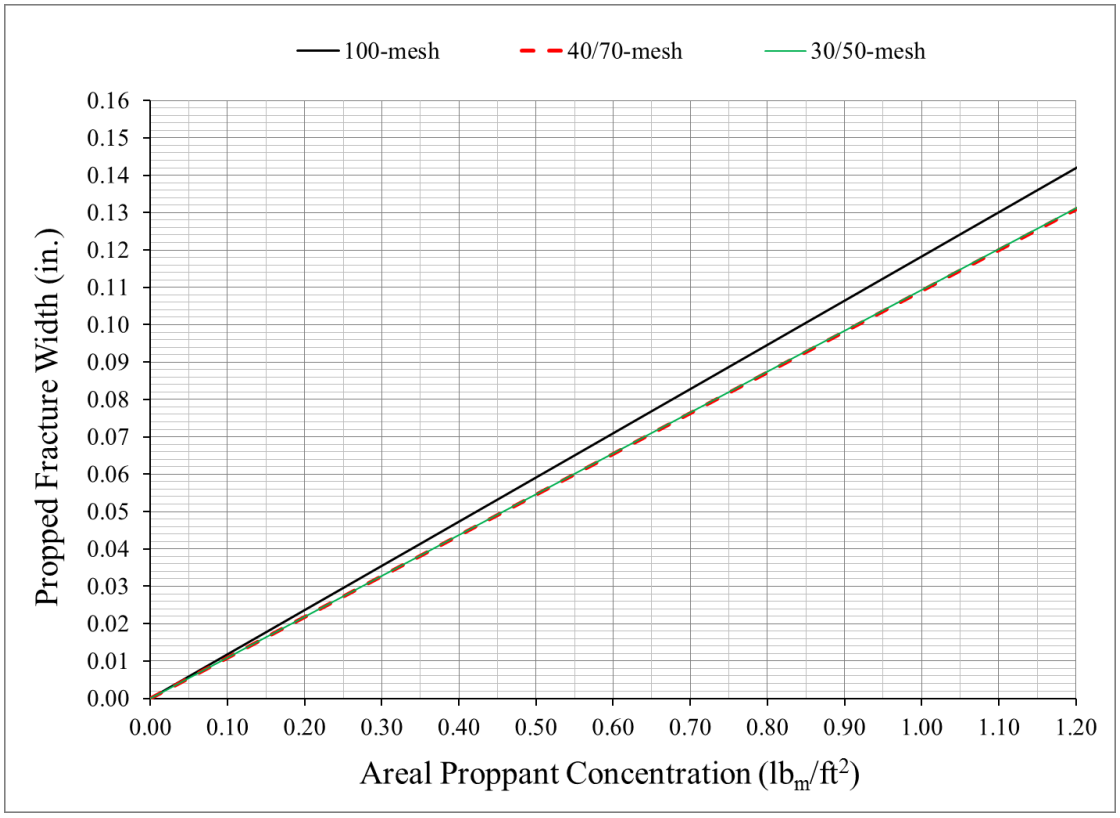

Figure 65 – Propped Fracture Width Dependence on Areal Proppant Concentration: 100-mesh, 40/70-mesh, and 30/50-mesh Sand.

The differences in propped fracture width is a result of their different bulk densities. Therefore, they have different widths for the same arbitrary fracture dimensions (length and height). 40/70 and 30/50 mesh sizes have a larger size distribution when compared to 100-mesh, and by this they can be better sorted, leading to a higher bulk density.

Based on **Figure 65**, the 100-mesh sand proppant concentrations of 0.1 lb_m/ft^2, 0.2 lb_m/ft^2, and 0.3 lb_m/ft^2, resulted in propped fracture widths of 0.0118 in., 0.0237 in., and 0.0355 in., respectively. The 40/70-mesh sand proppant concentrations of 0.05 lb_m/ft^2 and 0.1 lb_m/ft^2, resulted in propped fracture widths of 0.0055 in. and 0.0109 in., respectively. Similarly, the 30/50-mesh sand proppant concentration of 0.5 lb_m/ft^2, resulted in a propped fracture width of 0.0547 in.

In order to relate the areal proppant concentrations utilized in the experiments to sand concentration in a field-employed slurry in terms of pounds per gallon, C_{PPG}, **Eq. 15** can be used based on the pumped proppant concentration in terms of pounds per gallon added, C_{PPGA}, and relying on a quartz grain density value of 2.65 g/cm^3 (165.4341 lb_m/ft^3).

$$C_{PPG} = \frac{C_{PPGA}\,\rho_{grain(lb_m/ft^3)}}{\rho_{grain(lb_m/ft^3)} + C_{PPGA}\left(7.4805\,\frac{gal}{ft^3}\right)} \quad \text{.....(15)}$$

The areal proppant concentration can then be computed by assuming a dynamic fracture width of 0.150 in. with **Eq. 16** reliant on **Eq. 15** for C_{PPG}.

$$C_{lb_m/ft^2} = C_{PPG}\left(7.4805\frac{gal}{ft^3}\right)\left(\frac{w_{f\_dynamic(in.)}}{12\frac{in.}{ft}}\right) \quad \text{.....(16)}$$

The resulting propped fracture width can then be computed with **Eq. 14** reliant on **Eq. 16**. **Figure 66** shows the dependence of propped fracture width on pumped proppant concentration in terms of pounds per gallon added for the three proppant types considered in this study.

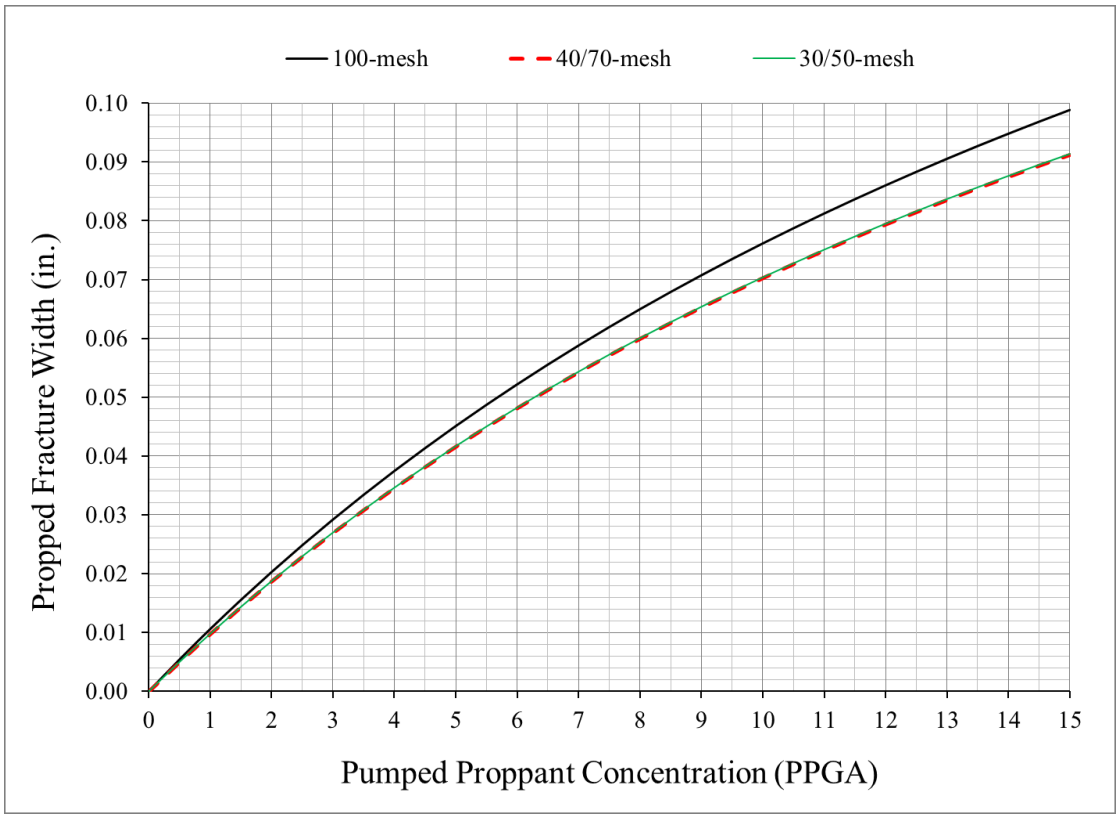

Figure 66 – Propped Fracture Width Dependence on Pumped Proppant Concentration: 100-mesh, 40/70-mesh, and 30/50-mesh Sand.

Given that the pumped proppant concentration is in terms of mass of proppant over the volume of fracturing fluid, the total bulk volume of proppant for each mesh size depends on the bulk density, resulting in differences in propped fracture width as shown in **Figure 66**.

Based on **Figure 66**, the pumped proppant concentrations in terms of C_{PPGA} of 1.121 PPGA, 2.372 PPGA, and 3.754 PPGA, corresponded to fracture widths of 0.0118 in., 0.0237 in., and 0.0355 in. for 100-mesh sand. Similarly, 0.553 PPGA and 1.123 PPGA, corresponded to fracture widths of 0.0055 in. and 0.0109 in. for 40/70-mesh sand. For 30/50-mesh sand, 7.058 PPGA corresponded to a fracture width of 0.0547 in.

In order to estimate the number of proppant layers given a particular proppant concentration, the proppant can be assumed to be composed of spherical particles of equal diameter, d, arranged in a face-centered cubic lattice (a form of close-packing) in order to achieve the largest fraction of space occupied by the spheres. This highest density of packing consists of a center-to-center spacing of spheres arranged in a tetrahedron, as shown in **Figure 67** for a stack of proppant particles. For this packing, the height between the fracture surface and the center of the first contacting proppant layer is $(1/2)d$, and the height for subsequent proppant layers beyond the fracture surface is $\left(\sqrt{6}/3\right)d$. As such, the fracture width, w_f, for a given number of proppant layers can be calculated with **Eq. 17**, where d is the proppant particle diameter and n is the number of proppant layers.

$$w_f = \frac{\sqrt{6}}{3} d(n-1) + d \quad \text{.....} (17)$$

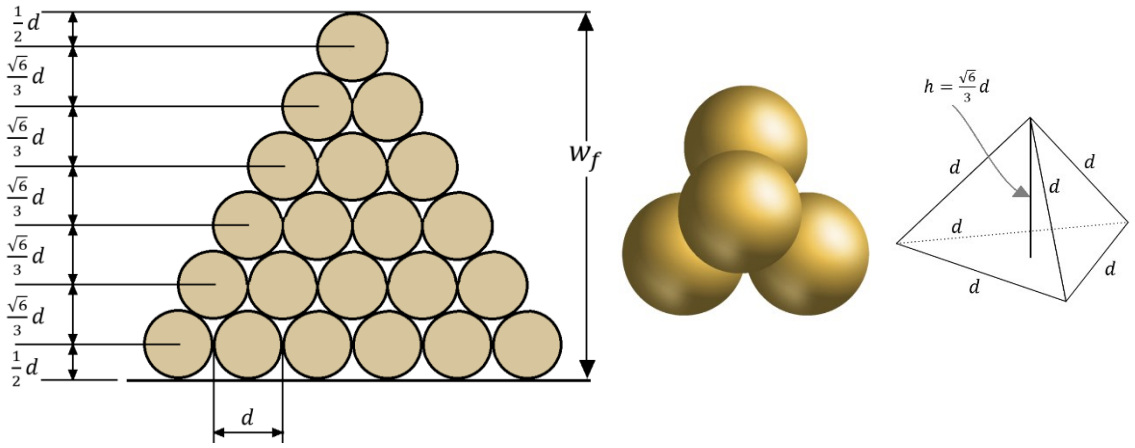

(a) (b)

Figure 67 – Proppant Packing Based on a Tetrahedron Lattice: (a) Side View of Proppant Pack; (b) Top View of Three Stacked Proppant Particles and The Corresponding Distance Between the Centers of Each Particle.

Eq. 17 is valid for values of $n \geq 1$. Rearranging **Eq. 17**, the number of proppant layers can be calculated with **Eq. 18**, based on fracture width, and valid for values of $w_f \geq d$.

$$n = \frac{3}{\sqrt{6}}\left(\frac{w_f}{d} - 1\right) + 1 \quad \text{.....(18)}$$

The fracture width from **Eq. 14** can be used to calculated the number of proppant layers for each proppant mesh size used in this study, by using the measured median diameter of the proppant, d_{50}, from Section 2.2.4.2 for each of the proppant types. **Figure 68** shows the proppant layers corresponding to areal proppant concentration for the three proppant types considered in this study.

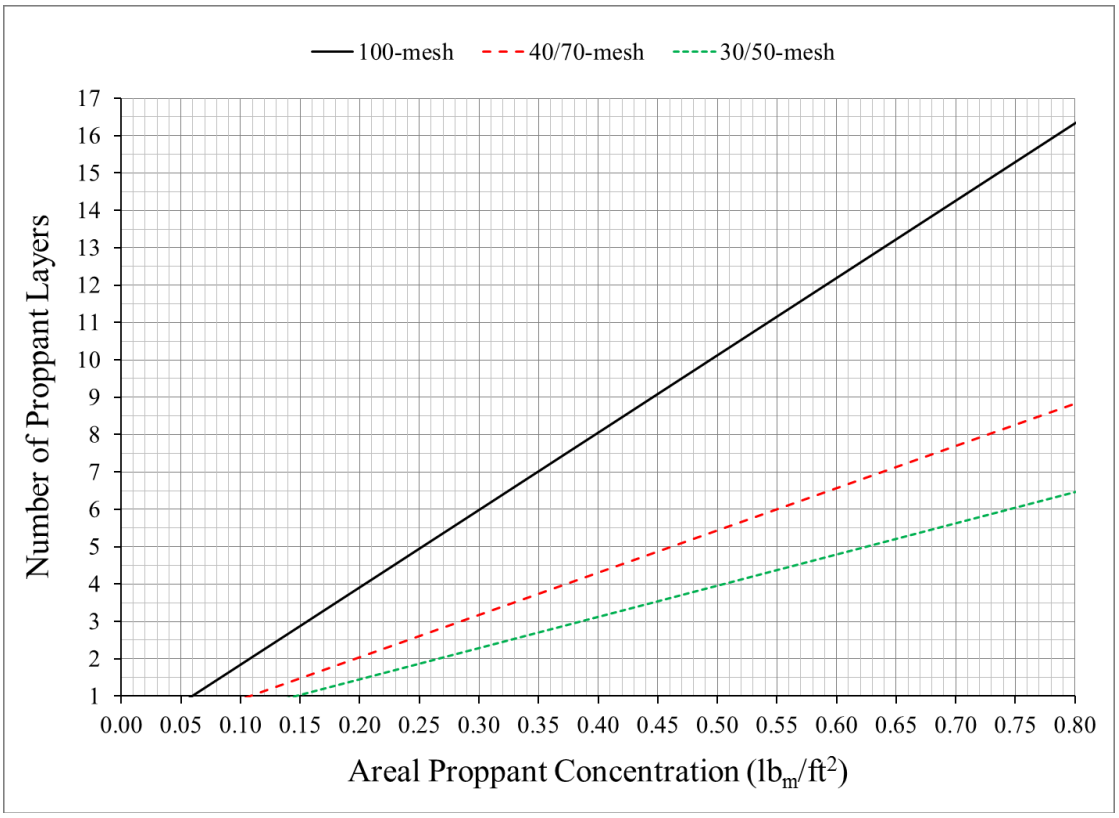

Figure 68 – Number of Propped Layers for 100-mesh, 40/70-mesh, and 30/50-mesh Sand.

Based on **Figure 68**, the areal proppant concentrations of 0.1 lb_m/ft^2, 0.2 lb_m/ft^2, and 0.3 lb_m/ft^2, for 100-mesh sand resulted in a calculated value of 1.84 layers, 3.92 layers, and 5.98 layers, respectively. Similarly, for 40/70-mesh sand with areal proppant concentrations of 0.05 lb_m/ft^2 and 0.1 lb_m/ft^2, the number of calculated proppant layers resulted in a value less than 1 for each, indicating a partial monolayer condition. For 30/50-mesh sand with a proppant areal concentration of 0.5 lb_m/ft^2, the number of calculated proppant layers resulted in 3.96 layers.

Proppant layer estimates shown in **Figure 68** can also be closely approximated by employing a relationship developed by Brannon et al. (2004) to calculate the minimum areal proppant concentration, C_a (in lb_m/ft^2), to achieve a full proppant monolayer, as shown in **Eq. 19**.

$$C_a = 5.20(1 - \emptyset)\gamma_d d_d \quad \text{.....(19)}$$

In **Eq. 19**, $\emptyset$ is the minimum achievable porosity of the proppant pack, γ_p is the specific gravity of the proppant (g/cm^3), and d_p is the average proppant diameter (in.). For example, by considering values reported in Section 2.2.4.2 for 100-mesh sand and assuming a minimum porosity of 0.3, $C_a = 5.20(1 - 0.3)(2.65)(0.0070) = 0.0675$ lb$_m$/ft^2.

4.6 Influence of Mechanical Properties

All the unpropped and propped fracture conductivity tests were analyzed and an exponential decline function was obtained for each based on a trend line. The two main parameters, the initial fracture conductivity and the exponential decline constant, were compared with the Young's modulus and the Poisson's ratio corresponding to each of the test samples. This comparison was conducted by differentiating between the formations, the bedding plane orientation, and the simulated fracture conditions, while also considering the average of the bulk mechanical properties of unit B1 and B2 to represent fracture conductivity test samples B1, and EF-1 through EF-3 (Eagle Ford formation).

The variation of the exponential decline constant with respect to the Young's modulus, presented in **Figure 69**, showed that for the majority of the fracture conductivity measurements, the exponential decline constants had relatively low values which corresponded in general with a moderate to high Young's modulus. This behavior is in agreement with expectations that the higher the Young's modulus, the lower the exponential decline constant (albeit not readily apparent based on the data evaluated). As such, the fracture conductivity is better preserved over the closure stress regime. For this dataset, however, further testing would be required to fully observe the aforementioned dependency.

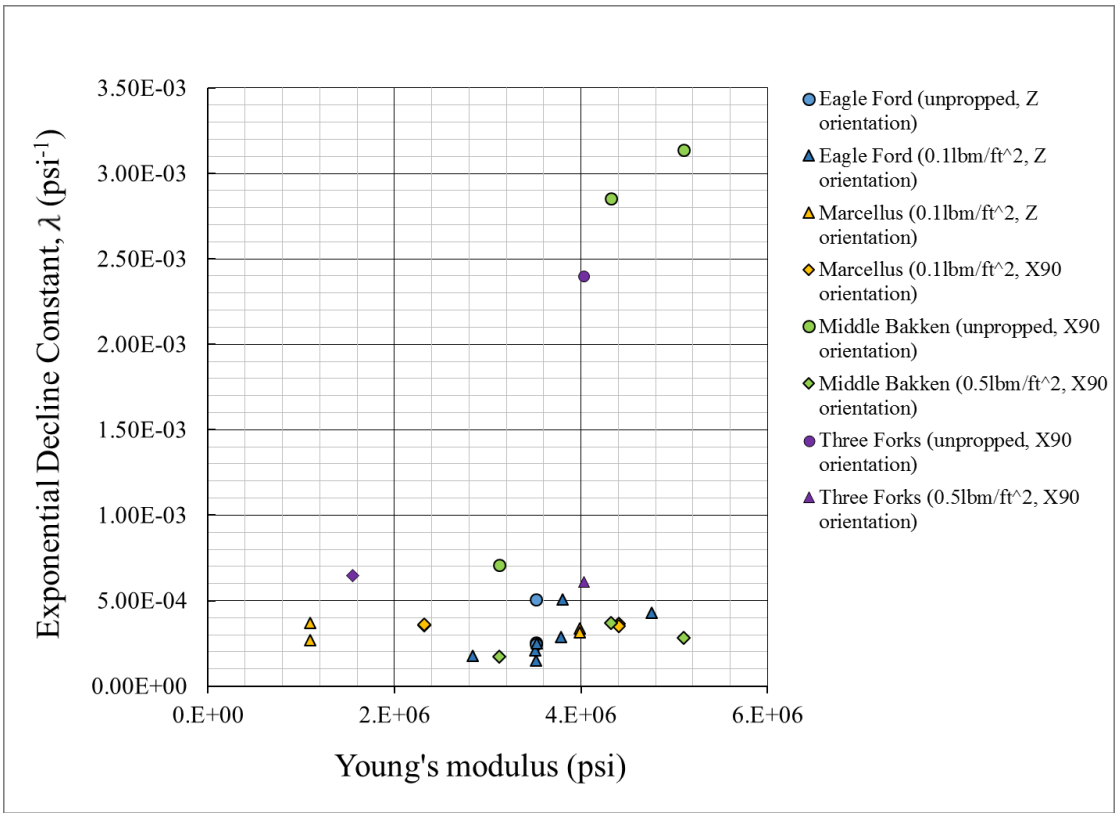

Figure 69 – Variation of Exponential Decline Constant with Young's modulus.

Unpropped fracture conductivity tests were conducted up to a closure stress of 4,000 psi, while the propped fracture conductivity tests in some cases reached 8,000 psi closure stress. In **Figure 69**, the three data points with the highest exponential decline constants were those from the unpropped fracture conductivity tests conducted on the Middle Bakken and Three Forks formations (up to 3,000 psi closure stress). By considering the unpropped fracture conductivity test samples, one noticeable difference between them is that those from the Eagle Ford formation had the lowest maximum height difference between the lowest and the highest point on the fracture surface (0.140 – 0.230 in.), compared to those form the Middle Bakken and Three Forks formations (0.480 – 0.960 in.), as discussed in Section 4.7.

It is expected that as the Poisson's ratio increases (and by such the rock propensity to deform and hinder the fracture width), the rate of fracture conductivity decline would increase as well. This behavior was better observed in the unpropped fracture conductivity measurements, as shown in **Figure 70**.

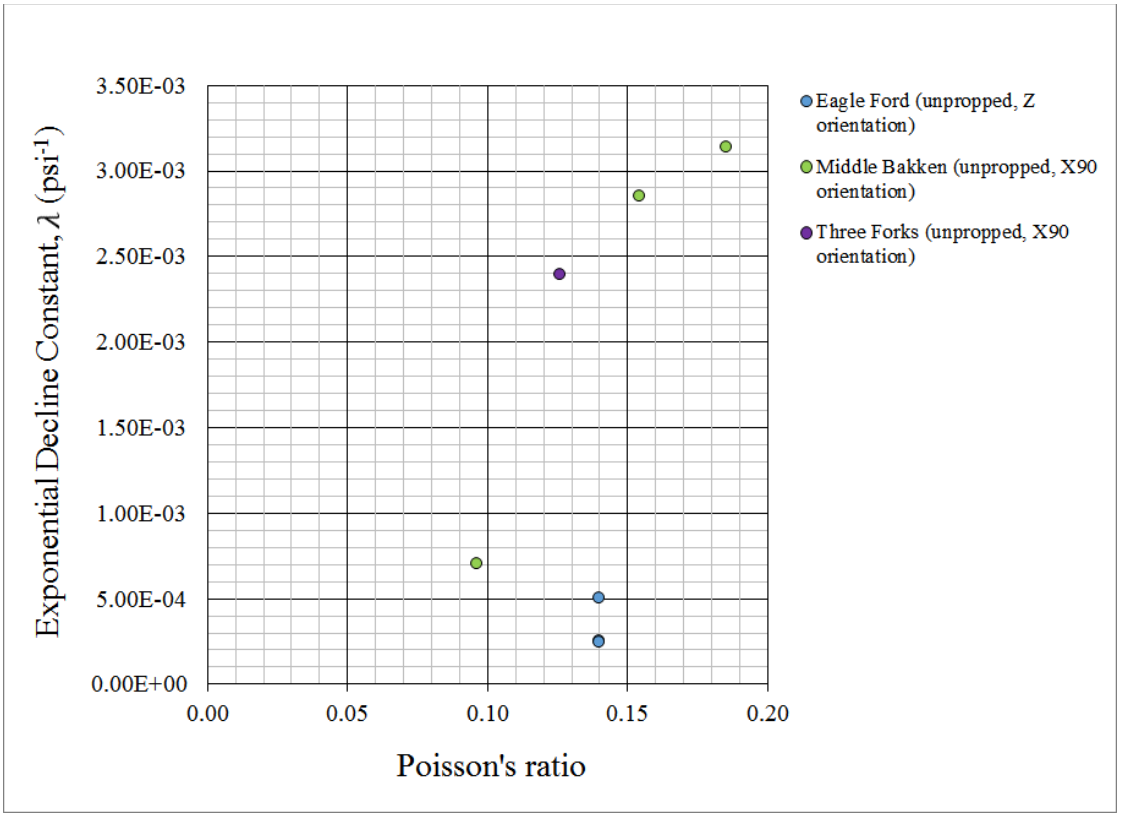

Figure 70 – Variation of Exponential Decline Constant with Poisson's ratio (Unpropped Tests).

The fracture conductivity decline rate variation with Brinell Hardness Number, shown in **Figure 71**, showed no correlation. It is expected that the harder the fracture surface, the higher the longevity of the fracture conductivity under increasing closure stress. Furthermore, the Brinell Hardness Number can represent the propensity for proppant embedment, given that the test is a surface indentation test.

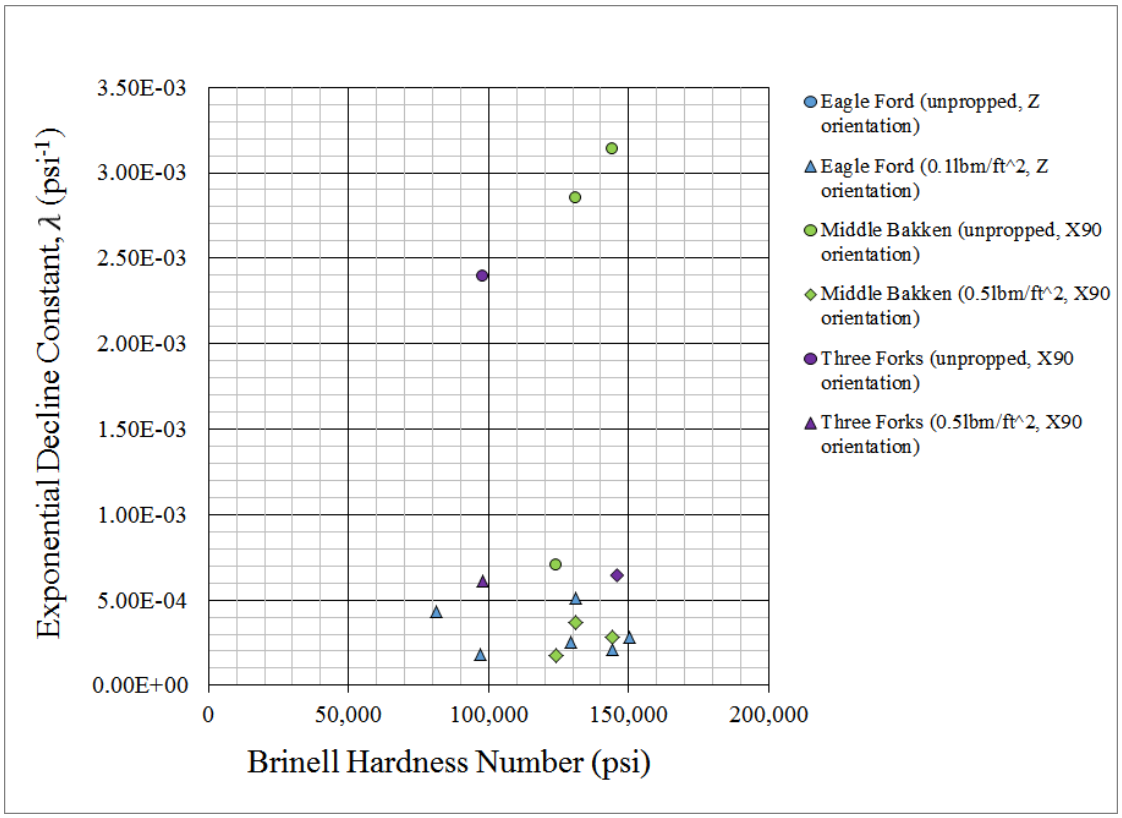

Figure 71 – Variation of Exponential Decline Constant with the Brinell Hardness Number.

4.7 Influence of Surface Attributes

Based on decline rate functions for the considered fracture conductivity tests, the initial conductivity (at zero closure stress) showed a weak direct relationship with surface roughness, as shown in **Figure 72**. This behavior is suggestive that the surface asperities are contributing to the fracture conductivity, especially at low closure stresses. The Eagle Ford formation showed one of the strongest correlations between initial conductivity and surface roughness, while the Bakken formation had less of a dependence.

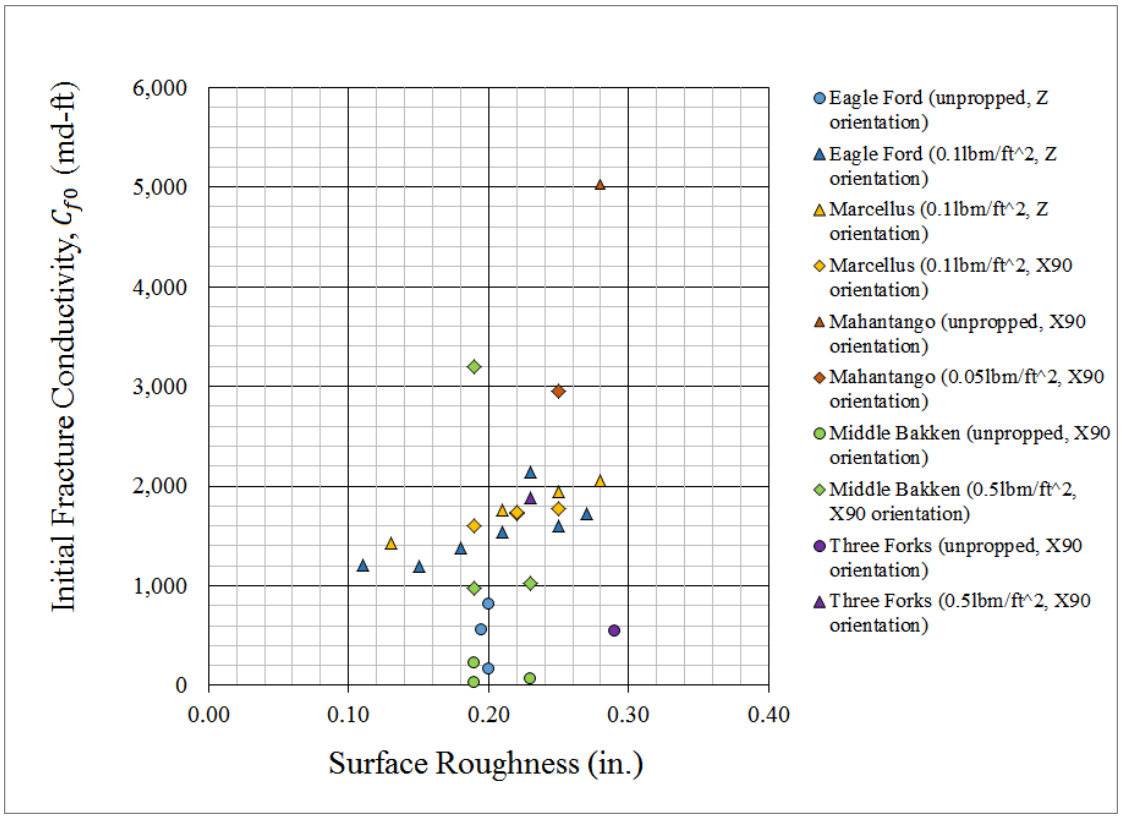

Figure 72 – Variation of Initial Conductivity At Zero Closure Stress with Surface Roughness.

The fracture conductivity decline rate also showed a correlation with the maximum height difference across the fracture surface of the fracture conductivity test sample (Δz_{max}), as shown in **Figure 73** for the propped fracture conductivity tests.

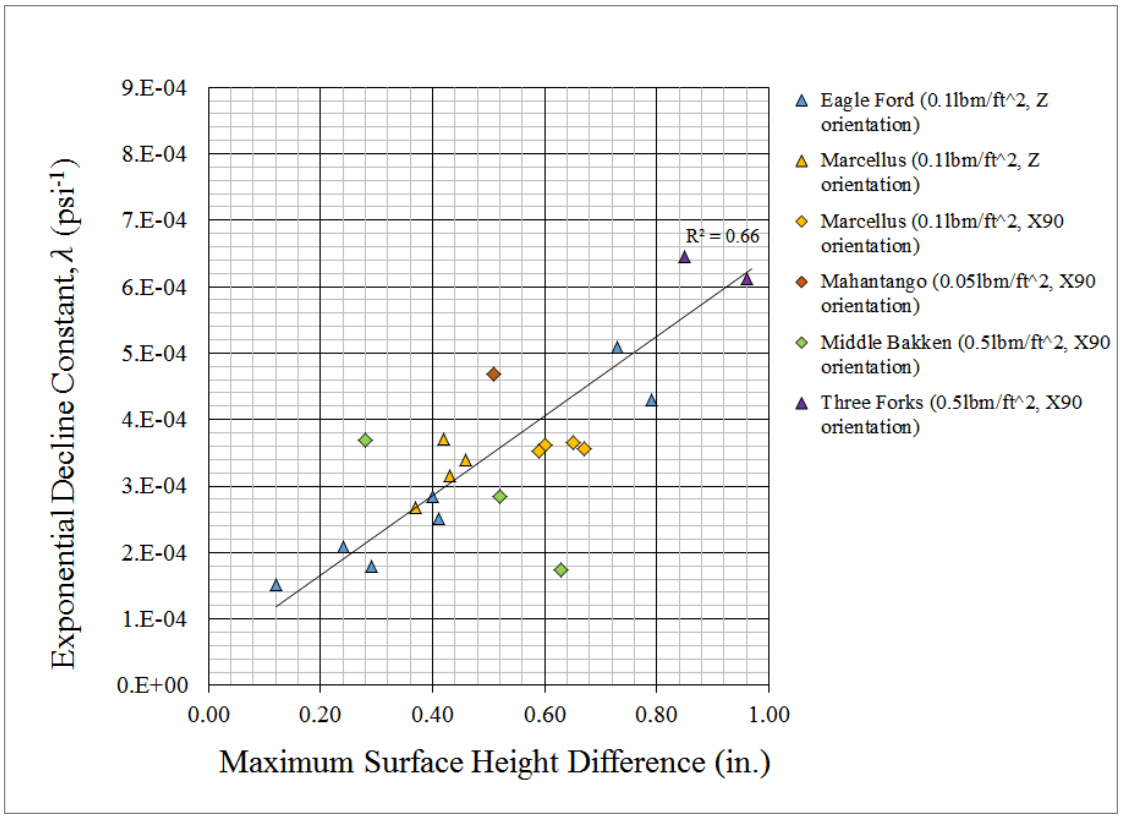

Figure 73 – Variation of Initial Conductivity At Zero Closure Stress with Maximum Surface Height Difference.

The influence of bedding plane orientation was manifested predominantly in a high degree of mechanical property anisotropy and differences in surface topography. However, any attempt to find a direct relationship to fracture conductivity based on bedding plane orientation proved difficult given the large data scatter, which not only was a result of the high degree of heterogeneity present in the formations, but also of the manner in which test samples were collected and then fractured. Furthermore, the scale in which tests are conducted may not capture the effect of bedding plane orientation, especially when comparing the dimensions of the fracture conductivity test sample to the thickness of bedding plane intervals present in the outcrop. Test samples originating from downhole core, however, proved to be more laminated, and in most

cases had a rougher and more tortuous surface topography, which in turn affected the fracture conductivity.

4.8 Self-Channeling in the Proppant Pack

A small subset of the baseline fracture conductivity measurements showed that initial proppant concentrations were altered during the process of measuring fracture conductivity, yielding a final proppant distribution that partially occupied the fracture surface. The remaining surface area was absent of proppant and served as channels of high conductivity relative to the areas occupied by the proppant. This behavior was caused primarily by high velocity gas flow at low closure stresses, without the installment of a screen immediately after the fracture conductivity cell (which would have mitigated the proppant displacement). That being said, the following experimental observations suggest the possibility of an optimum initial proppant concentration that can result in the highest channeling behavior for a particular fracture surface.

Self-channeling in the proppant pack was exhibited on fracture conductivity test samples EF-1 and EF-2 from the Eagle Ford formation. These baseline fracture conductivity tests involved propped fractures with 100-mesh sand with concentrations ranging from 0.1 to 0.3 lbm/ft^2. The sequence of fracture conductivity testing consisted of utilizing the same test sample for several fracture conditions. The first fracture conductivity test performed was with unpropped fracture conditions, followed by a propped fracture conductivity test –each with increasing concentrations, with the largest being that of 0.3 lbm/ft^2 (**Figure 74**).

The selected proppant with the desired concentration was manually placed evenly across the bottom fracture surface. **Figure 74** shows the proppant placement on the bottom-side fracture surface of the test sample. Due to the uneven fracture surface, the proppant tended to roll off the

high part of the fracture surface and accumulate at the low part of fracture. As such, the proppant concentration was not constant across the surface of the fracture, which would not occur if the fracture surface was smooth. This behavior was similar to fractures created in the field, which are expected to also have unevenly-distributed proppant.

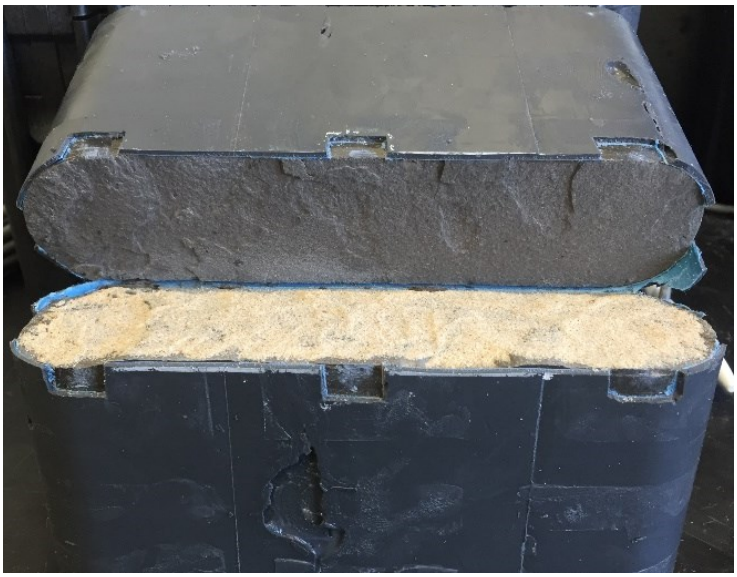

Figure 74 – Proppant Placement on Eagle Ford Formation Fracture Conductivity Test Sample EF-1, Showing the Proppant Concentration Was Not Constant Across the Fracture Surface (Guerra et al., 2017a).

Figure 75 shows the propped fracture conductivity measurements for test samples EF-1, EF-2, and EF-3. After testing was conducted, EF-1 and EF-2 showed a self-channeling behavior (as illustrated in **Figure 76** and **Figure 77**) which suggested a possible reasoning behind the fact that both EF-1 and EF-2 at proppant loadings of 0.2 lb_m/ft^2 had a higher fracture conductivity than test sample EF-3 at 0.3 lb_m/ft^2 (which did not show self-channeling behavior) at their final tested closure stress, as shown in **Figure 75**.

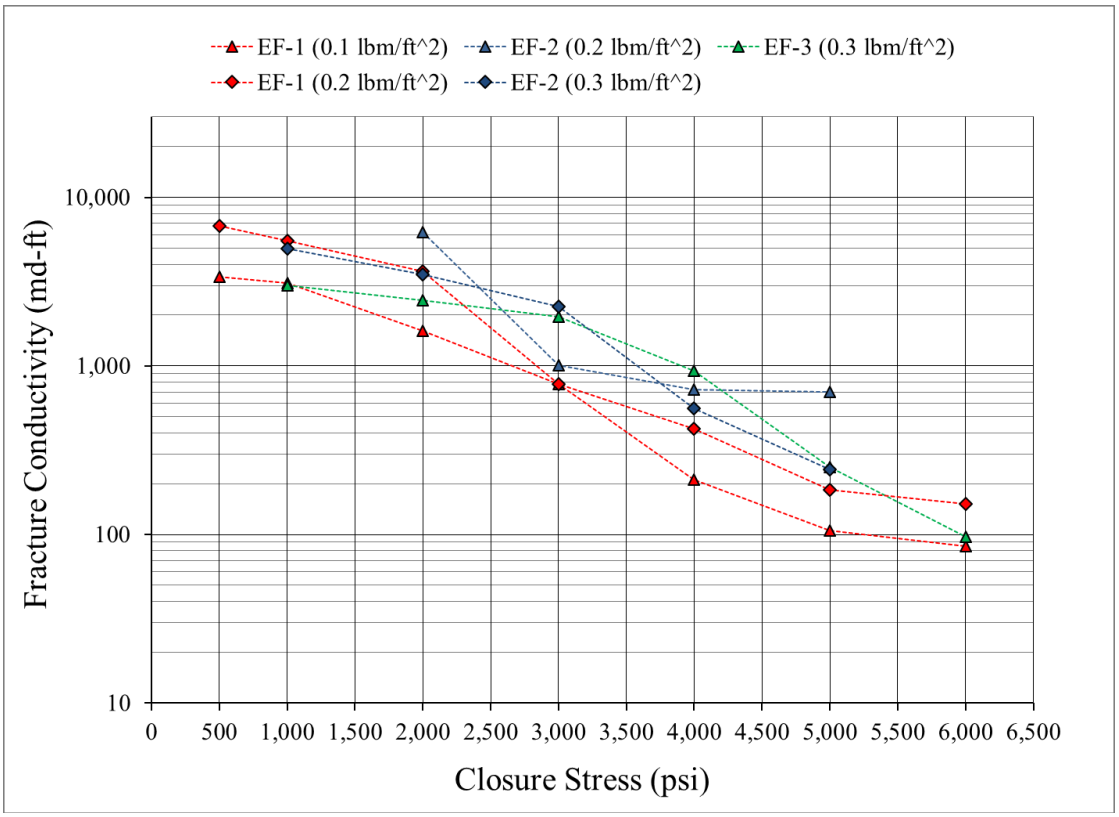

Figure 75 – Eagle Ford Formation Propped Fracture Conductivity (Adapted from Guerra et al., 2017a).

Conductivity decline is controlled by several factors, related to both formation rock and proppant properties. During closure, the competition between rock strength and proppant strength results in reduction of conductivity from its initial value at zero closure stress. If the rock is stronger than the proppant, the proppant crushes and rearranges, and both fracture width and permeability suffer. If the proppant is stronger, embedment may occur. On long term production, proppant failure and fines plugging may become dominant. Because the fracture surface was not smooth and flat in the experiments, non-uniformed loading of the proppant pack occurs. Proppant rolled off the high spots ("hills") and accumulated at the low spots ("valleys"). Thus, the conductivity obtained through the rough fracture surfaces is provided by different mechanisms; in some locations the rock surface is in direct contact, and in other locations the

proppant is packed between the rock surfaces. Once the flow starts, the fracture is propped open at the hills and proppant has the possibility to flow with gas (especially at high velocity). Sudden changes in conductivity measurement as closure stress was increased were suggestive of changes occurring in the proppant pack (such as proppant repacking). This behavior can be seen in EF-2 at 0.2 lb_m/ft^2 at 4,000 psi, where additional closure stress resulted in a slower rate of fracture conductivity decline (**Figure 75).**

Changes in the proppant pack are not only a function of gas flow rate, but also of fracture surface topography and proppant concentration. For the two low-concentration tests, significant repacking of proppant was observed. **Figure 76** and **Figure 77** show the proppant distribution along the fracture surface before and after the conductivity test at different proppant concentrations. The images on the left of **Figure 76** and **Figure 77** show the fracture surface with proppant before the test, and the images on the right of the figures show the proppant distribution after the conductivity test. Obviously for both tests, more areas of fracture surface were exposed with no proppant compared with the images before the conductivity tests. It is to be noted, however, that displacement of proppant within the fracture was not mitigated by a screen immediately following the outlet of the conductivity cell, however a screen was present further downstream.

An interesting comparison can be made by observing **Figure 76b**,**d** and **Figure 77b**,**d**, where the area that has no proppant (and is dark-colored) is similar to the channel fracture generated by the use of fibers. The dark-colored areas are the surface areas on which there is no proppant, and interestingly enough, such fracture condition is comparable with the channel fracture generated by fiber with the HiWAY flow-channel fracturing technique (by Schlumberger Limited), as shown in **Figure 78a** (which shows an artificially placed proppant

arrangement). For this study, the channels created in the experiments occurred without adding other materials to the slurry, and were a product primarily of high gas flow rate at low closure stress. Other factors that resulted in the proppant redistribution and channeling during the conductivity tests may have included the surface topography and the small proppant size.

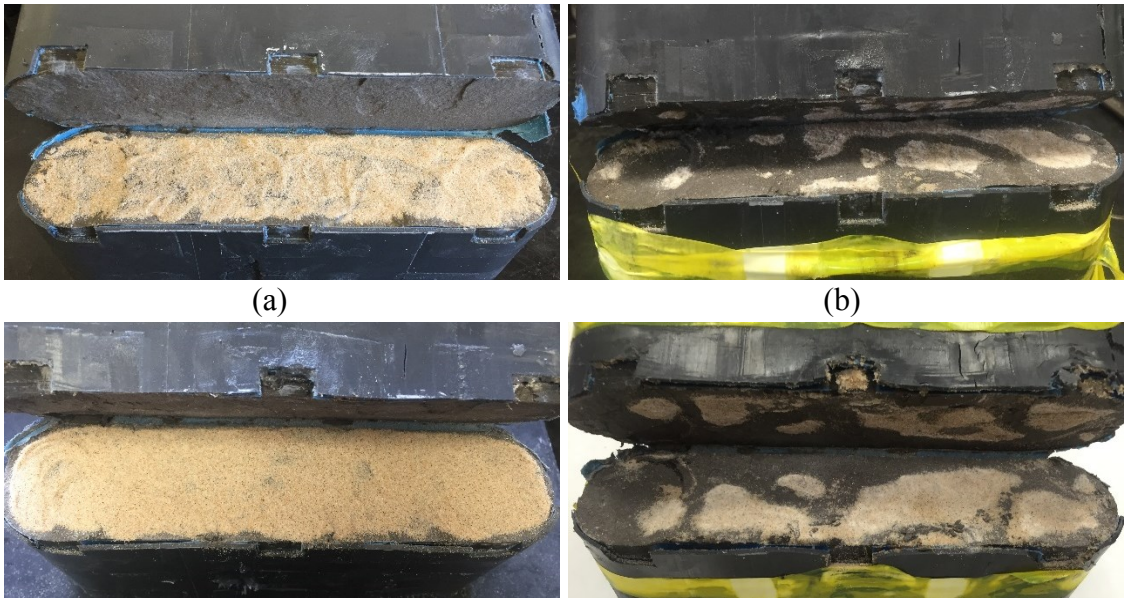

Figure 76 – Distribution of Proppant Along Fracture Surface for Fracture Conductivity Test Sample EF-1 (Guerra et al., 2017a): (a),(b) Proppant Loading of 0.1 lbm/ft^2 100-mesh Sand Before Fracture Conductivity Test, and Resulting Proppant Distribution After Fracture Conductivity Test; (c),(d) Proppant Loading of 0.2 lbm/ft^2 100-mesh Sand Before Fracture Conductivity Test, and Resulting Proppant Distribution After Fracture Conductivity Test.

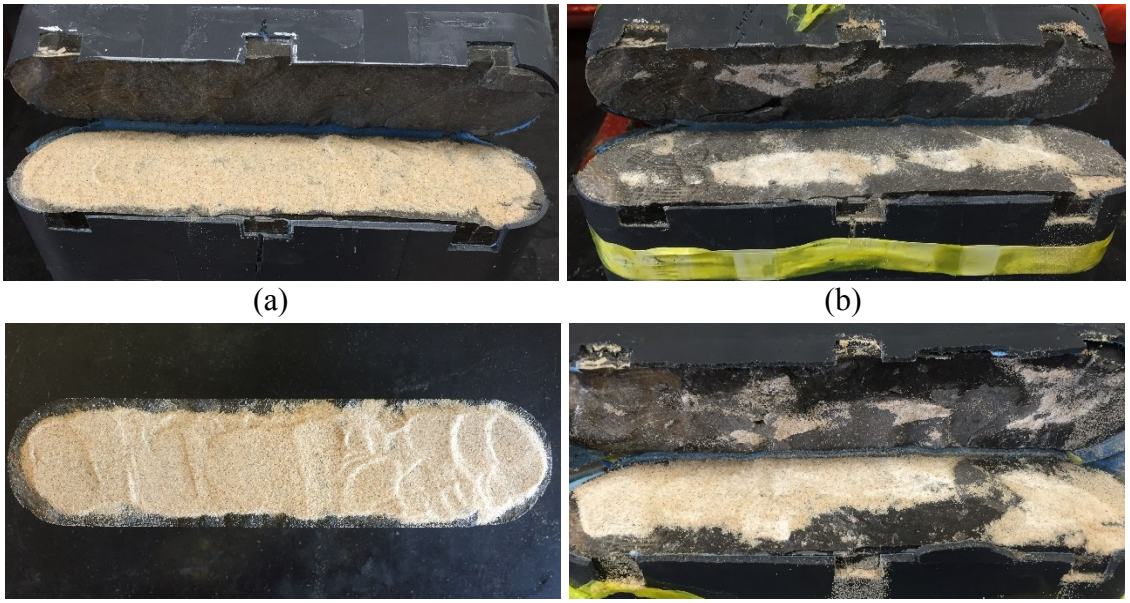

(a) (b)

(c) (d)

Figure 77 – Distribution of Proppant Along Fracture Surface for Fracture Conductivity Test Sample EF-2 (Guerra et al., 2017a): (a),(b) Proppant Loading of 0.2 lbm/ft^2 100-mesh Sand Before Fracture Conductivity Test, and Resulting Proppant Distribution After Fracture Conductivity Test; (c),(d) Proppant Loading of 0.3 lbm/ft^2 100-mesh Sand Before Fracture Conductivity Test (Epoxy Coating Was Reapplied), and Resulting Proppant Distribution After Fracture Conductivity Test.

(a) (b)

Figure 78 – (a) Channeling Observed with HiWAY Flow-Channel Fracturing Technique (Gillard et al. 2010); (b) Naturally Occurring Channeling (Guerra et al., 2017a).

However, the suggestion that the channeling phenomenon from this study was related to the non-smooth fracture surface created during fracturing can only be proved by conducting the same experiments (under same conditions) for test samples with smooth saw-cut fracture surfaces.

The way rock fails enabling the creation of a fracture depends on the stress distribution downhole in the field, and also on the mineralogy distribution of the formation. For whatever the reasons, the fractures created by hydraulic power in the field all have certain degree of unevenness along the fracture face. To understand fracture conductivity behavior, using artificially fractured samples represent an improvement to better emulate the fracture surfaces in the field. For an uneven surface, proppant concentration varied along the fracture surface. Meanwhile, some areas of the fracture surface carried a higher level of stress than others. This non-uniform stress profile along the fracture surface can occur any time the two fracture surfaces do not come in perfect contact with each other. These two features caused by fractured surface topography, uneven proppant distribution and uneven stress distribution, can both enhance fracture conductivity. Hundreds of fracture conductivity experiments were conducted under different test conditions, including by Enriquez (2016), and as summarized and analyzed by Kainer et al. (2017), and others using the same Modified API Fracture Conductivity Cell utilized in this study. All of them used a rough fractured surface instead of a saw-cut smooth surface. Yet, the self-channeling phenomenon was observed in only in a small portion of the tested samples.

The phenomenon may also be related to the concentration and size of proppant. It is more likely to happen when the concentration is low and proppant size is small. In order to compare proppant concentrations, a measurement was performed to estimate the fracture surface covered

by proppant after the conductivity tests for test samples EF-1 and EF-2. Under the same conditions, the difference between test sample EF-1 and EF-2 was that EF-1 used proppant concentrations of 0.1 and 0.2 lbm/ft^2, while EF-2 used 0.2 and 0.3 lbm/ft^2. **Figure 79** shows the proppant coverage as a function of proppant concentration. The proppant concentration of 0.3 lbm/ft^2 had the highest coverage. This can also be observed from **Figure 77d**, compared with **Figure 76b**,**d** and **Figure 77b**. This is of the same concept as partial mono-layer proppant placement, but suggests that it does not have to be a partial mono-layer concentration for partial coverage of proppant to occur. Naturally, the influence the fracture surface characteristics have on fracture conductivity begin to diminish as the proppant concentration reaches a point of governance.

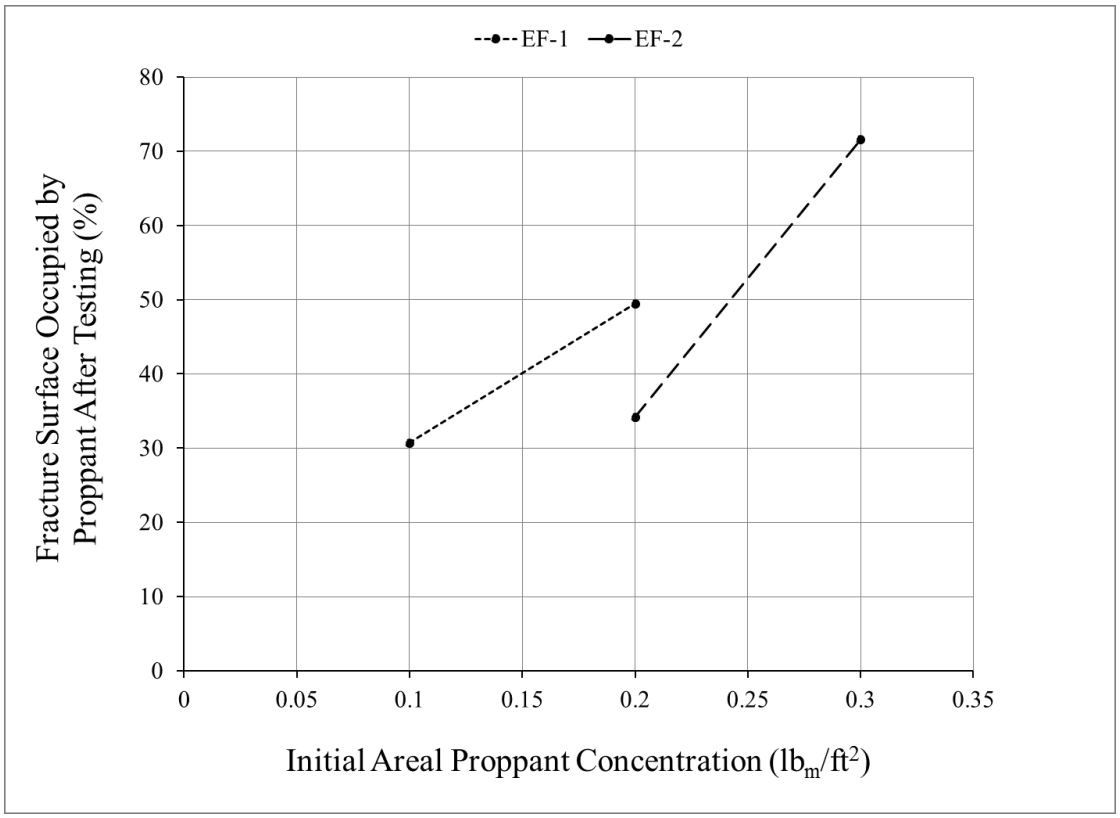

Figure 79 – Proppant Coverage at Different Proppant Concentrations (Adapted from Guerra et al., 2017a).

Proppant size may also be another reason for the self-channeling phenomenon. Smaller proppant has a lower permeability and therefore a lower conductivity in general. But because of the smaller size of the proppant grains, it is easier to rearrange and repack when carried by fluid. This argument supported the fact that the fine-meshed proppant created channels when flowing gas through the fracture cell.

Although there is a benefit with creating a higher conductive channel, it should be noted that the fracture surface is only partially covered with proppant, and hence the load on the proppant is higher than the experimental closure stress prescribed. For example, for test sample EF-2, if only approximately 70% of the surface is covered with proppant for the 0.3 lb/ft^2 test under 6,000 psi closure pressure, the worst case scenario is that the full load of closure is absorbed by the smaller area, causing an actual stress of 8,570 psi. Higher closure can result in proppant crushing and embedment, which should be considered when designing a fracture treatment. For this particular case, the actual closure stress seen by the proppant on the fracture surface exceeded the average strength of 100-mesh sand (approximately 6,000 psi).

The channeling phenomenon described in this study is not a new phenomenon. As mentioned earlier, the phenomenon is aligned with the partial mono-layer placement concept, HiWAY frac, alternate-slug injection, and maybe other approaches used in the field to create highly conductive and sustained fractures. While not adding any additional material to the injection, channeling only happened at low concentrations and small proppant size tests (with relatively high gas flow rates at low closure stresses). This special topic showed that in the case a smaller size proppant with low concentration is selected for the treatment, additional benefits of channeling may add more sustained conductivity than what standard prediction provides.

For baseline fracture conductivity tests, given the ranges and limits of the flowmeter(s) and the pressure transducers, the flow rates required to produce a registerable pressure drop typically needed to be high for propped fractures –especially as the proppant concentration departed from 0.1 lb_m/ft^2. Invariably, low closure stresses are coupled with high flow rates during the testing sequence, enabling possible displacement of proppant if any area of the proppant pack is unrestrained and free to move.

4.9 Water-Induced Fracture Conductivity Impairment

Impairment of fracture conductivity due to a simulated flowback resulted in some loss of unrecoverable fracture conductivity for the Eagle Ford and Marcellus formations, as shown in **Figure 80**. As observed, the loss of fracture conductivity was more severe in the Marcellus formation test samples, with an average of 42.5 % compared to 13.9% for the Eagle Ford formation.

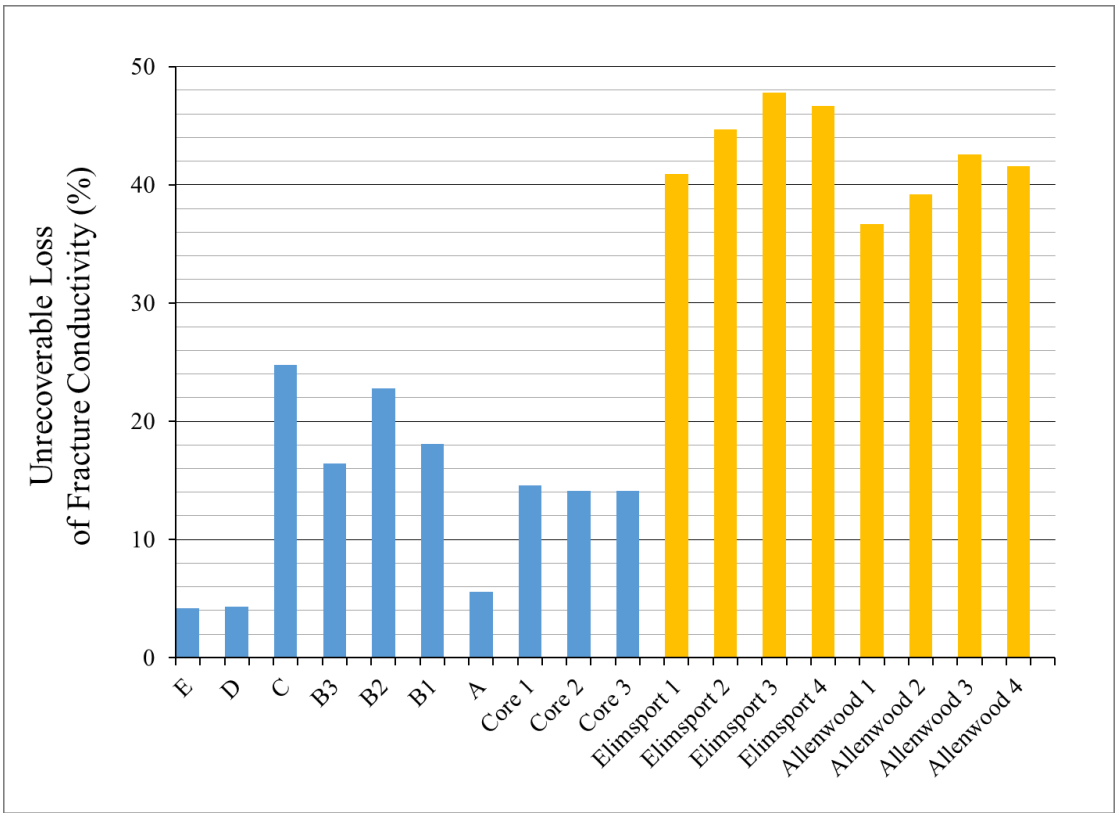

Figure 80 – Comparison of Unrecoverable Percent Loss of Fracture Conductivity for the Eagle Ford Formation and the Marcellus Formation.

The following sub-sections discuss the influence of mineralogy, fluid composition, mechanical properties, and surface attributes.

4.9.1 Effect of Minerology along the Fracture Surface

The unrecoverable percent loss of fracture conductivity for the Eagle Ford formation tests sample (Section 3.2.1) was tabulated alongside the amount of clay present in the test samples in **Table 28**. The total clay was computed by adding all the clay type percentages obtained by XRD. Similarly, the average element intensities obtained by XRF (Section 2.4.5) were used to estimate the element ratio K/Ca, which served as a proxy to the clay distribution along the fracture surface.

Table 28 – Summary of Unrecoverable Percent Loss of Fracture Conductivity for the Eagle Ford Formation Fracture Conductivity Test Samples with Corresponding Total Clay Percentage and K/Ca Clay Proxy (Adapted from Guerra et al., 2018).

Test Sample Name	Unrecoverable Loss of C_f (%) @ 4,000 psi	Total Clay (%) via XRD	K/Ca (-) via XRF
E	4.2	2.56	0.0054
D	4.3	2.71	0.0054
C	24.8	10.09	0.0313
B3	16.4	6.45	0.0194
B2	22.8	13.46	0.0288
B1	18.1	4.40	0.0217
A	5.6	3.46	0.0071
Core 1	14.6		0.0200
Core 2	14.1		0.0185
Core 3	14.1		0.0170

In **Table 28**, the total clay and the K/Ca proxy to clay displayed similar relative differences between the evaluated test samples and their respective percent loss of fracture conductivity. However, the relationship between the unrecoverable percent loss of fracture conductivity and total clay present in the test samples had an R-squared value of 0.74, whereas the relationship with the K/Ca clay proxy yielded an R-squared value 0.99. This suggested that measuring the mineral distribution along the fracture surface provided a more accurate measurement correlation. **Figure 81** shows the relationship of percent loss of fracture conductivity for the Eagle Ford formation with its respective clay distribution along the fracture surface of the test samples. It can be observed that there is a strong direct relationship between

the amount of clay on the fracture surface and the unrecoverable percent loss of conductivity, when exposing the fracture to water flow.

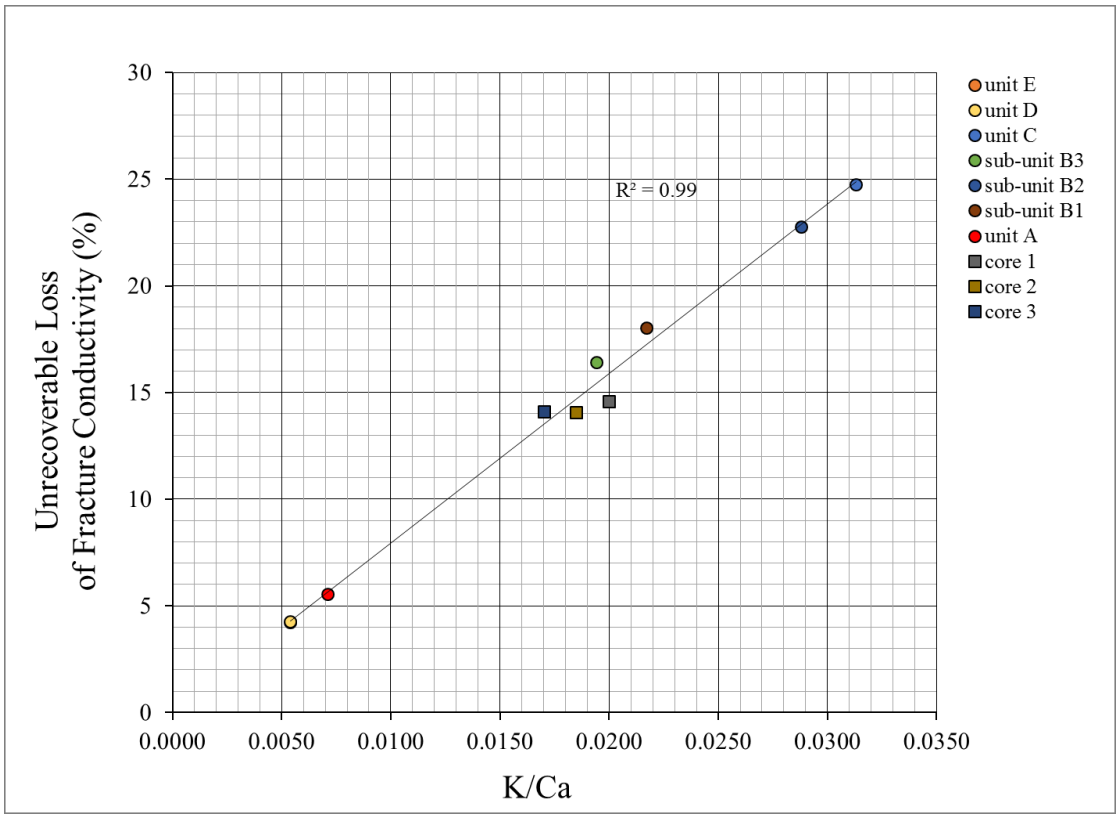

Figure 81 – Eagle Ford Formation Unrecoverable Percent Loss of Fracture Conductivity vs. K/Ca Proxy to Clay (via XRF) (Adapted from Guerra et al., 2017b).

Considering that scanning the fracture surface via XRF was a very time consuming task, an equivalent method that was much easier and accessible was to conduct XRD on a small quantity of material from the core plugs, notwithstanding with a penalty to accurately representing the mineral distribution along the fracture. **Figure 82** shows the relationship of percent loss of fracture conductivity for both the Eagle Ford formation and Marcellus formation test samples to their respective total clay content. It is to be noted that the clay content for the

Marcellus formation was averaged per collection site (individual test sample data was not measured), suggesting the percent clay might be scattered more than displayed in **Figure 82**.

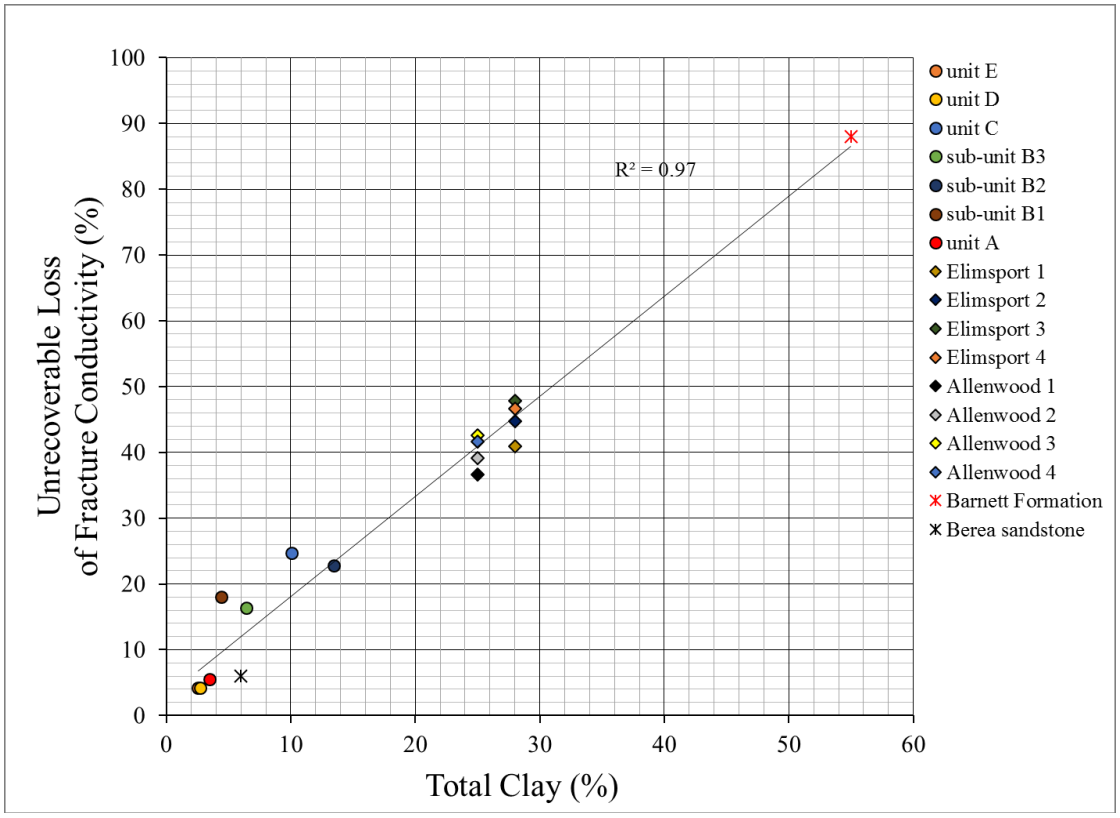

Figure 82 –Unrecoverable Percent Loss of Fracture Conductivity vs. Bulk Clay Content (via XRD) For Three Different Formations (Adapted from Guerra et al., 2017b).

From **Figure 82**, it can be observed that the influence of clay on fracture conductivity is evident for both unconventional formations. This dependency can be extended to include the Barnett formation and Berea sandstone for reference of extreme cases, in which the Berea sandstone with a 6% total clay showed a 6% loss of unrecoverable conductivity in contrast to the Barnett formation with a loss of up to 88% given its substantial clay content of 55%, according to Zhang (2014).

By comparing **Figure 81** and **Figure 82**, with an R-square value of 0.99 and 0.97, respectively, it can be observed that the unrecoverable loss of fracture conductivity has a direct relationship with the amount of clay present in the test samples –although, the K/Ca proxy to clay proved to have the strongest direct relationship. This can be attributed to the fact that the total clay was obtained from spot analysis via XRD on the cross-section of the core plug test samples, whereas the K/Ca ratio was derived from element distribution data gathered via XRF along the entire fracture surface of the fracture conductivity test samples. Ultimately, the fracture surface mineralogy better characterizes the fracture conductivity loss, as opposed to relying on bulk mineralogy.

By fitting a linear trend line to data in **Figure 82**, the resulting equation of the line has the form shown in **Eq. 20**, where $C_{f\_\%loss}$ is the unrecoverable loss of fracture conductivity (%), α is the slope constant (%/%) equal to 1.5192, and ξ is the y-intercept constant (%) equal to 2.938. This equation can be used to predict the fracture conductivity loss of the Eagle Ford and Marcellus formations, and possibly can be extended to apply to other formations based on clay percentage, as supported by **Figure 82**.

$$C_{f\_\%loss} \cong \alpha\left(\%_{clay}\right) + \xi \quad \text{.....} \quad (20)$$

Other factors that might affect fracture conductivity due to water flow through the fracture in the Eagle Ford formation, are the presence of Kaolinite- and Smectite-rich altered ash beds that create fracture conductivity pinch points, which in turn affect the potential well productivity, as reported by Xu et al. (2016). Collecting fracture conductivity test samples that contain the aforementioned ash beds presents difficult challenges in sample handling and subsequent fracture creation. Furthermore, water-rock interactions in the Eagle Ford formation

yields water that has particles with a high tendency for precipitation, which in turn can result in agglomeration of colloids, blocking the fracture aperture, as reported by Ali et al. (2015).

4.9.2 Effect of Fluid Composition

Flowback water compositions are a function of location and time (Horner et al., 2011). Fresher water and a higher chemical load dominate in the early flow, and as production continues, salt concentrations increase to relatively high levels in later flow, as widely stated in literature, including by King (2010). Flowback water flow rate, on the other hand, decreases with time (Slutz et al., 2012). Eventually, a constant flow rate is attained constituted by produced water only.

The reconstituted flowback water chemical composition and resulting TDS concentration utilized in the water-damaging fracture conductivity measurements conducted in this study, experimentally simulated a particular point in time for a particular geological and geographical location in the formation considered. This resulted in relative comparisons between formations, which provide directional findings rather than comprehensive trends that apply through time.

Additionally, even though the Eagle Ford formation reconstituted saline water was 'fresher' than the Marcellus formation reconstituted saline water, the influence of the nearly double the clay content of the Marcellus formation was sufficient to clearly surpass the Eagle Ford formation fracture conductivity impairment due to water damage.

4.9.3 Effect of Poisson's ratio

The Poisson's ratio showed a weak inverse relationship with water-damaged fracture conductivity, as shown in **Figure 83**. This can be attributed to the mid-range level of closure

stress imposed throughout the experiments (4,000 psi), and the clay content being the stronger factor in the fracture conductivity behavior when exposing the fracture to saline water. The Poisson's ratio values were according to fracture conductivity test sample orientation (Z or X90).

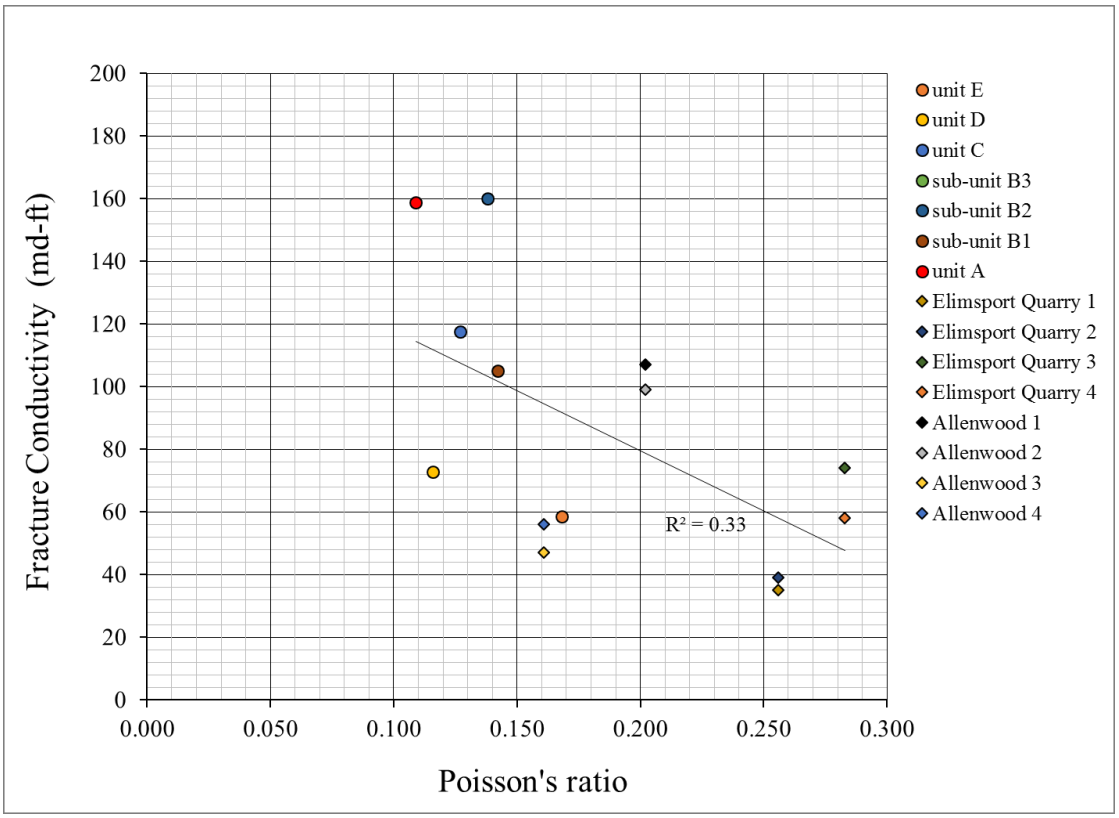

Figure 83 – Eagle Ford and Marcellus Formations Fracture Conductivity Measured by Saline Water Flow vs. Poisson's ratio (Adapted from Guerra et al., 2017b).

4.9.4 Effect of Fracture Surface Attributes

The majority of Eagle Ford formation outcrop rock test samples had a relatively smooth transition from low to high peaks over the fracture surface, resulting in a direct relationship between fracture surface roughness and initial undamaged fracture conductivity at a closure stress of 1,000 psi, as shown in **Figure 84**. All but test sample E exhibited such behavior, possibly due to the fracture surface having the largest maximum height difference within this set

of samples. The downhole core test samples, however, were heavily jagged and segmented along the fracture surface, with several abrupt height changes, which in turn were an artifact of the highly laminated downhole core itself and the subsequent fracture creation. It is possible such abrupt changes in the fracture surface served as pinch points hindering the undamaged fracture conductivity as the closure stress increased to 4,000 psi. Given the aforementioned topography, surface roughness was not observed to have an impact on undamaged fracture conductivity for this sub-set of test samples (these were excluded from **Figure 84**).

The Marcellus formation outcrop test samples also showed a relationship between fracture surface roughness and initial undamaged fracture conductivity at a closure stress of 1,000 psi. The test samples with X orientation (such as Allenwood 3), did not exhibit a clear difference from the surface roughness relationship observed for test samples with Z orientation, as shown in **Figure 84**.

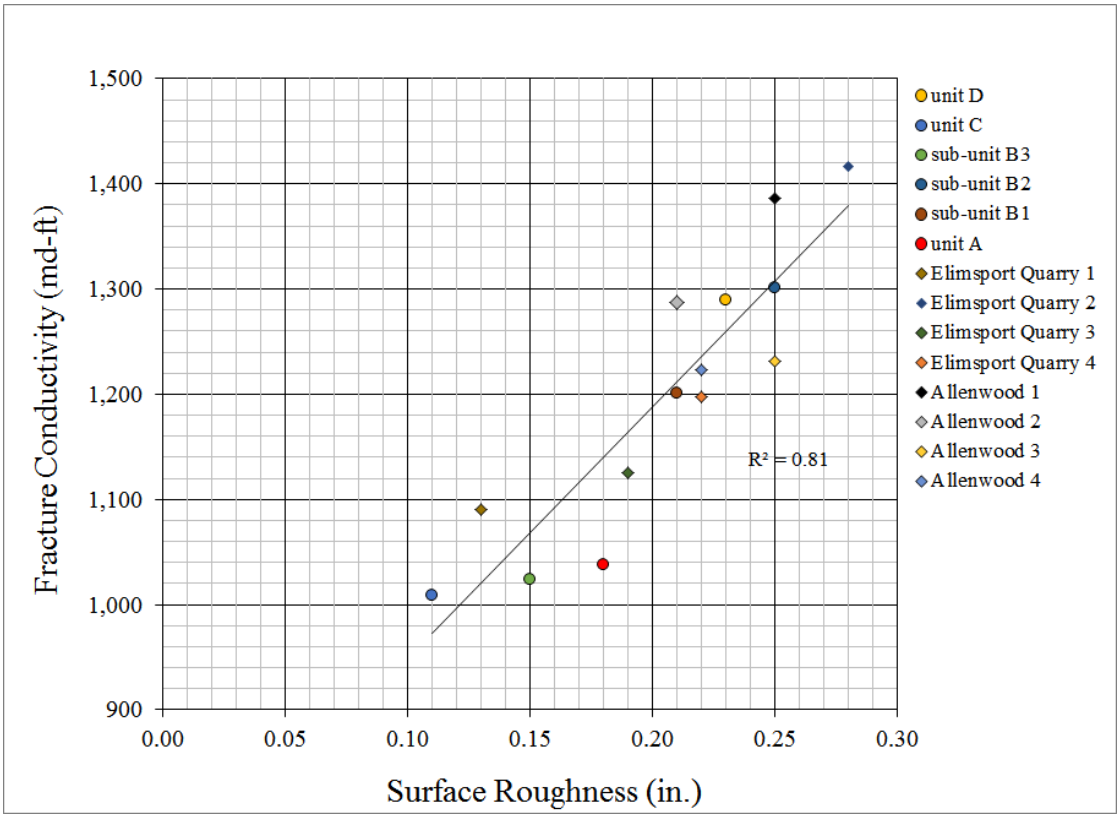

Figure 84 – Eagle Ford and Marcellus Formations Fracture Conductivity Measured by Dry Nitrogen Flow vs. Fracture Surface Roughness (Test Sample E, Core 1, 2, and 3 Were Excluded) (Adapted from Guerra et al., 2017b).

For all water-damaging fracture conductivity test samples, outcrop and downhole alike, the maximum height difference showed an inverse relationship in which lower maximum height difference on the fracture surface resulted in higher undamaged fracture conductivity values at 4,000 psi closure stress, as shown in **Figure 85**.

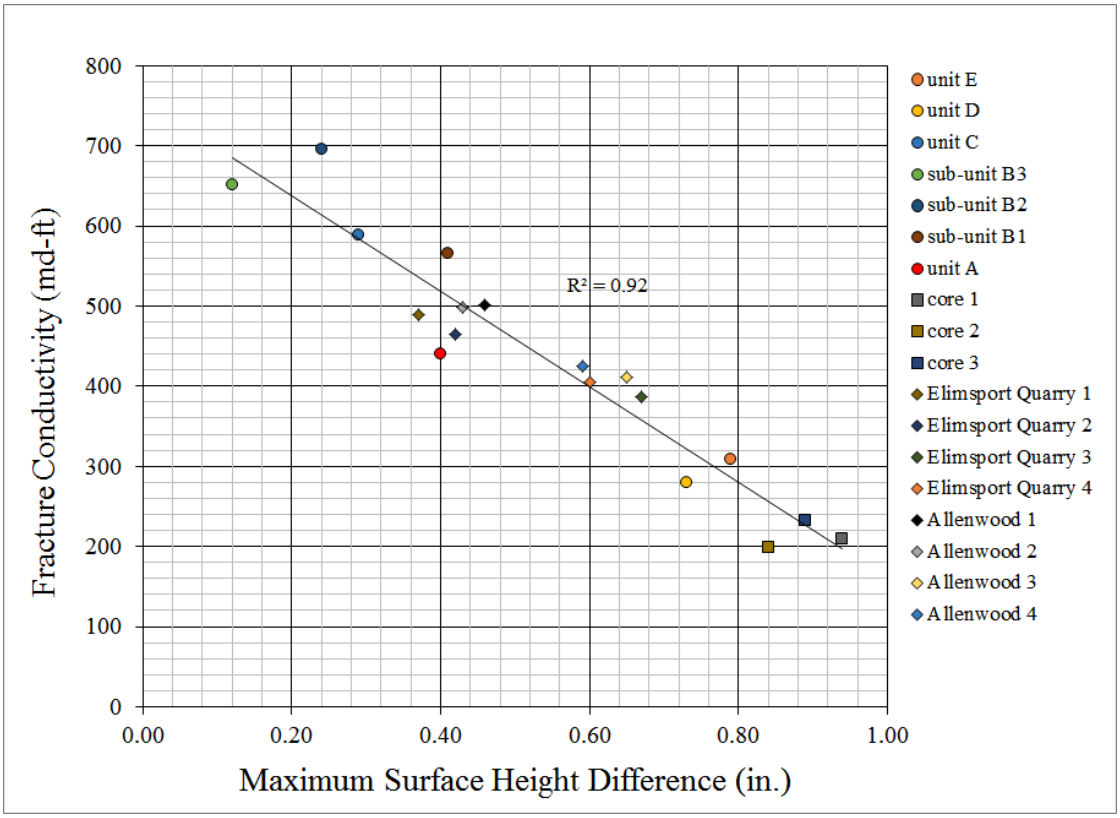

Figure 85 – Eagle Ford and Marcellus Formations Fracture Conductivity Measured by Dry Nitrogen Flow vs. Fracture Surface Maximum Height Difference (Adapted from Guerra et al., 2017b).

4.9.5 A Power Law Correlation

Water-damaging fracture conductivity experiments, summarized in Section 3.3, allowed for the comparison of undamaged fracture conductivity and post-damaged fracture conductivity at a closure stress of 4,000 psi. By contrasting the undamaged fracture conductivity (before saline water exposure) to the recovered fracture conductivity (after water exposure), a power law trend was observed, as shown in **Figure 86** and **Figure 87**, for the Eagle Ford formation and the Marcellus formation, respectively.

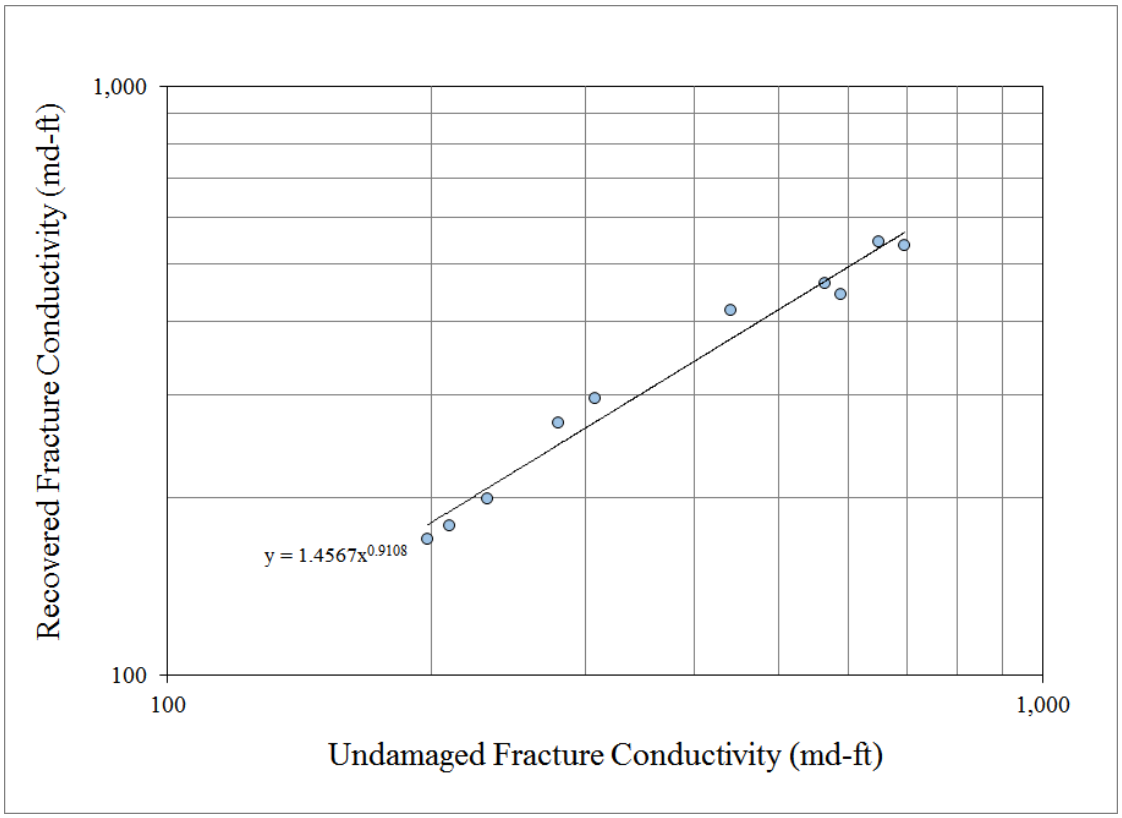

Figure 86 – Eagle Ford Formation Power Law Relationship Between Recovered and Undamaged Fracture Conductivity.

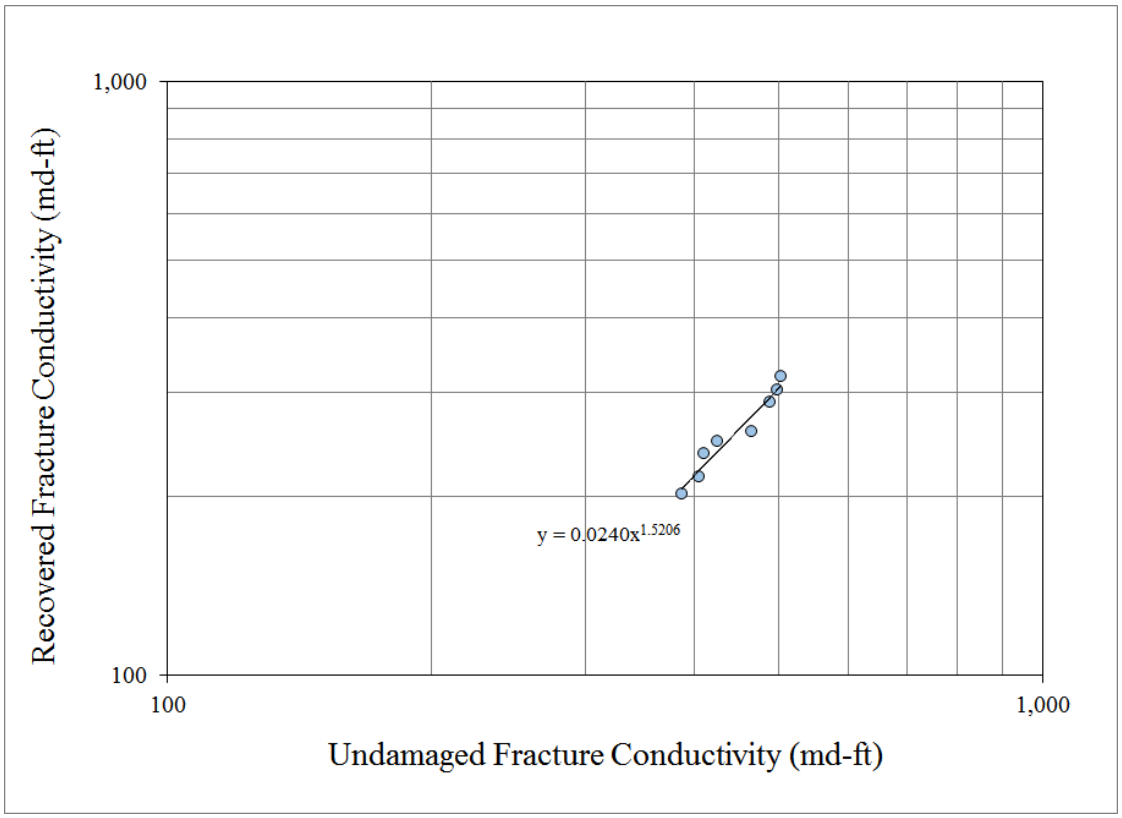

Figure 87 – Marcellus Formation Power Law Relationship Between Recovered and Undamaged Fracture Conductivity.

The relationship expressed in **Eq. 21** and **Eq. 22**, can be utilized to estimate the damaged fracture conductivity for the Eagle Ford formation and the Marcellus formation, respectively. It is to be noted that this relationships are based on experimental data gathered under specific testing conditions as outlined in Chapter 2, including a specific saline water chemical composition.

$$C_{f_damaged_EF} = 1.4567\left(C_{f_undamaged}\right)^{0.9108} \quad \ldots\ldots\ldots\

Earlier studies by Zhang et al. (2015) showed the existence of a power law correlation for the Barnett shale, expressed in **Eq. 23**, albeit with different empirical coefficients than **Eq. 21** and **Eq. 22**, given that in this study different formations were utilized to develop them.

$$C_{f\_damaged\_Barnett} = 0.0185\left(C_{f\_undamaged}\right)^{1.5168} \quad \ldots\ldots\ldots\ldots\ldots\ldots\ldots\ldots\ldots\ldots (23)$$

4.10 Load Hysteresis and Procedural Consistency

Procedural consistency and properly calibrating the test apparatus greatly reduced common sources of error (such as cell leakage, inconsistent proppant loading, etc.) under the given simulated environment, and drastically improved repeatability. However, given that no sample had the same exact fracture surface, results did inherently deviate from each other to some extent. The results presented in this study represent selected test runs where no common sources of error were detected during preparation, testing, and data analysis. Furthermore, given that all test samples underwent the same handling, testing, and analysis, the results were deemed accurate and devoid of factors that may adversely affect the relative comparison of fracture conductivity across the formations considered.

Load hysteresis at high closure stresses may occur due to matrix compaction and crushing of the fracture surface asperity, which if present would contribute to the overall impairment of fracture conductivity.

Sample integrity degradation usually involved test sample failure exhibited through the creation of fractures transverse to the flow direction, as shown in **Figure 88**, and/or rock crumbling. This was seldom observed, and occurred only when the test sample was reused

excessively for multiple fracture conductivity tests, or when the closure stress was considerably high (7,000 psi and above).

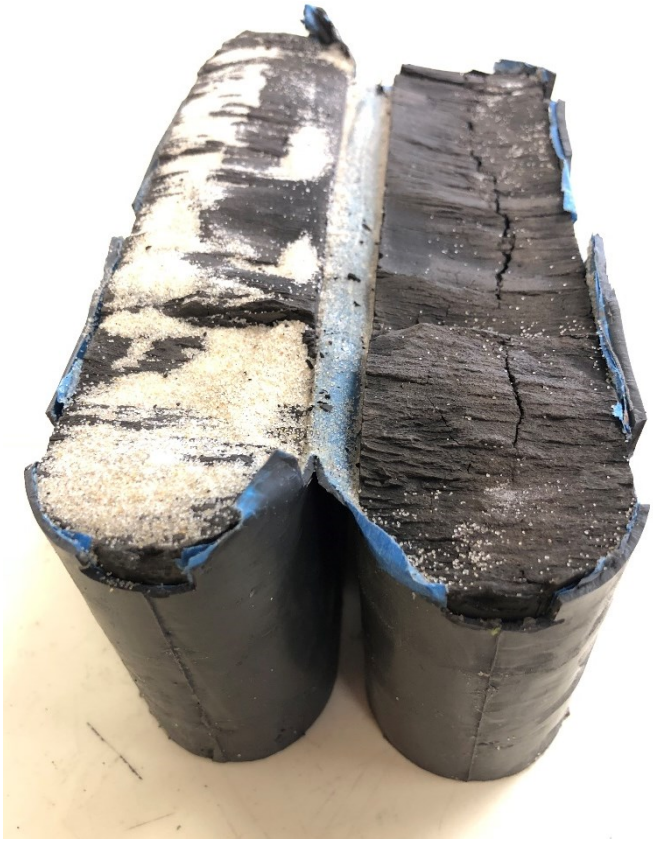

Figure 88 – Sample Integrity Degradation Through the Creation of Fractures Transverse to the Flow Direction.

5. A PRACTICAL APPLICATION TO FRACTURE CONDUCTIVITY

5.1 Introduction

This chapter presents the development of a practical workflow that translates the measured fracture conductivity behavior to downhole stress conditions. The Eagle Ford formation was used as a case study, with assumed parameters based on typical values and the latest known completion designs in that play.

The fracture conductivity behavior can be represented by an exponential decline rate function based on experimental measurements (Section 4.1). Reinforcing this notion, it should be noted that these empirically derived functions capture both the proppant behavior as well as the influence of the formation. In the absence of fracture conductivity measurements for varying proppant loadings, these measurement-based functions for lower proppant concentrations can be used to estimate the fracture conductivity behavior at higher proppant loadings for the same formation (albeit actual test data for those higher proppant loadings would be preferred). This content is presented in Section 5.2, 5.3.

These measurement-based and estimated fracture conductivity decline functions were then formulated as a function of time. Given a set of well and reservoir parameters, the effective closure stress in the reservoir was calculated based on poroelasticity theory, and subsequently the stress on the proppant was calculated (based on a particular drawdown). This content is presented in Section 5.4.

Based on the fracture conductivity decline functions (Section 5.3), the fracture conductivity accounting for the stress on the proppant was stated as a function of time (section 5.5). By this, the conductivity values measured in the laboratory were placed in the reservoir

setting by relating the known behavior to that of other stress conditions. This new perspective is an improvement over the normal procedure of simply relying on a standard ISO fracture conductivity test value in the design process, by also capturing the change in fracture conductivity as the simulated drawdown occurs.

The performance of a hydraulically fractured horizontal well is discussed in Section 5.6. Conclusions are drawn based on observations made during said discussion.

Section 5.7 includes a discussion on the reality of overestimated experimentally obtained fracture conductivity values, and how this might affect the simplified workflow described herein. A summary is included in Section 5.8.

5.2 Fracture Conductivity Decline Functions

Any baseline fracture conductivity measurement (Chapter 3) can be represented as a linear relationship on a semi-log plot. This exponential decline rate closely represents the fracture conductivity behavior with the form (duplicate of **Eq. 9**):

$$C_f \cong C_{f0} e^{-\lambda \sigma_c} \quad \ldots\ldots\ldots\

lb_m/ft^2 proppant loadings (0.2 lb_m/ft^2 is plotted to illustrate the aforementioned behavior, but is not included in the following sections).

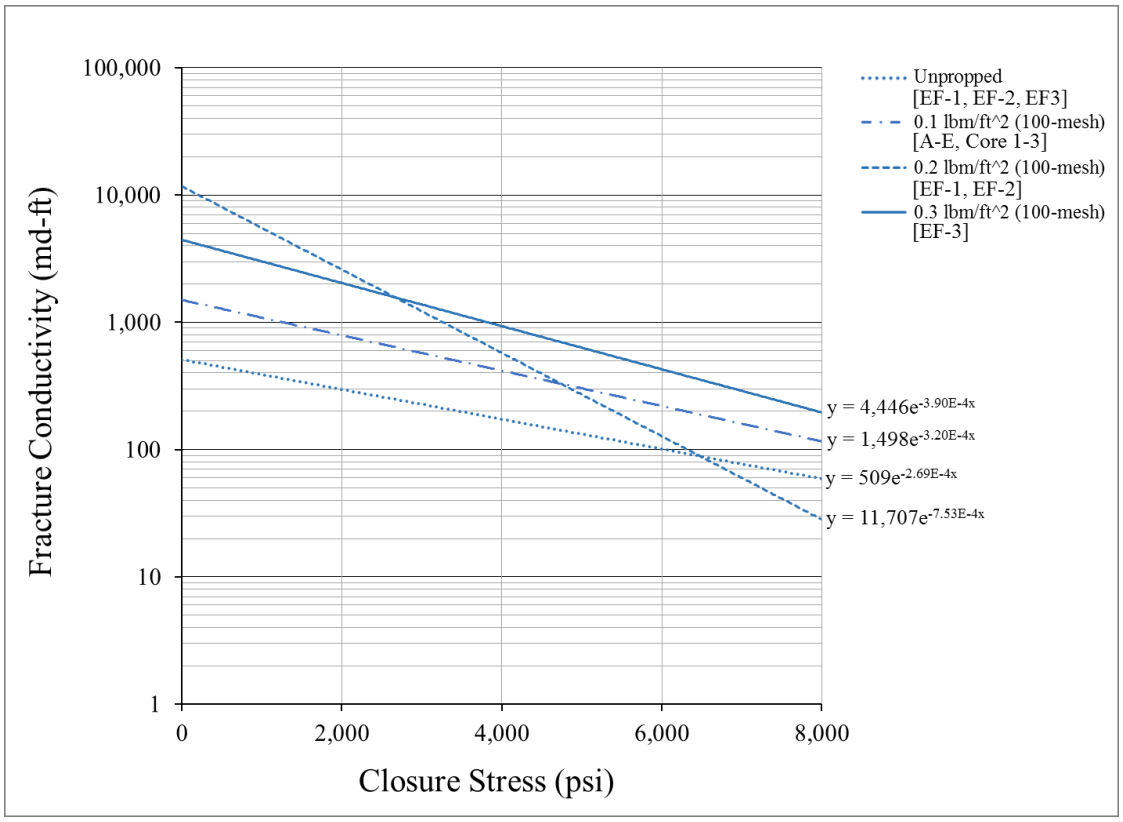

Figure 89 – Eagle Ford Formation Fracture Conductivity Exponential Decline Functions.

5.3 Building Additional Fracture Conductivity Decline Functions

In order to extend **Figure 89** to include additional proppant areal concentrations beyond 0.3 lb_m/ft^2 (given that there were no measurements conducted for those concentrations), it was assumed that when the proppant pack had greater than 3 layers of proppant, the permeability of the proppant pack would not change initially since it was not under load. This suggested that the measurement-based 0.3 lb_m/ft^2 curve (**Figure 89**) could be used to estimate fracture conductivity curves for higher proppant loadings, since that proppant loading had a calculated theoretical

width of 0.0355 in. with 5.98 proppant layers of 100-mesh sand proppant (Section 4.3.2); and the initial conductivity can be obtained from the exponential decline function shown in **Figure 89**. Therefore, the proppant permeability was estimated by **Eq. 25**, although yielded an extremely large and unrealistic permeability value (1.5E6 md). Given the nature of the fracture conductivity tests, the permeability being calculated is in fact the fracture permeability, hence the width used in **Eq. 25** is not entirely representative of the actual width (dependent not only on the proppant pack but also on the fracture surface asperities). Based on load piston displacement data, a total displacement of 0.0862 in. was recorded for test sample EF-3 with 0.3 lb_m/ft^2 proppant loading; which in turn can be used as an estimate for the actual fracture width, as shown in **Eq. 26**, which resulted in a more reasonable permeability value (618,786 md). Based on this, the fracture permeability is significantly larger than the theoretical proppant pack permeability, since the fracture surface attributes contribute to both width and permeability of the fracture (especially true in cases with uneven proppant loading, rock debris, and shear displaced fractures).

$$k_p = \frac{C_f}{w_f} = \frac{C_{f0}}{w_f} = \frac{4{,}446 \text{ md} - \text{ft}}{(0.0355 \text{ in.})\frac{1 \text{ ft}}{12 \text{ in.}}} = 1.5\text{E}6 \text{ md} \quad \text{..... (25)}$$

$$k_f = \frac{C_f}{w_f} = \frac{C_{f0}}{w_f} = \frac{4{,}446 \text{ md} - \text{ft}}{(0.0862 \text{ in.})\frac{1 \text{ ft}}{12 \text{ in.}}} = 618{,}786 \text{ md} \quad \text{..... (26)}$$

Accurately decoupling fracture conductivity into fracture permeability and fracture width is a nontrivial problem. For the purposes of this workflow, the value of $k_f = 618{,}786$ md was used. In order to predict the initial fracture conductivities for larger proppant concentrations, the estimated fracture permeability was used with the appropriate theoretical width (Section 4.3.2) for the proppant loading considered, while assuming that every successive increment of proppant

loading added to the known (measured) fracture width of 0.0862 in. at the 0.3 lb_m/ft^2 proppant loading. As such, the predicted initial fracture conductivity for a proppant loading of 0.4 lb_m/ft^2 was calculated as shown in **Eq. 27**.

$$C_{f_{0\_predicted}(0.3+0.1)^{lb_m}/_{ft^2}} = k_f w_f \quad \text{..... (27)}$$

$$= (618{,}786 \text{ md})(0.0862 \text{ in.} + 0.0118 \text{ in.}) \frac{1 \text{ ft}}{12 \text{ in.}}$$

$$C_{f_{0\_predicted}(0.3+0.1)^{lb_m}/_{ft^2}} = 5{,}053.42 \text{ md} - \text{ft}$$

This process was repeated for 0.5, 0.6, 0.7, and 0.8 lb_m/ft^2 proppant loadings. These predicted initial conductivities were then inserted into the original exponential decline function (assuming the decline rate remains constant with the increase of areal proppant concentration). The resulting fracture conductivity decline functions, measured-based and predicted, as a function of an arbitrary range of closure stress –set from 0 to 8,000 psi, are shown in **Figure 90**.

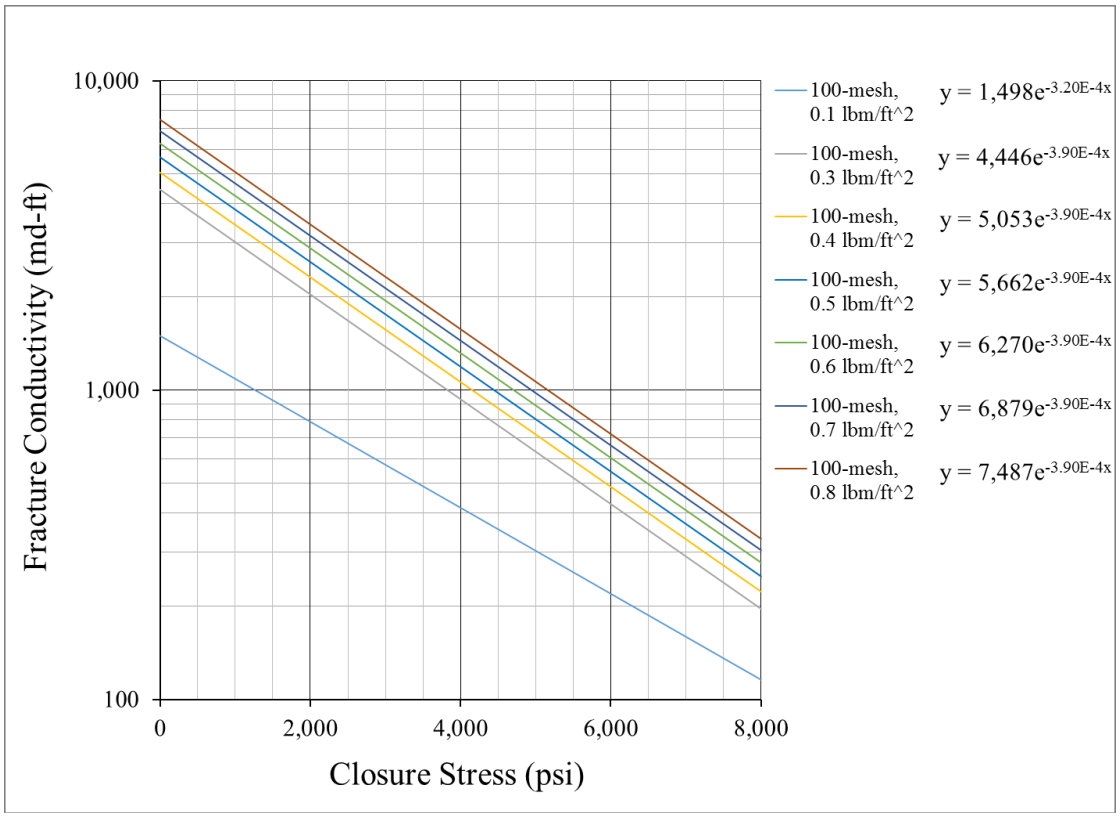

Figure 90 – Eagle Ford Formation Fracture Conductivity Exponential Decline Functions (Measured-Based and Predicted).

5.4 Stress of the Proppant Pack as a Function of Time

In order to predict fracture conductivity as a function of time, the effective fracture closure stress in the reservoir, and subsequently the stress on the proppant were estimated through time.

The closure stress downhole (σ_{cl}) was predicted by **Eq. 28**, where v is the Poisson's ratio, σ_v is the overburden stress, $\overline{P_{res}}(t)$ is the average reservoir pressure as a function of time, γ is the Biot's constant (assumed to be 0.7), E is the Young's modulus, $\epsilon_{tectonic}$ is the tectonic strain, α is a coefficient of thermal expansion, and ΔT is the change in temperature in the reservoir.

$$\sigma_{cl} = \frac{v}{1-v}\left(\sigma_v - \gamma\overline{P_{res}}(t)\right) + \gamma\overline{P_{res}}(t) \pm E\epsilon_{tectonic} + \alpha\Delta T \quad \ldots\ldots\ldots\ldots\ldots (28)$$

The relationship presented (**Eq. 28)** is a modification from that presented by Montgomery (2017), and can be used to estimate the stress on the proppant with **Eq. 29**, where P_{wf} is the bottomhole flowing pressure, and $\Delta\sigma_{width}$ is the incremental stress as a result of the strain in the reservoir rock to create the fracture aperture (**Eq. 30)**.

$$\sigma'_{Prop} = \sigma_{cl} + \Delta\sigma_{width} - P_{wf} \quad \ldots\ldots\ldots\ldots\ldots\ldots\ldots\ldots\ldots\ldots\ldots\ldots\ldots\ldots\ldots\ldots (29)$$

$$\Delta\sigma_{width} = \frac{2Ew_{prop}}{\pi H(1-v^2)} \quad \ldots\ldots\ldots\ldots\ldots\ldots\ldots\ldots\ldots\ldots\ldots\ldots\ldots\ldots\ldots\ldots (30)$$

Eq. 28 was used to develop the variation of closure stress downhole (σ_{cl}) through time (t), as shown in **Figure 91**. For this case example, a constant drawdown of 1,000 psi was assumed, where the initial reservoir pressure ($P_{res}(t=0)$) was set to 4,330 psi (an estimate based on a formation depth of 10,000 ft and a pore pressure gradient of 0.433 psi/ft). Furthermore, another simplification was to assume that $\overline{P_{res}}(t)$ decreased linearly 3,000 psi over a 24 month period, inevitably resulting in straight curve variations for the ensuing closure stress and stress on the proppant pack through time (this would not be linear if the variation in $\overline{P_{res}}(t)$ was not assumed to be linear). The overburden stress gradient was assumed to be 1 psi/ft, resulting in 10,000 psi overburden stress at formation depth. Representative Eagle Ford formation values for Young's modulus and Poisson's ratio were used, 3.5E6 psi and 0.163, respectively.

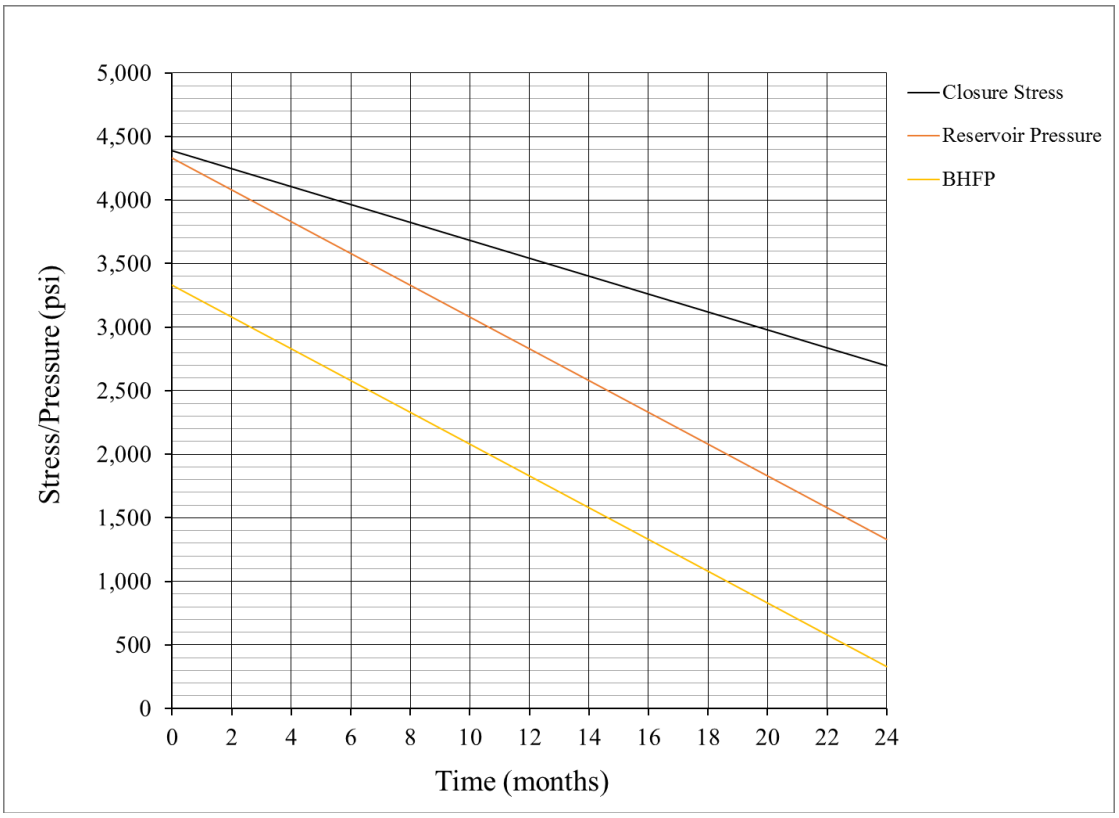

Figure 91 – Forecast Fracture Closure Stress, Reservoir Pressure, and Bottom Hole Flowing Pressure.

For the proppant concentrations considered (**Figure 90)**, the resulting proppant width (w_{prop}) was calculated to be 0.0862 in. plus 0.0118 in. for each increment of 0.1 lb_m/ft^2 proppant loading (as done in Section 5.3), such that for 0.4 lb_m/ft^2 the proppant width was 0.098 in. and for 0.5 lb_m/ft^2 the width was 0.1098 in; for the 0.1 lb_m/ft^2 proppant loading, the estimated proppant width was 0.0354 in. measured from the load piston displacement plus 0.0118 in. The complete set of proppant loading widths and the incremental stress as a result of the strain in the reservoir rock to create the fracture aperture ($\Delta\,\sigma_{width}$) (**Eq. 30**) are shown in **Figure 92**.

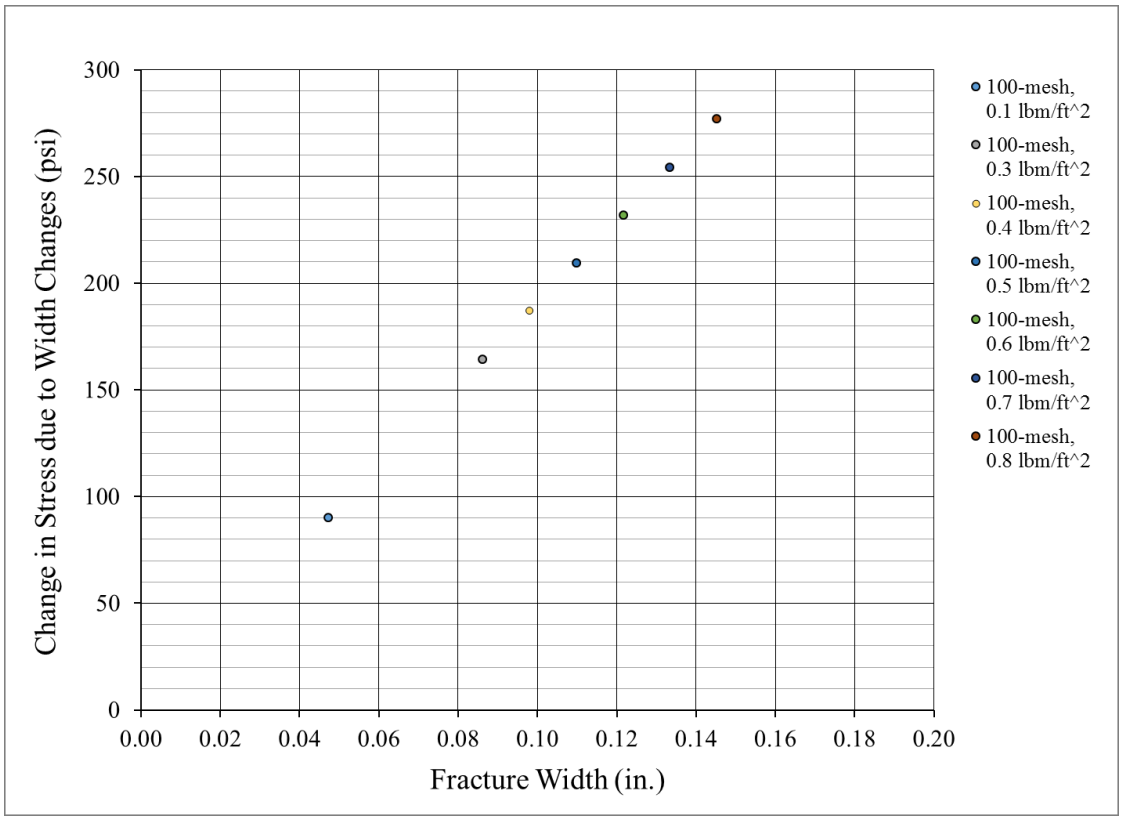

Figure 92 – Stress Change due to Fracture Width Reduction as a Function of Fracture Width.

The height of the fracture was assumed to be 100 ft. Accounting for the previous developments, the stress on the proppant pack (σ'_{Prop}) (**Eq. 29**) as a function of time is shown in **Figure 93**; accounting for the proppant concentrations considered in this case study.

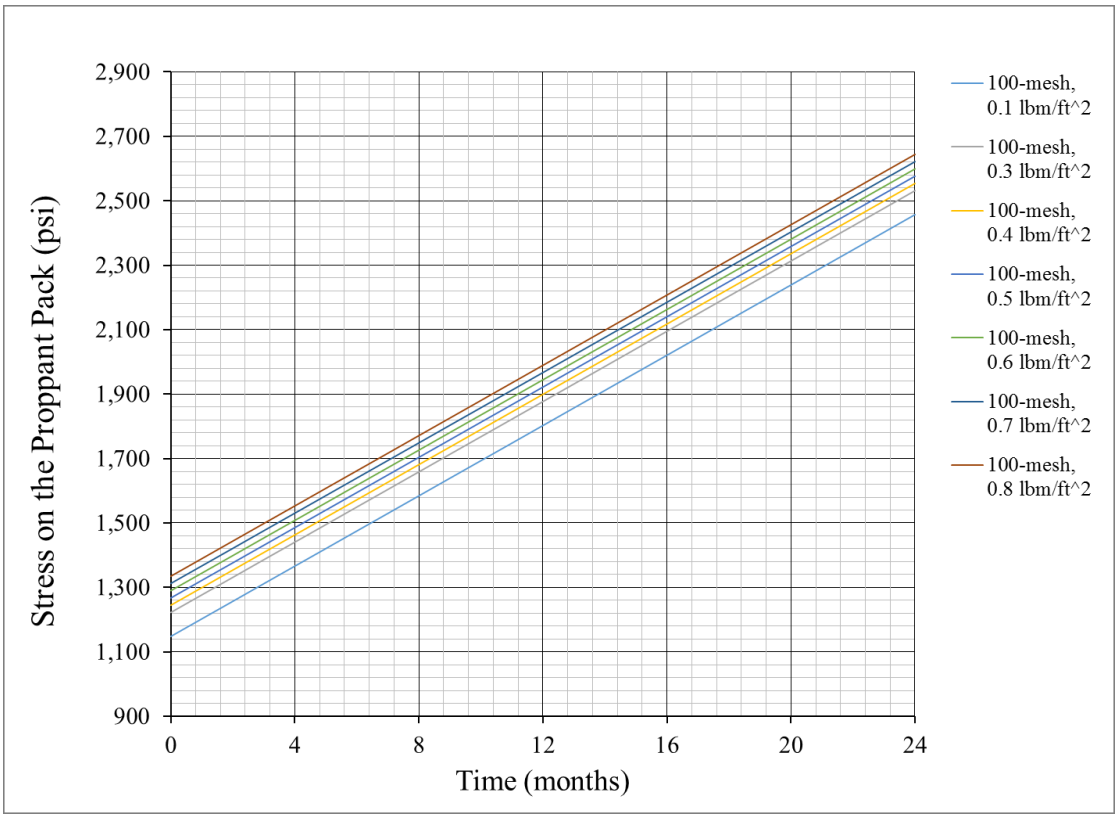

Figure 93 – Stress on the Proppant Pack as a Function of Time.

5.5 Fracture Conductivity as a Function of Time

By taking the fracture conductivity decline functions, measured-based and predicted (**Figure 90)** as a function of the stress on the proppant pack for each proppant loading (**Figure 93)**, the updated fracture conductivity behavior as function of time was obtained, as shown in **Figure 94**.

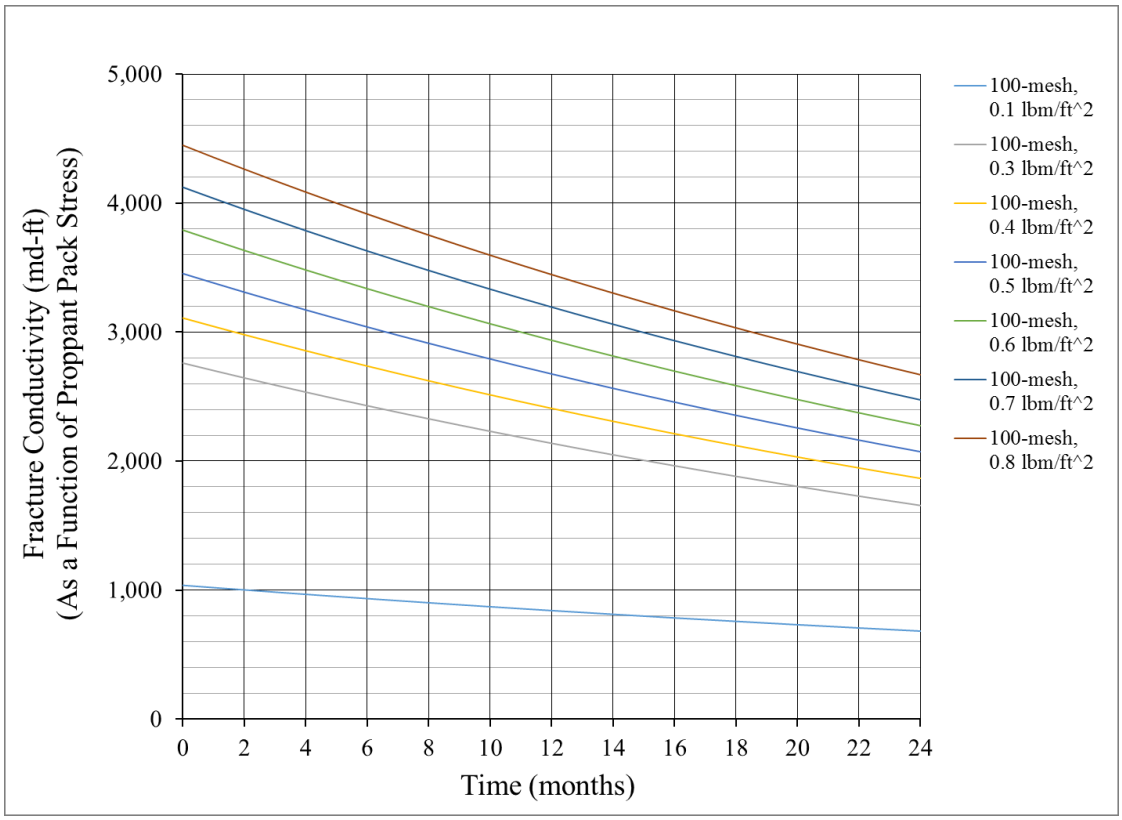

Figure 94 – Fracture Conductivity as a Function of Time.

For the same change in permeability of a proppant pack, the fracture conductivity declined the greatest for the concentration that had the largest aperture, as seen in **Figure 94** by comparing 0.1 to 0.8 lb_m/ft^2 proppant loadings (a small change in permeability times a relatively large fracture width results in a more pronounced decline).

5.6 Performance of a Hydraulically Fractured Horizontal Well

As stated in Section 1.2.14, for these low permeability reservoirs, the flow of a multistage fractured horizontal well during the majority of the productive life can be best modeled as transient linear flow from the matrix into the fracture system, according to work by Bello and Wattenbarger (2010).

For linear fractures, there are several semi-analytical models developed to describe the flow rate as a function of pressure drawdown (Bello, 2009). Because of the inherent complexity, most of these models assume infinite fracture conductivity.

In the work by Bello and Wattenbarger (2010), an analytical model with five different flow periods for a multistage fractured horizontal well was presented. A slab matrix dual porosity model for a linear reservoir was employed, in which, the horizontal well drains a rectangular geometry containing an array of fractures spaced by matrix blocks, as shown in **Figure 95**. The flow periods consisted of early transient linear flow in the fracture system, bilinear flow resulting from simultaneous transient flow in the fracture system and matrix, infinite-acting reservoir response, transient linear flow from the matrix into the fracture system, and when the reservoir boundary begins to influence the transient response.

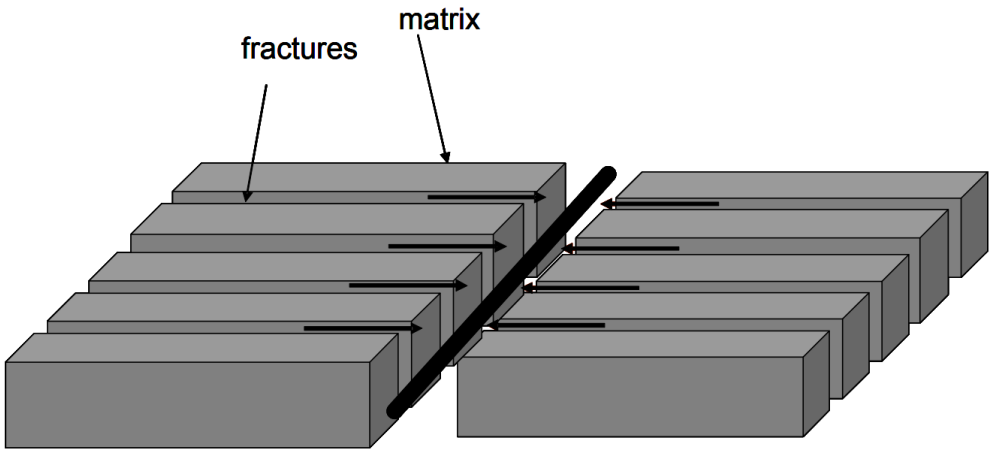

Figure 95 – Schematic of Slab Matrix Linear Model of a Hydraulically Fractured Horizontal Well (Bello and Wattenbarger, 2010).

The model was validated by Bello (2009), and shown to compare closely to results obtained with Fekete and ECLIPSE, with transient linear flow from the matrix into the fracture system believed to be representative of actual long-term field production.

Bello (2009) derived the matrix-dominated linear flow equation under transient flow condition based on the Laplace space solution presented by El-Bandi (1998) for a constant p_{wf} inner boundary, closed outer boundary reservoir (slab matrix), as shown in a simplified form herein in **Eq. 31**. It is to be noted that low permeability formations are typically produced with bottomhole pressure held relatively constant (Economides et al. 2013).

$$q_{DL} = \frac{1}{k_f}(2x_e h)^{\frac{3}{4}} \frac{1}{\pi\sqrt{\pi \frac{0.00633t}{(\phi\mu c_t)}}} \sqrt{\frac{k_m}{L^2} y_e} \quad \text{.....} \quad (31)$$

$$q_g = \frac{k_f \sqrt{A_{cw}}\left(p_i^2 - p_{wf}^2\right)}{1424 T \mu Z} q_{DL}$$

It can be observed in **Eq. 31** that the permeability of the fracture cancels out, reflective of the assumption that the flow is governed by the matrix.

Based on the previous discussions, and considering the fracture conductivity values obtained in this study under laboratory conditions, it appears that given the proppant loadings considered, a higher than needed fracture conductivity is obtained.

5.7 Reduction in Fracture Conductivity to Account for In-Situ Conditions

In an effort to acknowledge that the measured fracture conductivity values that served as the foundation for these derivations, are normally expected to be lower in account of damage mechanisms that were outlined in Section 1.2.4 (including matters such as fines migration and

multiphase flow), a correction factor can be applied. For instance, some software platforms account for this matter by estimating that a gas-based measurement roughly yields quadruple the realistic value; and if it were to be considered as such, taking this findings and reducing the original fracture conductivity values shown in **Figure 94** by 75%, the following plot is obtained (**Figure 96)**.

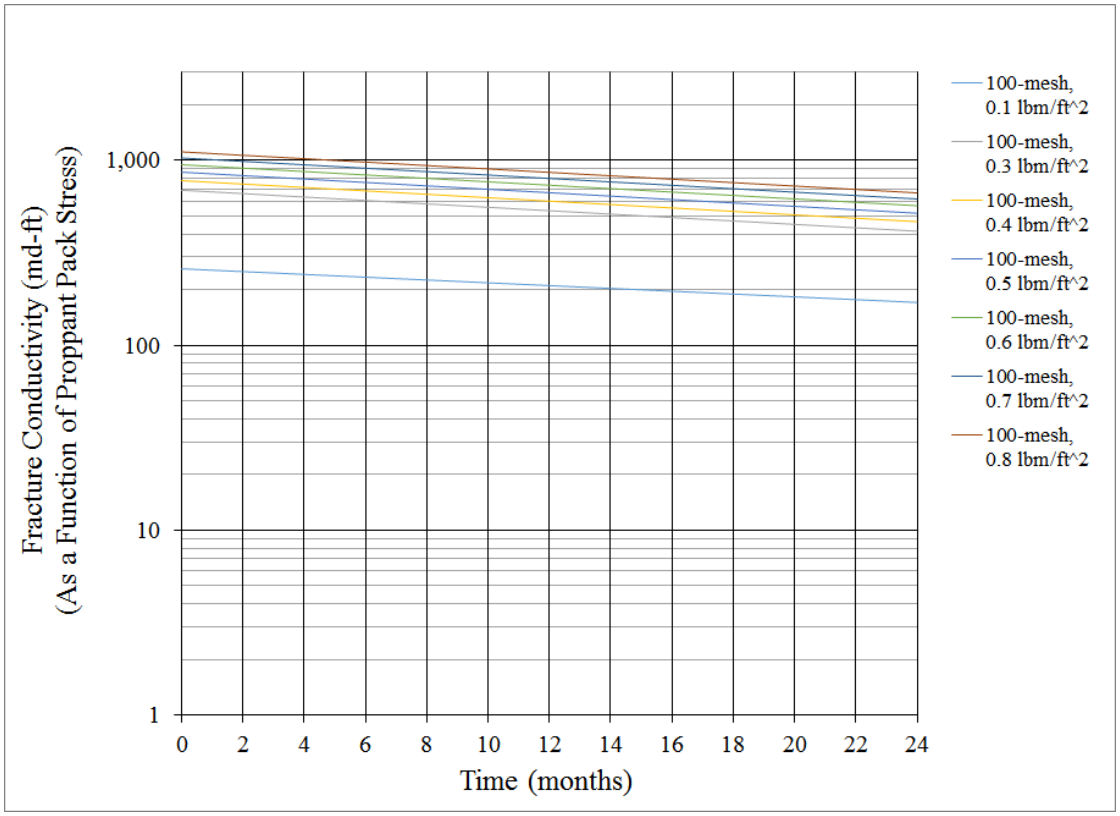

Figure 96 – Fracture Conductivity as a Function of Time (Reduced 75%).

Similarly, according to Palisch et al. (2010), fracture conductivity values can be as low as 2% of the API-based measurements; by assuming these findings as applicable, the fracture conductivity values shown in **Figure 94** were reduced by 98%, as shown in **Figure 97**.

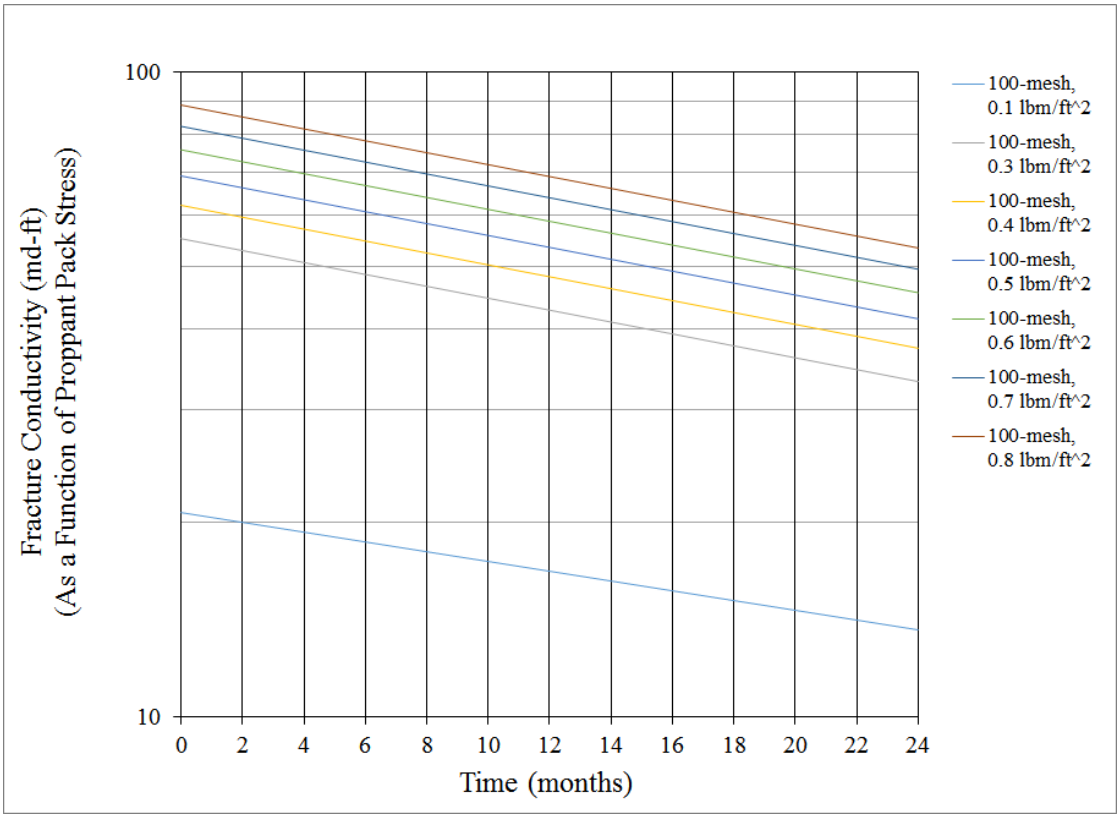

Figure 97 – Fracture Conductivity as a Function of Time (Reduced 98%).

Despite the significant reduction of fracture conductivity, these values are still orders of magnitude greater than the matrix permeability.

5.8 Summary

Baseline fracture conductivities represent an upper bound, signifying that the in-situ behavior is certainly lower than that measured. The presented workflow allows for laboratory measurements of fracture conductivity behavior to be represented as functions that can then be translated into the reservoir setting by utilizing poroelasticity theory, and ultimately expressed as a function of time. The fracture conductivity functions represent not only the influence of proppant loading, but also capture the influence of the formation rock properties and the surface

asperities of the fracture surface. This process can be repeated for other formations and proppant types, given available fracture conductivity data.

6. CONCLUSIONS AND RECOMMENDATIONS

6.2 Conclusions

Further studies are recommended to extend the scope and findings of this work. This study was undertaken under the premise that fracture conductivity is directly linked to hydraulic fracture deliverability, which in turn plays a significant role in well productivity. Henceforth, measuring and investigating what influences fracture conductivity is paramount.

This work represented a comprehensive, systematic, and comparative study on fracture conductivity of mudstone formations and its dependence on rock mechanical properties, minerology, and fracture surface attributes. Fracture conductivity measurements simulated undamaged and damaged fracture conditions, predicated on whether dry nitrogen or saline water was flowed. This included unpropped and propped fracture conditions. Special observations related to proppant pack self-channeling were also presented. Five mudstone formations were considered, namely the Eagle Ford, the Marcellus, the Mahantango, the Middle Bakken, and the Three Forks.

Additionally, a practical workflow was developed to relate the measured fracture conductivity behavior to downhole stress conditions, which can provide a more realistic estimate of fracture conductivity values during the fracture treatment design process, in order to improve well productivity.

Under the aims of the study, and within the context and boundaries of the statistical significance and limitations of this work, the following conclusions can be made.

A practical workflow for relating experimental fracture conductivity measurements to downhole conditions in terms of time, and ultimately to productivity,

1. It appears that given the proppant loadings considered, a higher than needed fracture conductivity is obtained, given that for most of the productive life of the well, the flow will be matrix-dominated. This is suggestive of achieving the same productivity with less proppant concentration and/or unpropped fractures.
2. Developing exponential decline functions based on averaged data showed to represent the laboratory measured fracture conductivity behavior.
3. The predicted fracture conductivity can be related to downhole conditions by accounting for the closure stress in the reservoir and subsequently the stress on the proppant.

Unpropped undamaged fracture conductivity behavior,

4. Surface roughness showed some direct influence on fracture conductivity, especially to initial values at low closure stresses.
5. The maximum height difference across the fracture showed a weak direct relationship with the fracture conductivity decline rate.
6. Downhole core usually had a higher value of height difference across the sample fracture.
7. Poisson's ratio is expected to have a direct relationship with fracture conductivity decline. This was observed in some of the data considered.

Propped undamaged fracture conductivity behavior,

8. Closure stress and proppant concentration dictated fracture conductivity values. Mechanical properties also contribute to fracture conductivity decline, albeit not always apparent.

9. Brinell Hardness Number is expected to have an inverse relationship with fracture conductivity decline. This was not readily observed in the data considered.

Mechanical properties, mineralogy, and bedding plane orientation,

10. The majority of Eagle Ford, Marcellus, Middle Bakken, and Three Forks formation test samples were categorized as brittle, with a relatively low Poisson's ratio and a moderately high Young's modulus.
11. A weak trend was observed between carbonate content and the Young's modulus for the aforementioned test samples.
12. The influence of bedding plane orientation with respect to the test samples, proved difficult to discern given the scatter in each respective formation data set.

Water-damaging fracture conductivity behavior under simulated flowback,

13. A direct relationship between clay content and the unrecoverable fracture conductivity loss after water exposure was observed.
14. The observed range in fracture conductivity loss due to water damage was approximately 4 to 25% for the Eagle Ford shale, and approximately 36 to 48% for the Marcellus shale. With the conductivity loss of up to 88% in Barnett shale, it is concluded that clay content of the rock is a key factor for fracture conductivity loss by water damage in shale formations. For the Eagle Ford shale, the range of loss of fracture conductivity is relative low when compared to other shale plays that have a higher clay content. This suggests that fracture conductivity loss due to water damage on the fracture surface might not be a

major factor in causing the large early decline rates observed in most Eagle Ford shale producing wells.

15. The aforementioned was confirmed with XRD and XRF measurements on the core plug cross-section and on the fracture surface, respectively.
16. Fracture surface topography had an effect on fracture conductivity as the closure stress increases. High surface roughness typically correlated with a high initial undamaged fracture conductivity (at 1,000 psi closure stress). On the other hand, the maximum height difference across the fracture surface was observed to be inversely related to undamaged fracture conductivity at 4,000 psi closure stress.
17. The Brinell hardness number did not exhibit a strong correlation to the fracture conductivity at 4,000 psi closure stress when flowing saline water. This can be attributed to the fact that the indentation tests were not gathered along the fracture surface, but rather on the cross-section of the core plugs.
18. The Poisson's ratio did not exhibit a strong correlation to the fracture conductivity at 4,000 psi closure stress when flowing saline water. Such behavior can be attributed to the mid-range level of closure stress used in the experiments.

Observed behavior suggesting proppant pack self-channeling,

19. A subset of fracture conductivity tests with Eagle Ford formation test samples showed an apparent self-channeling behavior, resulting from the injection procedure and the proppant concentration.
20. Under laboratory conditions, at low proppant concentration loading with small-sized proppant (100 mesh), fracture conductivity tests showed proppant pack self-channeling behavior.

21. This behavior was caused primarily by high velocity gas flow at low closure stresses, without the installment of a screen immediately after the fracture conductivity cell (mitigating proppant displacement).
22. Proppant channeling mechanism originates from fractured unsmooth surfaces, which results in stress profile variations and/or proppant concentration variations along the fracture due to fracture surface topography.
23. Channeling at this condition created fracture conductivity close to larger-sized proppant. Its rate of decline was less pronounced at high closure stresses.
24. Channeling diminished when proppant concentration increased.

6.2 Recommendations and Future Work

Further studies are recommended to extend the scope and findings of this work. Increasing the test sampling size would increase the strength of the findings. The major recommendations are as follows:

1. Ultimately, even though challenging to acquire, using preserved downhole core and revising the experimental setup to better instill downhole conditions might lead to even more realistic fracture conductivity measurements.
2. The fracture conductivity tests were all short-term tests, and inevitably do not account for the time sequence that the fractures undergo from fracturing operations to subsequent flowback. This may drastically reduce the water-induced damage fracture conductivity measurements.
3. Using field flowback water samples, if available, rather than reconstituted ones, may better represent the fluid aspect of the tests. By any measure, expanding the

saline solution flowed through the fracture to include the presence of clay control agents, and/or friction reducer, and/or linear gel may yield interesting findings.

4. Conducting a sensitivity analysis-based fracture conductivity workflow may lead to interesting findings. It could be theorized that exposing the same formation, albeit a new sample each time, to solutions of varying pH as well as other properties, might lead to defining what is the best solution constitution to ensure the least damage. This could in turn aid in designing the fracturing fluid to minimize the expected damage.

REFERENCES

Aguilar, G. 2014. XRF Elemental and Mineralogical Analysis of Core Sample and Well Cuttings in Granite Wash Area of Wheeler County, Texas. MS. Thesis, The University of Texas at Austin, Austin, Texas, U.S.A (December 2014).

Akrad, O., Miskimins, J., and Prasad, M. 2011. The Effect of Fracturing Fluids on Shale Rock Mechanical Properties and Proppant Embedment. Paper presented at the SPE Annual Technical Conference and Exhibition, Denver, Colorado, U.S.A., 30 October-2 November. Society of Petroleum Engineers. DOI: 10.2118/146658-MS.

Ali, M. and Hascakir, B. 2015. Water-Rock Interaction for Eagle Ford, Marcellus, Green River, and Barnett Shale Samples. Paper presented at the SPE Eastern Regional Meeting, Morgantown, West Virginia, U.S.A., 13-15 October. Society of Petroleum Engineers. DOI: 10.2118/177304-MS.

Alramahi, B. and Sundberg, M.I. 2012. Proppant Embedment and Conductivity of Hydraulic Fractures in Shales. Paper presented at the 46th US Rock Mechanics/Geomechanics Symposium, Chicago, Illinois, U.S.A., 24-27 June. American Rock Mechanics Association. ARMA 12-291.

Aoudia, K., Miskimins, J.L., Harris, N.B., and Mnich, C.A. 2010. Statistical Analysis of the Effects of Mineralogy on Rock Mechanical Properties of the Woodford Shale and the Associated Impacts for Hydraulic Fracture Treatment Design. Paper presented at the 44th US Rock Mechanics Symposium and 5th US-Canada Rock Mechanics Symposium, Salt Lake City, Utah, U.S.A, June 27-30. American Rock Mechanics Association. ARMA 10-303.

API RP-61. 1989. *Recommended Practices for Evaluating Short Term Proppant Pack Conductivity*. First Edition, October 1, 1989. Washington, D.C., U.S.A.: American Petroleum Institute.

API RP-19D. 2008. *Measuring the Long-Term Conductivity of Proppants*. First Edition, May 2008. Washington, D.C., U.S.A.: American Petroleum Institute.

ASTM Standard-D7012-14. 2014. *Standard Test Methods for Compressive Strength and Elastic Moduli of Intact Rock Core Specimens under Varying States of Stress and Temperatures*. West Conshohocken, Pennsylvania, U.S.A.: ASTM International.

ASTM Standard-E10-14. 2015. *Standard Test Method for Brinell Hardness of Metallic Materials*. West Conshohocken, Pennsylvania, U.S.A.: ASTM International.

Awoleke, O.O. 2013. Dynamic Fracture Conductivity -an Experimental Investigation Based on Factorial Analysis. PhD Dissertation, Texas A&M University, College Station, Texas, U.S.A. (May 2013).

Awoleke, O.O., Zhu, D., and Hill, A.D. 2016. New Propped-Fracture-Conductivity Models for Tight Gas Sands. *SPE Journal*. DOI: 10.2118/179743-PA.

Barree, R.D. and Conway, M.W. 2008. Multiphase Non-Darcy Flow in Proppant Packs. *SPE Production & Operations* **24** (2): 257-268. DOI: 10.2118/109561-PA.

Barton, N., Bandis, S., and Bakhtar, K. 1985. Strength, Deformation and Conductivity Coupling of Rock Joints. *Int J Rock Mech Min Sci & Geomech Abstr* **22** (3): 121-140.

Bello, R. O. 2009. Rate Transient Analysis in Shale Gas reservoirs With Transient Linear Behavior. PhD Dissertation, Texas A&M University, College Station, Texas, U.S.A. (May 2009).

Bello, R. O., and Wattenbarger, R. A. 2010. Multi-stage Hydraulically Fractured Horizontal Shale Gas Well Rate Transient Analysis. Paper presented at the North Africa Technical Conference and Exhibition, 14-17 February, Cairo, Egypt. Society of Petroleum Engineers. DOI:10.2118/126754-MS.

Branagan, P.T., Warpinski, N.R., Engler, B., and Wilmer, R. 1996. Measuring the Hydraulic Fracture-Induced Deformation of Reservoirs and Adjacent Rocks Employing a Deeply Buried Inclinometer Array: Gri/Doe Multi-Site Project. Paper presented at the SPE Annual Technical Conference and Exhibition, Denver, Colorado, U.S.A., 6-9 October. Society of Petroleum Engineers. DOI: 10.2118/36451-MS.

Brannon, H.D., Malone, M.R., Rickards, A.R., Wood, W.D., Edgeman, J.R., and Bryant, J.L. 2004. Maximizing Fracture Conductivity with Proppant Partial Monolayers: Theoretical Curiosity or Highly Productive Reality? Paper presented at the SPE Annual Technical Conference and Exhibition, Houston, Texas, U.S.A., 26-29 September. Society of Petroleum Engineers. DOI: 10.2118/90698-MS.

Britt, L.K., Smith, M.B., Haddad, Z., Lawrence, P., Chipperfield, S., and Hellman, T. 2006. Water-Fracs: We Do Need Proppant after All. Paper presented at the SPE Annual Technical Conference and Exhibition, San Antonio, Texas, U.S.A., 24-27 September. Society of Petroleum Engineers. DOI: 10.2118/102227-MS.

Chatellier, J.D., Moslow, T.F., and Haverslew, B. 2014. The Use of X-Ray Fluorescence for Sequence Stratigraphy and Geomechanics of Shale. Paper presented at the GeoConvention 2014: FOCUS, Calgary, Alberta, Canada, 12-16 May. CSPG Canada's Energy Geoscientists.

Cinco-Ley, H. and Samaniego-V, F. 1978. Transient Pressure Behavior for a Well with a Finite Conductivity Vertical Fracture. *Society of Petroleum Engineers Journal* **18**: 253-264.

Cinco-Ley, H. and Samaniego-V, F. 1981. Transient Pressure Analysis for Fractured Wells. *Journal of Petroleum Technology,* **SPE-7490** (33): 1749-1766.

Cipolla, C.L., Lolon, E., Mayerhofer, M.J., and Warpinski, N.R. 2009. The Effect of Proppant Distribution and Un-Propped Fracture Conductivity on Well Performance in Unconventional Gas Reservoirs. Paper presented at the SPE Hydraulic Fracturing Technology Conference, The Woodlands, Texas, U.S.A., 19-21 January. Society of Petroleum Engineers. DOI: 0.2118/119368-MS.

Cohen, C.-E., Kresse, O., and Weng, X. 2017. Stacked Height Model to Improve Fracture Height Growth Prediction, and Simulate Interactions with Multi-Layer Dfns and Ledges at Weak Zone Interfaces. Paper presented at the SPE Hydraulic Fracturing Technology Conference and Exhibition, The Woodlands, Texas, U.S.A., 24-26 January. Society of Petroleum Engineers. DOI: 10.2118/184876-MS.

Conway, M.W., Venditto, J.J., Reilly, P.B., and Smith, K.W. 2011. An Examination of Clay Stabilization and Flow Stability in Various North American Gas Shales. Paper presented at the SPE Annual Technical Conference and Exhibition, Denver, Colorado, U.S.A., 30 October-2 November. Society of Petroleum Engineers. DOI: 10.2118/147266-MS.

Cooke Jr., C.E. 1973. Conductivity of Fracture Proppants in Multiple Layers. *Journal of Petroleum Technology* **25** (9): 1101-1107. DOI: 10.2118/4117-PA.

Cooke Jr., C.E. 1975. Effect of Fracturing Fluids on Fracture Conductivity. *Journal of Petroleum Technology* **27** (10): 1273-1282. DOI: 10.2118/5114-PA.

Coulter, G.R., Benton, E.G., and Thomson, C.L. 2004. Water Fracs and Sand Quantity: A Barnett Shale Example. Paper presented at the SPE Annual Technical Conference and Exhibition, Houston, Texas, U.S.A, 26-29 September. Society of Petroleum Engineers. DOI: 10.2118/90891-MS.

Crandall, D., Li, L., Wen, H., and Hakala, A. 2014. Reactive Geochemical Flow Modeling with Ct Scanned Rock Fractures. In *ASME 2014 4th Joint US-European Fluids Engineering Division Summer Meeting*. Chicago, Illinois, USA, 3-7 August. FEDSM2014-21579.

Daal, J. A. and Economides, M. J. 2006. Optimization of Hydraulically Fractured Wells in Irregularly Shaped Drainage Areas. Paper presented at the SPE International Symposium and Exhibition on Formation Damage Control, Lafayette, Louisiana, U.S.A, 15-17 February. Society of Petroleum Engineers. DOI:10.2118/98047-MS.

Daniels, J.L., Waters, G.A., Le Calvez, J.H., Bentley, D., and Lassek, J.T. 2007. Contacting More of the Barnett Shale through an Integration of Real-Time Microseismic Monitoring, Petrophysics and Hydraulic Fracture Design. Paper presented at the SPE Annual Technical Conference and Exhibition Anaheim, California, U.S.A., 12-14 October. Society of Petroleum Engineers. DOI: 0.2118/110562-MS.

Darin, S.R. and Huitt, J.L. 1960. Effect of a Partial Monolayer of Proppant Agent on Fracture Flow Capacity. *AIME Petroleum Transactions* **219**: 31-37. 1291-G SPE General.

Donovan, A.D. and Staerker, T.S. 2010. Sequence Stratigraphy of the Eagle Ford (Boquillas) Formation in the Subsurface of South Texas and Outcrops of West Texas. *Gulf Coast Association of Geological Societies Transactions* **60**: 861-899.

Donovan, A.D., Staerker, T.S., Pramudito, A., Li, W., Corbett , M.J., Lowery, C.M., Romero, A.M., and Gardner, R.D. 2012. The Eagle Ford Outcrops of West Texas: A Laboratory for Understanding Heterogeneities within Unconventional Mudstone Reservoirs. *CGAGS Journal* **1**: 162-185.

Duenckel, R. J., Barree, R. D., Drylie, S., O'Connell, L. G., Abney, K. L., Conway, M. W., … Chen, F. 2017. Proppants- What 30 Years of Study has Taught Us. Society of Petroleum Engineers. DOI: 10.2118/187451-MS.

Economides, M.J. and Nolte, K.G. 2000. *Reservoir Stimulation*. Third Edition, March 2000. New York, New York, U.S.A and Chichester, U.K.: J. Wiley & Sons.

Economides, M. J., Oligney, R. E. and Valko, P. P. 2002. *Unified Fracture Design*. Alvin, Texas, U.S.A.: Orsa Press.

Economides, M.J. and Martin, T. 2007. *Modern Fracturing: Enhancing Natural Gas Production*. BJ Services Company. Houston, Texas, U.S.A.: Energy Tribune Publishing Inc.

Economides, M.J., Hill, A.D., Ehlig-Economides, C., and Zhu, D. 2013. *Petroleum Production Systems*. Second Edition, October 5, 2012. Englewood Cliffs, New Jersey, U.S.A.: Pearson Education, Inc., Prentice Hall.

Enriquez, O. 2016. A Comprehensive Study of the Eagle Ford Shale Fracture Conductivity. MS Thesis, Texas A&M Universtity, College Station, Texas, U.S.A. (August 2016).

Enriquez, O., Knorr, A., Zhu, D., and Hill, A.D. 2016. Relationships between Mechanical Properties and Fracturing Conductivity for the Eagle Ford Shale. Paper presented at the SPE Asia Pacific Hydraulic Fracturing Conference, Beijing, China, 24-26 August. Society of Petroleum Engineers. DOI: 10.2118/181858-MS.

Ereaux, B.A. 2017. Vibration Modification to A.P.I Fracture Short Term Conductivity Testing Procedure. MS Thesis, Montana Tech, Butte, Montana, U.S.A. (December 2017).

Fredd, C.N., McConnell, S.B., Boney, C.L., and England, K.W. 2000. Experimental Study of Hydraulic Fracture Conductivity Demonstrates the Benefits of Using Proppants. Paper presented at the SPE Rocky Mountain Regional/Low Permeability Reservoirs Symposium, Denver, Colorado, U.S.A., 12-15 March. Society of Petroleum Engineers. DOI: 10.2118/60326-MS.

Fredd, C.N., McConnell, S.B., Boney, C.L., and England, K.W. 2001. Experimental Study of Fracture Conductivity for Water-Fracturing and Conventional Fracturing Applications. *SPE Journal*: 288-298. DOI: 10.2118/74138-PA.

Gamero-Diaz, H., Miller, C.K., and Lewis, R. 2013. sCore: A Mineralogy Based Classification Scheme for Organic Mudstones. Paper presented at the SPE Annual Technical Conference and Exhibition, New Orleans, Louisiana, U.S.A., 30 September-2 October. Society of Petroleum Engineers. DOI: 10.2118/166284-MS.

Gardner, R.D., Pope, M.C., Wehner, M.P., and Donovan, A.D. 2013. Comparative Stratigraphy of the Eagle Ford Group Strata in Lozier Canyon and Antonio Creek, Terrel County, Texas, U.S.A. *GCAGS Journal* **2**: 42-52.

Ghassemi, A. and Suarez-Rivera, R. 2012. Sustaining Fracture Area and Conductivity of Gas Shale Reservoirs for Enhancing Long-Term Production and Recovery. *RPSEA 08122-48 Final Report*.

Geertsma, J. and de Klerk, F. 1969. A Rapid Method of Predicting Width and Extent of Hydraulically Induced Fractures. *Journal of Petroleum Technology,* **21** (12): 1571-1581. DOI: 10.2118/2458-PA.

Gidley, J.L., Holditch, S.A., Nierode, D.E., and Veatch Jr., R.W. 1989. *Recent Advances in Hydraulic Fracturing*. SPE Henry L. Doherty Series Monograph, Volume 12. Richardson, Texas, U.S.A.: Society of Petroleum Engineers.

Gillard, M.R., Medvedev, O.O., Hosein, P.R., Medvedev, A., Peñacorada, F., and Huteau, E. 2010. A New Approach to Generating Fracture Conductivity. Paper presented at the SPE Annual Technical Conference and Exhibition, Florence, Italy, 20-22 September. Society of Petroleum Engineers. DOI: 10.2118/135034-MS.

Gomaa, A.M., Hudson, H., Nelson, S., and Brannon, H. 2016. Hydraulic Fracturing Treatment Design Considerations for Effective Proppant Pillar Construction. Paper presented at the SPE Annual Technical Conference and Exhibition, Dubai, U.A.E., 26-28 September. Society of Petroleum Engineers. DOI: 10.2118/181508-MS.

Grieser, W.V. and Bray, J.M. 2007. Identification of Production Potential in Unconventional Reservoirs. Paper presented at the SPE Production and Operations Symposium, Oklahoma City, Oklahoma, U.S.A., 31 March-3 April Society of Petroleum Engineers. DOI: 10.2118/106623-MS.

Guerra, J., Uribe, J., Luna, E., Zhu, D. 2017a. Self-Channeling in Proppant Pack in the Eagle Ford Shale Formation. Presented at the SPE Latin American and Caribbean Petroleum Engineering Conference, Buenos Aires, Argentina, 17-19 May. Paper SPE-185561-MS. Copyright 2017 by the Society of Petroleum Engineers.

Guerra, J., Zhu, D., and Hill, A.D. 2017b. A Comparative Study of the Effects of Clay Content on the Fracture Conductivity of the Eagle Ford Shale and Marcellus Shale Formations. Paper presented at the Unconventional Resources Technology Conference, Austin, Texas, U.S.A., 24-26 July. Unconventional Resources Technology Conference. DOI: 10.15530/URTEC-2017-2716913.

Guerra, J., Zhu, D., and Hill, A.D. 2018. Impairment of Fracture Conductivity in the Eagle Ford Shale Formation. *SPE Production & Operations*. DOI: 10.2118/184857-PA.

Hayes, T. 2011. Characterization of Marcellus and Barnett Shale Flowback Waters and Technology Development for Water Reuse. Paper presented at the Gas Technology Institute, Hydraulic Fracturing Technical Workshop #4, USEPA Meeting Facilities, Arlington, Virginia, U.S.A., 30 March.

Horner, P., Halldorson, B., and Slutz, J. A. 2011. Shale Gas Water Treatment Value Chain – A Review of Technologies, Including Case Studies. Presented at the SPE Annual Technical Conference and Exhibition, Denver, Colorado, U.S.A., 30 October - 2 November. Society of Petroleum Engineers. DOI: 10.2118/147264-MS.

Hou, T., Zhang, S., Ma, X., Shao, J., He, Y., Lv, X., and Han, J. 2016. Experimental and Theoretical Study of Fracture Conductivity with Heterogeneous Proppant Placement. *Journal of Natural Gas Science and Engineering* (37): 449-461.

Huang, H. and Ayoub, J.A. 2008. Applicability of the Forchheimer Equation for Non-Darcy Flow in Porous Media. *SPE Journal* **13** (01): 112-122. DOI: 10.2118/102715-PA

Iriarte, J.G. 2017. Fluid-Shale-Proppant Interactions and the Degradation of Hydraulic Fracture Conductivity in the Niobrara Formation. MS Thesis, Colorado School of Mines, Golden, Colorado, U.S.A. (May 2017).

ISO-13503-2. 2008. *Recommend Practices for Measurement of Proppants Used in Hydraulic Fracturing and Gravel-Packing Operations*. RP 19C, ISO 13503-2:2006. New York, New York, U.S.A.: American Petroleum Institute.

ISO-13503-5. 2008. *Recommended Practices for Measurement of Long-Term Conductivity of Proppant*. ISO 13503-5:2006. New York, New York, U.S.A.: American Petroleum Institute.

Jansen, T.A. 2014. The Effect of Rock Properties on Hydraulic Fracture Conductivity in the Eagle Ford and Fayetteville Shales. MS Thesis, Texas A&M University, College Station, Texas, U.S.A. (December 2014).

Johri, M. and Zoback, M.D. 2013. The Evolution of Stimulated Reservoir Volume during Hydraulic Stimulation of Shale Gas Formations. Paper presented at the Unconventional Resources Technology Conference, Denver, Colorado, U.S.A., 12-14 August. Unconventional Resources Technology Conference. URTEC-1575434-MS.

Kainer, C., Guerra, D., Zhu, D., and Hill, A.D. 2017. A Comparative Analysis of Rock Properties and Fracture Conductivity in Shale Plays. Paper presented at the SPE Hydraulic Fracturing Technology Conference and Exhibition The Woodlands, Texas, U.S.A., 24-26 January. Society of Petroleum Engineers. . DOI: 10.2118/184877-MS.

Kainer, C.J. 2017. Predicting Hydraulic Fracture Conductivity in Shale Plays. MS Thesis, Texas A&M University, College Station, Texas, U.S.A. (August 2017).

Kamenov, A.N. 2013. The Effect of Proppant Size and Concentration on Hydraulic Fracture Conductivity in Shale Reservoirs. MS Thesis, Texas A&M Universtity, College Station, Texas, U.S.A. (May 2013).

Kassis, S.M. 2011. Fracture Permeability in the Barnett Shale: Effects of Roughness, Fracture Offset, Proppant, and Effective Stress. Paper presented at the AAPG Annual Convention and Exhibition, Houston, Texas, U.S.A., 10-13 April. AAPG.

Khristianovic(h), S.A. and Zheltov, Y.P. 1955. Formation of Vertical Fractures by Means of Highly Viscous Liquid. *Proc. Forth World Petroleum Congress*: Sec. II, 579-586.

Kias, E., Maharidge, R., and Hurt, R. 2015. Mechanical Versus Mineralogical Brittleness Indices across Various Shale Plays. Paper presented at the SPE Annual Technical Conference and Exhibition, Houston, Texas, U.S.A., 28-30 September. Society of Petroleum Engineers. DOI: 10.2118/174781-MS.

King, G.E. 2010. Thirty Years of Gas Shale Fracturing: What Have We Learned? Paper presented at the SPE Annual Technical Conference and Exhibition, Florence, Italy, 19–22 September. Society of Petroleum Engineers. DOI: 10.2118/133456-MS.

Knorr, A.F. 2016. The Effect of Rock Properties on Fracture Conductivity in the Eagle Ford. MS Thesis, Texas A&M University, College Station, Texas, U.S.A. (May 2016).

Malhotra, S., Lehman, E.R., and Sharma, M.M. 2014. Proppant Placement Using Alternate-Slug Fracturing. *SPE Journal*: 974-985. DOI: 10.2118/163851-PA.

Mao, D., Miller, D.S., Karanikas, J.M., Lake, E.A., Fair, P.S., and Liu, X. 2017. Influence of Finite Hydraulic-Fracture Conductivity on Unconventional Hydrocarbon Recovery with Horizontal Wells. *SPE Journal*: 1790-1807. DOI: 10.2118/187947-PA.

Marpaung, F., Chen, F., Pongthunya, P., Zhu, D., and Hill, A.D. 2008. Measurement of Gel Cleanup in a Propped Fracture with Dynamic Fracture Conductivity Experiments. Paper presented at the SPE Annual Technical Conference and Exhibition Denver, Colorado, U.S.A., 21-24 September. Society of Petroleum Engineers. DOI: 10.2118/115653-MS.

Mayerhofer, M.J., Lolon, E.P., Youngblood, J.E., and Heinze, J.R. 2006. Integration of Microseismic Fracture Mapping Results with Numerical Fracture Network Production Modeling in the Barnett Shale. Paper presented at the SPE Annual Technical Conference and Exhibition San Antonio, Texas, U.S.A., 24-27 September. Society of Petroleum Engineers. DOI: 10.2118/102103-MS.

McGinley, M.J. 2015. The Effects of Fracture Orientation and Anisotropy on Hydraulic Fracture Conductivity in the Marcellus Shale. MS Thesis, Texas A&M University, College Station, Texas, U.S.A. (May 2015).

Montgomery, C.T. 2017. Hydraulic Fracturing Course, Lecture No. 2: In Situ Stress. In *NSI Technologies Industry Course*. June 2017.

Nguyen, P.D., Vo, L.K., Parton, C., Heeter, J., Gashimov, R., and O'Connell, P. 2014. Evaluation of Low-Quality Sand for Proppant-Free Channel Fracturing Method. Paper presented at the International Petroleum Technology Conference, Kuala Lumpur, Malaysia, 10–12 December. IPTC-17937-MS.

Nordgren, R.P. 1972. Propagation of a Vertical Hydraulic Fracture. *Society of Petroleum Engineers Journal* **12** (04): 306-314. DOI: 10.2118/3009-PA.

Palisch, T.T., Duenckel, R.J., Bazan, L.W., Heidt, J.H., and Turk, G.A. 2007. Determining Realistic Fracture Conductivity and Understanding Its Impact on Well Performance - Theory and Field Examples. Paper presented at the SPE Hydraulic Fracturing Technology Conference, College Station, Texas, U.S.A., 29-31 January Society of Petroleum Engineers. DOI: 10.2118/106301-MS.

Palisch, T.T., Vincent, M., and Handren, P.J. 2010. Slickwater Fracturing: Food for Thought. *SPE Production & Operations*: 327-344. DOI: 10.2118/115766-PA.

Parker, M.A. and McDaniel, B.W. 1987. Fracturing Treatment Design Improved by Conductivity Measurements under in-Situ Conditions. Paper presented at the SPE Annual Technical Conference and Exhibition, Dallas, Texas, U.S.A., 27-30 September. Society of Petroleum Engineers. DOI: 10.2118/16901-MS.

Passey, Q.R., Bohacs, K., Esch, W.L., Klimentidis, R., and Sinha, S. 2010. From Oil-Prone Source Rock to Gas-Producing Shale Reservoir – Geologic and Petrophysical Characterization of Unconventional Shale-Gas Reservoirs. Paper presented at the CPS/SPE International Oil & Gas Conference and Exhibition China held in Beijing, China, 8-10 June Society of Petroleum Engineers. DOI: 10.2118/131350-MS.

Pedlow, J.W. 2013. A Study of the Effect of Stress and Fluid Sensitivity on Propped Fracture Conductivity in Preserved Reservoir Shales. MS Thesis, The University of Texas at Austin, Austin, Texas, U.S.A. (May 2013).

Pedlow, J. and Sharma, M. 2014. Changes in Shale Fracture Conductivity Due to Interactions with Water-Based Fluids. Paper presented at the SPE Hydraulic Fracturing Technology Conference The Woodlands, Texas, U.S.A., 4-6 February. Society of Petroleum Engineers. DOI: 10.2118/168586-MS.

Perez, P.A. 2015. The Effect of Rock Properties on Fracture Conductivity in the Marcellus Shale. MS Thesis, Texas A&M University, College Station, Texas, U.S.A. (December 2015).

Perez, P., Zhu, D., and Hill, A.D. 2016. The Effect of Rock Properties on Fracture Conductivity in the Marcellus Shale. Paper presented at the SPE Asia Pacific Hydraulic Fracturing Conference, Beijing, China, 24-26 August. Society of Petroleum Engineers. DOI: 10.2118/181867-MS.

Perkins, T.K. and Kern, L.R. 1961. Widths of Hydraulic Fracture. *Journal of Petroleum Technology* **13** (09): 937-949.

Prats, M. 1961. Effect of Vertical Fractures on Reservoir Behavior-Incompressible Fluid Case. *SPE Journal* **1** (02): 105-118. DOI: 10.2118/1575-G

Raimbay, A., Babadagli, T., Kuru, E., and Develi, K. 2015. Quantitative and Visual Analysis of Proppant Transport in Rough Fractures and Aperture Stability. Paper presented at the SPE Hydraulic Fracturing Technology Conference, The Woodlands, Texas, U.S.A., 3-5 February. Society of Petroleum Engineers. DOI: 10.2118/173385-MS.

Ramurthy, M., Barree, R.D., Kundert, D.P., Petre, J.E., and Mullen, M.J. 2011. Surface Area vs. Conductivity Type Fracture Treatments in Shale Reservoirs. *SPE Production & Operations* **26** (04): 357-367. DOI: 10.2118/140169-PA.

Reinicke, A. 2011. Mechanical and Hydraulic Aspects of Rock-Proppant Systems: Laboratory Experiments and Modelling Approaches. *Helmholtz-Zentrum Potsdam*: Scientific Technical Report STR11/09. DOI: 10.2312/GFZ.b103-11098.

Shekhawat, D.S. and Pathak, K. 2016. Proppant's Performance with Reservoir Rock under Variable Closure Pressure: Results of Experiments with a Newly Developed Experimental Set-Up. *Journal of Petroleum Science and Engineering* **147** (November 2016): 34-46. DOI: 10.1016/j.petrol.2016.05.003.

Shelley, R.F., Grieser, W.V., Johnson, B.J., Fielder, E.O., Heinze, J.R., and Werline, J.R. 2008. Data Analysis of Barnett Shale Completions. *SPE Journal* **13** (03): 366-374. DOI: 10.2118/100674-PA.

Slatt, R.M. and Abousleiman, Y. 2011. Merging Sequence Stratigraphy and Geomechanics for Unconventional Gas Shales. *The Leading Edge, Special Section: Shales* (March 2011): 274-282.

Slutz, J.A., Anderson, J. A., Broderick, R., & Horner, P. H. 2012. Key Shale Gas Water Management Strategies: An Economic Assessment Tool. Paper presented at the SPE/APPEA International Conference on Health, Safety, and Environment in Oil and Gas Exploration and Production Perth, Australia, 11–13 September. Society of Petroleum Engineers. DOI: 10.2118/157532-MS.

Smith, M.B. and Montgomery, C.T. 2015. *Hydraulic Fracturing*. First Edition, June 9, 2015. Boca Raton, Florida, U.S.A.: CRC Press, Taylor & Francis Group.

Sone, H. and Zoback, M. D. 2013. Mechanical Properties of Shale-Gas Reservoir Rocks - Part 2: Ductile Creep, Brittle Strength, and Their Relationship to the Elastic Modulus. *Geophysics* **78**(5).

Song, B., Economides, M. J., and Ehlig-Economides, C. A. 2011. Design of Multiple Transverse Fracture Horizontal Wells in Shale Gas Reservoirs. Paper presented at the SPE Hydraulic Fracturing Conference, The Woodlands, Texas, U.S.A., 24-26 January. Society of Petroleum Engineers. DOI: 10.2118/140555-MS.

Stim-Lab Proppant Consortium. 2018. Core Laboratories. U.S. Headquarters: Houston, Texas, U.S.A.

Suárez-Rivera, R., Green, S.J., McLennan, J., and Bai, M. 2006. Effect of Layered Heterogeneity on Fracture Initiation in Tight Gas Shales. Paper presented at the SPE Annual Technical Conference and Exhibition, San Antonio, Texas, U.S.A., 24-27. Society of Petroleum Engineers. DOI: 10.2118/103327-MS.

Suárez-Rivera, R., Deenadayalu, C., Chertov, M., Hartanto, R.N., Gathogo, P., and Kunjir, R. 2011. Improving Horizontal Completions on Heterogeneous Tight Shales. Paper presented at the Canadian Unconventional Resources Conference, Calgary, Alberta, Canada, 15-17 November. Society of Petroleum Engineers. DOI: 10.2118/146998-MS.

Suárez-Rivera, R., Burghardt, J., Edelman, E., Stanchits, S., and Surdi, A. 2013. Geomechanics Considerations for Hydraulic Fracture Productivity. Paper presented at the 47th U.S. Rock Mechanics/Geomechanics Symposium, San Francisco, California, 23-26 June. American Rock Mechanics Association. ARMA-2013-666.

Tek, M.R., Coats, K.H., and Katz, D.L. 1962. The Effect of Turbulence on Flow of Natural Gas through Porous Reservoirs. *Journal of Petroleum Technology* **14** (07): 799-806. DOI: 10.2118/147-PA.

Thompson, J. and Peña, A. 2015. Flow-Channel Fracturing Raises Production in the Eagle Ford. *World Oil, ShaleTech Report* (September 2015): S4-S7.

U.S. Energy Information Administration. 2013. Technically Recoverable Shale Oil and Shale Gas Resources: An Assessment of 137 Shale Formations in 41 Countries outside the United States. US Department of Energy, Washington, D.C., U.S.A. 20585 (June 2013).

U.S. Energy Information Administration. 2018. Drilling Productivity Report: For Key Tight Oil and Shale Gas Regions. (May 2018).

Valko, P. P. and Economides, M. J. 1998. Heavy Crude Production from Shallow Formations: Long Horizontal Wells Versus Horizontal Fractures. Paper presented at the SPE International Conference on Horizontal Well Technology, Calgary, Alberta, Canada, 1-4 November. Society of Petroleum Engineers. DOI: 10.2118/50421-MS.

van Dam, D.B. and de Pater, C.J. 1999. Roughness of Hydraulic Fractures: The Importance of in-Situ Stress and Tip Processes. Paper presented at the SPE Annual Technical Conference and Exhibition, Houston, Texas, U.S.A., 3-6 October. Society of Petroleum Engineers. DOI: 10.2118/56596-MS.

Warpinski, N.R. and Teufel, L.W. 1987. Influence of Geologic Discontinuities on Hydraulic Fracture Propagation. *Journal of Petroleum Technology* **39** (02): 209-220, 998-999 (includes associated SPE papers 17011 and 17074). DOI: 10.2118/13224-PA.

Warpinski, N.R. 1991. Hydraulic Fracturing in Tight, Fissured Media. *Journal of Petroleum Technology* **43** (02): 136-152, 208-209. DOI: 10.2118/20154-PA.

Warpinski, N.R., Mayerhofer, M.J., Vincent, M.C., Cipolla, C.L., and Lolon, E. 2008. Stimulating Unconventional Reservoirs: Maximizing Network Growth While Optimizing Fracture Conductivity. Paper presented at the SPE Unconventional Reservoirs Conference, Keystone, Colorado, U.S.A., 10-12 February. Society of Petroleum Engineers. DOI: 10.2118/114173-MS.

Warpinski, N.R. 2009. Stress Amplification and Arch Dimensions in Proppant Beds Deposited by Waterfracs. Paper presented at the SPE Hydraulic Fracturing Technology Conference, The Woodlands, Texas, U.S.A., 19-21 January. Society of Petroleum Engineers. DOI: 10.2118/119350-MS.

Weaver, J.D., Rickman, R.D., and Luo, H. 2008. Fracture Conductivity Loss Due to Geochemical Interactions between Man-Made Proppants and Formations. Paper presented at the SPE Eastern Regional/AAPG Eastern Section Joint Meeting, Pittsburgh, Pennsylvania, U.S.A., 11-15 October. Society of Petroleum Engineers. DOI: 10.2118/118174-MS.

Wei, Y. and Economides, M. J. 2005. Transverse Hydraulic Fractures from a Horizontal Well. Paper presented at the SPE Annual Technical Conference and Exhibition, Dallas, Texas. Society of Petroleum Engineers. DOI: 10.2118/94671-MS.

Wen, Q., Zhang, S., Wang, L., Liu, Y., and Li, X. 2007. The Effect of Proppant Embedment Upon the Long-Term Conductivity of Fractures. *Journal of Petroleum Science and Engineering* **55** (3): 221-227. DOI: 10.1016/j.petrol.2006.08.010.

Wu, W., Russell, R., and Sharma, M. 2017. An Experimental Method to Study the Impact of Fracturing Fluids on Fracture Conductivity in Heterogeneous Shales. Paper presented at the Unconventional Resources Technology Conference, Austin, Texas, U.S.A., 24-26 July. Unconventional Resources Technology Conference. DOI: 10.15530/URTEC-2017-2669936.

Xu, J., Fisher, K., Qiu, F., Malpani, R., Ejofodomi, E., and Viswanathan, A. 2016. Impact of Ash Beds on Production in Eagle Ford Shale. Paper presented at the SPE Hydraulic Fracturing Technology Conference, The Woodlands, Texas, U.S.A., 9-11 February. Society of Petroleum Engineers. DOI: 10.2118/179110-MS.

Zhang, J. 2014. Creation and Impairment of Hydraulic Fracture Conductivity in Shale Formations. Texas A&M University, College Station, Texas, U.S.A. (August 2014).

Zhang, J., Ouyang, L., Hill, A.D., and Zhu, D. 2014. Experimental and Numerical Studies of Reduced Fracture Conductivity Due to Proppant Embedment in Shale Reservoirs. Paper presented at the SPE Annual Technical Conference and Exhibition, Amsterdam, The Netherlands, 27-29 October. Society of Petroleum Engineers. DOI: 10.2118/170775-MS.

Zhang, J., Zhu, D., and Hill, A.D. 2015. Water-Induced Fracture Conductivity Damage in Shale Formations. Paper presented at the SPE Hydraulic Fracturing Technology Conference, The Woodlands, Texas, U.S.A., 3-5 February. Society of Petroleum Engineers. DOI: 10.2118/173346-MS.

Zhang, J., Zhu, D., and Hill, A.D. 2015. A New Theoretical Method to Calculate Shale Fracture Conductivity Based on the Population Balance Equation. *Journal of Petroleum Science and Engineering* **134** (2015): 40-48. DOI: 10.1016/j.petrol.2015.07.019.

Zheng, X., Chen, M., Hou, B., Ye, Z., Wang, W., Yin, C., and Chen, X. 2017. Effect of Proppant Distribution Pattern on Fracture Conductivity and Permeability in Channel Fracturing. *Journal of Petroleum Science and Engineering* **149** (2017): 98–106. DOI: 10.1016/j.petrol.2016.10.023.